The Pennsylvania State University

The Graduate School

College of Engineering

THE 12 CC PENN STATE PEDIATRIC VENTRICULAR ASSIST DEVICE: A FLOW VISUALIZATION STUDY OF BRIDGE-TO-RECOVERY AND WEANING

A Dissertation in

Bioengineering

by

Breigh Nonte Roszelle

Submitted in Partial Fulfillment
of the Requirements
for the Degree of

Doctor of Philosophy

December 2010

The dissertation of Breigh Nonte Roszelle was reviewed and approved* by the following:

Keefe B. Manning
Associate Professor of Bioengineering
Dissertation Advisor
Chair of Committee

Steven Deutsch
Senior Scientist
Professor Emeritus of Bioengineering

William J. Weiss
Howard E. Morgan Professor of Surgery and Bioengineering

Lacy A. Holowatz
Assistant Professor of Kinesiology

Herbert H. Lipowsky
Professor and Chairman of Bioengineering
Head of the Department of Bioengineering

*Signatures are on file in the Graduate school.

ABSTRACT

While mechanical circulatory support systems have shown success as bridge-to-transplant devices for end-stage heart failure patients, recent evidence shows that sufficient myocardial recovery may occur during device use to allow for explantation without transplant. As Penn State continues development on a 12 cc pulsatile pediatric ventricular assist device (PVAD), studying the impact of this device in clinically relevant situations, such as bridge-to-recovery and weaning is important. The device fluid mechanics are of importance, because a major problem is thromboembolic events, which can be prevented in pulsatile VADs with adequate wall shear rates (>500 s^{-1}). In order to observe the PVAD flow particle image velocimetry was performed on an acrylic model of the PVAD in a mock circulatory loop. Two flow rate reduction studies were performed. The first used a beat rate reduction protocol, focused on 50 and 75 bpm. This study found that a beat rate reduction led to flow more conducive to thrombus deposition, and would not be recommended for weaning. The second used a stroke volume reduction protocol that incrementally reduced the device output from 100 to 40%, and included two filling methods, a quick and slow fill. The study found that the quick fill method produced desirable flow in the PVAD for stroke volumes of 100% to 60%, and the fluid dynamics were preferable over the beat rate reduction method. The slow fill method showed poor flow and is not recommended. The study also found that regardless of the filling method, a reduction in stroke volume below 60% led to greatly reduced wall shear rates that could increase the thrombogenicity of the device. These conclusions are also based on a newly developed thrombus susceptibility potential metric that incorporates wall shear rate information into a single metric to be used for comparison of device variations. Overall, this study identified an acceptable flow reduction method using stroke volume reduction with a quick fill method.

TABLE OF CONTENTS

LIST OF TABLES ……viii

LIST OF FIGURES ……ix

ACKNOWLEDGMENTS ……...……..xx

Chapter 1: INTRODUCTION ……1

1.1 Clinical Need 1

1.1.1 Pediactric Cardiovascular Disease 1

1.1.2 Ventricular Assist Devices 3

1.1.3 Pediatric Circulatory Support 4

1.1.4 Thromboembolic Events 7

1.1.5 Bridge-to-Recovery 7

1.1.6 Weaning 9

1.2. Fluid Mechanics of Ventricular Assist Devices ……10

1.3 Fluid Mechanics of Pediatric Ventricular Assist Devices 13

1.3.1 PVAD Valve Selection Study 15

1.3.2 PVAD Three-Dimensionality Study 19

1.3.3 PVAD Valve Orientation Study 25

1.3.4 PVAD Operational Protocol Study 29

1.3.5 PVAD Analog Hematocrit Study 34

1.4 Current Study 36

Chapter 2: PARTICLE IMAGE VELOCIMETRY …….……37

2.1 Pariticle Image Velocimetry Basics ……..…….....37

2.1.1 Displacement Theory 38

2.1.2 Particles..... 40

2.1.3 Illumination 41

2.1.4 Image Capture 42

2.2 Processing 42

2.3 Sources of Error 49

2.3.1 Peak Locking 49

2.3.2 Projection Error 50
2.3.3 Out-of-Plane Motion 51
2.4 Using PIV to Measure Flow in VADs 52

Chapter 3: METHODOLOGY 53
3.1 Pediatric Ventricular Assist Device Model 53
3.2 Mock Circulatory Loop 55
3.3 Blood Analog 62
3.4 High Speed Video 64
3.5 Particle Image Velocimetry 64
3.5.1 PIV Setup and Data Collection 64
3.5.2 PIV Processing 68
3.5.2.1 Wall Finding 68
3.5.2.2 Vector Calculation 69
3.5.2.3 Wall Shear Rate Calculation 70
3.5.3 PIV Error Analysis 73

Chapter 4: BEAT RATE REDUCTION STUDY 75
4.1 Specific Aim 75
4.2 Conditions 75
4.3 Results 78
4.3.1 Seventy-Five Beats Per Minute 79
4.3.1.1 Diastole 79
4.3.1.2 Transition from Diastole to Systole 81
4.3.1.3 Systole 82
4.3.2 Fifty Beats Per Minute 83
4.3.2.1 Diastole 83
4.3.2.2 Transition from Diastole to Systole 87
4.3.2.3 Systole 88
4.4 Discussion 89
4.4.1 Diastole 89

4.4.2 Transition from Diastole to Systole 96
4.4.3 Systole 97
4.5 Conclusion 100

Chapter 5: STROKE VOLUME REDUCTION STUDY ……... 101
5.1 Specific Aim 101
5.2 Conditions 102
5.3 Results 110
5.3.1 Diaphragm Motion 110
5.3.2 PIV Results 112
5.3.2.1 12 cc Quick Fill 112
5.3.2.2 12 cc Slow Fill 120
5.3.2.3 9.6 cc Quick Fill 127
5.3.2.4 9.6 cc Slow Fill 133
5.3.2.5 7.2 cc Quick Fill 139
5.3.2.6 7.2 cc Slow Fill 146
5.3.2.7 4.8 cc Quick Fill 153
5.3.2.8 4.8 cc Slow Fill 157
5.4 Discussion 160
5.4.1 Stroke Volume Comparison – Quick Fill 160
5.4.1.1 Inlet Jet Formation 161
5.4.1.2 Rotational Flow Development 166
5.4.1.3 Diastolic Recirculation 169
5.4.1.4 Outlet Port Recirculation 171
5.4.2 Stroke Volume Comparison – Slow Fill 173
5.4.2.1 Inlet Jet Formation 173
5.4.2.2 Rotational Flow Development 177
5.4.2.3 Diastolic Recirculation 179
5.4.3 Filling Method Comparison 181
5.4.4 Reduction Method Comparison 183
5.5 Conclusion 188

Chapter 6: DEVELOPMENT OF A THROMBUS SUSCEPTIBILITY POTENTIAL METRIC FOR PIV DATA 190

6.1 Specific Aim 190

6.2 Thrombus Susceptibility Potential Metric Development 190

6.2.1 Equation 191

6.2.2 Use with PIV Data 192

6.2.3 Limitations 194

6.2.3.1 Temporal Study 194

6.2.3.2 Metric Sensitivity 195

6.3 TSP Application 202

6.3.1 Valve Orientation Study 202

6.3.1.1 Results 202

6.3.1.2 Discussion 203

6.3.2 Stroke Volume Reduction Study 210

6.3.2.1 Results 210

6.3.2.2 Discussion 211

6.4 Conclusions 213

Chapter 7: SUMMARY AND CONCLUSIONS 215

7.1 Summary 215

7.2 Conclusions 217

7.3 Future Work 217

BIBLIOGRAPHY 218

LIST OF TABLES

Table 1: Stroke volume values used for flow reduction ……... 6

Table 2: Conditions of each stroke volume and filling method ……..……..… 12

Table 3: Diaphragm deployment and collapse times for each condition ….…….. 16

Table 4: TSP values of surfaces 1-4 for valve orientation results …… 202

Table 5: TSP values for stroke volume reduction results ……..……...…… 210

LIST OF FIGURES

Figure 1: Artists rendition of the implanted PVAD...……... 6

Figure 2: Visualization of flow inside a VAD ……..……..… 12

Figure 3: Valve comparison of 8.2 mm plane …….…….. 16

Figure 4: Systolic blockage of the BSM valve in the 7 mm plane ……..… 17

Figure 5: CM valve regurgitation in the 8.2 mm plane …… 18

Figure 6: Three-dimensionality examples in the 8.2 mm and body planes …….. 20

Figure 7: Recirculation examples in the 8.2 mm and outlet planes …… 21

Figure 8: Flow penetration example of BSM valve in 8.2 mm and inlet planes …..…. 22

Figure 9: Flow penetration example of CM valve in 8.2 mm and inlet planes …….…. 23

Figure 10: Comparison of valve wall shear rate maps along the device apex …… 24

Figure 11: Valve orientation examples …….…….….. 25

Figure 12: Inlet jet development of five valve orientations ……...…… 26

Figure 13: Systolic blockage of three valve orientations ……...……. 27

Figure 14: Wall shear rate maps of valve orientation combinations ……. 28

Figure 15: Waveforms of different EDDs …….…… 30

Figure 16: Comparison of inlet jets of three EDDs in the 8.2 mm plane ……... 31

Figure 17: Comparison of rotational flow fields of EDDs in the 8.2 mm plane …….. 32

Figure 18: Wall shear rate maps of EDDs of the 8.2 mm plane ……. 33

Figure 19: Blood analog comparisons of the 8.2 mm plane …….…….….. 34

Figure 20: Wall shear rate maps of blood analogs of the 7 mm plane …….. 35

Figure 21: Example PIV setup …… 37

Figure 22: Example PIV particle path …….. 39

Figure 23: Example PIV interrogation regions ……. 43

Figure 24: PIV cross-correlation schematic …….. 44

Figure 25: Example PIV cross-correlation peaks ……... 45

Figure 26: Example of overlapping interrogation regions ……. 47

Figure 27: Example peak locking histograms ……. 49

Figure 28: Schematic of projection error …….. 50

Figure 29: Acrylic PVAD model ……. 53

Figure 30: Valve orientations …… 54

Figure 31: Schematic of the mock circulatory loop ……..55

Figure 32: Picture of the mock circulatory loop …… 56

Figure 33: Picture of the compliance chamber from the mock circulatory loop …. 58

Figure 34: Picture of the resistance plate from the mock circulatory loop ……. 59

Figure 35: Pictures of the fluid reservoir from the mock circulatory loop …… 60

Figure 36: Pneumatic driver from the mock circulatory loop ……. 61

Figure 37: Example viscoelastic curves of the blood analog …….. 63

Figure 38: Schematic of PIV laser setup …… 65

Figure 39: Cardiac cycle time steps used for data collection …….. 66

Figure 40: PIV planes taken ……. 67

Figure 41: Example of PIV masking technique …….. 68

Figure 42: Example flow field map …… 70

Figure 43: PIV masking and centroid shifting technique ……. 71

Figure 44: Example flow and wall shear rate map ……. 72

Figure 45: Surfaces used for wall shear rate walls of each plane …… 72

Figure 46: Example 75 and 50 bpm waveforms …….… 76

Figure 47: Waveform with complete ejection and filling ……..…… 77

Figure 48: 8.2 mm parallel plane at 75 bpm at 54% of diastole ……...… 79

Figure 49: 8.2 mm parallel plane at 75 bpm at 65%, 76%, and 87% of diastole …..…. 80

Figure 50: 7, 8.2 and 11 mm parallel planes at 75 bpm at 98% of diastole and 12% of systole……...…… 81

Figure 51: 7 and 8.2 mm parallel planes at 75 bpm at 85% of systole …….…….. 82

Figure 52: 7, 8.2 and 11 mm parallel planes at 50 bpm at 50% of diastole ……..….. 83

Figure 53: 7 and 8.2 mm parallel planes at 50 bpm at 31% and 44% of diastole ……... 84

Figure 54: 7 and 8.2 mm parallel planes at 50 bpm at 56% and 63% of diastole ….….. 85

Figure 55: 7, 8.2 and 11 mm parallel planes at 50 bpm at 87% and 100% of diastole ... 86

Figure 56: 7, 8.2 and 11 mm parallel planes at 50 bpm at 13% of systole ….……... 87

Figure 57: 7 and 8.2 mm parallel planes at 50 bpm at 37% of systole ……..... 88

Figure 58: 7 mm parallel plane at 50 bpm at 63% of systole …….. 89

Figure 59: Wall shear rate map along surface 2 of the 8.2 mm parallel plane at 75 and 50 bpm …….. 90

Figure 60: 8.2 mm parallel plane at 75 and 50 bpm at 43% of diastole …….…. 91

Figure 61: 8.2 mm parallel plane at 75 and 50 bpm at 63% of diastole ……..……. 92

Figure 62: 8.2 mm parallel plane at 75 and 50 bpm at 87% of diastole ……. 93

Figure 63: Streamtraces of the 8.2 mm parallel plane at 75 and 50 bpm at 63% of diastole ……. 94

Figure 64: 11.25 mm normal inlet and 8.2 mm parallel planes at 75 and 50 bpm at 87% of diastole ……...……. 95

Figure 65: 11.25 mm normal outlet and 8.2 mm parallel planes at 75 and 50 bpm at 87% of diastole …… 96

Figure 66: 8.2 mm parallel plane at 75 and 50 bpm at 40% of systole ……..…. 97

Figure 67: Wall shear rate map along surface 4 of the 8.2 mm parallel plane at 75 and 50 bpm …….. 98

Figure 68: 3.75 mm normal inlet and 8.2 mm parallel planes at 75 and 50 bpm at 40% of systole ……..……...……. 99

Figure 69: Waveforms of the quick and slow fill at the 12 cc SV ……..…..…. 105

Figure 70: Waveforms of the quick and slow fill at the 9.6 cc SV ……..… 106

Figure 71: Waveforms of the quick and slow fill at the 7.2 cc SV …….. 107

Figure 72: Waveforms of the quick and slow fill at the 12 cc SV …….. 108

Figure 73: Picture of maximum diaphragm deployment at each SV …… 110

Figure 74: All three parallel and all three normal inlet planes of the 12 cc quick fill condition at 100 ms ……. 112

Figure 75: All three parallel and all three normal inlet planes of the 12 cc quick fill condition at 150 ms ……. 113

Figure 76: All three normal inlet planes of the 12 cc quick fill condition at 200 ms ... 114

Figure 77: The 8.2 mm parallel plane of the 12 cc quick fill condition at 250, 350 and 450 ms ……..…….. 115

Figure 78: All three normal outlet planes of the 12 cc quick fill condition at 300 and 400 ms …….. 116

Figure 79: The 8.2 mm parallel plane of the 12 cc quick fill condition at 600-800 ms …… 117

Figure 80: All three normal outlet planes of the 12 cc quick fill condition at 600 and 650 ms …….. 118

Figure 81: All three parallel and all three normal outlet planes of the 12 cc quick fill condition at 750 ms ……. 119

Figure 82: The 7 mm parallel plane of the 12 cc slow fill condition at 100-300 ms ... 120

Figure 83: All three normal inlet planes of the 12 cc slow fill condition at 100, 200 and 300 ms ……..…….. 122

Figure 84: The 7 mm parallel plane and 11.25 normal inlet plane of the 12 cc slow fill condition at 350-450 ms ……..…….. 123

Figure 85: The 8.2 and 11 mm parallel planes of the 12 cc slow fill condition at 350-450 ms ……. 124

Figure 86: The 8.2 mm parallel plane and 11.25 normal inlet plane of the 12 cc slow fill condition at 550, 650 and 750 ms …….…… 125

Figure 87: The 7.5 mm normal outlet plane at 450 ms and the 11.25 normal outlet plane at 450 and 500 ms of the 12 cc slow fill condition ……126

Figure 88: All three parallel planes of the 9.6 cc quick fill condition at 100 ms …... 127

Figure 89: All three parallel planes of the 9.6 cc quick fill condition at 150, 250 and 350 ms …….…… 128

Figure 90: All three inlet normal planes of the 9.6 cc quick fill condition at 150 and 250 ms ……..…… 129

Figure 91: All three outlet normal planes of the 9.6 cc quick fill condition at 150 and 200 ms ……..…… 130

Figure 92: All three outlet normal planes of the 9.6 cc quick fill condition at 300 and 400 ms ……..…… 131

Figure 93: The 7 mm parallel and 11.25 mm normal planes of the 9.6 cc quick fill condition at 400 and 450 ms ……. 132

Figure 94: The 8.2 mm parallel plane of the 9.6 cc slow fill condition at 150-250 ms..133

Figure 95: The 7 mm parallel plane of the 9.6 cc slow fill condition at 250-400 ms… 134

Figure 96: The 7.5 and 11.25 mm inlet normal planes of the 9.6 cc slow fill condition at 250 and 300 ms ……. 135

Figure 97: The 8.2 and 11 mm parallel planes of the 9.6 cc slow fill condition at 350-450 ms ……...…….. 136

Figure 98: All three parallel and all three inlet normal planes of the 9.6 cc slow fill condition at 400 ms ……..……. 137

Figure 99: The 8.2 mm parallel and 7.5 inlet normal planes of the 9.6 cc slow fill condition at 500, 600 and 700 ms …….…… 138

Figure 100: All three parallel planes of the 7.2 cc quick fill condition at 50-150 ms .. 140

Figure 101: All three inlet normal planes of the 7.2 cc quick fill condition at 150 ms ……..... 141

Figure 102: All three outlet normal planes of the 7.2 cc quick fill condition at 300 and 400 ms ……..... 142

Figure 103: The 7 and 8.2 mm parallel planes of the 7.2 cc quick fill condition at 350-450 ms ……..…… 143

Figure 104: All three inlet normal planes of the 7.2 cc quick fill condition at 350-450 ms …… 144

Figure 105: The 8.2 mm parallel and 7.5 mm inlet normal plane of the 7.2 cc quick fill condition at 550, 650 and 750 ms ……..…….. 145

Figure 106: The 7 mm parallel plane of the 7.2 cc slow fill condition at 100, 200, 300 400, 500, and 600 ms …….…… 146

Figure 107: The 8.2 and 11 mm parallel plane of the 7.2 cc slow fill condition at 400 and 450 ms ……..…… 147

Figure 108: The 3.75 mm inlet normal plane of the 7.2 cc slow fill condition at 200, 300 and 400 ms …… 148

Figure 109: The 7.5 and 11.25 mm inlet normal planes of the 7.2 cc slow fill condition at 200, 300, and 400 ms ……. 149

Figure 110: The 7.5 mm outlet normal planes of the 7.2 cc slow fill condition at 200, 300, and 400 ms ……. 150

Figure 111: The 8.2 mm parallel and 7.5 mm inlet normal plane of the 7.2 cc slow fill condition at 500, 600, and 700 ms …….. 151

Figure 112: The 11 mm parallel and 11.25 mm outlet normal plane of the 7.2 cc slow fill condition at 600, 700 and 800 ms ……...……. 152

Figure 113: The 7 and 8.2 mm parallel and 3.75 mm inlet normal plane of the 4.8 cc quick fill condition at 50-150 ms …….….. 153

Figure 114: All three parallel planes of the 4.8 cc quick fill condition at 200, 300 and 400 ms ……..…….….. 154

Figure 115: The 11.25 mm outlet plane of the 4.8 cc quick fill condition at 250, 350, and 450 ms …… 155

Figure 116: The 8.2 mm parallel plane of the 4.8 cc quick fill condition at 500, 600 and 700 ms …….. 156

Figure 117: The 7 mm plane of the 4.8 cc slow fill condition at 150, 250 and 350 ms …….….. 157

Figure 118: The 8.2 mm parallel, 7.5 normal inlet and 7.5 normal outlet planes of the 4.8 cc slow fill condition at 350-450 ms …….. 158

Figure 119: The 7 and 11 mm parallel planes of the 4.8 cc slow fill condition at 550, 650 and 750 ms ……..…… 159

Figure 120: The 7 mm parallel plane of all stroke volumes with quick fill at 100 and 150 ms …… 161

Figure 121: Surface 1 of the 7 mm parallel plane of all stroke volumes with a quick fill …….…… 162

Figure 122: The 8.2 mm parallel plane of all stroke volumes with a quick fill at 150-200 ms …….. 163

Figure 123: The 3.75 mm inlet normal plane of all stroke volumes with a quick fill at 50, 150 and 250 ms …… 164

Figure 124: Surface 4 of the 3.75 mm inlet normal plane of all stroke volumes with a quick fill ……. 165

Figure 125: A plot of the maximum velocities versus time of all four quick fill SVs in the 8.2 mm parallel plane …….. 166

Figure 126: The 11 mm parallel plane of all stroke volumes with a quick fill at 200, 300 and 400 ms …….….. 167

Figure 127: Surface 3 of the 11 mm parallel plane of all stroke volumes with a quick fill ……. 168

Figure 128: The 11.25 mm parallel plane and its associated surfaces 2 and 3 of all stroke volumes with a quick fill …….…… 170

Figure 129: Surface 2 of the 11.25 mm parallel plane of all stroke volumes with a quick fill ……. 172

Figure 130: The 7 mm parallel planes at all stroke volumes with a slow fill at 100, 200 and 300 ms …….. 174

Figure 131: Surface 1 of the 7 mm parallel plane of all stroke volumes with a slow fill ……...175

Figure 132: The 3.75 mm inlet normal plane at all stroke volumes with a slow fill at 100, 200 and 300 ms …….. 176

Figure 133: Surface 4 of the 3.75 mm inlet normal plane of all stroke volumes with a slow fill ……...177

Figure 134: Surface 3 of the 11 mm parallel plane of all stroke volumes with a slow fill ……...178

Figure 135: The 11.25 mm parallel plane and its associated surfaces 2 and 3 of all stroke volumes with a slow fill …… 180

Figure 136: The 8.2 mm parallel plane of the 9.6 cc stroke volume with a slow and quick fill at 150, 250 and 350 ms …….. 182

Figure 137: The 8.2 mm parallel plane of the 50 bpm and 12 cc quick fill condition at 25%, 35% and 50% of diastole …….. 185

Figure 138: Surface 1 of the 8.2 mm parallel plane for the 50 bpm and 12 cc quick fill condition ……..... 186

Figure 139: Surface 3 of the 11 mm parallel plane for the 50 bpm and 12 cc quick fill condition ……..... 187

Figure 140: Example wall shear rate map and associated TSP surface plot …..… 193

Figure 141: Surfaces 3 and 4 and TSP values of the high magnitude results and associated TSP values …….. 194

Figure 142: Surfaces 1 and 2 of the 8.2 mm plane at 0 inlet 0 outlet used for the TSP sensitivity studies …… 196

Figure 143: The sensitivity curve of the TSP with variable $\dot{\gamma}_{peak}$ …… 196

Figure 144: The sensitivity curve of the TSP with variable $\dot{\gamma}_{cutoff}$ …… 197

Figure 145: The sensitivity curve of the TSP with variable t_{crit} …….. 197

Figure 146: TSP surface plots along surface 4 of the high magnitude TSP with a variable t_{crit} …… 199

Figure 147: TSP surface plots along surface 4 of the high magnitude TSP with varying time step intervals and t_{crit}……. 201

Figure 148: Surfaces 2 and 3 of 0° inlet 0° outlet with TSP surface plots ……....….. 204

Figure 149: Surface 1 of the 8.2 mm plane at 0° inlet 0° outlet, +15° inlet 0° outlet +30° inlet 0° outlet and TSP values …… 205

Figure 150: Surface 4 of the 8.2 mm plane at 0° inlet 0° outlet, 0° inlet +15° outlet 0° inlet +30° outlet and TSP values …… 206

Figure 151: TSPs along Surface 4 of the 8.2 mm plane at 0° inlet 0° outlet, 0° inlet +15° outlet 0° inlet +30° outlet and TSP values ……... 207

Figure 152: Surfaces 1-4 of the 8.2 mm plane at 0° inlet +15° outlet and +15° inlet +15° outlet and the TSP values …….…… 208

Figure 153: TSP surface plots of surfaces 1-4 of the 8.2 mm plane at 0° inlet +15° outlet and +15° inlet +15° outlet …….…… 209

Figure 154: Surface 1 of the 7 mm plane of all four quick fill stroke volumes and the TSP values ……...……. 211

Figure 155: Surface 1 of the 7 mm plane of all four slow fill stroke volumes and the TSP values ……...……. 212

Figure 156: TSP surface plots of surface 1 of the 7 mm plane for the quick and slow fill of all four stroke volumes ……. 213

ACKNOWLEDGMENTS

The NIH – NHLBI Contract HV 48191, funded this study. I also received support form the Applied Research Laboratory's Exploratory and Foundational Graduate Student Research Program.

I would first like to thank Dr. Keefe Manning for serving as my Dissertation Adviser. Throughout this process Dr. Manning has served as a mentor and friend and I appreciate all of the time and effort he took to work with me over the past four years. I would like to thank Dr. Steven Deutsch for his wisdom and insight into my research, and especially for his help in taking my writing from unreadable to "not so bad." I would also like to acknowledge Dr. William Weiss for his support from Hershey Medical Center as the Primary Investigator on the PVAD project and a member of my committee, and also Dr. Lacey Holowatz for serving as a committee member.

I also could not have completed this work without the help and friendship of the other members of the Artificial Heart Lab. Especially my fellow graduate students, Luke Herbertson, Ning Yang, Varun Reddy, George Long, Jason Nanna and Katie Chorpenning. I would also like to give a special thank you to all members of Team Pulsaflow, even if all you did was give me more work, I'm sure I learned an important lesson.

I would also like to thank my family and friends for their unwavering, long distance support. Especially my parents, Wayne and Cherie Roszelle, for believing in my dreams

and always encouraging me to be the best person I could. And of course I would like thank all of my siblings, Lance, Ram, Kirsten and Spencer, for harassing me just enough as a child to give me the determination to take on whatever challenge was ahead of me. And finally, thank you to Bryan for understanding my goals and unconditionally believing in me and supporting me for the past few years.

Chapter 1

INTRODUCTION and BACKGROUND

1.1 Clinical Need

Cardiovascular disease (CVD) is the leading cause of death among Americans. Over 81 million adults (>20 years of age) in the United States have one or more forms of CVD (AHA 2010). While countless advancements in many areas of treating these diseases have been made over the past century, the development of cardiovascular medical devices has provided many successful treatment options. These devices include implants such as arterial stents and inferior vena cava filters, and more complex devices such as pacemakers and ventricular assist devices. While these devices have helped treat millions of patients, they also come with the complications that arise from using foreign materials inside the human body. One of the major concerns is thromboembolic events, which stem from the interaction of a device and blood (Hanson 1993). Because of this, it is necessary to investigate the potential for thrombogenicity during the development of all blood contacting medical devices, especially those associated with the cardiovascular system.

1.1.1 Pediatric Cardiovascular Disease

Since the American Heart Association began keeping track in the mid 20th century, there have been over 2 million patients born with congenital cardiovascular defects, in the United States. This means about 9 infants per 1000 live births are born with a cardiovascular defect that is detected within the first 30 days of life. Over a quarter of these defects will require an invasive procedure or result in death within the first year of

the patient's life. Many more minor defects are not detected until later in a patient's life, and are not included in this number (AHA 2005, Morrow 1997).

Countless advancements have been made in the field of congenital heart surgery over the past few decades. Many patients that may have not survived their first few months of life have been saved by the Norwood or Fontan procedures. The goals of congenital heart surgery have also shifted from pallative care and increasing survival rates, to minimizing late morbidity and providing a patient with an excellent quality of life (Ohye 2001). While the field is continually transforming and advancing, for some pediatric patients the only option available is heart transplantation.

Transplantations in pediatrics, including neonates, are viable in a large number of patients and new developments are allowing for more patients to survive long enough to be put on a transplant list. The bottleneck to transplantation for all patients is the limited availability of organs. The number of pediatric heart transplants has plateaued since the early 1990s at around 400 transplants per year, as that is the number of viable organs that become available (Ohye 2001). In fact, pediatric patients remain the group with the lowest number of available organs, with nearly 50% of patients under one year of age dying while awaiting a transplant organ. Limited organ availability is not, however, unique to pediatric heart patients, and has lead to an increased desire for bridge-to-transplant options for all patients awaiting donor organs (AHA 2005).

1.1.2 Ventricular Assist Devices

The idea of aiding patients during the bridge-to-transplant time period was first formulated for adult patients. Over 50 years ago the National Heart, Lung and Blood Institute (NHBLI) began to sponsor the development of short and long-term methods of mechanical circulatory support for patients awaiting a heart transplant, or for those not eligible to receive a transplant (Goldstein 1998). The idea behind the support was to improve the patient's chance of surviving long enough for a viable organ to become available, by supporting the circulation of the patient's blood, even after their injured heart was no longer able to provide adequate support. Many of the initial devices were large pneumatic models worn extracorperally and attached to drivers the size of washing machines. Over time it became desirable and possible to reduce the size of the devices in order to increase the quality of life for the patients that were bed-ridden and tethered to machines. This need lead to the development of smaller, electrically driven, implantable devices that gave the patient more freedom (Olsen 2000).

In 1994 the FDA approved the use of ventricular assist devices (VADs) as bridge-to-transplant tools. The short-term use of VADs was proven to normalize hemodynamics, improve end-organ dysfunction and allow for exercise tolerance (Rose 2001). The use of VADs allowed formerly bed-ridden patients to leave the hospital, and in fact, 91% of patients with severe congestive heart failure were able to be discharged and maintain a reasonable quality of life with a relatively low incidence of major adverse effects (Goldstein 1998; Rose 2001). The long-term use of VADs by patients ineligible for transplant has also been examined, and the 2001 REMATCH study compared the use of a

VAD versus optimal medical management. The study found that the patients using a VAD were 48% less likely to die within an intial two-year period (Rose 2001).

1.1.3 Pediatric Circulatory Support

As the use of VADs became more established for adult end-stage heart failure patients, the possibility of a similar solution for pediatric patients was explored. The development of mechanical circulatory support for pediatric patients has lagged behind that of adults, due mainly to the lower patient numbers (there are only 400 pediatric transplants performed each year in the United States compared to the over 3,000 performed on adult patients (HRS 2005)). Along with the smaller patient population, pediatrics also present unique challenges in device development not seen with adults including a much smaller total blood volume, a larger range of patient sizes from infants to adolescents, the smaller and more fragile vessels, and the possibility of growth of the patient during device use. Pediatric patients also pose the unique challenge of having a large range of anatomical differences stemming from congenital heart defects, which are often to blame for the origin of the patient's cardiovascular failure (Baldwin 2006).

Currently, the most common form of mechanical circulatory support for children is extracorporeal membrane oxygenation (ECMO), which is highly effective in children, for short-term support (del Nido 1994). When used for longer than 72 hours, ECMO can result in complications such as blood damage, infection and bleeding (Black 1995). Because many patients must wait much longer than three days for a viable organ to become available, this support is not useful for many transplant patients. Some adult

sized VADs have been approved for eligible pediatric patients for humanitarian use, however, these devices are too large for most patients, especially infants (Reinhartz 2002).

The only pediatric VAD currently approved for use in the United States is the Berlin Heart EXCOR Pediatric VAD, and that is only available through the FDA's investigative device exemption. This device has been used in Europe for the past several years where it has been given the Conformite Europeenne (CE) certification. The Berlin Heart is a pneumatically driven, extracorporeal device available in 10, 25 and 30 cc sizes (50, 60 and 80 cc volumes are also available for adults). A review by Potapov et al. looked at the use of the VAD in pediatric patients at the Deutsches Herzzentrum, the German Heart Institute in Berlin, Germany (Potapov 2007). In the last five years, three-quarters of patients implanted with the device have been discharged after recovery or transplantation. However, thromboembolic events remain a problem for a large number of patients (Potapov 2007). In a review of their use of the Berlin Heart pediatric VAD as a humanitarian device in the United States, Malaisrie et al. noted that of the eight patients receiving the device, five developed post-operative neurological events, four of which could be explained by embolisms or hemorrhage (Malaisrie 2008).

This lack of long term support options along with the concerns of thrombogenicity of the devices that were available, led to the start of the National Heart, Lung and Blood Institute's Pediatric Circulatory Support Program which awarded funding to research groups developing long-term circulatory support options for pediatric patient's ranging

form 2-25 kg (Baldwin 2006). As part of this program, Penn State has continued development of a 12 cc pulsatile pediatric ventricular assist device (PVAD), a sketch of which is shown in Figure 1. The pneumatically driven device is based on the successful adult sized 70 cc Pierce-Donachy VAD, which is currently in clinical use as the Thoratec® VAD (Slaughter year). A major directive of the device development is to reduce the chances of thromboembolic events by focusing on the device biocompatibility and fluid mechanics, the latter of which is the focus of this study.

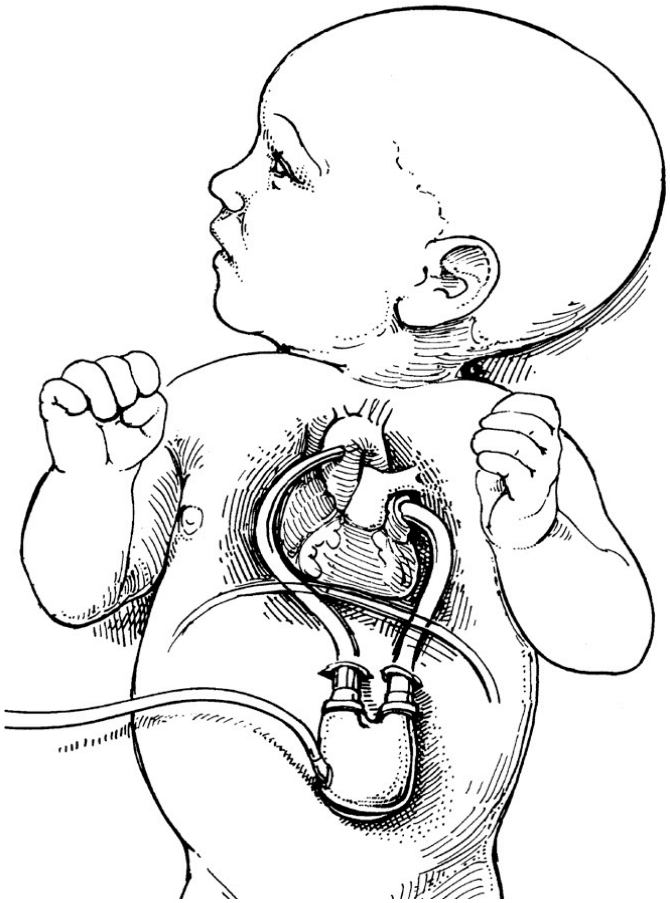

Figure 1: Artist's rendition of the 12 cc pulsatile pediatric ventricular assist device as it would be implanted in a patient.

1.1.4 Thromboembolic Events

Thromboembolic events are a major concern of any device with blood-material contact. This concern is intensified in cardiovascular devices because of their complex fluid interaction. When blood interacts with artificial surfaces, the surface absorbs protein, which leads to the activation and aggregation of platelets. Because platelet activation works in a positive feedback loop, this cycle continues and thrombus formation may occur (Colman 1993). Thrombi, in turn, disturb blood flow or even detach, as emboli, to cause stroke or ischemia. VADs have an increased probability of thromboembolic events because of their large surface area, complex flow patterns, and long-term use (Hanson 1993). Because the thrombogenicity of the device is often exacerbated by the fluid dynamic characteristics of the complex flow, it is necessary to study these characteristics during device design and development.

1.1.5 Bridge-to-Recovery

While VADs are most commonly used for bridge-to-transplant and palliative care, there has been a movement towards using these devices for bridge-to-recovery. It has been noted that some patients show myocardial recovery while on VAD support (Mancini 1998). When the VAD takes over the major support of the circulatory system, the weakened ventricle experiences chronic unloading. This unloading can lead to significant improvement of the ventricle. A multi-center study by the LVAD Working Group followed 67 cases of VAD use over a two-year period and assessed the myocardial recovery of the weakened ventricles. They found that almost every patient showed significant improvement in cardiac function after device implantation, and about 10%

recovered sufficiently to be explanted and to no longer require a transplant (Maybaum 2007). Another multi-center study followed bridge-to-recovery patients after they had been explanted and discovered that their survival rate was the same as patients receiving a transplanted heart (Farrar 2002). In a study by Frazier et al., 31 patients were supported by the HeartMate LVAD for a mean of 137 days. These patients showed significant improvement in the ejection fraction, an increase in the cardiac index and mean aortic pressure and a decrease in left ventricular end-diastolic dimension and pulmonary vascular resistance (Frazier 1996). These studies suggest that bridge-to-recovery is promising and may reduce the number of heart transplants necessary.

Previous studies have also shown successful use of VADs in children as bridge-to-recovery devices (Hetzer 1998 and Ishino 1997). Hetzer et al. observed the use of the pneumatically driven "Berlin Heart" VAD (12 to 30 cc) on several pediatric patients at different stages of cardiac failure, including five patients with acute myocarditis. Two of these patients showed successful myocardial recovery after using the device for 11 and 21 days (Hetzer 1998). Duncan et al. performed a study of 15 pediatric patients, all with myocarditis, that were supported either by ECMO or a centrifugal VAD (the 50 or 80 cc Biopump). Of the 15 patients, seven showed successful myocardial recovery and survived weaning from the device, while five survived after receiving transplantations (Duncan 2001). The use of VADs, as bridge-to-recovery, could also be important for patients having difficulty coming off of cardiopulmonary bypass after surgery, a problem more common in children than in adults (Duncan 1999). These opportunities for expanded VAD use are especially appealing for pediatrics, where organ availability is

highly limited; however, off-design VAD use may lead to problems not accounted for during the original development.

1.1.6 Weaning

When used as a bridge-to-recovery device, it is necessary to wean the patient from the VAD once their ventricle has adequately recovered. Weaning is done over time and requires changes in the operation of the VAD so that it provides less and less support. This process, which also allows for clinicians to see whether or not the patient's native ventricle is capable of taking back full support, may require the device to operate off design. No single weaning protocol has been established for VADs, so that a range of different methods have been used, which include changing the flow conditions of the VAD to switching to a different support system, such as ECMO (Slaughter 2001 and Hetzer 1998). Many groups that have successfully weaned patients agree that a gradual unloading from the ventricle is necessary (Maybaum 2007). For pulsatile devices, the gradual unloading often includes a reduction in the flow of the VAD, by a decrease in beat rate or stroke volume (SV) (Slaughter 2006). The reduction in flow rate leads to significant changes in the fluid dynamics of the device, the effects of which require inquiry.

1.2 Fluid Mechanics of Ventricular Assist Devices

Virchow generally outlined the thomboembolic reaction between blood and foreign materials over 100 years ago. This outline, known as Virchow's triad, includes three components: the properties of the blood, the properties of the blood contacting material,

and the fluid mechanics of the blood flow (Didisheim 1994). Because VADs can be used as long-term devices and have flow patterns of a highly unique and complex nature, their fluid mechanics are of increased concern when considering thrombogenicity (Hanson 1993). Pulsatile VADs, such as the one being observed in this study, often use mechanical heart valves (MHVs), which can cause blood hemolysis and platelet activation from the high velocity forward flow of blood, or from cavitation and strong regurgitant jets that occur at closure (Deutsch 2006, Lamson 1993) making it important to characterize the fluid dynamics with the understanding that platelet activation has arguably already occurred. Because of these considerations, the fluid mechanics of VADs have been studied in-depth in order to understand and reduce the overall thrombogenicity.

In 1972, while developing an artificial ventricle at Penn State, Phillips et al. began exploring *in vitro* flow visualization techniques to supplement *in vivo* testing of the blood pump (Phillips 1972). The group found that by using *in vitro* visualization in blood analog filled mock circulatory loops, specific flow conditions could more easily be measured without the variability and expense that occurs with animal models. In one of the first flow visualization techniques used on assist devices, a basic particle tracking technique, a tracer fluid of pearl essence or resin particles that was illuminated with slit lighting. Tracer images or streaklines were photographed using high-speed cameras. Frame by frame analysis was then used to evaluate the flow patterns. These initial studies were groundbreaking in the evaluation of VAD flow patterns, and also in the observation

of the effects of conditional changes such as valve type and flow rate to the flow field (Phillips 1972).

As the fluid mechanics of VADs have been studied over the past 40 years, the technology of both the devices and the flow visualization tools used to observe the fluid mechanics have advanced greatly. Both local and global fluid mechanic patterns of VADs have been characterized using advanced techniques such as hot film anemometry, laser Doppler anemometry (LDA), and particle image velocimetry (PIV) (Deutsch 2006). Each method has specific advantages. For example, hot film anemometry is useful in evaluating wall shear stresses and LDA can be used to quantify turbulence inside devices. Particle image velocimetry (PIV) is useful in characterizing whole planar flow fields, a valuable tool for studying the flow patterns of devices such as VADs in which structures, such as the inlet jet, influence much of the flow field. PIV has also been used to calculate the wall shear rates within the device, with a technique developed in our laboratory (Hochareon 2004a). The flow profile and wall shear rate information found *in vitro* has showed reasonable correlation with areas of thrombus formation in *in vivo* animal models (Hochareon 2004b).

By using multiple flow visualization techniques, the basic flow patterns of pulsatile VADs have been detailed, permitting the determination of which patterns are the most desirable for these devices. Baldwin et al performed in-depth flow visualization studies on the pulsatile 70 cc Pierce-Donachy VAD. This study used LDA at 195 points within the device in order to quantify the mean velocities and Reynolds stresses (Baldwin,

1994). Observations from this study helped characterize the diastolic rotational flow desired in current VAD design, which includes a strong diastolic jet that leads to good rotational flow in the body of the device prior to systole, and a smooth transition into systole as the fluid leaves the device. An example of this desired flow field is shown in Figure 2.

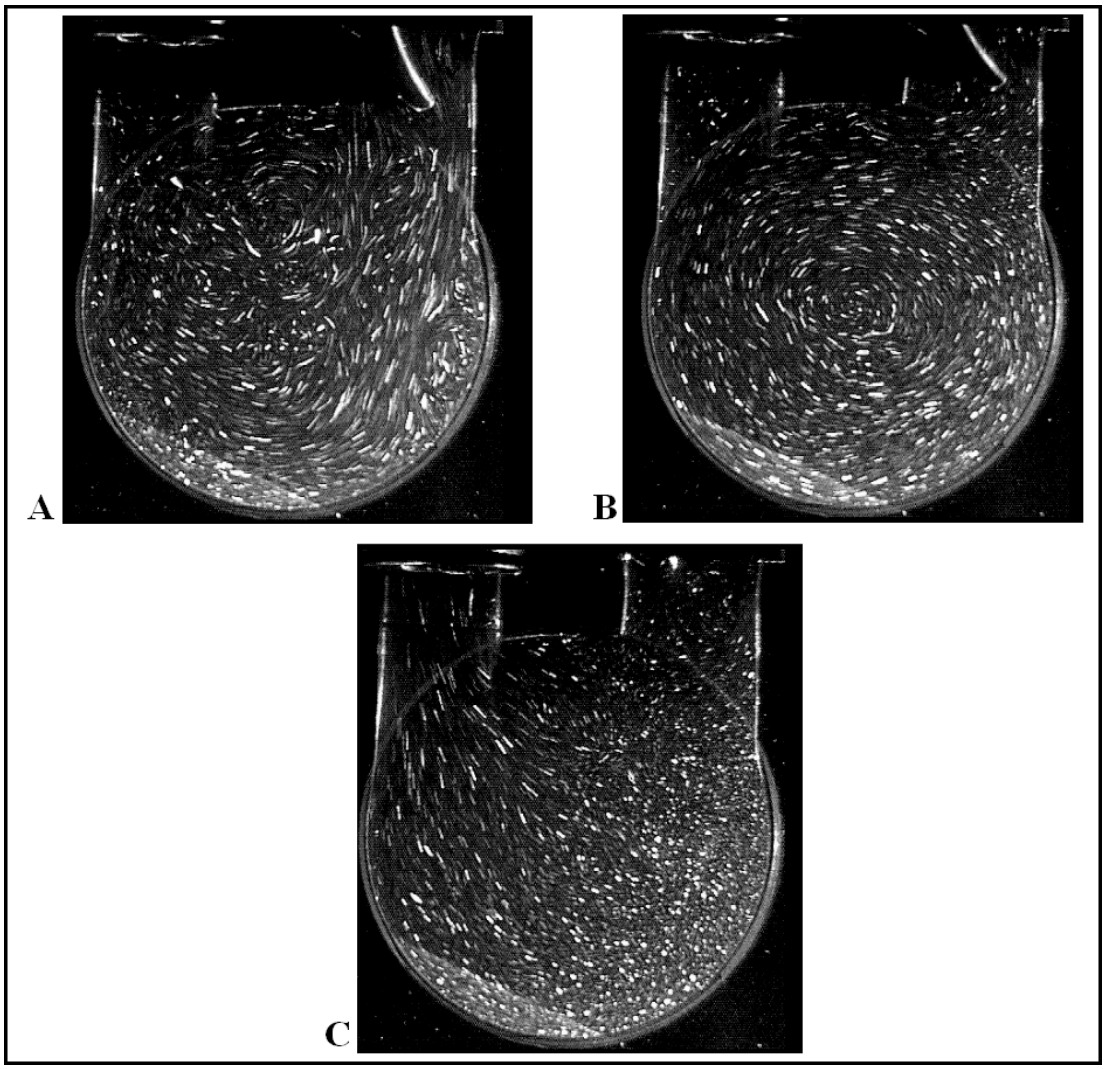

Figure 2: Flow visualization of the 50 cc adult device. Image A) the strong inlet diastolic jet on the right hand side penetrates to the bottom of the device and sets up the desired rotational flow. Image B) shows the rotation in the body of the device through the end of diastole and into the beginning of systole. Image C) highlights mid systole when the flow begins the leave the device through the outlet valve as seen on the left hand side.

While these and other studies have established the desired basic flow pattern for pulsatile VADs, they have also observed characteristics necessary for the prevention of thrombus deposition. This prevention requires avoiding areas of low flow near the walls, as these areas of stagnation have long blood residence times (Baldwin 1994). Studies by Hubbell and McIntire have established that a shear rate of $< 500\ s^{-1}$ on segmented polyurethane, the material used for the blood sacs in the Penn State PVAD, can promote thrombus deposition (Hubbell and McIntire 1986). Experimentation suggests that a useful design goal for similar VADs is to establish a fluid dynamic pattern, which consists of a strong diastolic jet that sets up a continuous movement of the fluid throughout diastole.

1.3 Fluid Mechanics of the Pediatric Ventricular Assist Device

Development of a pediatric sized VAD at Penn State began in the late 1980s when the 70 cc Pierce-Donachy device was scaled down to 15 cc. Some modifications were made to the device geometry which included angling the inlet and outlet valves, and developing in house manufactured pediatric sized ball and cage valves. Initial animal implantations of the device showed high thrombus formation and fibrin and platelet deposits throughout the blood sac as well as embolization in the kidneys of the animals (Daily 1999). Because the device used the same blood contacting materials and animal models as the adult device, which did not have the same thrombus deposition, it was concluded that the reduction in volume had led to changes in the flow field, which made the device more conducive to thromboembolic events. Because of this, Bachmann et al. looked at both the geometric scaling of the device, as well as the flow field patterns. They determined that there were significant differences in both the Strouhal and Reynolds numbers between the

adult and pediatric sized devices, indicating that the pumps were not geometrically similar (Bachmann 2000). Bachmann et al. also used two component laser Doppler velocimetry to characterize the internal flow field, and found that the wall shear rate in the pediatric devices had dropped significantly below the 500 s^{-1} threshold established by Hubbell and McIntire, leading to a flow environment conducive to clot formation.

Design changes were then made to the PVAD in order to reduce the chances of thrombus formation, which included a widening of the inlet and outlet ports to accommodate newly, commercially available pediatric MHVs. Because the fluid mechanics was a critical element in the poor performance of the first PVAD design, it was desirable to study the flow *in vitro* during the development process. In the past few years, extensive flow studies have established the basic flow pattern of the PVAD as well as the affect of changes made to the flow properties or to the PVAD itself (Manning 2008, Roszelle 2008, Cooper 2008, Cooper 2010, Roszelle 2010a, Roszelle 2010b). These studies used PIV in an acrylic model of the PVAD placed in a mock circulatory loop. The most significant results of these studies are summarized here.

1.3.1 PVAD Valve Selection Study

The valve selection study by Cooper et al. was performed to observe the fluid mechanics associated with two different pediatric sized mechanical heart valves. These were 17 mm Björk-Shiley Monostrut (BSM) tilting disc valves and 16 mm CarboMedics bileaflet (CM) valves. These valves were chosen for comparison because of Penn State's extensive knowledge of the BSM valve and the known clinical success of the CM valve. The purpose of this study was to compare the fluid dynamics inside the PVAD associated with both valves to aid in determining which valve would be used clinically (Cooper 2008).

Both sets of valves showed the desired features of strong diastolic jets and rotational flow through diastole. The comparison between the two models during diastole is shown in Figure 3. In the BSM device, the diastolic jet passes through the major orifice of the valve and shows high velocities along the outside wall and rotational flow in the body of the device as early as 250 ms into the cycle. In comparison, the diastolic jet of the CM device begins as 3 separate jets, one from each opening in the bileaflet valve. The jet then combines along the outside wall, similarly to the BSM device; however, this occurs later in the cycle, around 350 ms. This difference in diastolic jet formation corresponds to a difference in the time to set up the rotational flow in the body of the device. The BSM device shows a quicker transition into rotational flow that moves smoothly through diastole and early systole. The CM device shows similar rotational patterns, but it takes 100 ms longer for this flow to emerge. Because of this the BSM device maintains higher

wall shear rates for longer durations along the inlet walls of the device, a property that is important for the reduction of thrombus formation on the sac of the device.

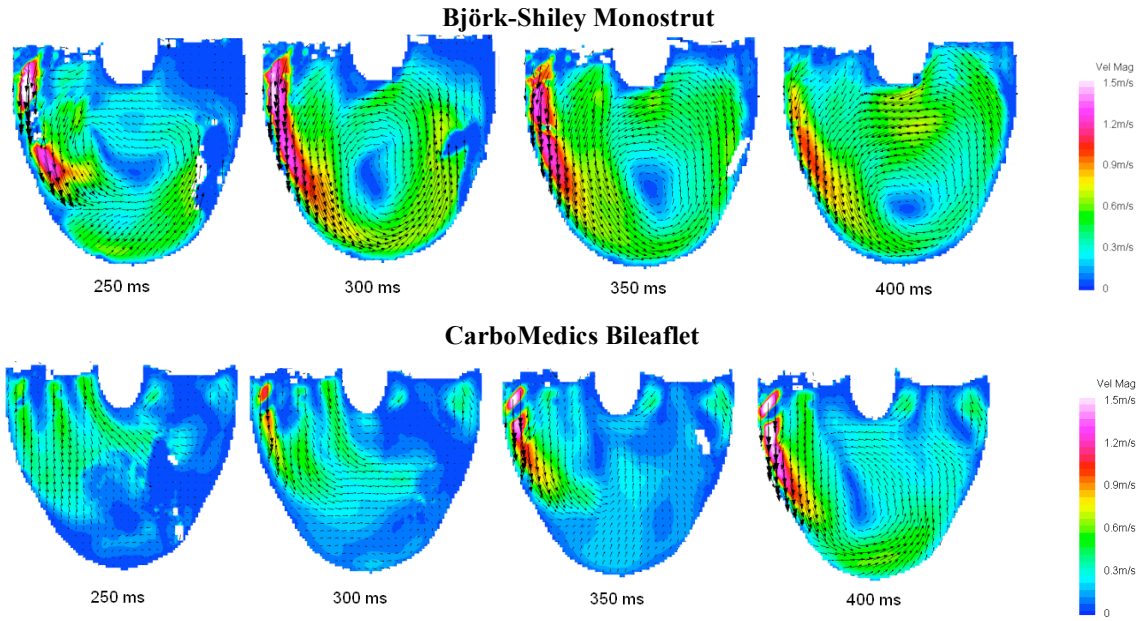

Figure 3: The 8.2 mm plane of the BSM (top) and CM (bottom) devices during mid to late diastole. The BSM device shows a strong inlet jet at 250 ms and the desired rotational pattern penetrating to the bottom of the device is achieved at 300 ms and continues through the end of diastole (450 ms, not shown). The inlet jet of the CM device begins as three separate jets as shown at 250 ms. At 350 ms these jets combine along the outside wall, mimicking what is seen 100 ms earlier in the BSM device. The desired rotation also appears 100 ms in the CM device close the end of diastole at 400 ms.

Unique observations were also made in the outlet port of each device. For the BSM device this included an area of blockage during mid to late systole. As shown in Figure 4, this blockage occurs around the leaflet of the BSM valve. The concern with such a separation is that it can lead to a larger than normal pressure drop across the valve at the outlet of the device, and higher shear stresses in the outlet port that could lead to increased blood damage.

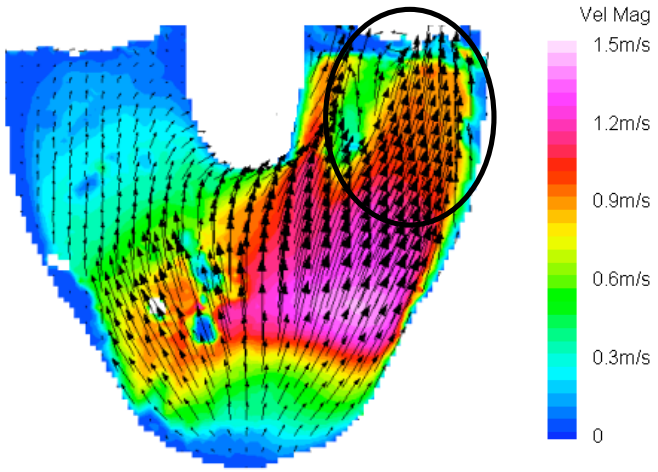

Figure 4: The 7 mm plane of the BSM device at 700 ms (late systole). The area of blockage found in the outlet port is circled in black. This characteristic was unique to the BSM device, and could lead to concerns about blood damage during systole.

The CM device did not show any areas of separation but did show regurgitation from the outlet valve during systole as shown in Figure 5. This retrograde flow appears to interfere with the rotational pattern of the flow within the body of the CM device, and may also increase blood damage around the outlet valve.

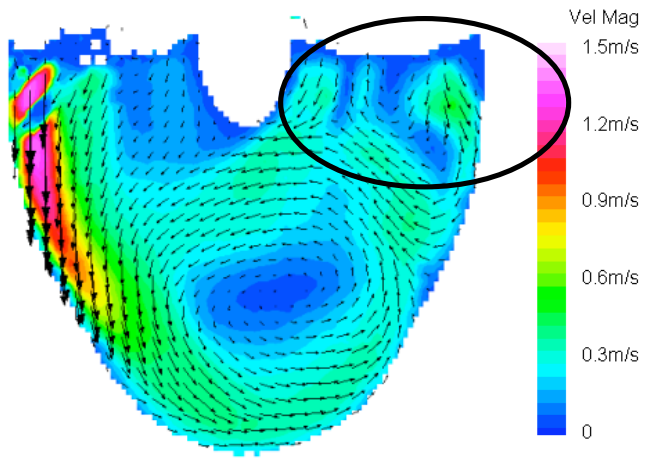

Figure 5: The 8.2 mm plane of the CM device at 450 ms (end of diastole). Regurgitation from the outlet valve is highlighted in black. This regurgitation is a concern because of the increased chance of blood damage as well as the effect it has on the rotational flow in the body of the device.

While the valve selection study found that both the BSM and CM valves contained positive and negative aspects regarding the fluid dynamics of the PVAD, the BSM valve was chosen for clinical studies. This decision was based on the BSM's superior ability to form a cohesive and timely diastolic inlet jet earlier in diastole, leading to penetration into the bottom of the device and set up of the desired rotational flow. The negative aspects of the CM device including shorter periods of desired wall shear and interference from outlet jet regurgitation. The largest limitation of this study was the use of 2D PIV to observe highly three-dimensional flow. Therefore, future studies of the PVAD contained observations of the flow field physics normal to the diaphragm as well.

1.3.2 PVAD Three-Dimensionality Study

As described earlier, the reduction in volume to 15 cc had led to changes in the fluid mechanics when compared to the adult sized device. Design changes such as an increase in diameter and angling of the inlet and outlet ports resulted in better fluid mechanics, however, flow visualization studies showed that this change in volume led to an increase in the three-dimensionality of the flow. This indicated that, unlike in the adult devices, the early diastolic flow was no longer parallel to the diaphragm motion. Because previous studies of the PVAD had only observed flow planes parallel to the diaphragm, the objective of this study by Roszelle et al. was to include flow visualization normal to the diaphragm (Roszelle 2010). In order to achieve this, data was taken normal to the diaphragm in the inlet port, in the outlet port, and in the body of the device.

The results of the study not only highlighted the three-dimensional nature of the PVAD flow field, but also verified that the results of the previous two-dimensional work and the conclusions reached from it were sound.

A good example of the three-dimensionality predicted by previous studies (Daily 1996 and Bachmann 2000), was found in the body planes of the PVAD. As presented in Figure 6, the body planes of the BSM device signify fluid movement normal to the diaphragm during the initial filling of the device, early to mid diastole. As the rotational flow becomes stronger, the cross flow decreases and the flow velocities drop below 0.25 m/s, an indication that the parallel flow dominates during late diastole and early systole in this part of the device.

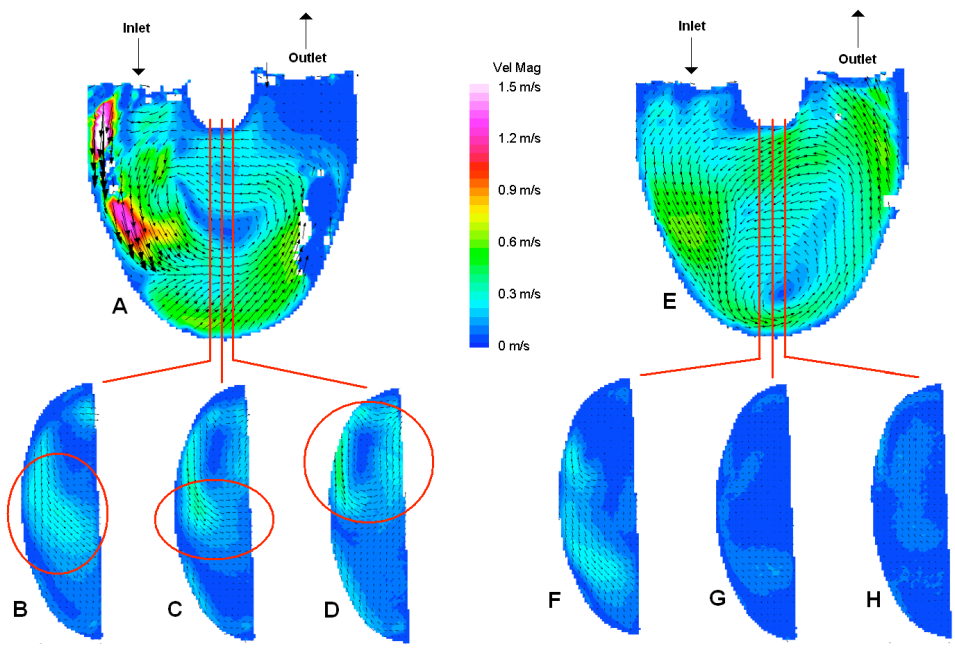

Figure 6: The 8.2 mm parallel plane and 2.5, 5.0 and 7.5 mm normal body planes of the BSM devices at 250 (A, B, C, D) and 450 ms (E, F, G, H). The normal body planes show some cross flow in mid diastole (B, C, D), which is highlighted with red circles. As the device finishes diastole this cross flow is eliminated and the flow in the normal body planes remains below 0.25 m/s (F, G, H). This is an indication of the dominate flow in the parallel planes as the desired rotational flow continues (Figure from Roszelle 2010a)

Data from the normal planes allowed for observation of aspects of the PVAD flow not originally found in the parallel planes that could affect the thrombogenicity of the device. These included an area of regurgitation found in the outlet port of the BSM device. While

the parallel plane data from the valve selection study indicated that the outlet valve of the CM device contained areas of regurgitation, no such observations were made in the BSM device. However, as shown in Figure 7, one of the normal outlet planes (11.25 mm) contained regurgitation during diastole that became an area of recirculation. While this flow characteristic does not appear to affect the rotational flow in the body of the BSM device, it may affect the overall thrombogenicity, thus highlighting the importance of viewing the flow field physics of the PVAD as a whole.

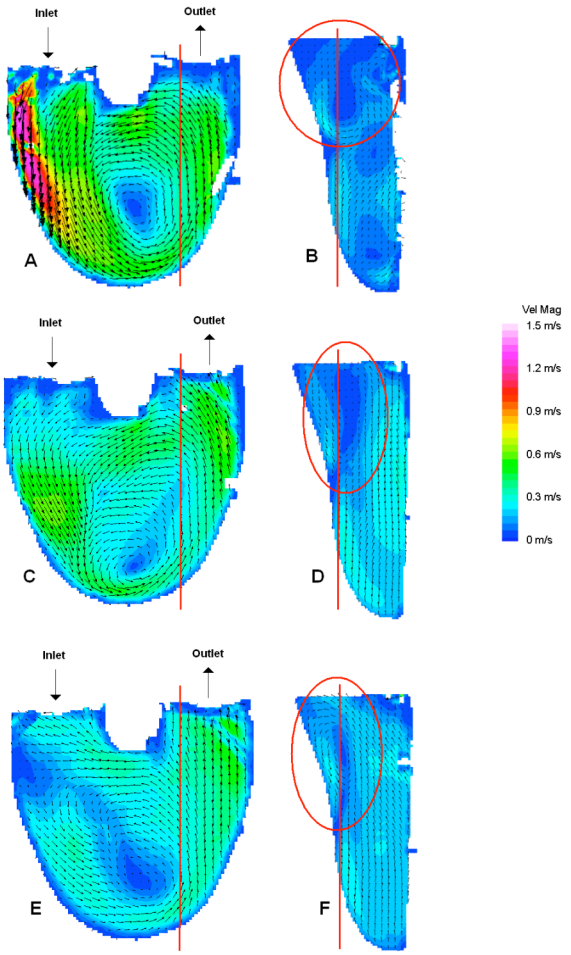

Figure 7: The 8.2 mm parallel and 11.25 mm outlet normal planes of the BSM device at 350 (A, B), 450 (C, D) and 550 ms (E, F). The cross-locations of the normal and parallel planes are shown by red lines. The 11.25 mm plane contains an area of regurgitation (A) that continues into an area of recirculation (D, E) during systole (highlighted by red circles). The recirculation does appear in the 8.2 mm parallel plane and the desired rotational flow continues unaffected during systole (Figure from Roszelle 2010a).

Much of the behavior of the device found previously in the two-dimensional studies was confirmed and clarified by the data observed in the normal planes. One such characteristic was the nature of the diastolic inlet jet. As noted previously during the valve selection study, the BSM device set up rotational flow more quickly and had greater wall shear rates in the bottom of the device than did the CM device. Figures 8 and 9 present the 8.2 mm parallel plane and inlet normal planes of both devices at mid diastole, confirming this earlier penetration by the jet of the BSM device.

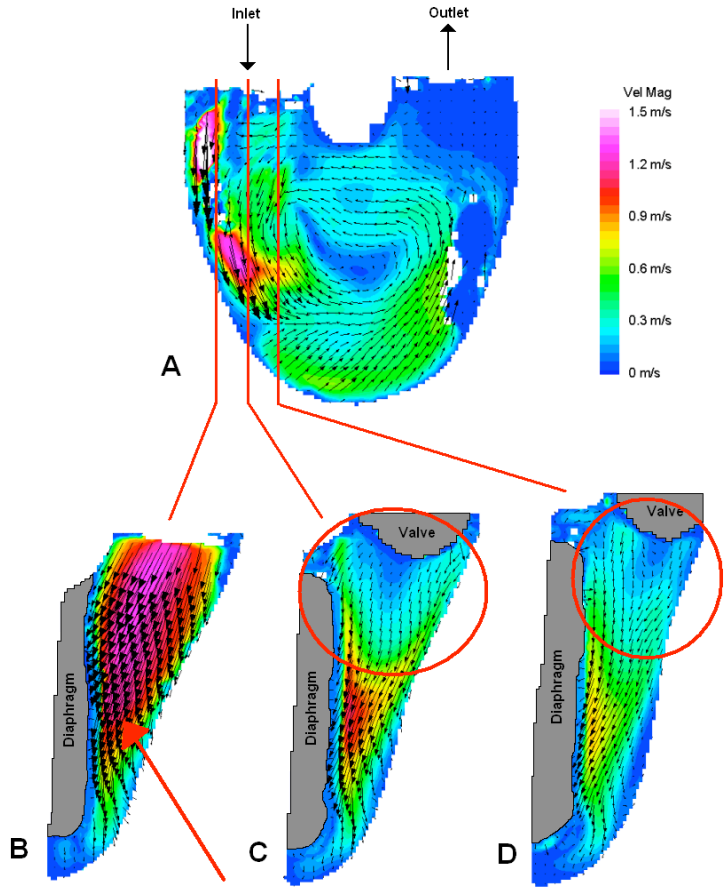

Figure 8: The BSM 8.2 mm parallel plane (A) and 3.75 (B), 7.5 (C) and 11.25 mm (D) normal planes at 250 ms. Gray areas are disturbances in the visual flow field from either the diaphragm or valve motion or shadowing. The cross-locations of the normal and parallel planes are shown by red lines. As indicated by the red arrow, the jet in the 3.25 mm plane shows convergence as it enters the pump. In contrast the 7.5 and 11.25 mm planes show reduced flow at the top of the ports (as indicated by red circles), effects from the wake of the inlet jet. The normal planes also correspond well to the 8.2 mm parallel plane which indicates the highest jet magnitudes along the outer wall and spreading of the jet as it moves into the bottom of the device (Figure from Roszelle 2010a).

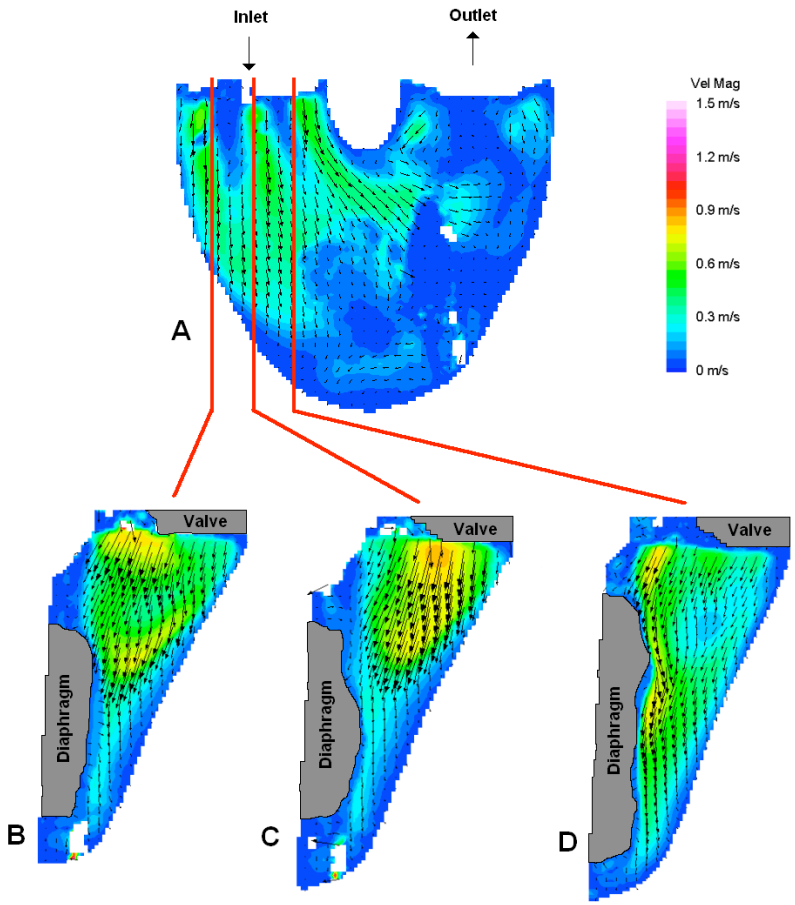

Figure 9: The CM 8.2 mm parallel plane (A) and 3.75 (B), 7.5 (C) and 11.25 mm (D) normal planes at 250 ms. Gray areas are disturbances in the visual flow field from either the diaphragm or valve motion or shadowing. The cross-locations of the normal and parallel planes are shown by red lines. The CM valve produces three inlet jets, which can be observed in the 8.2 mm parallel plane. Each of the normal planes also contains velocities of similar magnitude, a large difference from the BSM device (Figure from Roszelle 2010a).

The wall shear maps from the walls along the bottom of the normal planes also confirm higher wall shear rates 100 ms earlier in the BSM device, as shown in Figure 10. In general the study found that the data from the two sets of orthogonal planes correlated well with each other, indicating that 2D PIV is a reasonable approach to flow measurements in the PVAD, but new flow field aspects discovered from the normal plane data suggest that cross plane data should be acquired when feasible.

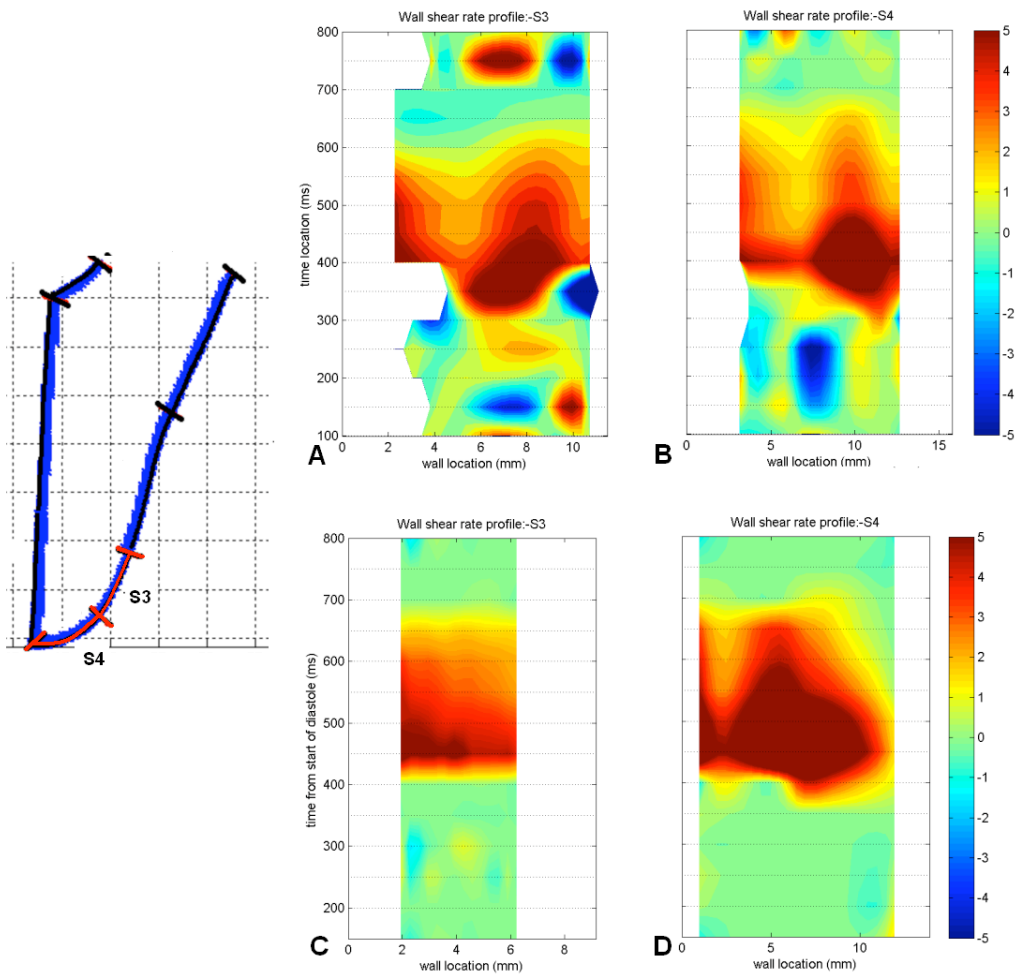

Figure 10: The wall shear of surfaces 3 and 4 of the 11.25 mm inlet normal plane, which are highlighted on the left, for the BSM device (A, B) and CM device (C, D). Positive numbers on the legend indicate shear in the clockwise direction while negative numbers indicate shear in the couter-clockwise direction. The legend has been normalized by the 500 s^{-1} threshold, therefore the low shear area is between 1 and -1. The shear rate increases above the 500 s^{-1} threshold in the BSM device around 300 ms but not until 400 ms for the CM device. Both devices show a decrease in shear around 600 ms (Figure from Roszelle 2010a).

1.3.3 PVAD Valve Orientation Study

Previous studies of adult sized VADs using similar MHVs showed that changes in the orientation of the inlet valve led to desirable changes in the fluid mechanics of the device. Once the BSM valve had been selected for the PVAD, it was necessary to perform a parametric study that looked at valve orientation and its effect on the fluid mechanics. Previous studies had focused solely on the inlet valve of adult sized VADs because the outlet valve had shown little effect on the fluid mechanics inside the body of the device (Krieder 2006; Akagawa 2007). Because the flow field PVAD has a greatly reduced volume and has shown a strong sensitivity to valve type, it was decided to look at the orientations of both the inlet and outlet valve separately and in combination. The valves were rotated parametrically in intervals of 15° between -15° and +45°, where a negative angle indicates the valve was rotated towards the diaphragm and a positive angle indicates the valve was rotated towards the fluid side of the device. Examples of valve combinations are shown below in Figure 11.

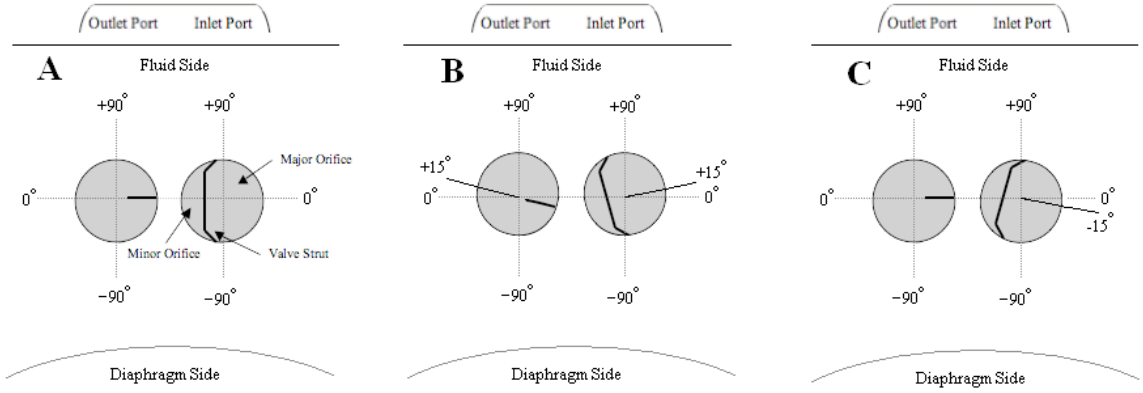

Figure 11: Examples of the valve orientations studied. (A) shows the 0° orientation of both the inlet and the outlet. In (B) the major orifice of both the inlet and the outlet valves are rotated by 15° towards the fluid side of the device, which is defined as a +15° orientation for both valves. In contrast (C) shows the outlet valve at 0°, while the inlet valve has been rotated by 15° towards the diaphragm side of the device, resulting in a -15° orientation for the inlet valve (Figure from Roszelle 2010b).

The results show that a rotation of the inlet valve up to +30° leads to an increase in the surface area and duration of favorable wall shear rates of greater than 500 s^{-1} by improving the cohesion of the inlet jet. Orientations of -15° and +45° resulted in inlet jets without good penetration reaching the bottom of the device. An example of this is shown in Figure 12. This conclusion varied from that of the adult devices, which found that increasing the valve up to +45° was useful, and also that rotations towards the diaphragm side (negative) were as effective as those towards the fluid side (positive) (Krieder 2006; Akagawa 2007).

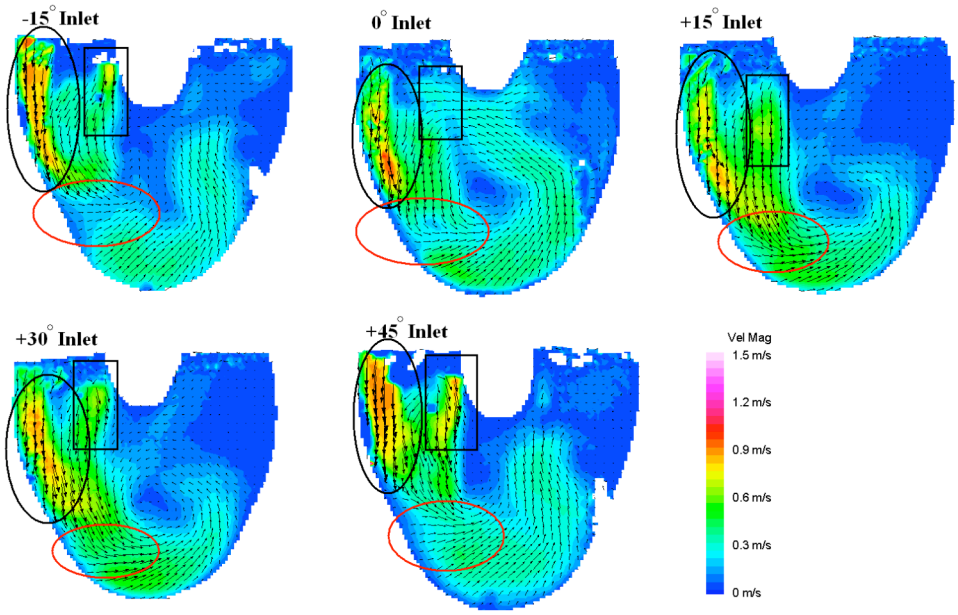

Figure 12: The 8.2 mm plane with inlet orientations of -15°, 0°, +15°, +30° and +45° and outlet orientations all at 0° at early-to-mid diastole (200 ms). As highlighted with black ovals, the inlet jet begins to spread when the valve is rotated towards the fluid side of the device. As this occurs there is also a strong minor orifice jet present as highlighted with black rectangles. The red ovals show an area of discontinuity between the inlet jet and the beginning of the rotational flow field in the body of the device. This area reduces in size as the valve is rotated up to +45°, at which point it again increases in size (Figure from Roszelle 2010b).

Orientations of the outlet valve up to +30° lead to an increase in wall shear rates to above the 500 s^{-1} threshold along the outlet wall. Previous studies of the BSM outlet valve have shown an area of blockage upstream of the valve. When the valve was rotated towards the fluid side this blockage increased slightly in size, as shown in Figure 13. We believe that the increase in the wall shear rate with the rotation outweighed the concern of the increase in the outlet blockage size.

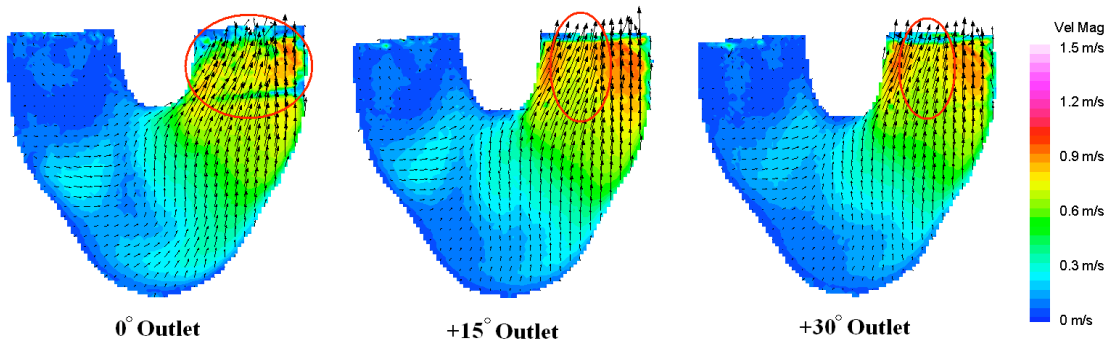

Figure 13: The 8.2 mm plane of the PVAD where the inlet valve remains at 0° and the outlet valve is oriented at 0°, +15°, and +30° at mid systole (600 ms). The area of blockage (highlighted in red) is similar to that seen in previous studies of the PVAD. The characteristic becomes more evident as the valve angle increases. While the difference between the +15° and +30° characteristic is less prominent, the velocity magnitudes in the middle of the separation are lower, indicating a greater area of stasis (Figure from Roszelle 2010b).

The best combined flow and wall shear rate patterns occurred when the valves were rotated together towards the fluid side of the device. The general desired flow pattern of the PVAD was maintained with a strong diastolic inlet jet, good rotation throughout the body of the device, and smooth transition to systole. Many of the wall locations for all of the valve combinations showed adequate shear rates for at least a portion of the cycle, however, as shown in Figure 14, the +15° inlet and +15° outlet combination had the most desirable wall shear. It was ascertained from this study that both the inlet and outlet valves of the PVAD would be rotated +15° for clinical use.

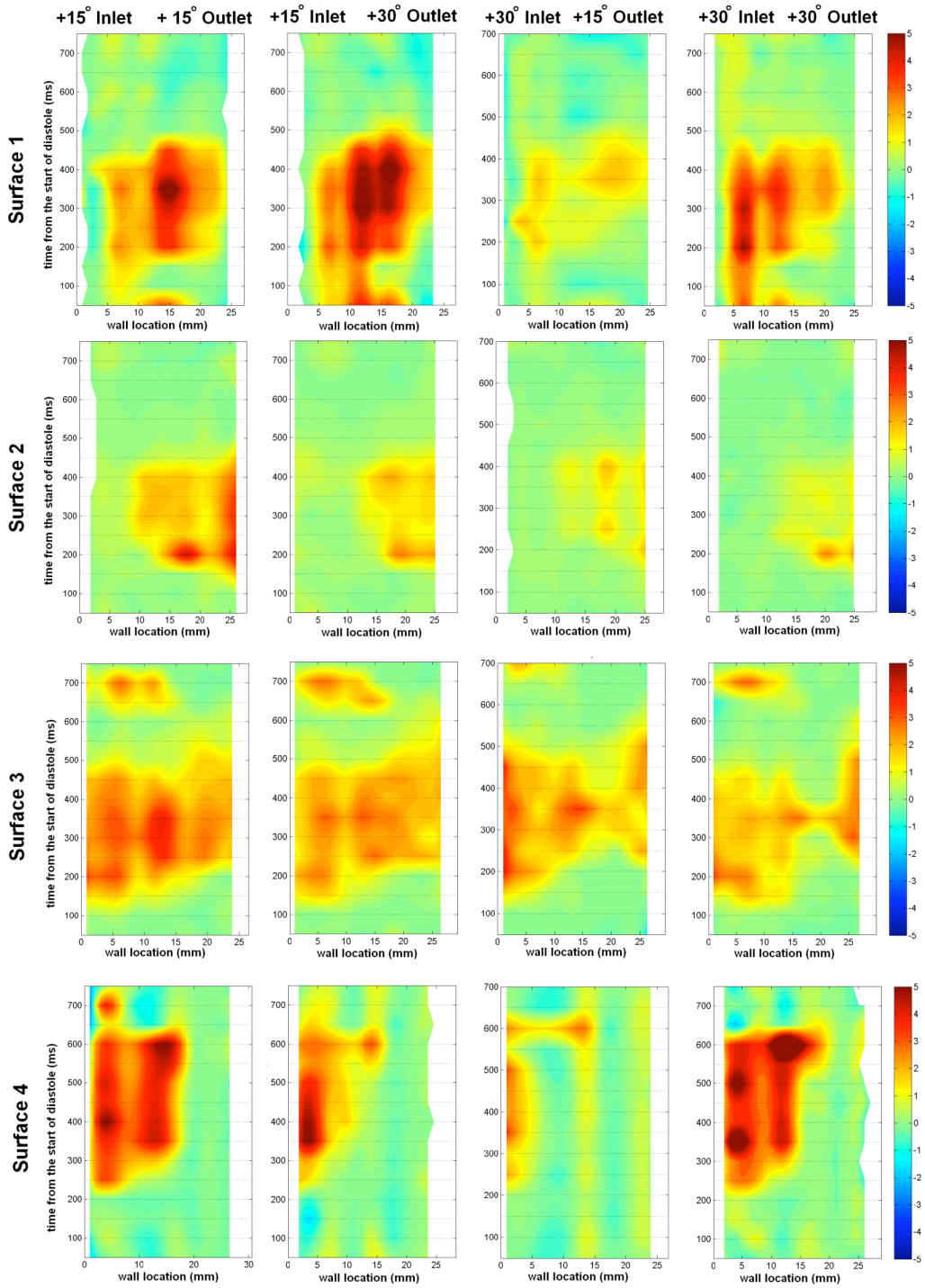

Figure 14: The wall shear maps for all four surfaces (Figure 4B) of the 11 mm plane for the (+15°, +15°), (+15°, +30°), (+30°, +15°) and (+30°, +30°) combinations. The maps are normalized to the 500 s^{-1} threshold, therefore 1=500 s^{-1} on the color legend. The data observed contains many areas of shear above the threshold value of 500 s^{-1} (indicated by shades of yellow to red and dark blue), much of which occurs for period of several hundred ms. While a good portion of the wall shear data observed is adequate, the +15° +15° orientation possesses the most desirable shear patterns for prevent thrombus formation (Figure from Roszelle 2010b).

1.3.4 PVAD Operational Protocol Study

Because initial flow studies observed an increased sensitivity in the PVAD flow field to valve changes, type and angle, it was hypothesized by Cooper et al., that alterations to the operating protocol may aid in developing positive flow characteristics. Investigating these types of protocol changes *in vitro* is helpful because it allows for the changes in the fluid mechanics to be observed and assessed prior to device implantation, giving clinicians a better idea of what device conditions are safe for patients. For this study the operational change was an increase in the end diastolic delay (EDD) between the end of inflow and the start of positive drive pressure (highlighted in Figure 15). The changes in the EDD compress the diastolic duration and led to lower blood residence times inside the device, a desired aspect for reducing thrombus formation. For this study a beat rate of 50 bpm was observed with EDDs of 10, 50 and 100 ms. These waveforms are shown in Figure 15 (Cooper 2010).

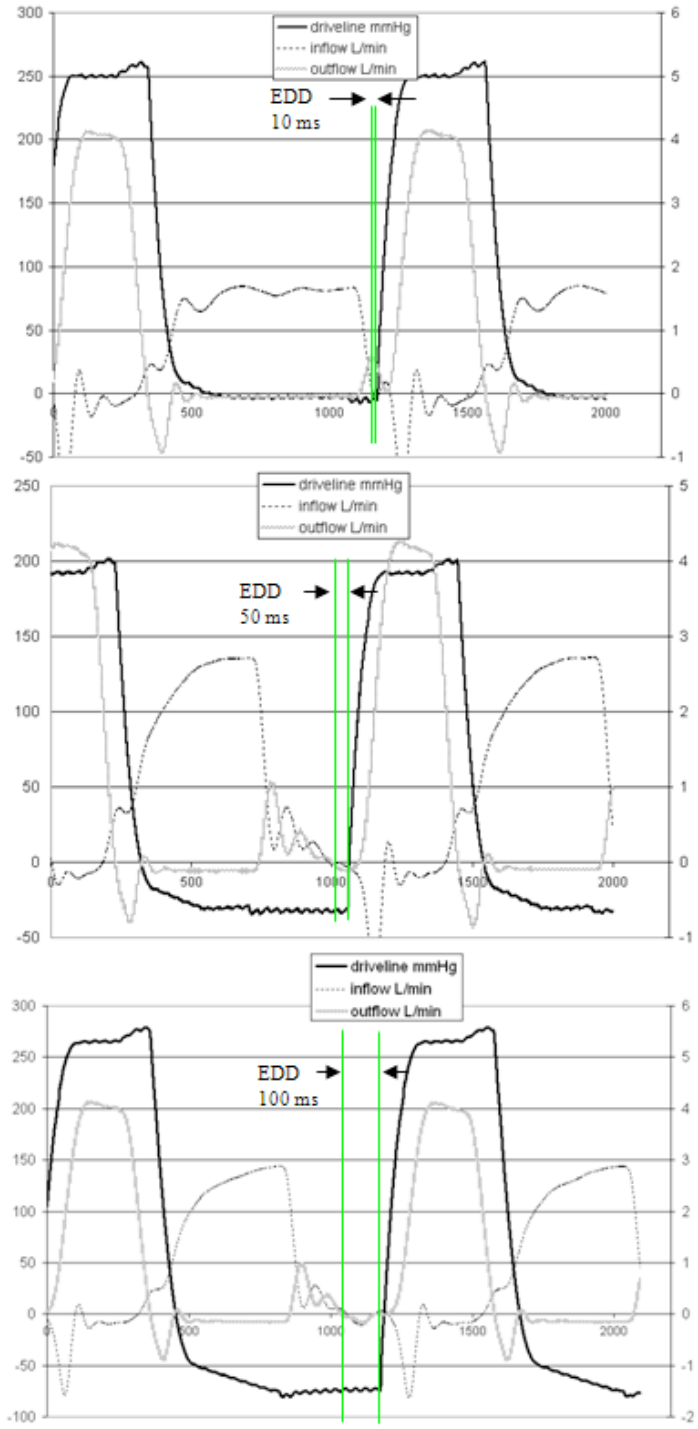

Figure 15: Waveforms for each of the end diastolic delays used, from top down: 10, 50 and 100 ms. The green lines show where the inflow crosses zero and then where the positive driveline pressure begins. The distance between these two lines represents the length of the EDD (Figure from Cooper 2010).

Comparisons between the EDD delays found that the 50 ms delay lead to the best overall flow results. As presented in Figure 16, the 50 ms delay resulted in a higher velocity inlet jet and stronger rotational flow in the body of the device during diastole than the 10 ms delay used originally in the beat reduction study. As also shown in Figure 16, the 100 ms delay results in a tight rotation during diastole which may appear desirable, but also leads to a large area of separation at the inlet port of the device.

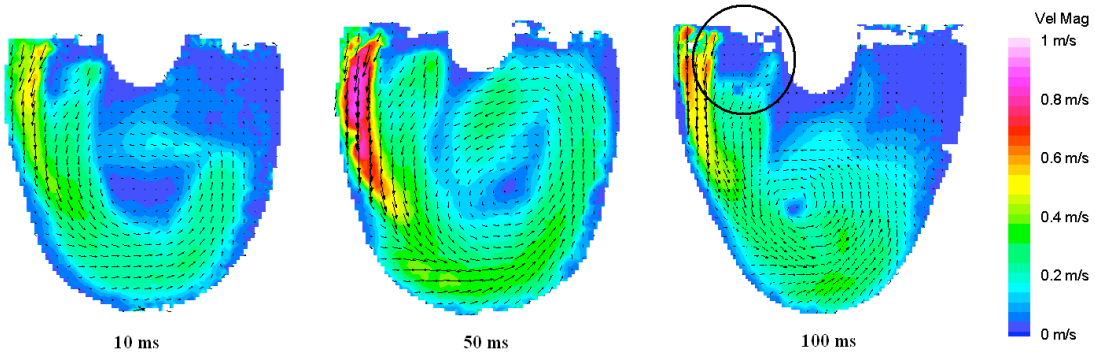

Figure 16: The 8.2 mm plane at 450 ms into the cycle (mid diastole) for 10, 50 and 100 ms EDD from left to right. The 50 ms delay clearly has the strongest inlet jet at this point in the cycle and the desired rotational flow pattern is organized throughout the body of the device. The 100 ms delay results in a tight rotation near the bottom of the device, but also an area of stagnation in the inlet port as highlighted with a black circle (Figure from Cooper 2010).

As the flow transitions into systole the 100 ms delay continues to show problems, especially highlighted by the dissipation of the rotational flow. In contrast Figure 17 shows that the 10 and 50 ms delays continue to produce an organized rotational pattern during systole.

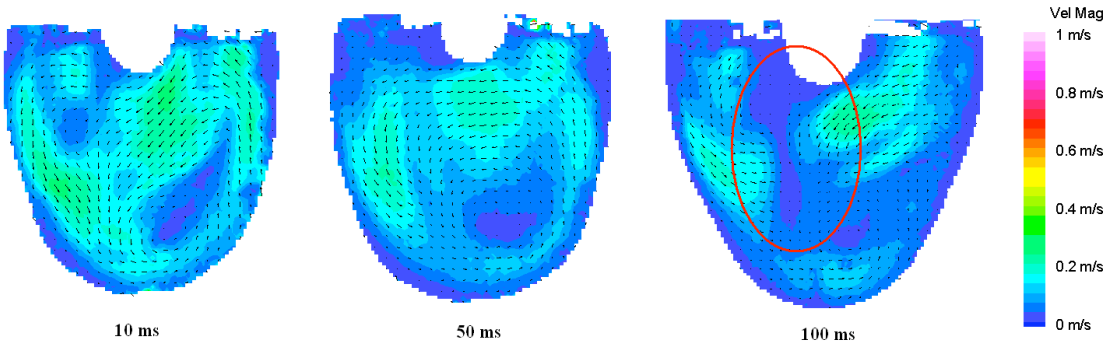

Figure 17: The 8.2 mm plane at 850 ms into the cycle (onset of systole) for 10, 50 and 100 ms EDD from left to right. While both the 10 and 50 ms delays show a continued rotational flow from diastole, the flow of the 100 ms delay has dissipated, leaving a large area of stagnant flow highlighted in red (Figure from Cooper 2010).

The wall shear data confirmed the superiority of the 50 ms delay. The 50 ms delay contained the highest magnitude of wall shear along the outside walls, and also the longest duration above threshold values. This is especially apparent along the lower wall of the inlet of the device (labeled as Surface 2). Figure 18 shows the 50 ms delay produced wall shear levels above the desired threshold value of 500 s^{-1} along the entire surface at some point in the cycle, many of which lasted around 300 ms. Figure 18 also highlights the deficiencies along this wall for the other two delays, both of which barely reach the threshold value for any significant part of the cycle.

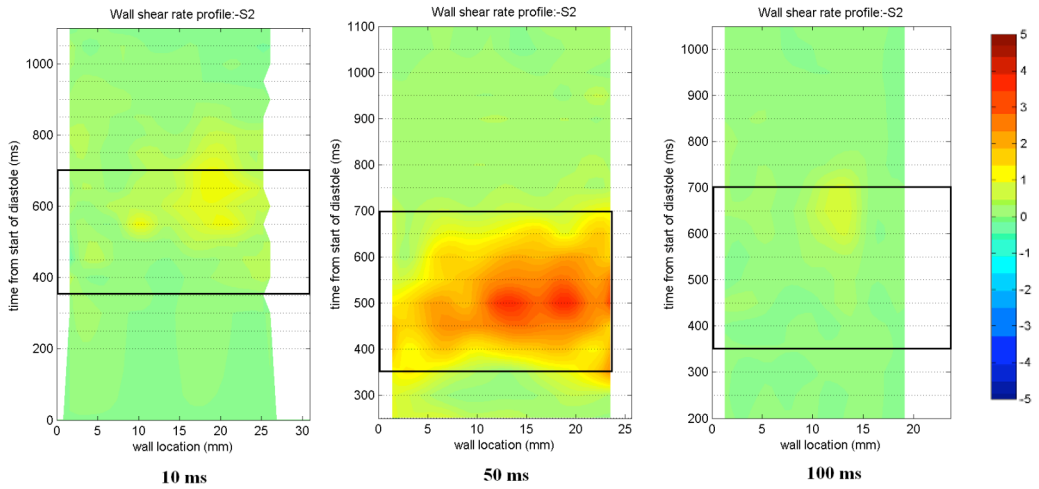

Figure 18: The wall shear along Surface 2 (see Figure 7) for the 8.2 mm plane of 10, 50 and 100 ms EDD from left to right. The black box highlights 350 to 700 ms of the cardiac cycle, which comprises mid to late diastole. It is clear that the delay of 50 ms is superior to the other delays in strength of the wall shear rate, location across the entire surface, and length of time during which the wall shear rate is above the 500 s^{-1}threshold (Figure from Cooper 2010).

These results not only bring insight into the use of EDD changes for possible flow reduction conditions used for myocardial recovery, but also highlight the importance of operational protocol overall. This study shows that a simple change in this protocol can lead to significant changes in the flow field physics of the device, both positive and negative. Bringing into light the necessity to observe what possible operating conditions may be seen during implantation in order to use the PVAD in a safe and effective way.

1.3.5 PVAD Analog Hematocrit Study

Previous studies have shown that pediatrics have a large range of blood hematocrit, from 20 to 60% (Long 2005). Because of blood's unique viscoelastic properties, it was necessary to observe the effect of this hematocrit range on the fluid mechanics. This difference in viscoelastic properties is also applicable to the animal models used during PVAD testing, which contained reduced elasticity. In order to observe the possible flow differences, Roszelle et al. performed PIV studies on blood analog fluids corresponding to 60% and 40% hematocrit pediatric blood and 26% hematocrit goat blood (Roszelle HCT).

In general the flow pattern seen in previous studies was retained by all of the analogs. However, there were differences between the fluids including variations in the profiles of the inlet and outlet jets, the penetration of flow into the bottom of the device, and the overall coherence of the rotational flow field. These differences were most noticeable between the pediatric analogs and the goat analog, as highlighted in Figure 19.

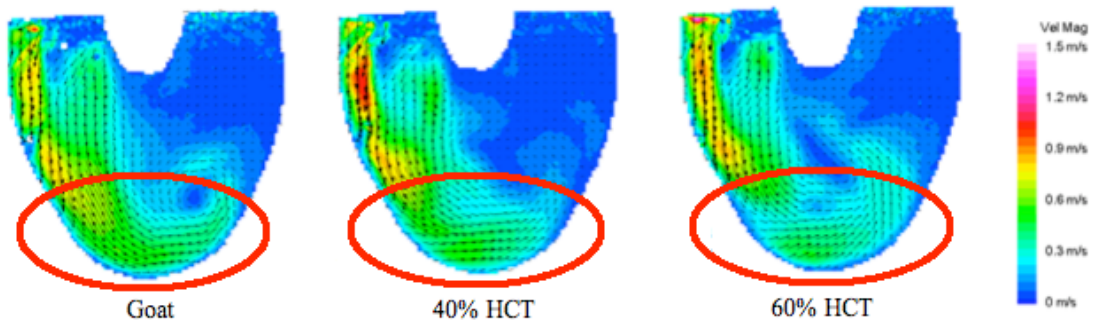

Figure 19: The 8.2 mm plane of the PVAD at 200 ms (mid-diastole) for all three blood analogs goat, 40% hematocrit pediatric, and 60% hematocrit pediatric from left to right. As highlighted in red at mid diastole the goat analog shows penetration to the bottom of the device without much evidence of three-dimensionality. In contrast the pediatric analogs show more evidence of three-dimensionality, which is flow not from the inlet jet. This is one example of the differences between the goat and pediatric analogs that continued throughout the cardiac cycle.

The differences between the analogs were also noticeable in the wall shear rates, as shown in Figure 20, which again highlights the variation between the pediatric and goat analogs.

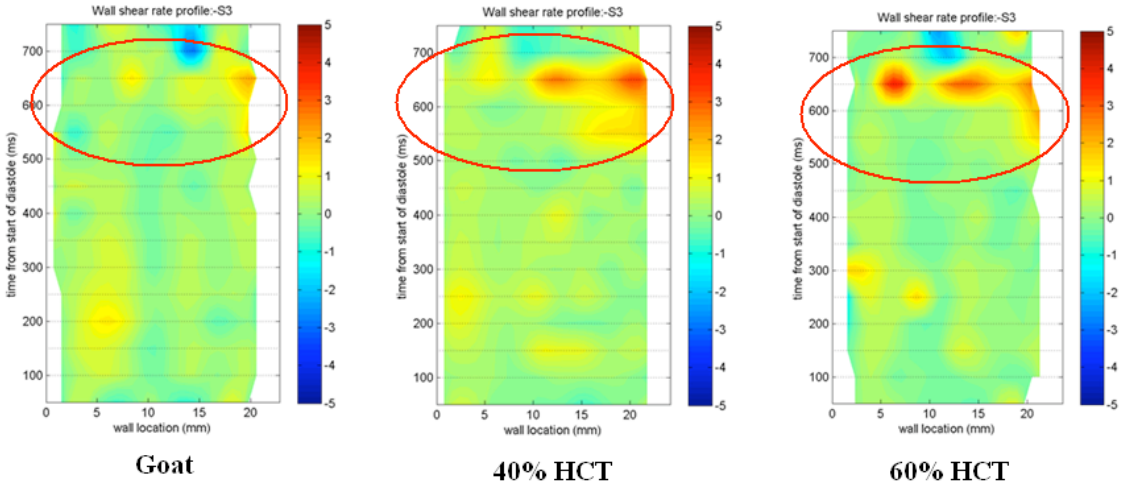

Figure 20: The wall shear rate maps of the lower portion of the outlet port for the 7 mm plane. As highlighted in red the 40 and 60% pediatric analogs both show an increase in shear rate during diastole, while the goat analog does not show a similar pattern. This is an example of how the local wall shear rates varied between the goat and pediatric analogs.

Overall, the analog comparisons found that the differences in analogs led to differences in the flow field. However, these were most prominent when compared to the goat and pediatric analogs, indicating that results from animal testing should account for these differences. The study also reiterated the importance in using non-Newtonian fluids for fluid mechanic studies of VADs, as the fluid type does affect the flow patterns. Lastly, it should be noted that since the differences between the 40 and 60% hematocrit pediatric analogs were less noticeable. Therefore, the investigators concluded using the 40% hematocrit for future studies was acceptable.

In summary, the basic fluid dynamic patterns inside the PVAD have been observed through studies of valve selection and three-dimensionality. These studies have also shown that PIV is an accurate and adequate flow visualization system for our model. A study on valve selection also showed that the flow field of the PVAD is sensitive to changes, which is important to note when considering operational changes that could occur during a process such as weaning.

1.4 Current Study

As a result of these previous studies the specific aim of this study is to introduce a weaning protocol to the PVAD by reducing the flow rate and observe this effect on the fluid mechanics of the device. This weaning protocol will be necessary for using the PVAD as a bridge-to-recovery device, and requires a reduction in the flow rate of the device. The flow rate reduction will be accomplished using two different methods, a beat rate reduction and a stroke volume reduction. These conditions will be maintained and monitored in an *in vitro* setup using a mock circulatory loop system. The flow patterns will be visualized using particle image velocimetry. The results will be presented as both whole flow field maps and wall shear rate maps. The goal of the studies will be to observe the flow patterns associated with flow rate reduction methods, specifically focusing on characteristics related to thrombus deposition. This information can then be used to help suggested operational protocols and limitations of the device during clinical applications, in this case related to bridge-to-recovery applications.

Chapter 2

PARTICLE IMAGE VELOCIMETRY

2.1 Particle Image Velocimetry Basics

Particle image velocimetry (PIV) is a non-invasive, optical measurement technique that can be used on both air and liquid flow fields, as well as for some multiphase flows. The basic concept involves illuminating a single plane of particle laden fluid and capturing images to track the movement of the particles and correlate this movement to that of the fluid. Both 2D and 3D techniques exist and are praised for their ability to obtain whole flow field measurements nearly instantaneously (Raffel 1998). An example of a basic PIV setup is given in Figure 21:

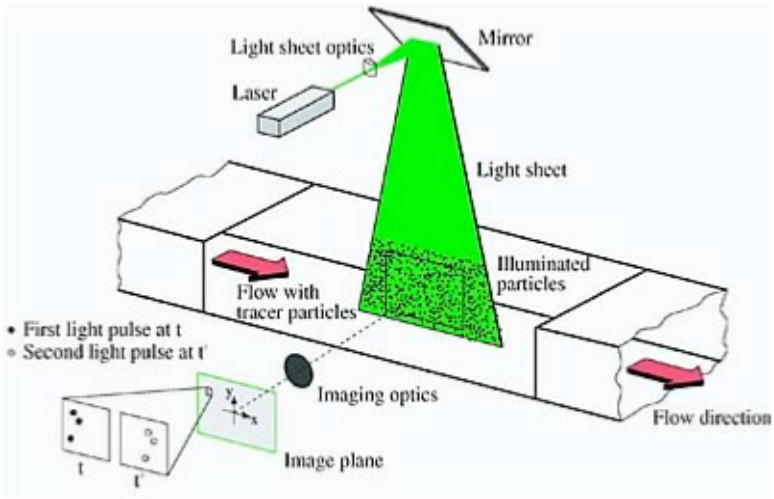

Figure 21: Example of a PIV set up in a windtunnel (Raffel, 1998).

PIV was developed from the evolution of several technological advancements in photography, optical measurements, image processing, and flow visualization (Grant 1994). The idea of using PIV to measure flow fields came from an extension of speckle

metrology. This method measures the roughness of solid surfaces by illuminating the surface with a laser and measuring the scattering of the light. This use of measuring the 'speckle' from the light was then shifted to fluid measurements by using high density seeding to scatter the light, similar to what was seen by the roughness of the solid surfaces (Grant 1994). Since the inception and development of the original PIV technique in the 1980s, the technology has expanded greatly, allowing for more accurate and more widespread uses of the tool over the past two decades (Prasad 2000).

The basic set-up of current PIV systems, as shown in Figure 21, includes an optically clear test model filled with particle-laden fluid, which matches the refractive index of this model. The particles of the fluid are then illuminated, most often by a thin laser light sheet. Images of the particle laden flow moving through the test model are then captured using recording hardware, most often a charge-coupled device (CCD) camera or, in cases of older systems, a film camera. Finally, a computer system is used to collect all of the recorded images and convert them to velocity vector maps (Prasad 2000). This chapter details the process of capturing PIV images and obtaining quantitative flow field maps.

2.1.1 Displacement Theory

PIV has been considered both a Eulerian and Lagrangian technique. Some consider the technique Eulerian because the motion of the fluid through a specified plane or volume is measured, while others consider it to be Lagrangian because the technique requires following the movement of individual particles. In a review of PIV by Grant et al. it is claimed that, "The velocity obtained from the flow-following particles is implicitly

Lagrangian while the assumption is often made that Eulerian velocities are measured." (Grant, 1994). Because of this, the equations used to describe the particle displacement are based on Eulerian theory where velocity is a function of position and time. The change in position of the particle over a specified time is used to calculate the velocity, as shown by Equations 1 and 2, where u, v and Δx, Δy are the velocity and change in position of the particle in the x and y direction, respectively, and ΔT is the laser pulse delay, which is the time between the two laser pulses (Grant 1994 and Raffel 1998).

$$u = \frac{\Delta x}{\Delta T} \tag{1}$$

$$v = \frac{\Delta y}{\Delta T} \tag{2}$$

An image depicting this movement is shown in Figure 22.

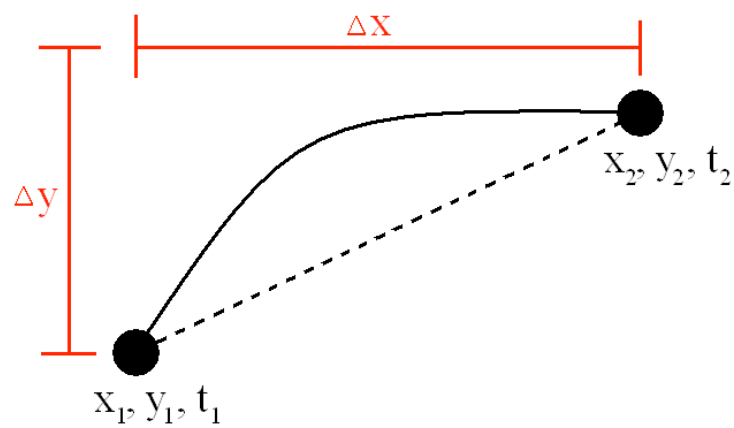

Figure 22: A particle in a fluid flow field shifts from position 1 (x_1, y_1) to position 2 (x_2, y_2) during a finite time Δt (where $\Delta t = t_2 - t_1$). The original path of the particle is shown by the solid black line, while the calculated path is shown by the dotted black line. This calculated path is found by calculating Δx and Δy. The velocity in both the x and y direction can then be calculated using the particle displacements Δx and Δy over the known change in time Δt.

As seen above in Figure 22, the particle path calculated by the Eulerian equation may not exactly match the particle's original path. In order to reduce this error, PIV acquisition and processing techniques have been developed so that the path calculated by the

measurement method matches that of the particle as close as possible and thus, corresponds accurately to the fluid motion (Westerweel 2000).

2.1.2 Particles

The selection of the type of particles used in the fluid, as well as the seeding density is crucial. In order for the movement of the particles to match that of the fluid, it is necessary for the densities of both to be similar, which is easier with liquid flows than air flows. The size, usually measured as the diameter, of the particle must also be carefully selected to provide for optimum optical measurements, while not affecting the fluid flow. A modified Stokes number that considers the properties of both the fluid and particles is used to ensure that the particles chosen follow the fluid movement. This number is defined as $\tau_s/\Delta T$ where ΔT is the laser pulse delay and τ_s is the particle relaxation time, which is defined by Equation 3.

$$\tau_s = d_p^2 \frac{\rho_p}{18\mu} \qquad (3)$$

where d_p and ρ_p are the diameter and density of the particle, respectively, and μ is the dynamic viscosity of the fluid. If $\tau_s/\Delta T$ is $<< 1$ than the particle path matches the fluid path (Raffel, 1998).

The desired seeding density for each measurement depends on several factors including the type of flow, resolution of the camera and the method of processing chosen. When the seeding density is low, one or two particles per measurement region, individual particle displacement can be measured resulting in a Lagrangian measurement technique. This is called particle tracking velocimetry (PTV) and is often used in situations were PIV is

impractical, such as for near wall or very high-resolution measurements. PIV uses higher density seeding, with 5 to 15 particles per measurement area. Because of the increased number of particles, it is no longer possible to identify particle pairs unambiguously, therefore, tracking algorithms based on pattern recognition are used. This allows for more information to be obtained from the measurements, including better spatial resolution and smaller particle displacements relative to PTV (Grant 1994, Raffel 1998, Westerweel 2000).

2.1.3 Illumination

In order to locate the particle positions in the fluid, they are illuminated by a thin sheet of light, most often from a laser source. Lasers are commonly used because they can be easily manipulated into monochromatic light sheets. The type of laser used depends on the study, but common sources are helium-neon, semiconductor, argon-ion, ruby and Neodym-YAG or Nd:YAG lasers (as used in this study). Dual laser systems are often used because it allows for very small laser pulse delays, ΔT, to be employed (Raffel 1998).

Light sheet optics are used in order to form the light source into a sheet of desirable width. Most often these are a combination of spherical or cylindrical lenses, the size and position of which are specific to the study and the lasers being used. The goal of the optics chosen is provide a thin, uniform light sheet of high intensity and an appropriate focal length for the specific flow field being studied (Raffel 1998 and Prasad 2000).

2.1.4 Image Capture

One of the most advantageous developments in PIV technology over the past two decades comes from the use of digital image recording. This switch from film photography allows for immediate image availability and feedback, as well as easier collaboration with computational tools for processing and storage (Grant 1997).

Currently, most PIV systems employ charge coupled device (CCD) cameras. CCD cameras are electronic sensors that convert light into an electrical charge, which allow for the images to be stored electronically. The individual elements in a CCD sensor are referred to as pixels. The resolution of an image is based on how many pixels are on the CCD chip, and how far away the camera is from the image plane on which it is focused. There are advantages to using both high and low resolution magnitude images, and this can be altered by the placement of the camera in relation to the imaging plane (Raffel 1998).

In order to capture images at desired times, a synchronizer is often used to coordinate the pulses of the laser and the camera. The synchronizer, camera and lasers can be run using a computer that allows the user to select the desired ΔT and the camera exposure time.

2.2 PIV Processing

Once images have been captured, each pair is processed using a cross-correlation technique. This technique begins by breaking down the entire image that has been captured by the CCD chip into interrogation regions. During processing the PIV

algorithms assume that the particles in each of these interrogation regions move in a similar direction with a similar magnitude. This means that when the processing is complete each interrogation region will have a single averaged vector that represents the magnitude and direction of the velocity at the centroid of the area (Raffel 1998 and Prasad 2000). An example of what these regions look like is shown in Figure 23:

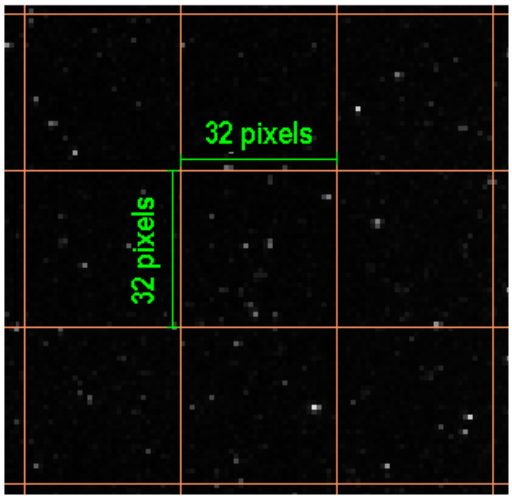

Figure 23: An example of a PIV image divided into 32 pixel by 32 pixel interrogation regions. The size of the interrogation region can be chosen based on the resolution of the image, and usually contains 5 to 15 particles.

In order to correlate the images, statistical PIV uses pattern recognition of the particle displacement instead of the exact averaged displacements of the particles. Figure 24 shows an example of cross-correlation between two images, named Frame A and Frame B. During the first step of cross-correlation, the selected algorithm observes the particles in each interrogation region in the first image frame (Frame A). The location of the particles in Frame A are saved as a 'spot mask,' which serves, in essence, as a fingerprint of the particles location. The algorithm then takes this spot mask and attempts to match the pattern to the particle locations in Frame B. A correlation value is given to each location in the interrogation region, and the best match of the spot mask is given the

highest correlation value. The displacements of the particles are then correlated from the original particle positions in Frame A and using the known ΔT, a velocity vector is calculated at the centriod of each interrogation region (Grant 1997, Raffel 1998, Prasad 2000).

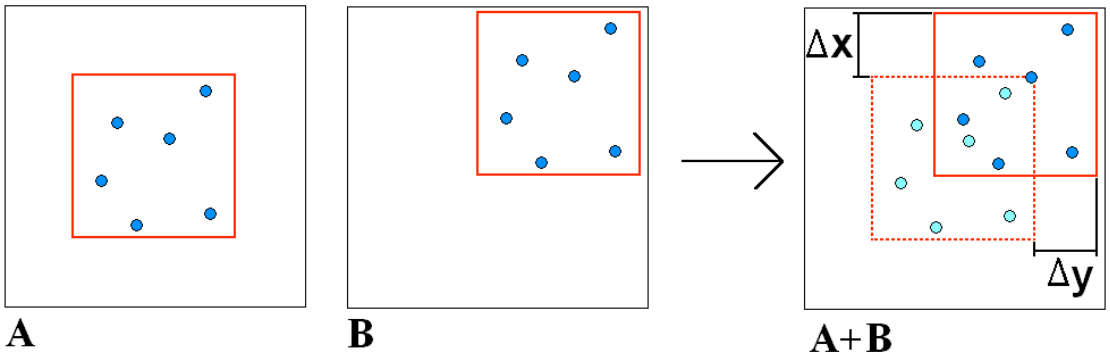

Figure 24: The cross-correlation process uses the particle pattern found in Frame A as a spot mask for comparison with Frame B. The process then searches the interrogation region of Frame B for a pattern similar to the spot mask from Frame A. Once the area that most closely correlates to the spot mask is found the distance between this new found location in Frame B and the original spot mask in Frame A in both the x and y direction are calculated, as shown on the far right. This distance combined with the know ΔT is then used to find the velocity vector at the centroid of the interrogation region.

When cross-correlating two interrogation regions (in this case referred to as Frame A and Frame B) in a set of image pairs Equation 4 is used.

$$R_{II}(\vec{s},\vec{\Gamma},\vec{D}) = \left\langle I_A(\vec{x},\vec{\Gamma}_A) I_B(\vec{x}+\vec{s},\vec{\Gamma}_B,\vec{D}) \right\rangle \qquad (4)$$

Where I is the transmitted light intensity for each frame, x is the position of the vectors in the interrogation region, s is the shifting vector for frame B, and Γ is the series of location vectors for each particle which describes the state of the ensemble at the given time. A detailed mathematical analysis of this equation can be found in the literature (Raffel 1998). When the cross-correlation function is mapped it contains a composition of the

peaks in intensity found across the interrogation region. The highest peak then corresponds to the mean particle displacement for the region, which can be used with the known ΔT to calculate the velocity vector at the region's centriod. Examples of these maps are shown in Figure 25.

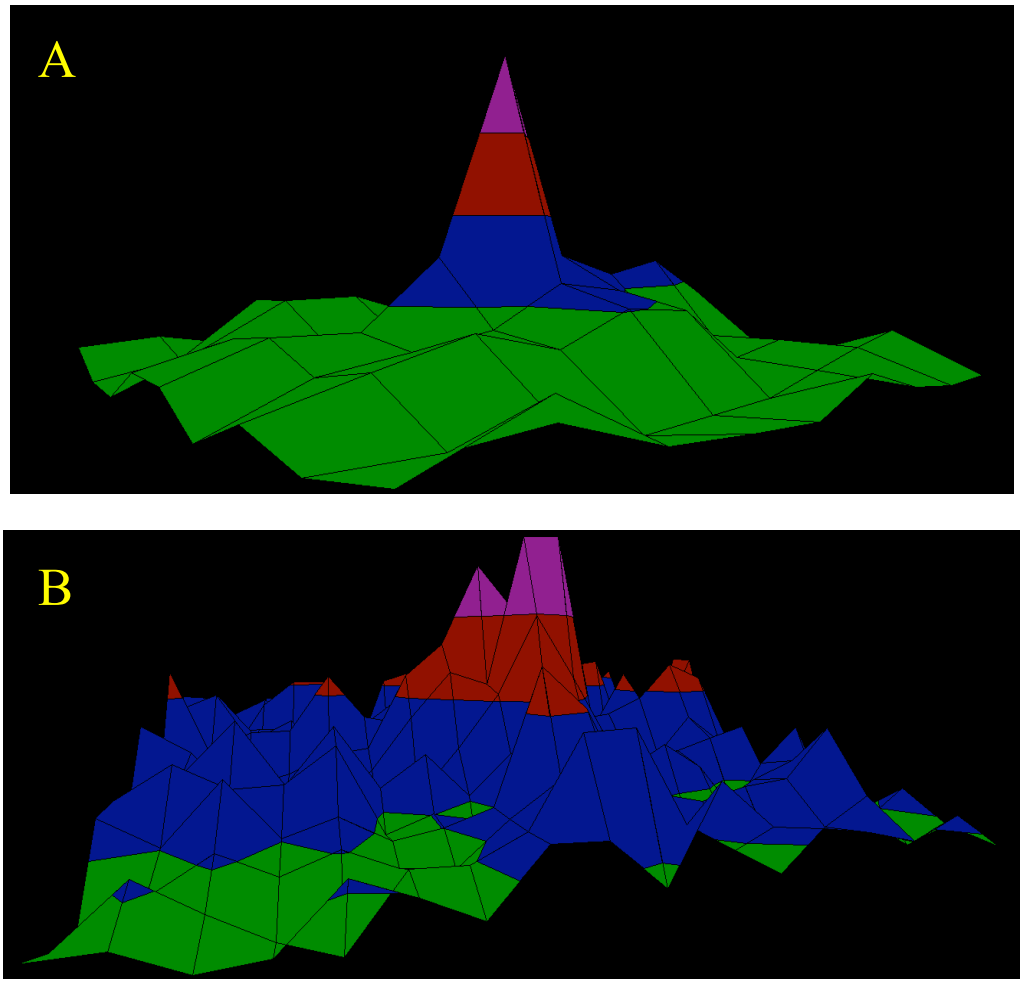

Figure 25: Examples of correlation maps from PIV data. (A) is a passing map, with a single peak that corresponds to the mean displacement of the particles and results in a valid vector. (B) is a failed map that contains two larger peaks that are not differentiable to select a single mean displacement and also contains a large amount of smaller peaks, which are considered noise. (B) results in a non-valid vector that would be removed from the vector map.

In order to help verify that the maximum peak corresponds to the mean particle displacement, the software requires a certain level of tolerance. This means that if there are two large peaks of similar intensities in the region and one is not a certain percentage larger, there is no clear maximum peak (Figure 25B). No velocity vector would be calculated for this region. Other verification tools can also be used to determine if a velocity vector is valid. One example would be using a local validation filter that compares the velocity vector of a region to that of the surrounding regions and removes any vectors that are not within a specified tolerance. Once non-valid vectors are located, they can either be replaced, usually with a vector corresponding to the mean or median of the neighboring vectors, or removed completely. Because it is likely that not every region will have a valid vector for each image pair, ensemble averaging of pairs is often necessary to guarantee enough information to calculate accurate flow field maps (Westerweel 2000).

Vector density may also be increased during processing with the use of overlapping regions. This method increases the number of interrogation regions by making new regions that overlap the original grid. Figure 26 shows an example of the use of a 50% overlap. The new region consists of 50% from each of the two original neighboring regions. A velocity vector will then be calculated at the centroid of this new region, increasing the total vector density. This method does not increase the resolution of the image, because the spatial correlation is still computed over the same interrogation region size.

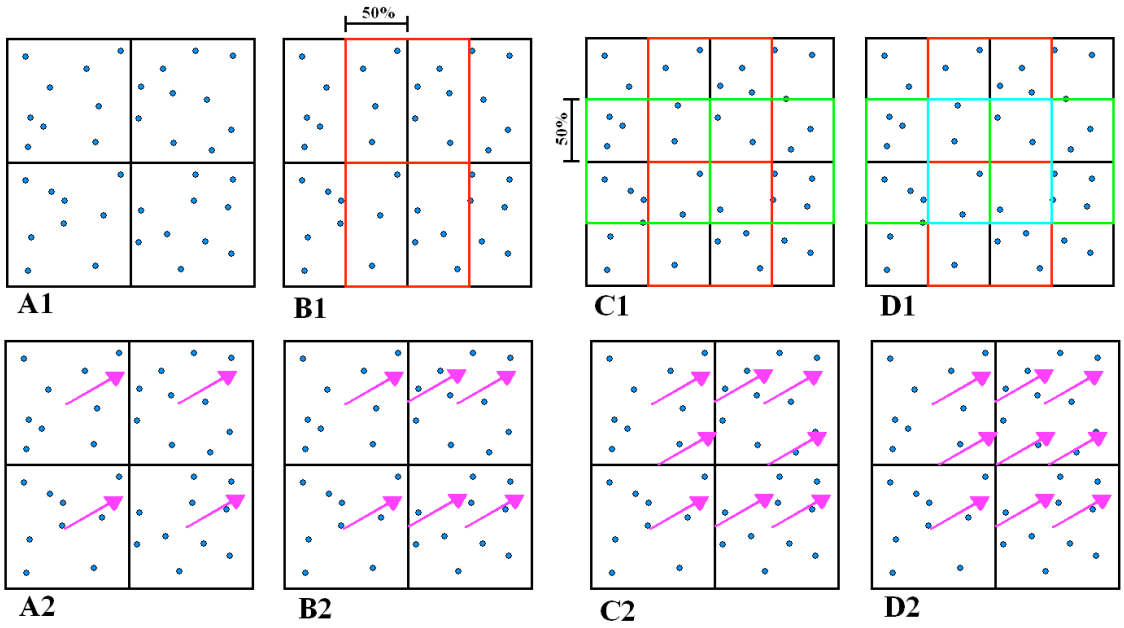

Figure 26: During PIV processing, each interrogation region with a valid correlation peak contains a single vector at the centroid of the region as shown by A. Many processing techniques use an overlap of the interrogation regions to increase the vector density. As shown by B and C, by overlapping the interrogations regions horizontally and vertically the vector density can be doubled. In some cases these new regions can also be overlapped, as shown in D, adding even more vectors. This increase in vector density does not increase the resolution of the image, but uses the information in each image to its full potential.

The spatial resolution for the velocity vectors found using PIV is determined by the maximum and minimum particle displacements, which are constituted by the size of the interrogation regions and the resolution of the image, M. The maximum particle displacement is determined as the length of the interrogation region, although many processing techniques limit this displacement to a portion of the interrogation region, usually between 25 and 50% of the maximum. This helps maintain accuracy because there is less movement of particles into and out of the interrogation region between image captures. The pattern recognition used by the cross-correlation also allows for sub-pixel displacement resolution, making the minimum particle displacement between 1/10 and 1/20th of a pixel. The spatial resolution of the velocity vector is then calculated using the maximum and minimum particle displacements and the known laser pulse delay, ΔT. This is illustrated with Equation 5, for the range of velocities in the x-direction, U, where dx is the maximum displacement in the x direction and X is the size of the interrogation region in the x direction. The equation is the same for velocities in the y direction (Raffel 1998, Prasad 2000, Westerweel 2000).

$$\frac{dx(X)(M)}{\Delta T} \geq U \geq \frac{0.1(M)}{\Delta T} \qquad (5)$$

Once each pair of images is processed, the individual vector maps are ensemble averaged to form one representative vector map. The number of image pairs needed to form an accurate averaged flow map is dependent on the type of flow, image resolution, and other factors.

2.3 Sources of PIV Error

Like any measurement tool, there are sources of error associated with PIV images. Many of these errors can be overcome by practicing good PIV collection techniques. These include using the appropriate particle size and density, ΔT, camera resolution, and model material and fluid. The alignment of the camera and laser are also important to good data collection. Some common forms of error and the techniques used to overcome them are discussed below.

2.3.1 Peak Locking

Peak locking occurs when a cross-correlation peak is biased towards an integer that is not characteristic of the flow, leading to false reporting of passing vectors for an interrogation region. This happens when a particle image is too small for the interrogation region and sub-pixel displacement cannot be accurately calculated, leading to peaks at the integer values of the pixels. This can also occur when the ΔT is too short for the flow, not allowing the particle sufficient time to move across an interrogation region. In this case a single peak around one pixel can be observed, again biasing the data. An example of how peak-locking appears in histograms of displacement data is shown in Figure 27.

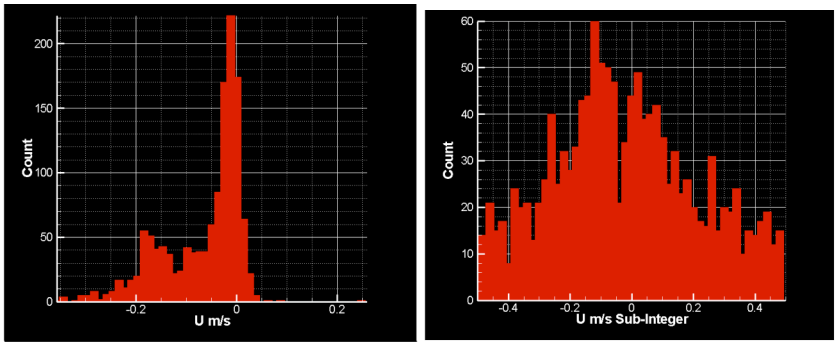

Figure 27: Examples of displacement histograms showing data that is peak locked (left) and data this is not peak locked (right). As shown at the left, the sub-pixel displacement is highly biased towards 0, indicating that the particle displacements have been biased towards whole integers, not allowing for sub-pixel information to be obtained.

In order to reduce the chances of peak locking, it is best to increase the image size of the particles. When this is not an option, a pre-processing tool can be used to help increase or optimize the particle diameter with respect to the peak estimator. The ΔT should also be kept at a reasonable value. The ΔT can be checked during data collection, which is a practical option available with current PIV tools. The camera resolution or interrogation region size can also be altered if the particle diameter or ΔT cannot be changed (Raffel 1998).

2.3.2 Projection Error

Because the light sheet used for PIV measurements has a certain thickness the interrogation region is in reality an interrogation volume. For 2D PIV this leads to projection error by particles because of movement across this thickness, which is labeled as the "z-direction." The image recorded by the CCD chip assumes that the particle only moves in the x and y-directions, when in fact there can also be movement in the z-direction. This is illustrated in Figure 28.

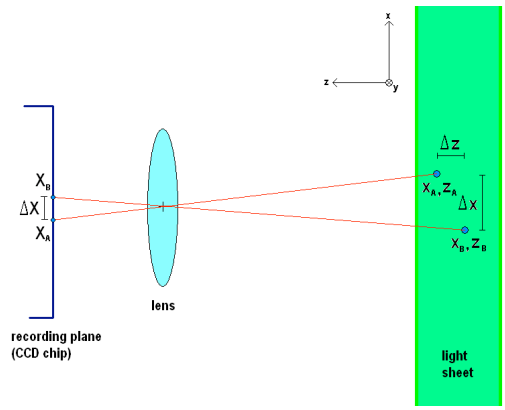

Figure 28: An example of how projection error occurs during PIV imaging. As shown in the light sheet, there is movement by the particle from frame A to frame B in both the x and z directions. However when this information is passed through the camera lens and recorded on the CCD chip, the displacement in the z direction is ignored, leading to a false recording of the particle displacement.

Projection error is of concern for highly three-dimensional flows, in which particles move more readily across the light sheet thickness. Ways to help reduce this error include maintaining a larger resolution, as this will keep the thickness of the light sheet smaller in comparison to the size of the interrogation region. This is the reason that high magnitude PIV studies have large projection errors, because the thickness of the light sheet is much greater than the size of the interrogation region. Keeping the ΔT small, while still avoiding peak locking, is also helpful because the particles cannot travel as far. This is also aided during processing by using a maximum displacement of 0.25 the size of the interrogation region. In some cases the three-dimensionality may lead to projection errors that are too large to overcome, and stereoscopic or 3D PIV may be necessary (Raffel 1998).

2.3.3 Out-of-Plane Motion

Another error similar to projection error is due to out of plane motion. This occurs when particles move completely out of the light sheet thickness during the ΔT. This results in losing the information from this particle, and possibly reducing the number of valid vector counts. Because of this loss of vectors, it is important to check the vector counts in the final averaged velocity map to ensure a proper amount of vectors for a valid average, a number that varies based on the experimental set up. In order to obtain enough valid vectors for the ensemble average and greater number of total images is taken (Raffel 1998). For example, if it has been determined that 50 vector pairs are necessary for an accurate ensemble average, than 100 images may be taken to ensure enough valid velocity vectors.

2.4 Using PIV to Measure Flow in VADs

As mentioned previously in Chapter 1, several flow measurement tools such as laser Doppler anemometry and hot film anemometry had been used successfully to visualize the flow inside VADs. These tools were quite helpful and accurate in characterizing flow and developing VAD design, however as the speed of development increased it became desirable to find a technique that could comprehensively characterize VAD flow fields in a time efficient manner. In studies by Hochareon et al. on a 50 cc adult VAD, it was determined that PIV was a useful choice for observing whole flow fields in a timely manner (Hochareon 2003). Hochareon et al. were also able to develop a technique for locating the walls of 2D PIV images and calculating the wall shear rates along these walls using near wall velocity information from PIV velocity flow maps (Hochareon 2004a). Information obtained from PIV studies, including flow maps and wall shear rates, also compared well to *in vivo* studies that showed areas of clot formation in the device corresponded to areas of low flow found using PIV (Hochareon 2004b).

Chapter 3

METHODOLOGY

3.1 Pediatric Ventricular Assist Device Model

The pediatric ventricular assist device (PVAD) used in the flow visualization studies was made from an optically clear acrylic, a picture of which is shown in Figure 29. The acrylic was molded to match the geometry of the PVAD's blood sac. Openings were left in the model to place the mechanical heart valves and the corresponding aluminum cannulae connectors. Openings were also left in the bottom of the device for the attachment of the pneumatic driveline and for a tap to drain fluid from the model. The model was designed in two pieces to allow for ease of access to the diaphragm. The pieces were sealed using an o-ring.

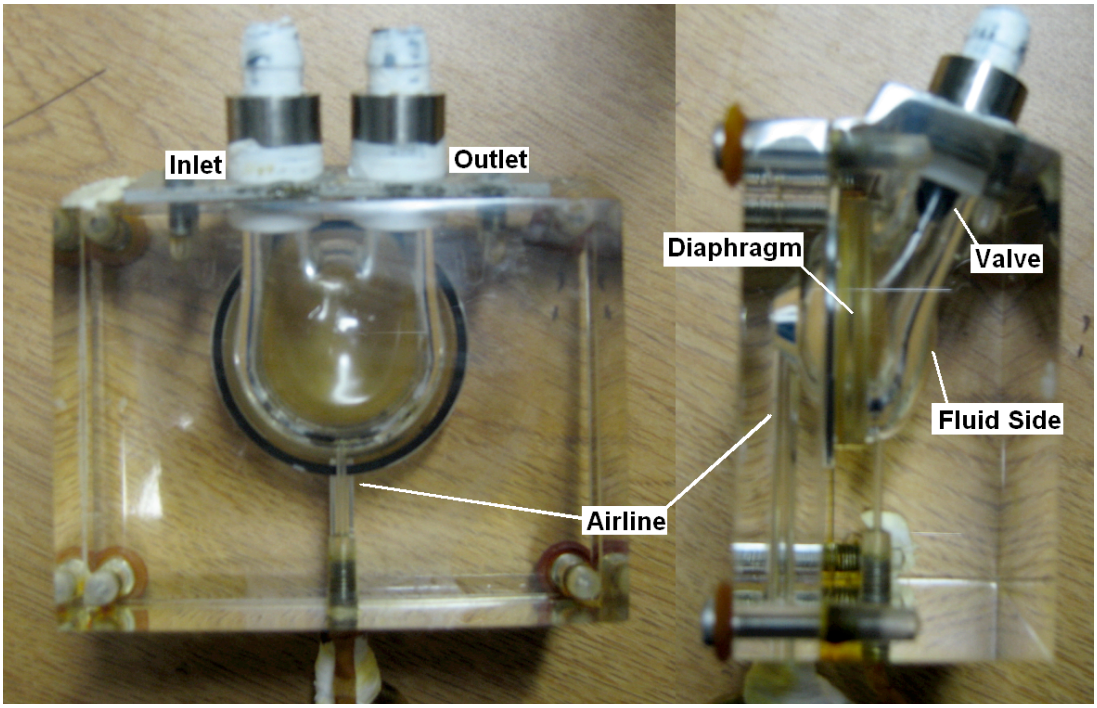

Figure 29: The acrylic model of the PVAD. The model was made to follow the contour of the blood sac. The diaphragm is located next to the airline and opens toward the fluid side.

The model was fitted with 17 mm Björk-Shiley Monostrut (BSM) tilting disc valves. These valves were selected in previous studies over a bi-leaflet valve because of their superior ability to set up a diastolic inlet jet and penetrate to the bottom of the device (Cooper 2008). Depending on the study, the valves were orientated at 0º or at +15º. At an orientation of 0º, the major orifice of both the inlet and the outlet valve is positioned to open along the outside of the port, as shown in Figure 30A. In this orientation the strut of the BSM valve is perpendicular to the diaphragm of the PVAD. As shown in Figure 30B, at an orientation of +15º the major orifices of both the inlet and outlet valves have been rotated 15º towards the fluid side of the PVAD. The +15º orientation was used in some later studies because previous work had indicated that this orientation showed the best inlet jet development and wall washing (Roszelle 2010).

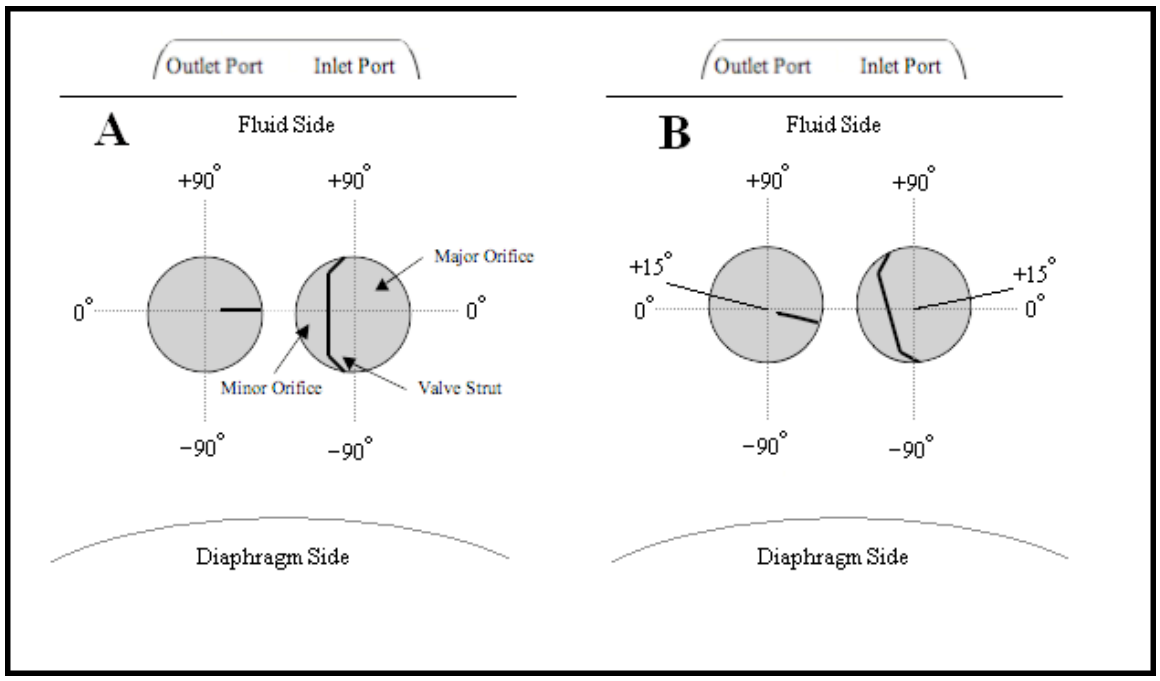

Figure 30: The two valve orientations used in the study. A) shows the 0º orientation where the major orifice of the valve is directed towards the outside of the inlet and outlet port and set perpendicular to the diaphragm. B) shows the +15º orientation where the major orifice is rotated 15º towards the fluid side of the device.

3.2 Mock Circulatory Loop

In order to simulate the systemic circulation, the acrylic model was placed in a mock circulatory loop. The loop was based on the system originally developed by Rosenberg et al. (Rosenberg 1981). This *in vitro* system was specifically designed to test total artificial hearts and VADs. In order for the system to be used for the PVAD, it was necessary to decrease the total volume of the loop and increase the overall resistance. A schematic and picture of this loop is shown in Figures 31 and 32.

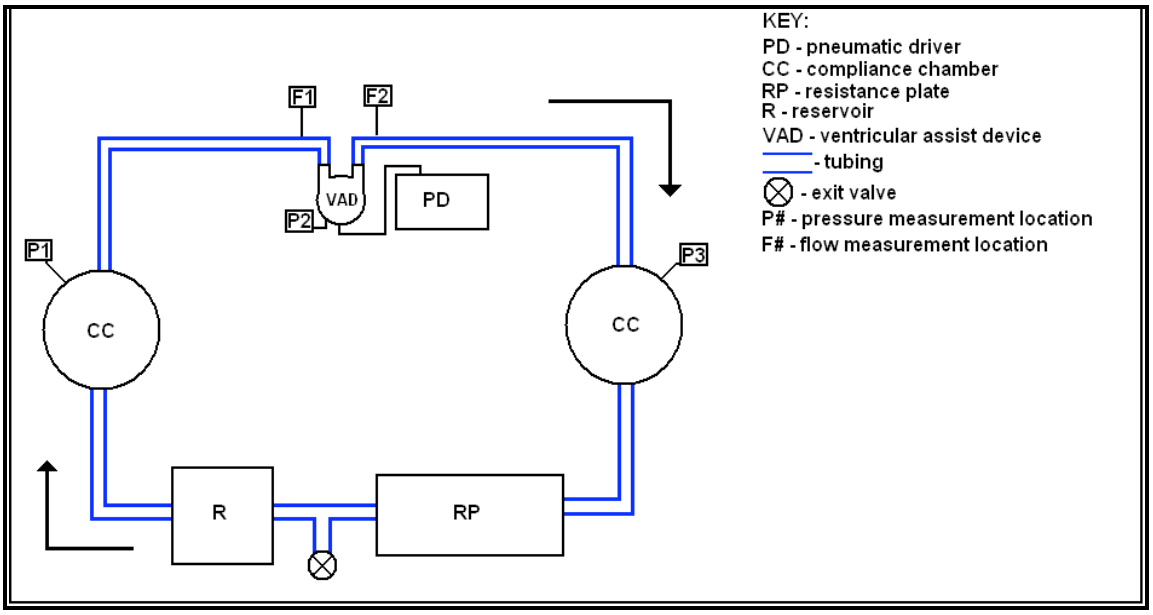

Figure 31: A schematic of the mock circulatory loop used. Each of the loop elements is labeled by the key, as well as the measurement locations for pressure and flow. The arrows indicate the direction of the flow.

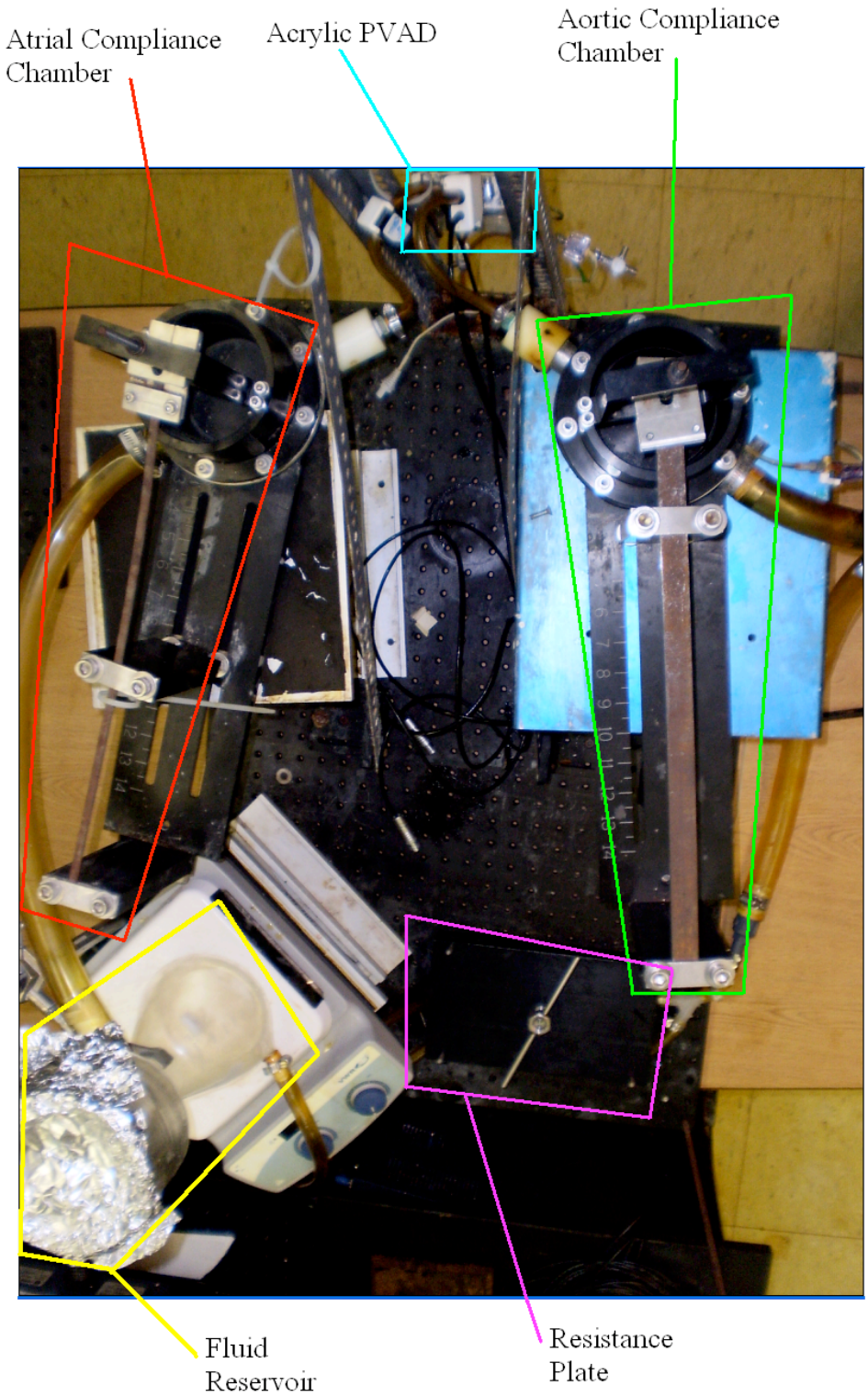

Figure 32: A picture from above the mock circulatory loop. The major elements are highlighted and labeled.

The loop was based on the concept of reproducing the capacitance, resistance and inertance of the circulatory system. Two compliance chambers were used to mimic the atrial and aortic compliance. The design of the chamber was based on Equation 6 where Q is the total flow rate through the chamber, C is the capacitance and dP/dT is the fluctuating pressure.

$$Q = C\frac{dP}{dt} \qquad (6)$$

The chambers have a piston resisted by a variable spring force, which is a cantilevered flat metal rod. The capacitance, C, of the chamber is related to this spring force as shown by Equation 7 where A is the area of the chamber and K is the spring constant of the flat rod.

$$C = \frac{A^2}{K} \qquad (7)$$

K can be varied by using the length, l, of the rod as shown by Equation 8 where E and I are Young's modulus and the moment of inertia respectively:

$$K = \frac{3EI}{l^3} \qquad (8)$$

Combing these relationships allows for the chamber volume fluctuations to be varied during a pressure pulse, allowing for a desired capacitance to be reached. The cantilevered beams on these chambers may be adjusted to obtain the desired difference between the high and low pressures. A picture of the chambers is given in Figure 33.

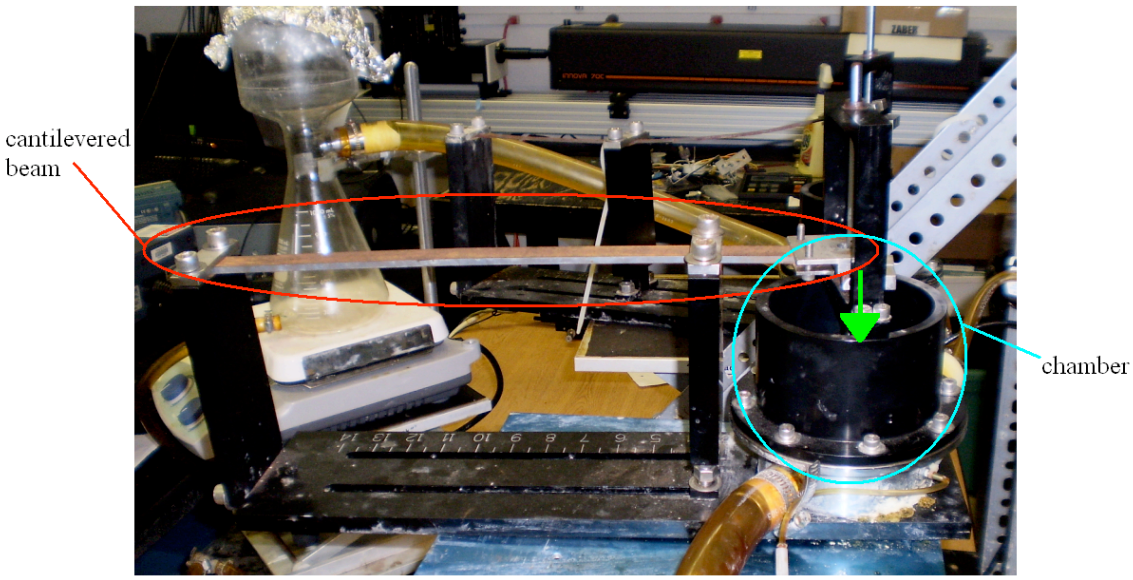

Figure 33: Picture of a compliance chamber used in the mock circulatory loop. The force exerted by the cantilevered beam, circled in red, could be altered to obtained the desired compliance for the inlet and outlet pressures.

A single resistance plate located downstream of the aortic compliance mimics the systemic resistance. This is possible because physiologically the resistance of the arteries, veins and capillaries act in series and can be summed to one value. The resistance in the circulatory loop is based on Equation 9, relating resistance to the change in pressure where R is the resistance and ΔP is the change in pressure.

$$Q = \frac{\Delta P}{R} \qquad (9)$$

In order to vary the resistance, tubing is placed between two 10 x 6 inch plates fitted with a threaded rod. A threaded handle is then place on this rod and tightened, changing the cross sectional area of the tubing, and increasing the resistance. This relationship is given in Equation 10, which is derived from Poiseuille flow and where A is the cross sectional area, L is the length of the tubing and μ is the viscosity:

$$R = \frac{8\mu L\pi}{A^2} \qquad (10)$$

A picture of this plate configuration is shown in Figure 34.

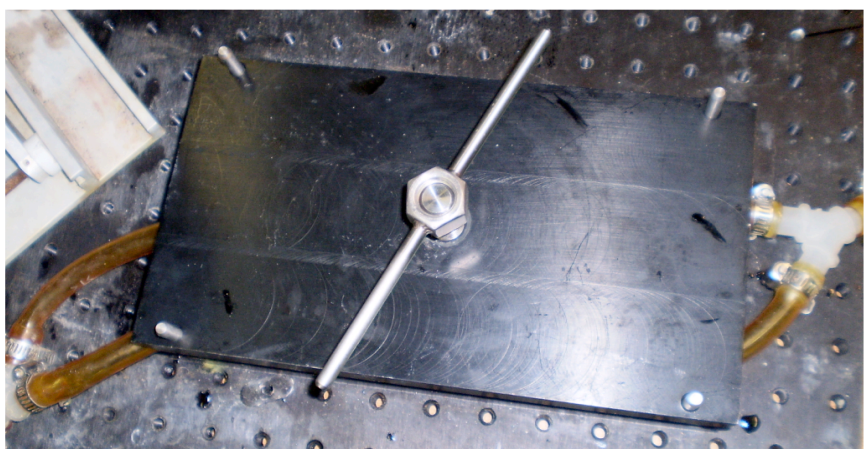

Figure 34: A picture of the resistance plate used in the mock circulatory loop. The plate could be tightened using the handle shown to obtain the desired venus resistance, which correlated to changes in the outlet or aortic pressure.

The inertance of the loop, ϕ, is based on the system equation, show in Equation 11.

$$\Delta P = \phi \frac{dQ}{dt} \qquad (11)$$

The intertance can then be related to the area, A, and length, L, of the tubing, as well as the density, ρ, of the fluid, as shown in Equation 12.

$$\phi = \frac{\rho L}{A} \qquad (12)$$

Therefore, in order to vary the inertance, the length and cross sectional area of the tubing could be varied. For this study flexible Tygon® 3603 tubing (Saint-Gobain Performance Plastics, Aurora, OH) was used to connect all of the loop elements. This tubing varied in diameter from one inch to a quarter inch depending on the necessary connection. A fluid reservoir was specially made to allow for filling of the loop and for the variable total volume of the loop. This reservoir is shown in Figure 35.

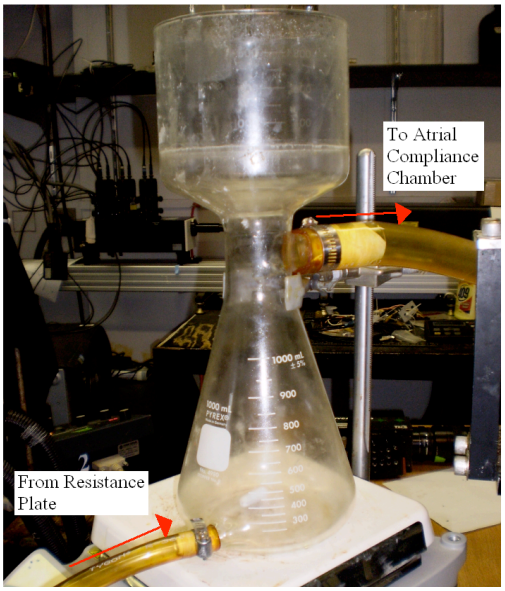

Figure 35: A picture of the fluid reservoir used in the mock circulatory loop. The reservoir was specially made to allow for flow from the resistance plate to the inlet or atrial compliance chamber. Changes in the fluid level of the reservoir effected the inlet pressure as well as the overall intertance of the loop.

The loop was run by a pneumatic driver attached to the airline of the acrylic PVAD model. This driver consisted of a pressure and vacuum pump that produced pulsatile square pressure waves of air to expand and collapse the diaphragm. The driver allowed for the beat rate and the systolic duration to be altered. The "systolic" pressure, or maximum pressure, and "diastolic" pressure, or maximum vacuum could be altered to

allow for changes in the total flow rate of the loop as well as for the timing of the device filling. A picture of the driver is shown in Figure 36.

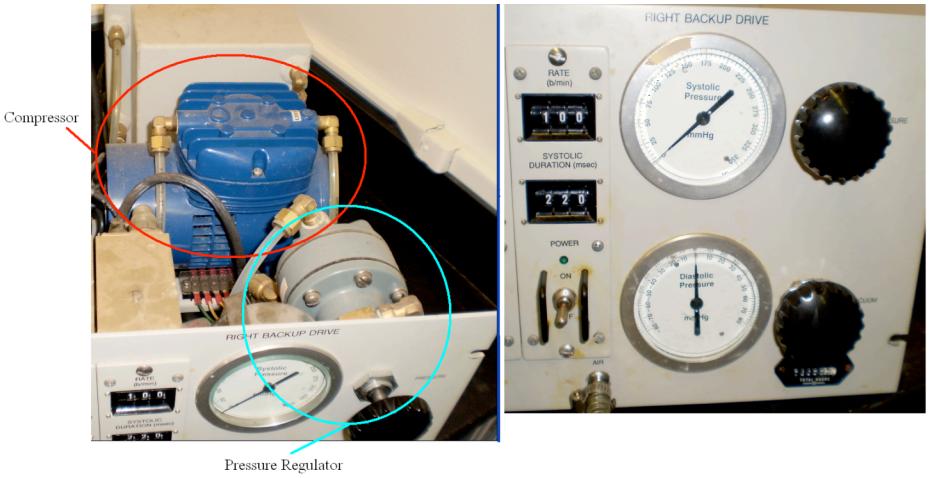

Figure 36: Image of the pneumatic driver used to run the mock circulatory loop. The driver was designed to send a square wave pulse of air to the PVAD diaphragm through the airline. The beat rate, systolic duration and systolic and diastolic pressure were all maintained and altered through the drivers controls shown on the right hand side.

The conditions of the loop, such as flow and pressures, were set to specific conditions for each study. Ultrasonic flow probes (Transonic Systems, Inc., Millis, MA) were used to measure the flow through the loop. These flow probes were placed at the inlet and outlet of the PVAD, the locations for which are labeled as F1 and F2 on the schematic in Figure 31. Both the average flow rate and the instantaneous flow waveforms can be obtained using the probes. Pressure signals were obtained using pressure transducers (Maxxim Medical, Athens, TX). These were placed at the two compliance chambers as well as on the airline of the driver, which are labeled as P1, P2 and P3 in Figure 31. Signals were amplified using a universal strain gauge signal conditioner/amplifier (Validyne Engineering Corp., Northridger, CA). The amplified signals were converted and displayed using a WaveBook acquisition system and WaveView software (IOtech, Inc., Cleveland, OH).

3.3 Blood Analog

Blood is a non-Newtonian viscoelastic fluid, meaning its viscosity and elasticity change with changes in shear rate. Because of the importance viscosity and elasticity have in fluid mechanics, it was important that these properties of blood were matched during *in vitro* testing. It was also necessary for the fluid to be optically clear for the flow visualization tools used. Because of these requirements, a viscoelastic blood analog developed to mimic 40% hematocrit pediatric blood was used in all of the studies. This fluid was selected because it maintains the viscoelastic properties of blood while also matching the refractive index of the acrylic PVAD model, allowing for flow visualization to be used.

The fluid was specifically developed to match the properties of pediatric blood at 40% hematocrit and is fully described by Long et al. (Long 2005). The fluid consisted of Xanthan gum (0.03%), glycerin (16%), sodium iodide (50%), and water (35%), where all the measurements given are a percentage of the total weight. The glycerin and water mixture gave the fluid its increased viscosity to match that of blood, while the Xanthan gum provided the fluid with its elasticity and shear thinning properties. The sodium iodide is used to match the refractive index of the fluid to that of the acrylic (1.49). The properties of the fluid were tested using the VILASTIC-3 Viscoelasticiy Analyzer (Vilastic Scientific, Austin, TX). The viscosity and elasticity were compared to known values of 40% hematocrit pediatric blood at shear rates ranging from 10 to 1000 s^{-1}. An example of these plots is shown in Figure 37.

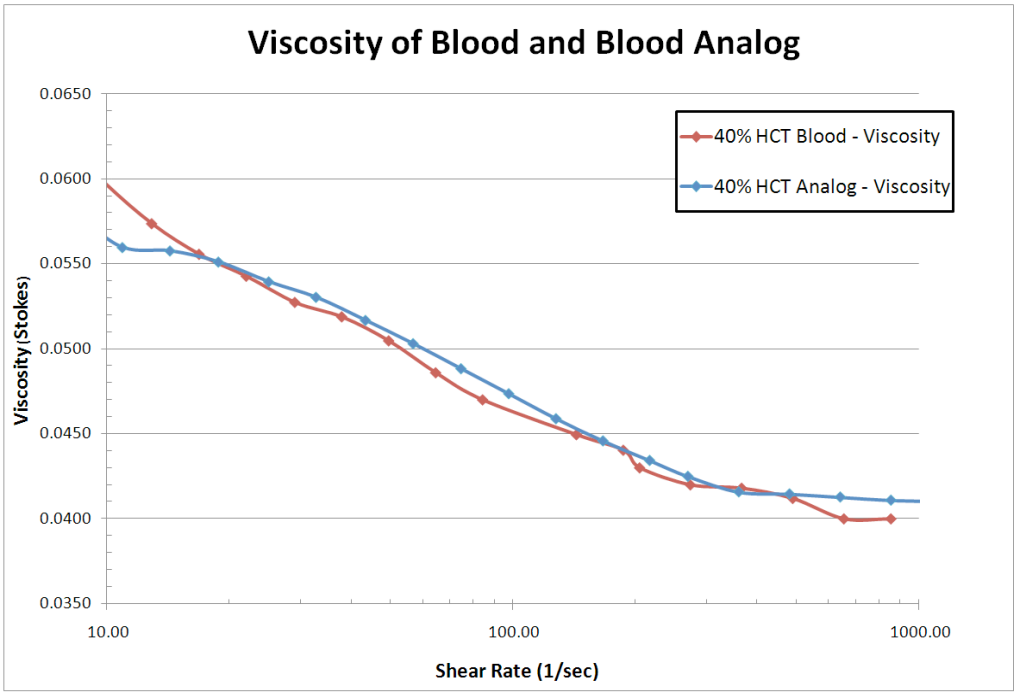

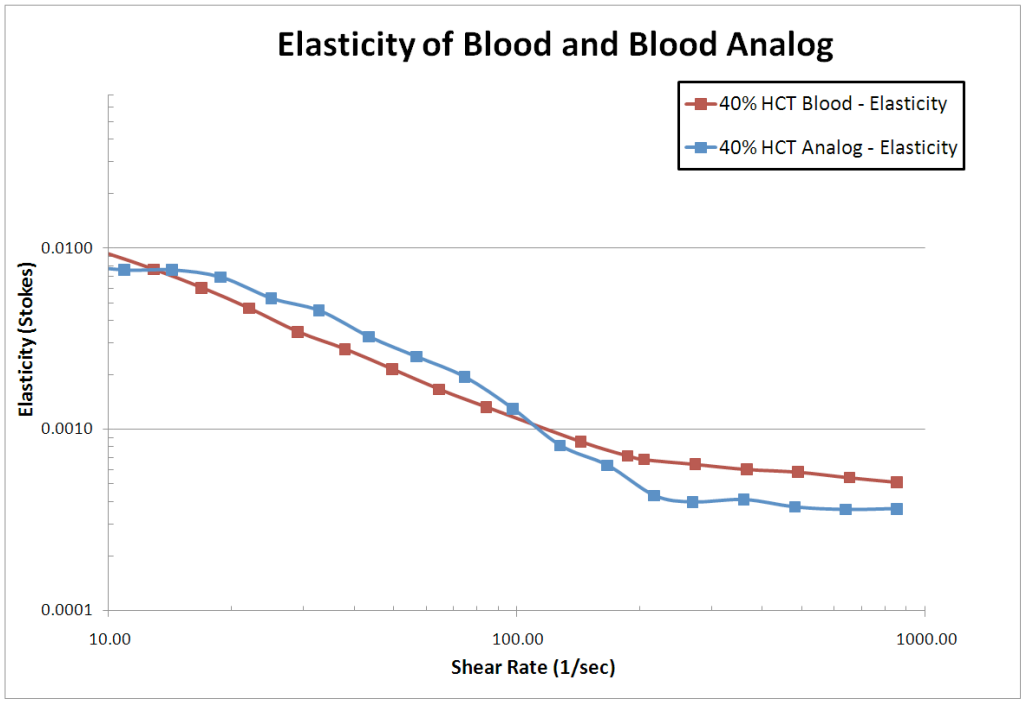

Figure 37: Viscosity (top) and elasticity (bottom) comparison of blood and analog. The viscosity properties of the analog (blue) very closely match those of pediatric blood (red) as the shear rate is increased, indicating that the unique viscoelastic properties of blood have been maintained. Like the viscosity, the elasticity of the analog (blue) closely matches that of pediatric blood (red) as the shear rate is increased.

In order to perform the hemodynamic measurements, the fluid was seeded with 10 μm hollow glass bead particles (Potters Industries Inc., Valley Forge, PA). With a density of 2.5 g/cm^3, the glass beads have a Stokes number of 3.47 e-7 which is much less than one, guaranteeing the particle path will match that of the fluid.

3.4 High-Speed Video

High-speed video was taken to assess the movement of the PVAD diaphragm, while the PVAD was in the mock circulatory loop. A Kodak Motion Corder Analyzer, model SR Ultra (Kodak, San Diego, CA) camera was used with a fiber-optic light source (Edmund Optics, Barrington, NJ) to take the video at a rate of 125 frames/sec.

3.5 Particle Image Velocimetry

Particle image velocimetry (PIV) was chosen as the flow visualization tool because of its ability to capture whole flow field images in a reasonable time.

3.5.1 PIV Setup and Data Collection

PIV was performed using a Gemini PIV 15 system (New Wave Research, Inc., Fremont, CA). The system included dual Nd:YAG lasers that produced 6 mm laser beams with a wavelength of 532 nm. The energy of the laser was controlled with a variable attenuator to avoid damaging the acrylic or diaphragm of the model. The laser beams were converted to a 200 μm thick light sheet by -25 mm cylindrical lens coupled with a 500 mm spherical lens. A 25 mm diameter high-energy mirror was used to direct the laser

through the light sheet optics and the model. A schematic of this basic laser set up is shown in Figure 38.

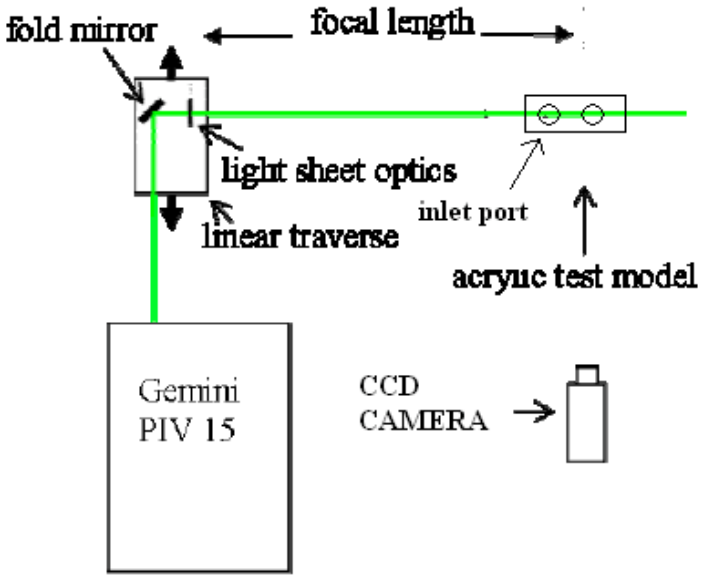

Figure 38: Basic setup of the PIV system. The laser continues from the source to a mirror where it is turned and sent through laser optics that form a light sheet. The light sheet is then passed through the acrylic model of the PVAD (Figure from Cooper 2008).

The images were captured using a one-megapixel charge-coupled device (CCD) camera (TSI, Inc., Shoreview, MN) with a Micro-Nikkor 60mm f/2.8D lens (Nikon Corporation, Tokyo, Japan) or a two megapixel CCD camera (TSI, Inc., Shoreview, MN) with a Nikkor 28mm f/2.8Af lens (Nikon Corporation, Tokyo, Japan). The one megapixel camera contained a CCD chip size of 1000 pixels x 1060 pixels, while the two megapixel camera contained a CCD chip size of 1200 pixels x 1600 pixels. A LaserPulse Synchronizer (TSI, Inc., Shoreview, MN) and a personal computer (Dell, Inc., Round Rock, TX) were used in combination to develop a frame-straddling technique between the lasers and camera.

Insight™ software (TSI, Inc., Shoreview, MN) was used to capture and save the PIV images. The software allowed for images to be previewed in order to select the desired image position, resolution, and laser intensity. The laser pulse delay, ΔT, was selected for each time step based on the resolution and velocities of the flow as determined by preliminary PIV images. Two hundred images were taken at each time step, as this was found to be sufficient to provide enough valid vectors to provide an accurate ensemble average (Hochareon 2003b). A trigger delay box was used with this system to capture the images at known time steps every 50 ms throughout the entire cardiac cycle. The trigger was based on the start of inflow into the PVAD, information that was obtained from the inflow flow probe. Figure 39 highlights these time steps throughout the cardiac cycle.

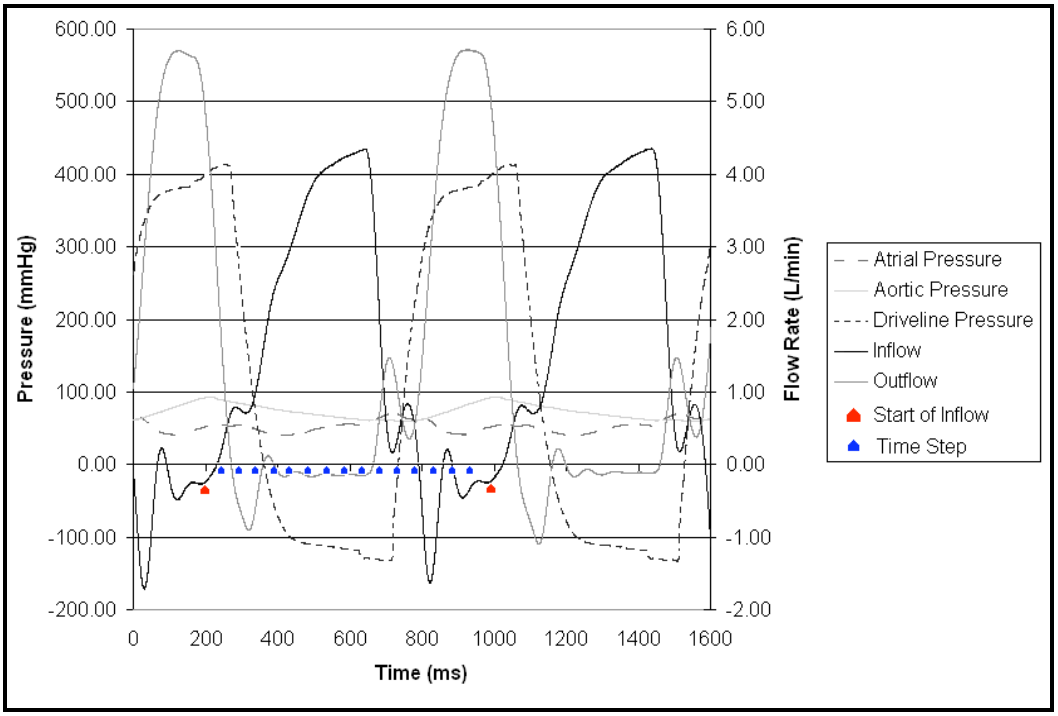

Figure 39: A set of waveforms highlighting the time steps taken. The red arrows indicate the start of a new inflow cycle. Each time step is highlighted every 50 ms with a blue arrow. Some of the time steps shown has insufficient data because of diaphragm interference and were not used.

While there are limitations in using two-dimenional PIV to observe flows that contain three-dimensionality, as discussed in Chapter 2, previous studies of the PVAD have found that this deficiency could be remedied by taking planes in multiple directions (Roszelle 2010). In this study planes were taken both parallel and normal to the diaphragm, as shown in Figure 40. The planes parallel to the diaphragm were taken at 7, 8.2 and 11 mm from the edge of the valve ports. These planes were chosen because they allow for measurements in both the ports and in the body of the device without losing too much information to diaphragm interference. Three planes were taken in both the inlet and outlet ports at 3.75, 7.5 and 11.25 mm from the outside edge of the ports. The 3.75 mm plane passed through the major orifice jet, while the 11.25 mm plane was located through the minor orifice jet. The 7.5 mm plane was in the center of the ports. The last normal plane was a single plane taken in the center of the device.

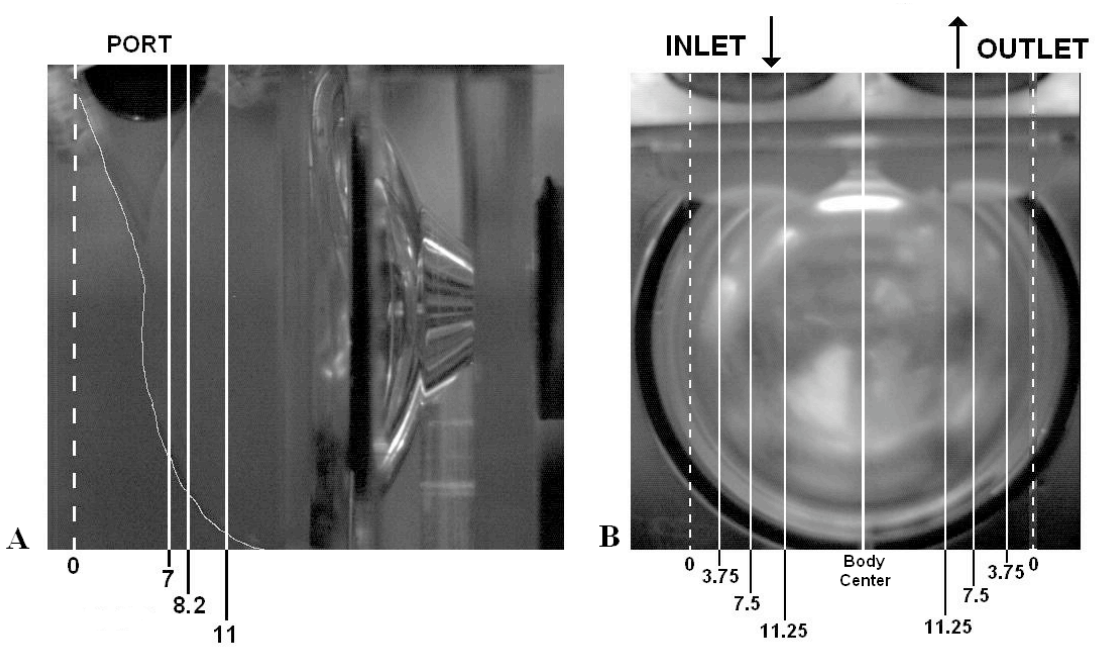

Figure 40: The PIV planes used. All of the distances are in mm. A) shows the 7, 8.2 and 11 mm planes parallel to the diaphragm of the device. B) shows the 7 planes taken normal to the diaphragm. Three planes each were taken in the outlet and inlet ports, and one plane was taken directly in the center of the device.

3.5.2 PIV Processing

3.5.2.1 Wall Finding

The first step in processing the image pairs was to apply a masking technique that removed the non-fluid portions of the PIV image. This was done by first finding the acrylic wall of the device, which was the fluid boundary of the image, with a custom Matlab program (The MathWorks, Inc., Natick, MA). Using the program, the walls were first traced by eye by the program user. The program then scans a designated number of pixels from this trace and found the largest intensity gradient, which designated the transition between the wall and the non-fluid region. In order to allow for a better curve fit, the wall of the device was divided into sections. Once the walls were located, the non-fluid region was selected and removed from the image. An example of this is shown in Figure 41.

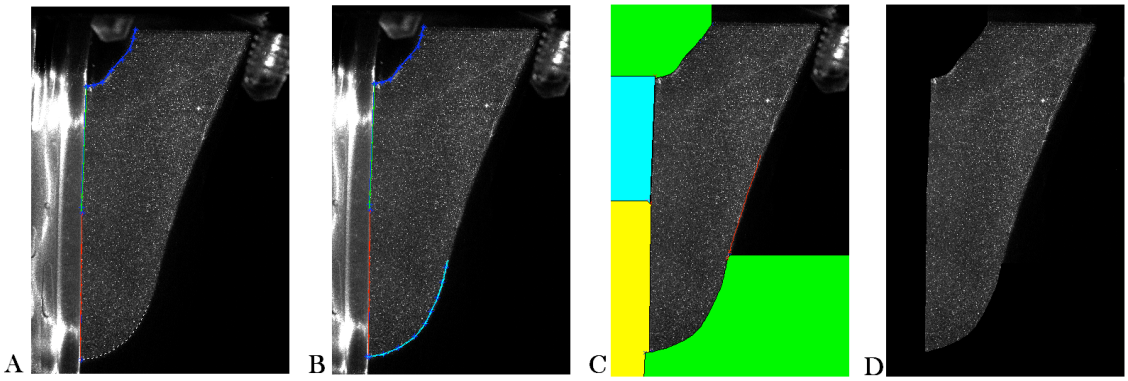

Figure 41: The wall finding technique used to locate the fluid boundaries, as well as remove background noise. A) shows the wall location as originally found by the eye of the program user. In B) the wall has been located using the intensity gradient. C) shows the program user removing the none fluid regions from the image. D) shows the final masked image with the wall located and the background removed.

3.5.2.2 Vector Calculation

Insight™ 3G (TSI, Inc., Shoreview, MN) was used to process the image pairs and calculate the vector fields. The resolution of the images ranged from 35 to 55 μm/pixel depending on the plane being observed and the camera being used. The calibration was performed using manual measurements based on known geometry of the model. The images were processed using a Recursive Nyquist Grid. This grid engine used a double pass technique, which obtained information from the first pass to optimize the number of good vectors found using the second and final pass. A 32 pixel by 32 pixel interrogation region was used for the first pass, and a size of 16 pixel by 16 pixel was used for the final pass. The Recursive filling technique used a local mean filling method and smoothing was performed with a low-pass filter. Local validation was also performed using a median test with a velocity tolerance of 2 pixels by 2 pixels and bad vectors were replaced using the local median. A maximum displacement of 0.50 to 0.25 pixels was used based on the resolution and ΔT of the specific plane and time step. An overlap of 50% was used in order to increase the vector density of the flow field. For cross-correlation, the Hart Correlation algorithm was used because it efficiently uses information acquired from correlation algorithms that overlap interrogation regions (Hart 1999). Once all 200 images were processed for a time step, the average flow field was computed. These average flow fields were plotted using TecPlot™ software (TecPlot Inc., Bellevue, WA), an example of which is shown in Figure 42.

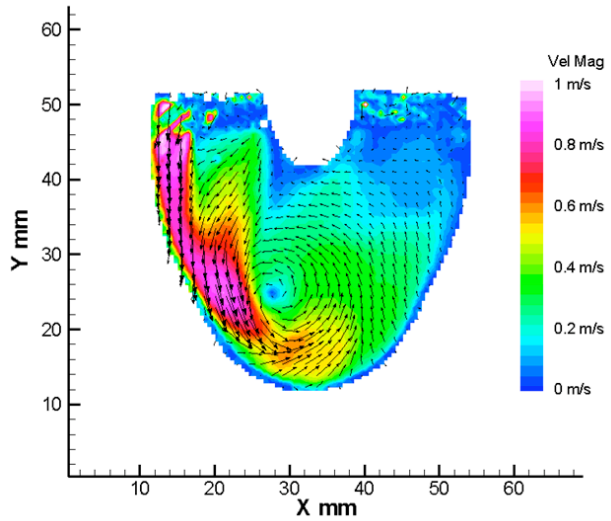

Figure 42: An example of a flow field map. The arrows of the map indicate the direction of the flow. The size of the arrows also corresponds to magnitude, however the magnitude is observed mainly by the color legend. Higher velocities are shown in red and pink, which the bottom of the spectrum is denoted by blue.

3.5.2.3 Wall Shear Rate Calculation

The wall shear rates along the fluid boundaries of the images were found using information from the wall finding technique and the velocities calculated during cross-correlation. The first step was to locate the centroid of the interrogation regions near the wall. As explained previously in Chapter 2, the cross-correlation of PIV images calculates a single velocity vector at the centroid of each interrogation region. This can be problematic when dealing with interrogation regions near the wall of the device, because quite often, the interrogation region contains areas inside and outside of the fluid boundary as shown in Figure 43. When this occurs the velocity vector calculated is based on information only from the fluid region, where particles are located, but the location of the vector is based on the entire region. In order to fix this bias for the wall shear calculation, a centroid shifting technique was performed. This process used the wall location information gained during the wall finding technique and moved the centroid

from the center of the interrogation region to the center of the fluid region, an example of which is shown in Figure 43.

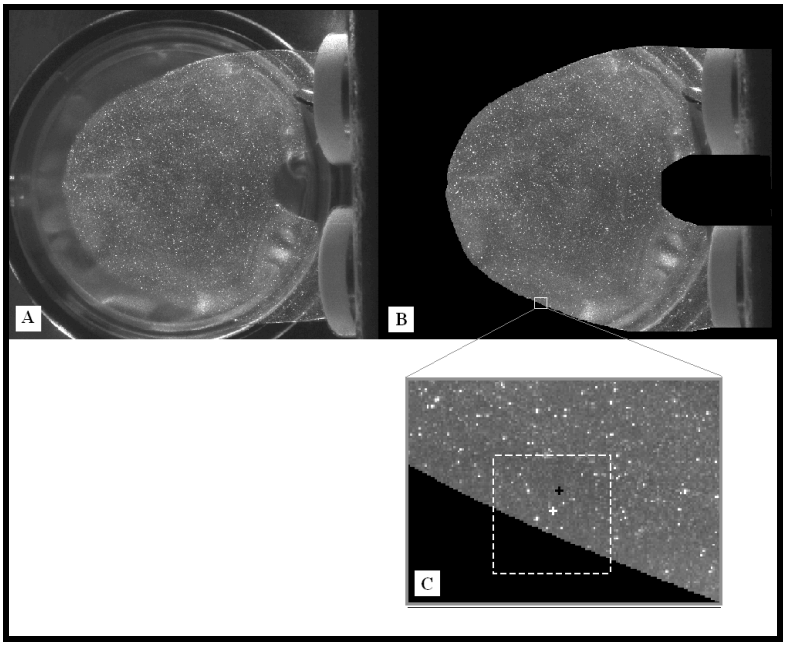

Figure 43: A representation of the PIV images used. A) is an example of a raw image. B) shows the same image after the masking technique is performed. C) is the highlighted section from B showing a near wall area. The area highlighted by the dashed box represents a possible interrogation region. Because the region includes an area outside of the fluid region the original centroid (noted by the white plus) needs to be shifted to only encompass the fluid (noted by the black plus). The centroid shifting is especially important because the PVAD has highly curved walls.

Once this new centriod was established, the wall shear rate could be found. The wall shear rate was calculated from the tangential near wall velocity and the distance between the location of this vector, the new fluid region centroid, and the wall. This wall shear rate was calculated for each of the 200 image pairs and then averaged at each time step. Wall shear rate maps were made by plotting the wall shear rate at each location and time step and interpolating between these points to form a single plot, an example of which is shown in Figure 44. A separate wall shear map was plotted for each section of the wall made during the wall finding process. The walls used for each set of planes are presented in Figure 45.

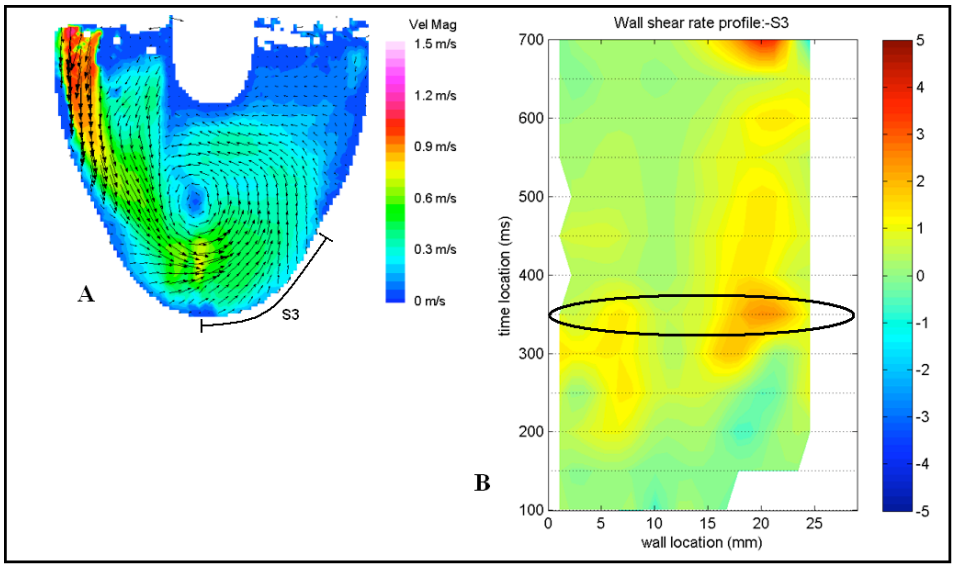

Figure 44: An example of a flow map (A) and the corresponding wall shear rate map (B). The section highlighted and labed S3 is the surface shown in the wall shear map in B. An example wall shear rate profile B) where positive shear is defined in the clockwise direction and negative shear is in the counter-clockwise direction. The oval highlights the time step shown in the flow map A. The shear rate is normalized by the threshold shear of 500 s^{-1}, so that 1 to -1 on the shear map is equivalent to 500 s^{-1} to -500 s^{-1}.

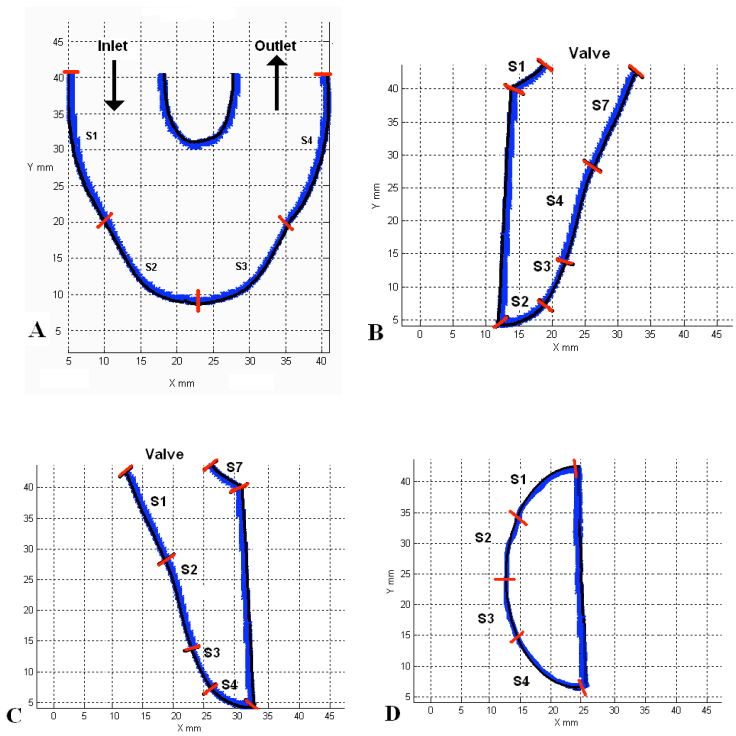

Figure 45: The wall surface sections for the PIV planes taken for the A) parallel planes B) inlet port C) outlet port D) and body of the device. A separate wall shear rate map was made for each wall section.

3.5.3 PIV Error Analysis

PIV has been accurately used as a flow visualization tool in the PVAD in many previous studies (Manning 2008, Roszelle 2008, Cooper 2008, Roszelle 2010a, Cooper 2010, Roszelle 2010b). However it is still necessary to reduce possible errors while taking PIV data. Many of the errors associated with PIV were discussed in section 2.3 including peak locking and out-of-plane motion. An effort was taken to reduce these errors for these studies.

To reduce the chances of peak locking, appropriate ΔTs were selected for each data set. These were tested as the PIV data was being taken using the Insight 3G software. Sample images were also taken and tested for peak locking by plotting histograms of particle displacements for different velocity values, and determined that there was no peak locking for velocities greater than 0.05 m/s.

Out-of-plane motion was of concern for the PVAD because of the three-dimensionality observed in previous studies (Cooper 2008, Roszelle 2008). However, efforts were taken to keep ΔT small enough to reduce the chances of losing particles between images, while still maintaining enough movement to avoid peak locking. A larger number of image pairs than necessary was also taken. Two-hundred images were taken at each time step, however only 50 valid vectors were necessary to produce an accurate vector. This allowed for the removal of bad vectors and considered vectors lost due to out-of-plane motion. Images were also taken both parallel and normal to the diaphragm. This meant that characteristics that may have been caused by out-of-plane flow could be checked in

other planes. This was found to be an accurate method of using 2D PIV in 3D flow previously (Roszelle 2010a).

In the absence of peak locking, the major source of possible error for our measurements is the bias error associated with our PIV system (Cooper 2008). PIV error analysis has shown that measurements are sub pixel accurate up to 10 – 20% of the spatial resolution (Raffel 1998). The lowest resolution used in these studies was 60 μm /pixel. Assuming 20%, this yields a minimum distance of 12 μm. By diving by our minimum ΔT of 150 μs, we obtain minimum velocities of 0.07 m/s. Any velocities above this value are accurately represented.

Chapter 4

BEAT RATE REDUCTION STUDY

4.1 Specific Aim

In order to allow the patient's native ventricle to resume primary circulatory support, it is necessary to reduce the flow rate of the VAD. Usually this requires a step down in the flow rate of the device in order to wean the patient from the VAD. In previous studies of weaning for pulsatile adult sized VADs, flow rate reductions were accomplished through changes in the beat rate or stroke volume (Slaughter 2006). For this study, beat rate reduction was selected to decrease the flow rate because of the desire to maintain complete ejection and filling of the PVAD. Therefore, PVAD flows for a beat rate reduction from 75 beats per minute (bpm) to 50 bpm were observed using particle image velocimetry (PIV) in 10 planes of the PVAD.

4.2 Conditions

The study looked at two beat rates. The first, 75 bpm with a systolic duration of 340 ms, an outlet pressure of 90/60 mmHg and an inlet pressure of 70/40 mmHg, was the condition used in previous studies and is considered the "normal operating" condition. These conditions provided an average flow rate around 1.35 L/min. The second condition was the reduced beat rate condition, and consisted of a beat rate of 50 bpm, a systolic duration of 400 ms, an outlet pressure of 90/60 mmHg and an inlet pressure of 65/35 mmHg. With this condition the flow rate dropped to around 0.88 L/min, a decrease in flow of 35%. Flow waveforms of each condition are shown in Figure 46.

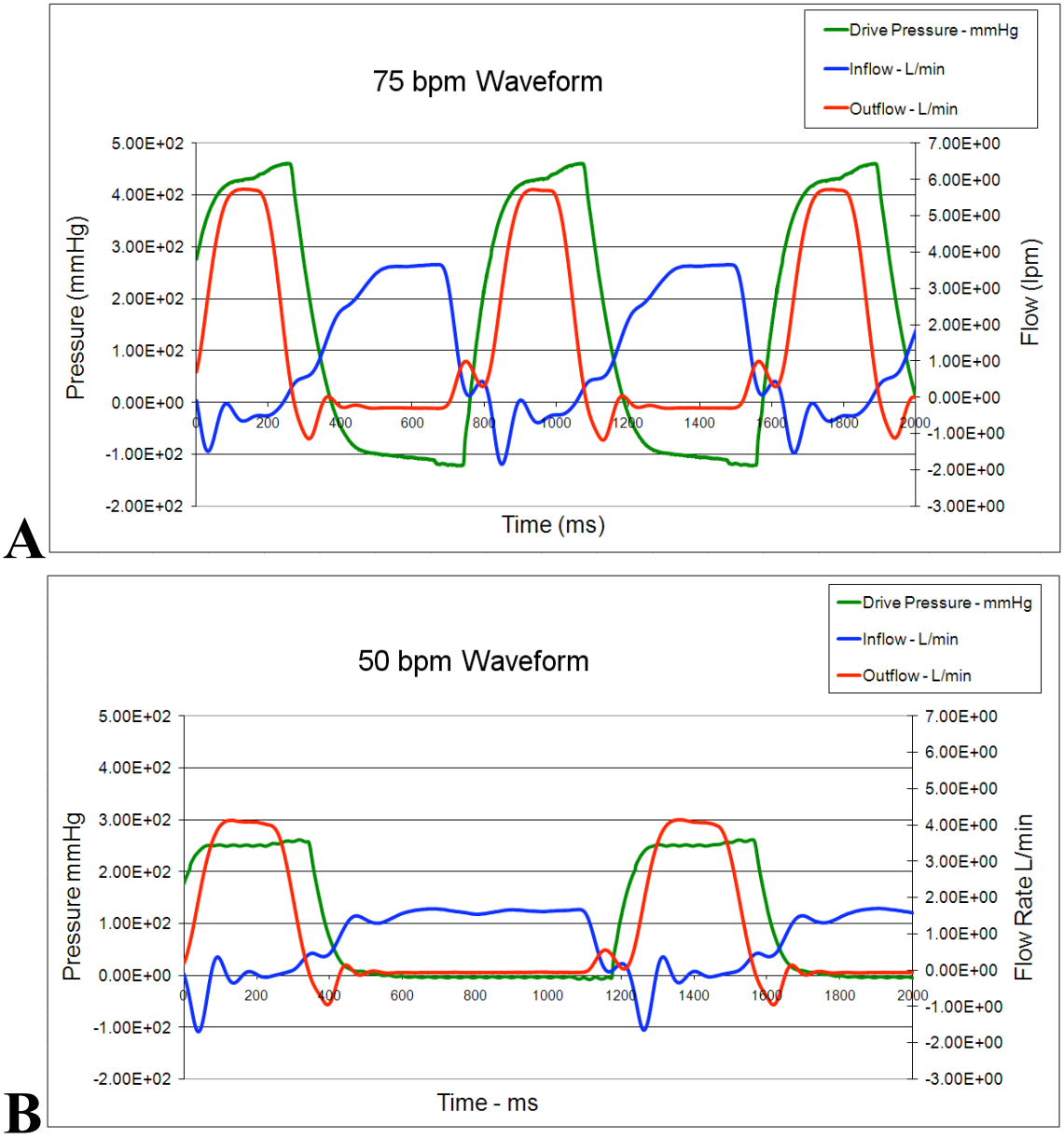

Figure 46: Example waveforms at (A) 75 bpm and (B) 50 bpm . Comparison of the waveforms inflow rates shows a lower maximum flow rate at 50 bpm, as well as an increased diastolic cycle time.

For both conditions, complete filling and complete ejection for each cardiac cycle was maintained. Complete filling is defined as the inflow to the PVAD reaching zero L/min before the start of systole, which is indicated by the rise in driveline pressure that leads to the expansion of the diaphragm and the ejection of fluid from the PVAD. The time

between the end of filling and the start of systole is referred to as the end-diastolic delay (EDD). The EDD was kept as close to 10 ms as possible for both flow conditions. This is highlighted in Figure 47 by points A and B. Complete ejection of the pump was defined as the completion of outflow, which is indicated by the outflow reaching 0 L/min, occurring before the end of systole. Systolic flow can be found on the waveform by locating the start of systole, again the rise in the driveline pressure, and adding the systolic duration. The complete ejection is highlighted in Figure 47 by points B and C.

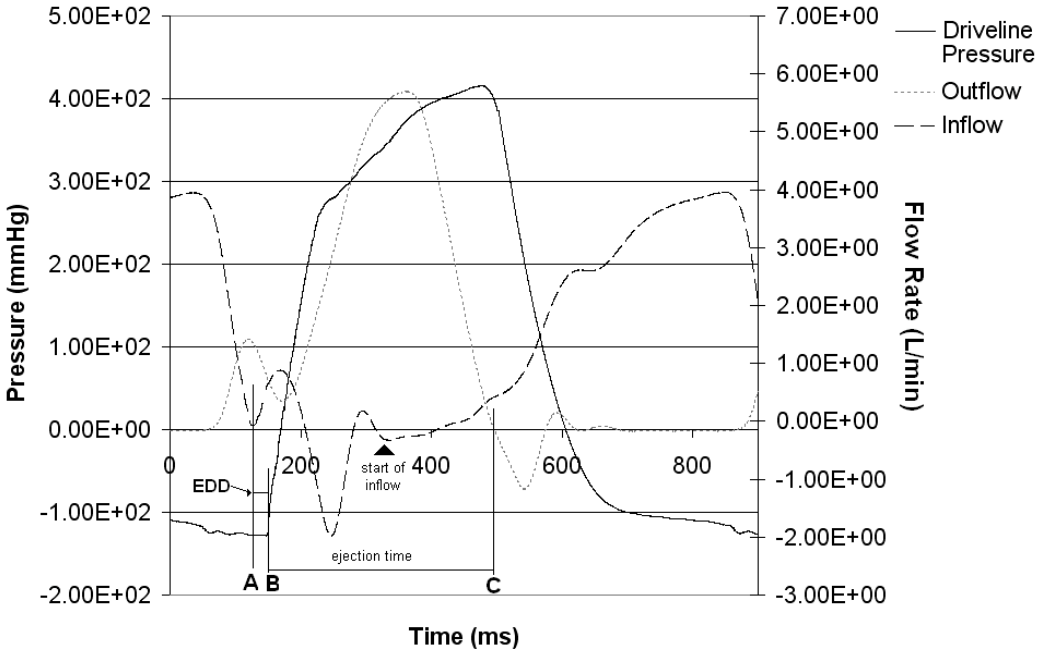

Figure 47: Representative waveforms for the BSM model at 75 bpm. Point A shows where the inflow reaches zero, signifying the end of diastole. The driveline pressure is the pressure from the pneumatic driver and indicates the position of the diaphragm during the cycle. Point B shows where the driveline pressure begins to increase which indicates the movement of the diaphragm at the beginning of systole and displacing the fluid. The time between A and B is the end-diastolic delay (EDD) or the time between the end of diastole and the beginning of systole for the device, in this case 10 ms. Point C indicates where the outflow reaches zero, signifying that the pump is empty. In order to fulfill the design goal of complete ejection the time between point B and C, known as the ejection time, must be less than the systolic duration. The black triangle indicates the start of the inflow, which designates the start of diastole. From this starting point, data were taken every 50 ms throughout the cardiac cycle.

PIV was performed in ten planes throughout the model, highlighted previously in Figure 40. The three PIV planes parallel to the device diaphragm had a resolution around 60 μm/pixel and the seven normal planes had a resolution around 45 μm/pixel. The ΔT varied from 200 to 300 μs depending on the beat rate and location in the cardiac cycle.

4.3 Results

Because of the difference in flow rates between the two conditions, the flow maps were normalized in order to separate the scaling effects of the flow reduction from the more complex changes in the flow field. The maps were normalized using the average velocity of the pump, which was found by dividing the known average flow rate by the size of the BSM valve's effect orifice area. When desired the original velocity magnitudes were still available for analysis and comparison.

It was also necessary for us to normalize the temporal rate because of the time difference in the total cardiac cycle, 800 versus 1200 ms for 75 and 50 bpm, respectively. In addition, to allow for a direct comparison of the flow fields, the results are presented as a percentage of diastole or systole. Therefore, a time step of 200 ms for the 75 bpm condition and 350 ms for the 50 bpm condition would both represent a time 43% into the diastolic cycle. This allowed for the best direct comparison of the flow behavior throughout the total cardiac cycle.

4.3.1 Seventy-Five Beats Per Minute

4.3.1.1 Diastole

While a large portion of early diastole could not be measured due to diaphragm interference, formation of the inlet jet appears in the PIV planes at 32% into diastole. The inlet jet remains the dominate flow feature during early diastole, and started to strengthen around 43% into diastole. At the mid way point, or 53% into diastole, the inlet jet velocity showed a peak of 1.12 m/s and the desired rotational flow pattern began. That is, as shown in Figure 48, a center of rotation appears at this point. Figure 48 also highlights an area of three dimensionality that appears during the starting rotation. As described in previous studies (Roszelle 2010), the three-dimensionality occurs when flow comes from areas not in the current measurement planes, and is a consistent characteristic of the PVAD flow field.

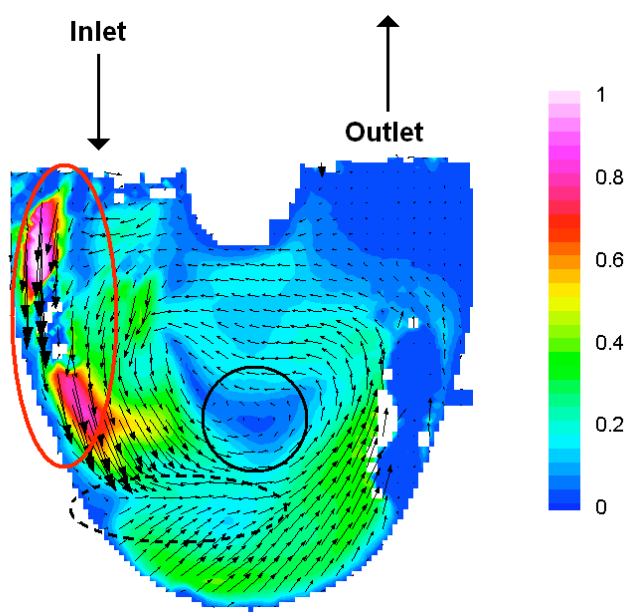

Figure 48: The normalized velocity flow field of the 8.2 mm plane at 75 bpm and 54% of the diastolic cycle. As highlighted in red, the inlet jet has formed along the outer wall and began to set up the rotational flow field, the center of which is highlighted by the black circle. Three-dimensionality can be seen at the bottom of the device and is highlighted by the dashed black oval.

As diastole continues the rotational flow field is established, and a center of rotation remains in the parallel planes throughout diastole. Figure 49 highlights the 8.2 mm plane from mid to late diastole, which shows the desired rotational flow field as well as the slow reduction in velocity in the inlet jet. However, this loss of momentum from the inlet jet does not affect the rotational field, and velocities across the flow field remain around 0.4 m/s as the device transitions into systole.

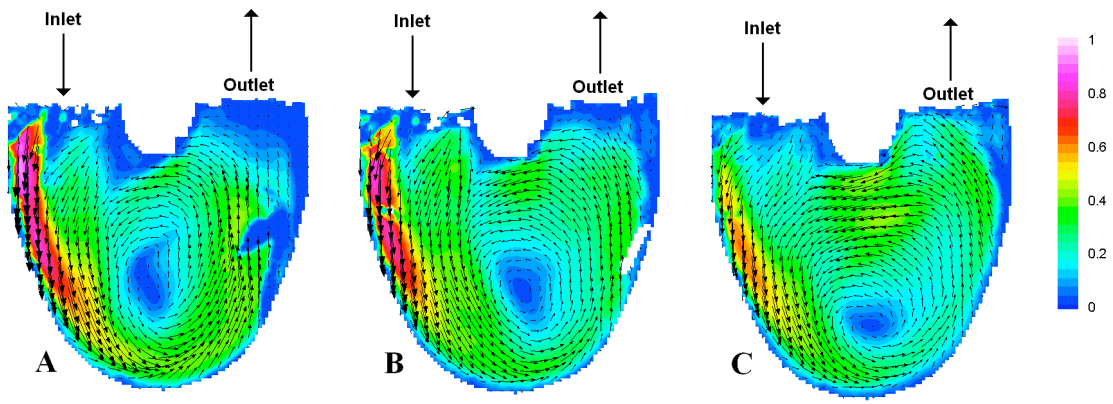

Figure 49: The 8.2 mm plane at 75 bpm as it moves through mid to late diastole, specifically (A) 65%, (B) 76%, and (C) 87% of the diastolic cycle. As the flow continues the magnitude of the inlet jet reduces, however, the rotational flow field stays in tact.

4.3.1.2 Transition From Diastole to Systole

For the 75 bpm condition, the transition from diastole to systole occurs at 460 ms into the total cardiac cycle. Therefore, the time steps observed at 450 and 500 ms show this transitional period. Figure 50 contains all three parallel planes at these time steps.

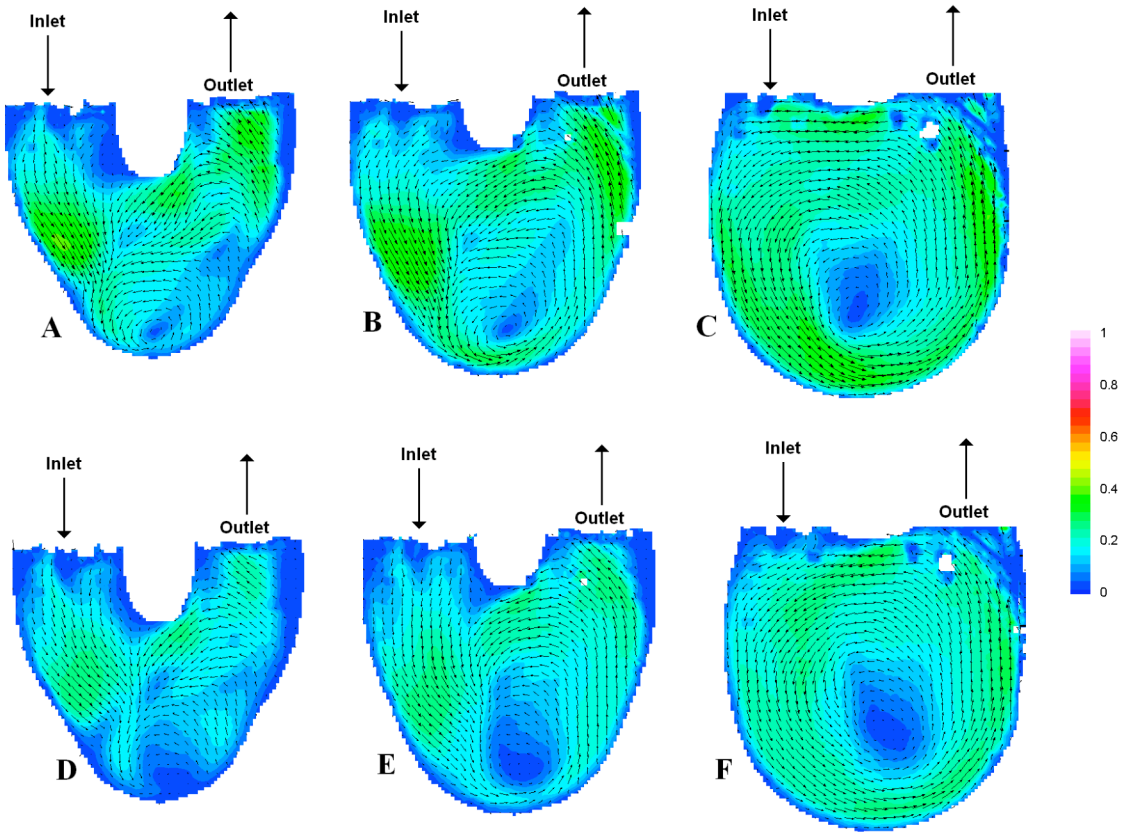

Figure 50: The 7, 8.2 and 11 mm planes at (A, B, C) 98% of diastole and (D, E, F) 12% of systole while running at 75 bpm. As diastole ends and systole begins, there is a slight reduction in the cohesion of the rotational flow, especially noticeable in the 7mm plane (D). The centers of rotation remain in both the 8.2 and 11 mm planes (E and F), however, there is expansion in their size.

Notice not until right before the end of diastole, 450 ms or 98% of the diastolic cycle, the center of rotation is maintained in all three parallel planes. However, this rotational flow is most organized in the 11 mm plane. As the flow transitions into early systole, 500 ms or 12% of the systolic cycle, only the 7 mm plane loses the center of rotation. Both the

8.2 mm and 11 mm planes maintain rotational flow with slightly lowered overall velocities and an increase in the size of the center of rotation.

4.3.1.3 Systole

In systole the flow shifts to the outlet port as the flow is ejected from the device. At 41% of systole, a uniform movement of flow through the outlet port can be observed. At 56% of the cycle there is an increase in velocity magnitude along the outer walls of the port. This characteristic is consistent with the convergence of fluid through a smaller opening, in this case, the outlet port and BSM valve. At 70% into systole a blockage of flow appears in the outlet port, as shown in Figure 51, which is consistent with previous observations of the PVAD using BSM valves (Cooper 2008).

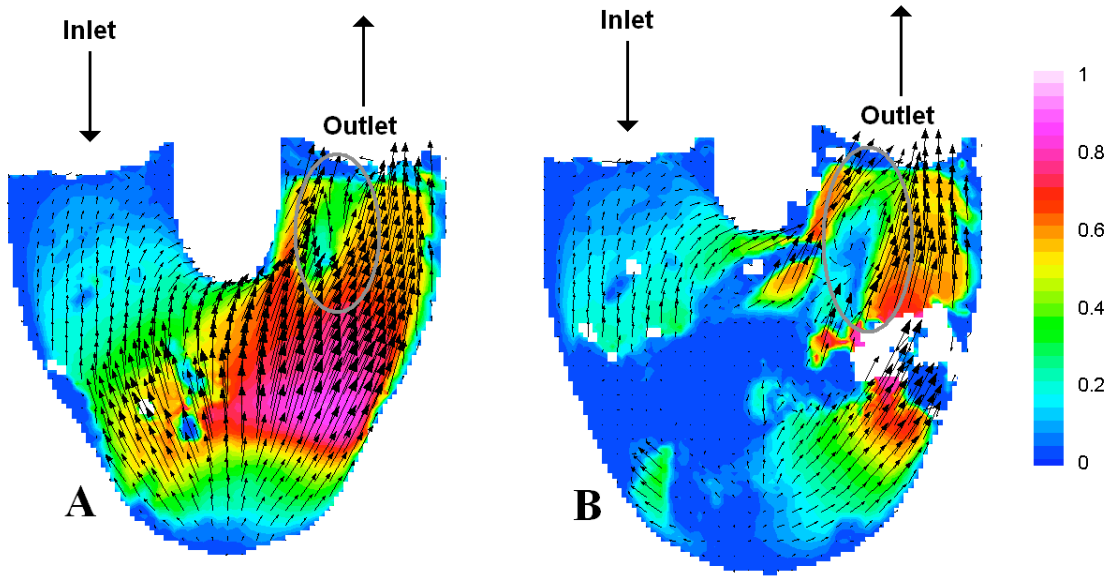

Figure 51: The (A) 7 mm and (B) 8.2 mm planes at 85% of systole at 75 bpm. Both planes show an area of blockage in the outlet port, highlighted in grey. This characteristic is consistent with previous PVAD data using the BSM valve.

4.3.2 Fifty Beats Per Minute

4.3.2.1 Diastole

At 50 bpm the inlet jet formation is observed at 25% into diastole. The jet then continued to gain momentum up to 50% into the diastolic cycle, where the maximum velocity of 0.7 m/s was observed. Halfway through the diastolic cycle the center of rotation becomes apparent within the body of the device. This is observed in all three parallel planes and is shown in Figure 52. In early diastole it can also be seen that the 11 mm plane shows less organization than the 7 and 8.2 mm planes.

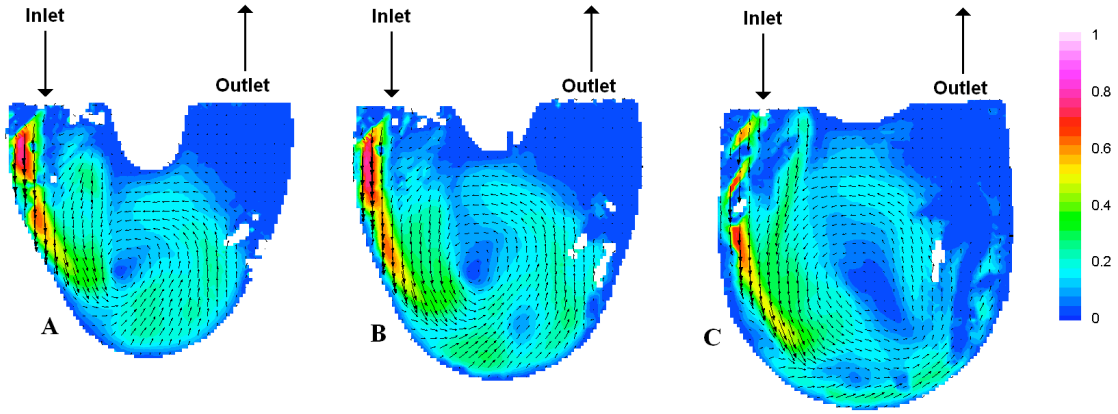

Figure 52: The (A) 7, (B) 8.2 and (C) 11 mm planes at 50% of the diastolic cycle for 50 bpm. All three parallel planes show the rotational flow field has begun and there is penetration into the bottom of the device. The flow at the 11 mm plane shows less organization and a larger center of rotation than the other two planes.

Before reaching the rotational flow halfway through diastole, three-dimensionality can be seen from 31 to 43% of diastole. This is more apparent in the 7 and 8.2 mm planes, as highlighted in Figure 53, were there is flow around 0.4 m/s originating from the apex of the device that is not consistent with the inflow jet.

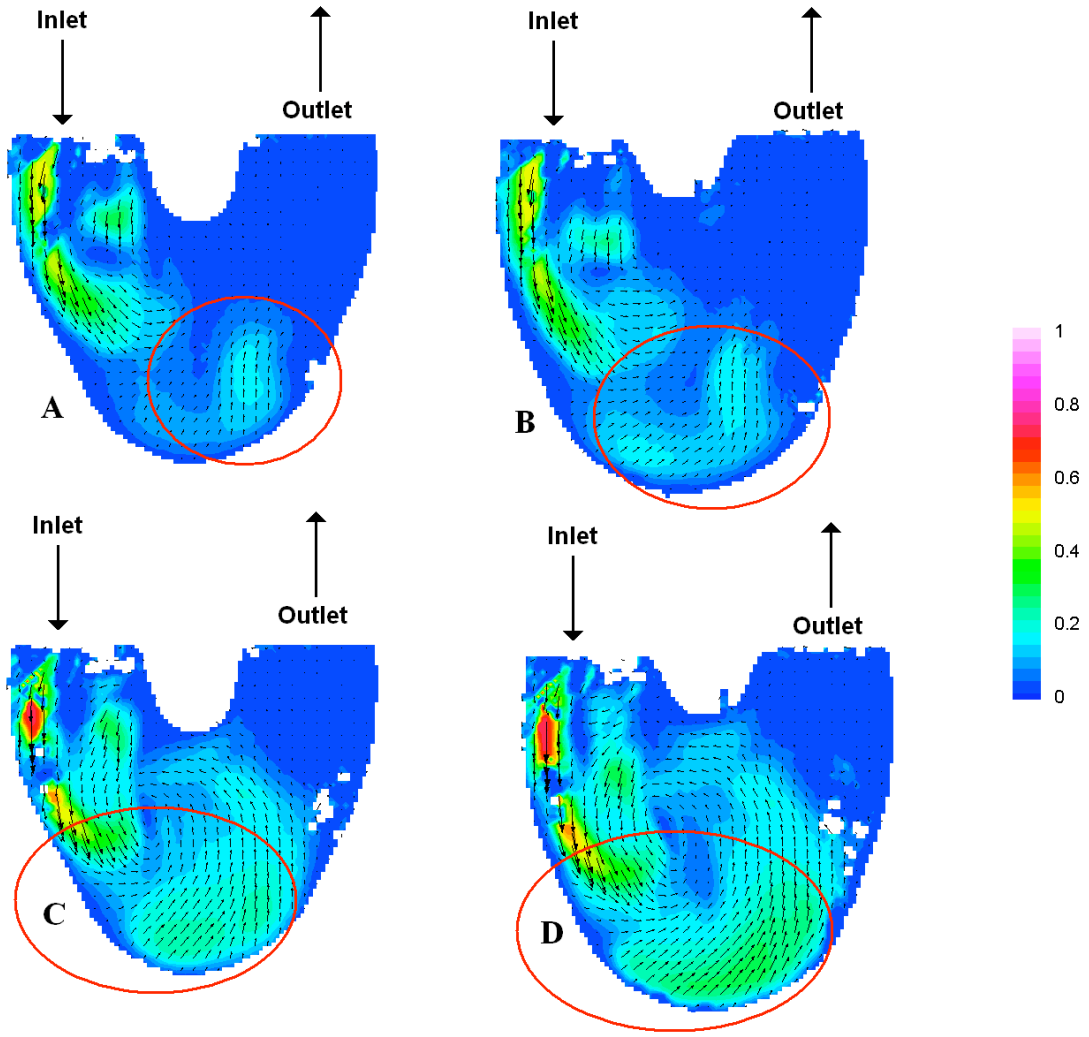

Figure 53: At 50 bpm the 7 and 8.2 mm planes at (A, B) 31% and (C, D) 44% of the diastolic cycle. During the early to mid diastolic cycle the three-dimensionality can be observed, as highlighted in red. At 31% into diastole the three-dimensional flow appears from the bottom of the device, however, this begins to transition into the rotational flow field later in diastole as seen in C and D.

As diastole continues the center of rotation became larger. The rotational flow begins to dissipate at 63% of diastole. As highlighted in Figure 54, the center of rotation expands quickly just after mid diastole.

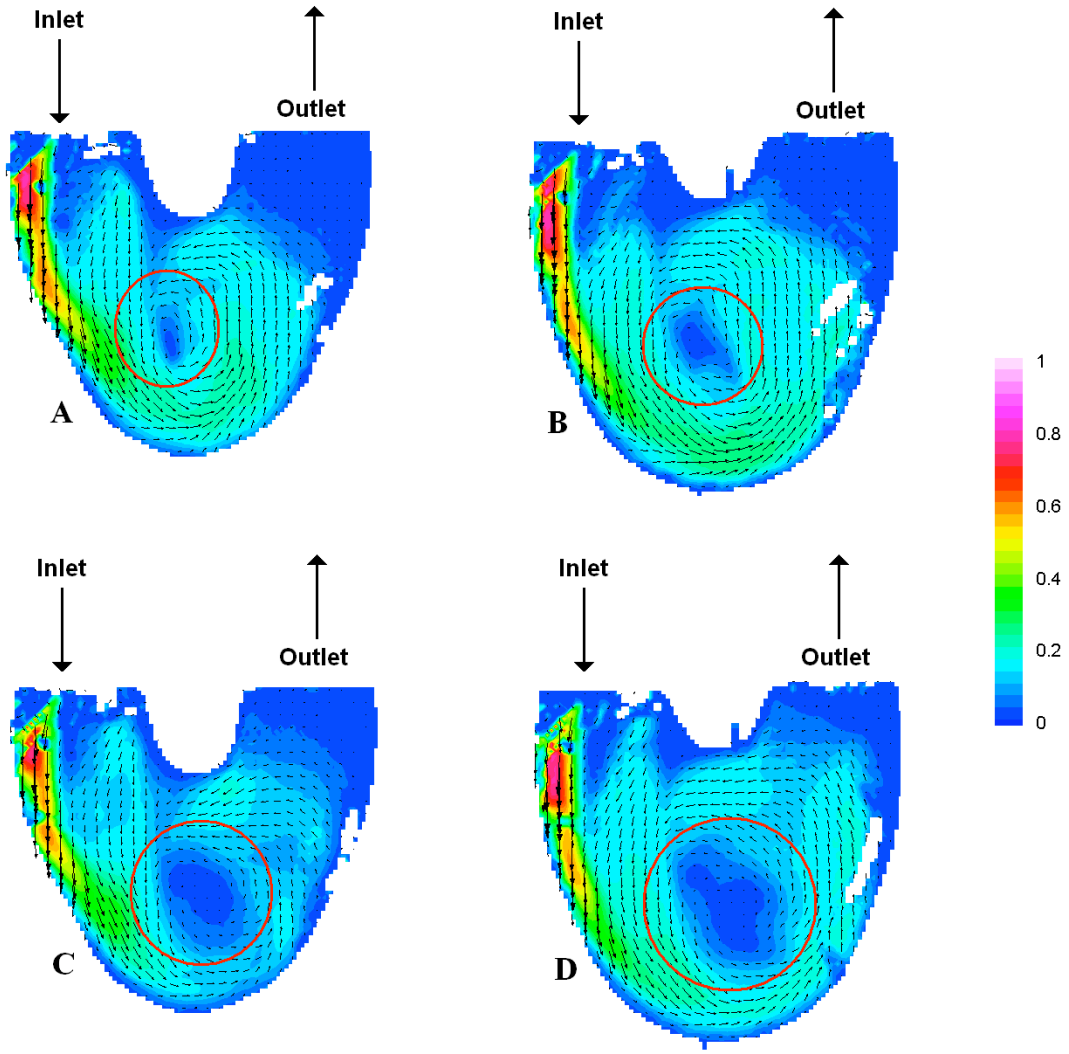

Figure 54: The 7 and 8.2 mm planes at (A, B) 56% and (C, D) 63% of diastole at 50 bpm. As diastole passes through the midway point the center of rotation begins to expand, as highlighted in red. This expansion shows a reduction in the tightness of the rotational flow field, which indicates the field has started to dissipate.

In the 7 mm plane, the center of rotation moves towards the outlet side of the device and the rotational flow quickly becomes disorganized, breaking down completely at 87% of diastole. The 8.2 and 11 mm parallel planes contain similar flow patterns to that of the 7 mm plane, however, unlike the 7 mm plane, the basic rotational flow pattern remains until the end of diastole. Figure 55 shows this break down in the rotation.

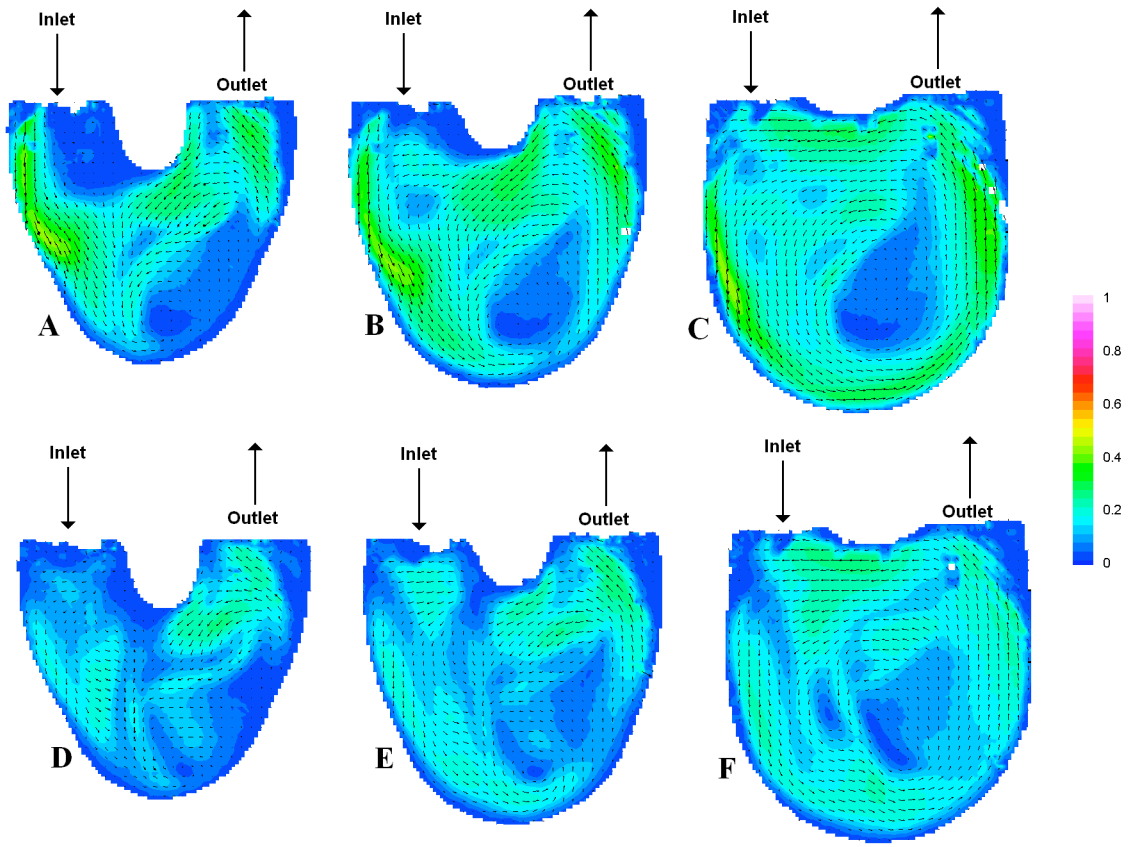

Figure 55: At 50 bpm the 7, 8.2 and 11 mm planes at (A, B, C) 87% of the diastolic cycle and at the (D, E, F) end of diastole. At 87% of diastole the rotational flow in the 7 mm plane (A) breaks down, although it remains in the 8.2 and 11 mm planes (B and C). At the end of diastole (D, E, F) all three planes show a disappearance of the organized rotation and a drop in the overall velocity magnitude.

4.3.2.2 Transition From Diastole to Systole

The transition between diastole and systole is observed at 750, 800 and 850 ms into the cardiac cycle, which were 93 and 100% of diastole and 13% of systole, respectively. As seen previously in Figure 55, the rotational flow pattern breaks down at the end of diastole, resulting in reduced velocities and disorganized flow. As systole begins these low velocities remain and result in many areas of stagnation, which are highlighted in all three parallel planes in Figure 56.

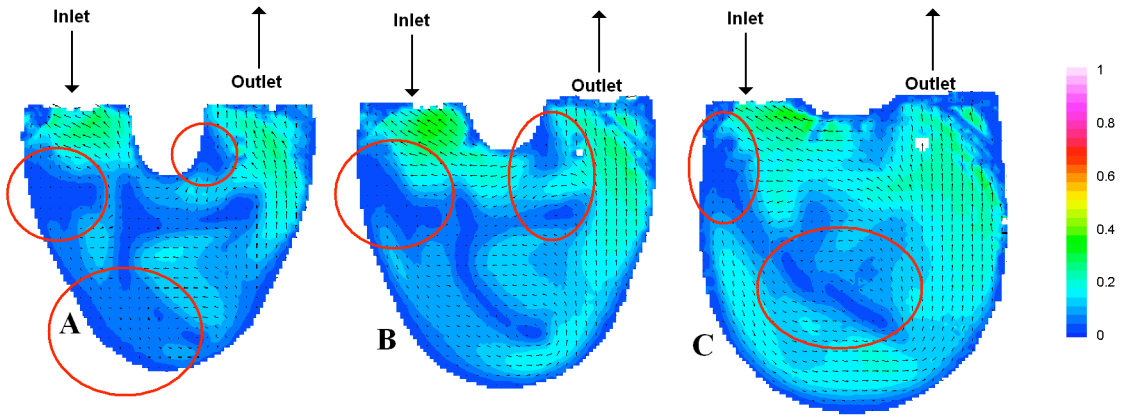

Figure 56: At 50 bpm the (A) 7, (B) 8.2 and (C) 11 mm planes at 13% of systole. As systole begins the rotational flow has dissipated leaving areas of low flow and stagnation, especially near the inlet side, as highlighted in red.

4.3.2.3 Systole

Fluid movement towards the outlet port of the PVAD becomes dominant at 25% of systole. At 38% of the systolic cycle, velocities along the outside wall of the outlet port increase in magnitude, compared to those in the center of the port. Again, this is consistent with the convergence of fluid through the outlet valve and is highlighted in Figure 57.

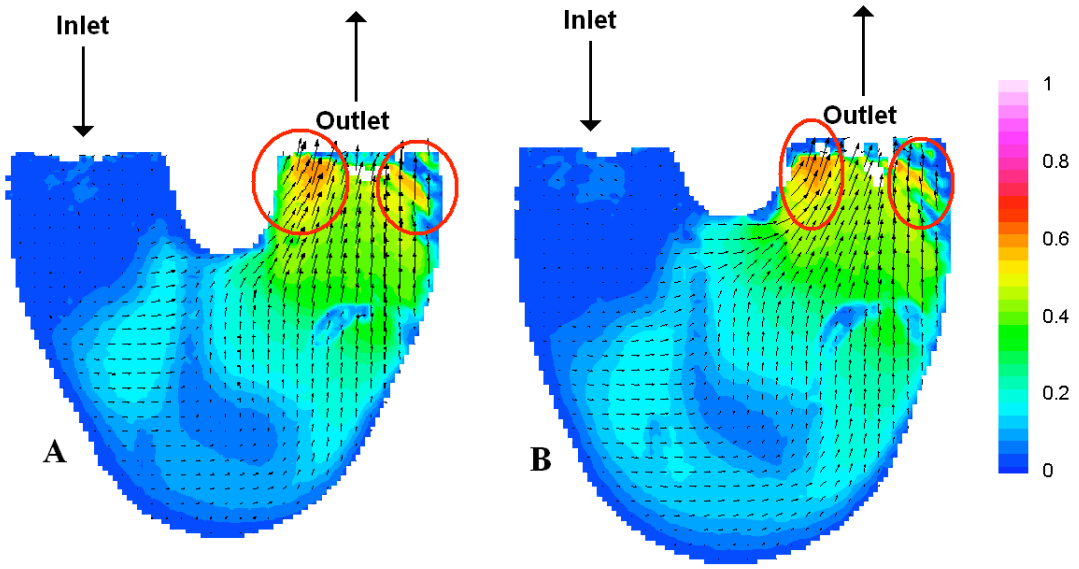

Figure 57: The (A) 7 and (B) 8.2 mm at 37% of the systolic cycle at 50 bpm. Both planes show an increase in velocity along the outer sides of the outlet port, highlighted in red. This is consistent with previous data and shows the convergence of the flow into the narrowed outlet port.

Towards the end of systole, 63% of the systolic cycle, there is a blockage observed upstream of the outlet valve. This can only be seen in the 7 mm plane, because of diaphragm interference in the other parallel planes, and is highlighted by Figure 58.

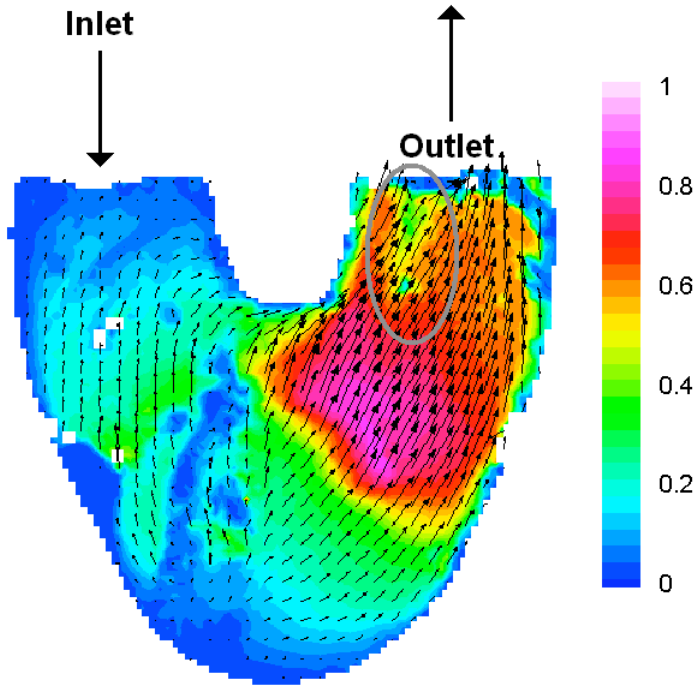

Figure 58: The 7 mm plane at 63% of systole at 50 bpm. The blockage downstream of the outlet valve is highlighted in gray.

4.4 Discussion

4.4.1 Diastole

As diastole begins both beat rates show similar flow patterns, including strong diastolic jets. There is a noticeable difference in velocity magnitudes of the jets between the two beat rates, with 75 bpm producing a maximum velocity of 1.12 m/s and 50 bpm producing a maximum of 0.7 m/s. However, the maximum velocity of each condition corresponds to a ratio of 80% of the average flow rate, indicating that the flow patterns are similar at this point in the cycle. The velocity difference does correlate with a drop in wall shear rates along the inlet wall at 50 bpm. The wall shear rates along the inlet wall at

75 bpm show a higher magnitude over a larger area, than the same surface at 50 bpm. This is especially apparent near the apex of the device, a problem area for the pump as shown by previous studies (Daily 1996, Bachman 2000). This reduction in wall shear rate is of concern because of the increased chance of thrombus formation on areas that do not contain shear rates greater then 500 s^{-1}. Figure 59, shows this area of low shear rate on the lower inlet surface of the 8.2 mm parallel plane.

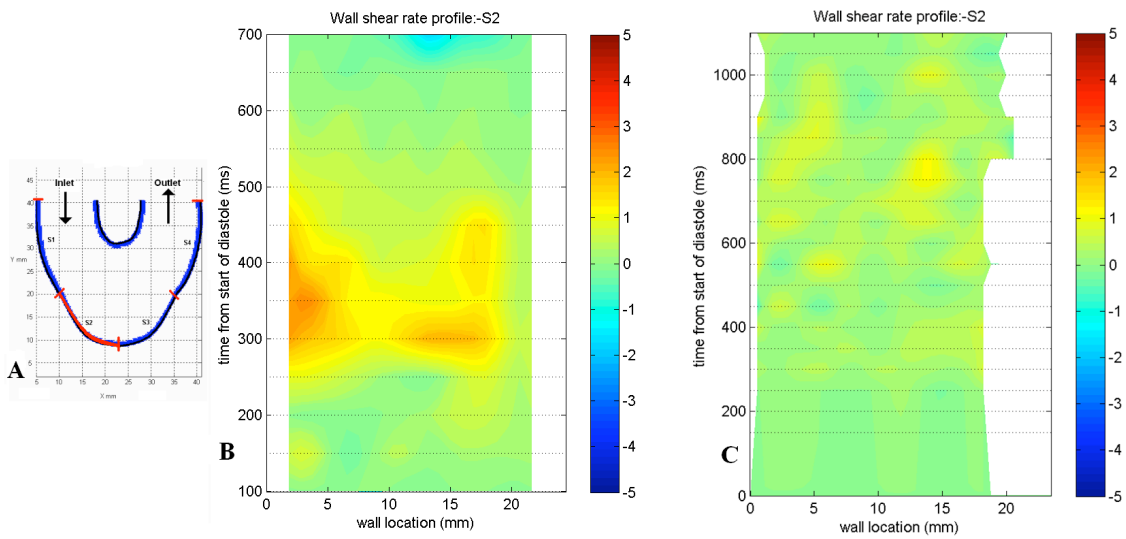

Figure 59: Surface 2 (S2), which is the lower inlet surface highlighted in (A) in red, of the 8.2 mm plane at (B) 75 and (C) 50 bpm. As can be seen on the maps, there is higher wall shear rates (> 500 s^{-1}) for the 75 bpm condition during mid to late diastole, while the 50 bpm condition shows low overall shear rates throughout the cycle. This indicates the desirable wall washing is not occurring at this surface at an operating rate of 50 bpm.

Through mid-diastole, both beat rates maintain similar rotational flow patterns. The strong inlet jets, the start of a rotational flow field and the signs of three-dimensionality, are highlighted in Figure 60.

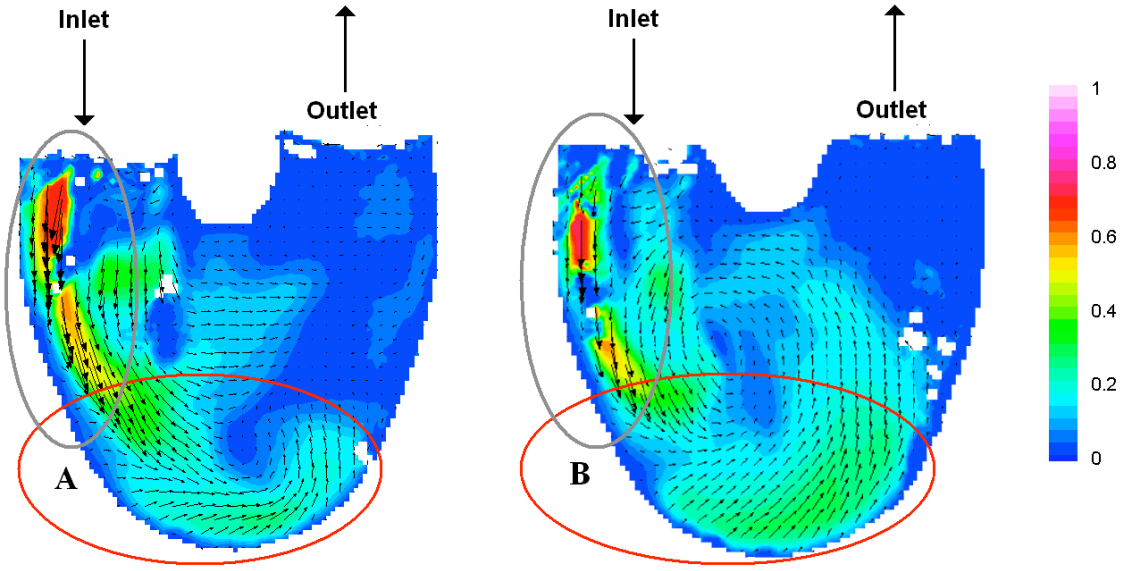

Figure 60: The 8.2 mm plane at 43 % of diastole for (A) 75 and (B) 50 bpm. At this point in diastole, the two beat rates show similar flow patterns. As highlighted in grey, both have strong inlet jets that are starting to set up the desired rotational flow. Both beat rates also show signs of three-dimensionality as highlighted in red.

After mid-diastole both beat rates have rotational flow fields, however, at 75 bpm the flow maintains a stronger and tighter rotation. At 63% into the diastolic cycle, as shown in Figure 61, the 75 bpm condition shows good rotation along the inlet wall, while at 50 bpm this rotation is not as strong and the center of rotation has expanded in size, leaving an area of stagnation. Wall shear rate maps confirm that this difference in patterns could lead to reduced wall shear rates, as shown previously in Figure 59. This indicates that at 50 bpm, there is less wall washing along the outer surfaces of the PVAD. This is of concern because of the increased chances of thrombus formation on surfaces that do not contain shear rates of greater than 500 s^{-1}.

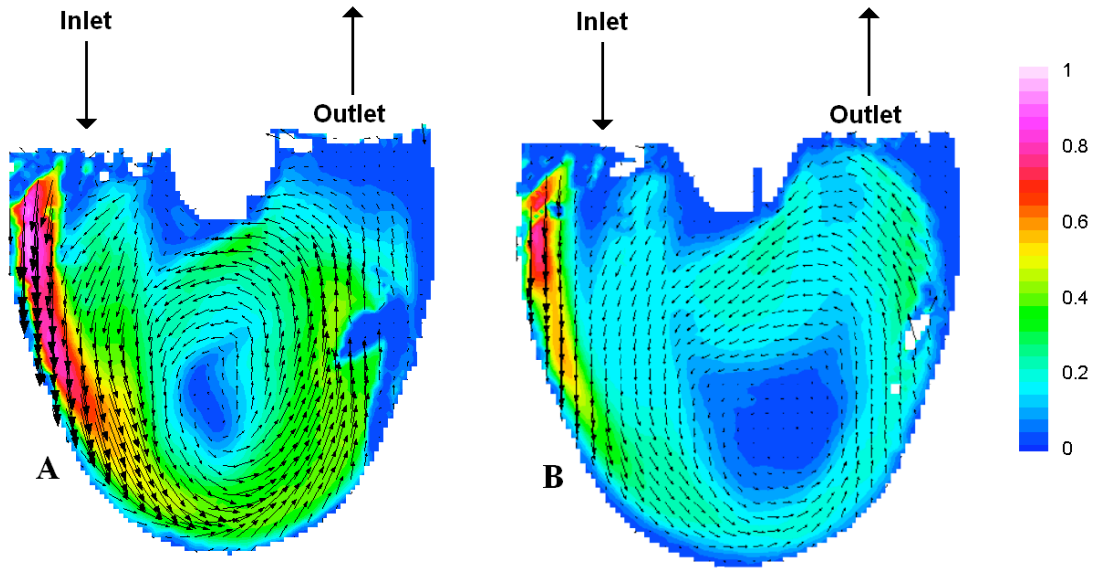

Figure 61: The 8.2 mm plane at 63% of diastole (A) 75 and (B) 50 bpm. At this point in diastole, both beat rates show rotational flow, however, at 75 bpm the center of rotation is smaller and the overall rotation is tighter. This makes a difference when comparing wall shear rates, as seen in Figure 59.

As diastole progressed the 50 bpm condition continued to lose rotational strength compared to the 75 bpm condition. This was likely due to the increased diastolic cycle time, as well as the reduced flow rate. Initial velocities two-thirds the size of the 75 bpm condition, as well as a diastolic cycle that was nearly twice as long, means that the rotational flow pattern could not be maintained as well by the 50 bpm condition. Figure 62 shows this difference at 87% of the diastolic cycle.

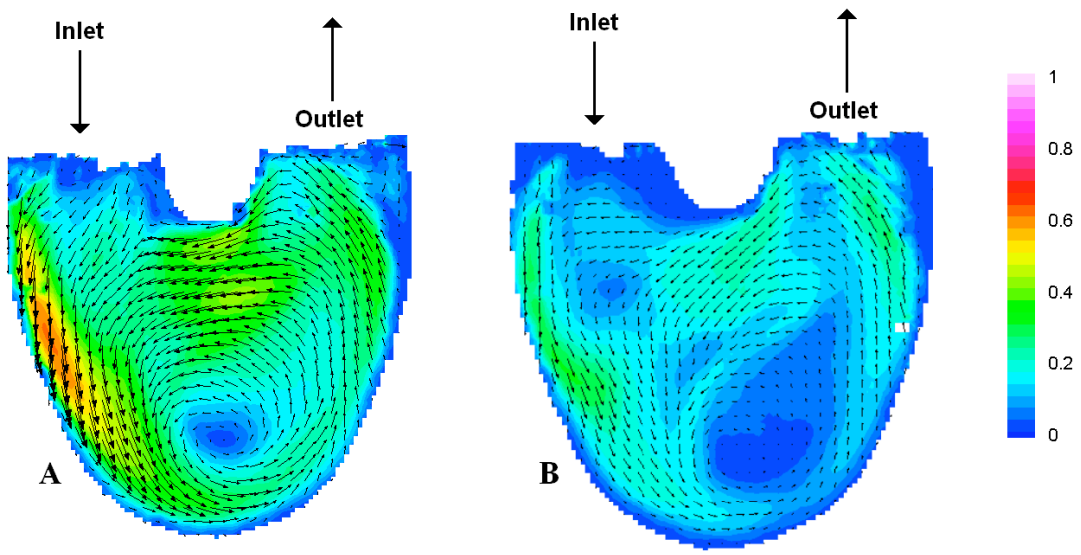

Figure 62: The 8.2 mm plane at 87% of diastole for (A) 75 and (B) 50 bpm. While the rotational flow field remains at this late point in diastole at 75 bpm, at 50 bpm the rotation has dissipated greatly.

During early diastole, there are more areas of low flow and stagnation at 50 bpm than at 75 bpm, especially in the inlet side of the device. To help illustrate this point, "stream traces" were created at 87% of diastole as shown in Figure 63. These stream traces represent the path a mass less particle would take if released into the flow at this time in the cardiac cycle. They are helpful in both observing the pattern of the rotation during a time in the cycle and in finding the center of rotation. They are not equivalent to fluid streamlines as they represent a path during this instantaneous time in the cycle, not the path of a particle throughout the entire cycle. Here, we notice that at 75 bpm the center of rotation is much tighter and at 50 bpm the flow in the body of the device contains an area of stagnation where there is no fluid movement.

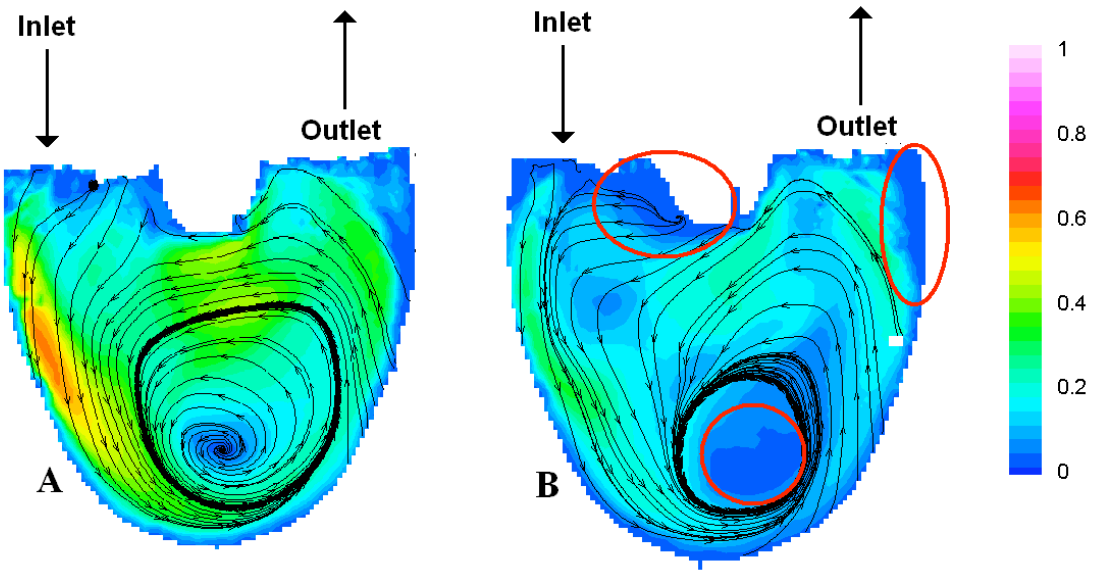

Figure 63: Streamtraces of the 8.2 mm plane at 87% of diastole for (A) 75 and (B) 50 bpm. The streamtraces help to visualize the rotational pattern of the flow. At 75 bpm the rotation is tighter, continuing all the way to the center of the body. At 50 bpm the center of rotation is stagnant, and there are other areas of stagnation in the plane, as highlighted in red.

The planes taken normal to the diaphragm confirm the reduction in flow during late diastole at 50 bpm. Planes in the inlet port of the device show similar patterns between the two beat rates, however, there is an obvious reduction in the velocity magnitudes at 50 bpm, leading to more areas of stagnation. In Figure 64 we can see that the normal plane closest to the inside of the inlet port, 11.25 mm, contains areas of stagnation along the wall of the fluid side of the device, as well as a large area of stagnation between the diaphragm side of the device and the valve. This also confirms that the areas of stagnant flow seen in the parallel planes were indeed areas of stagnation, and not the result of PIV error by out-of-plane flow.

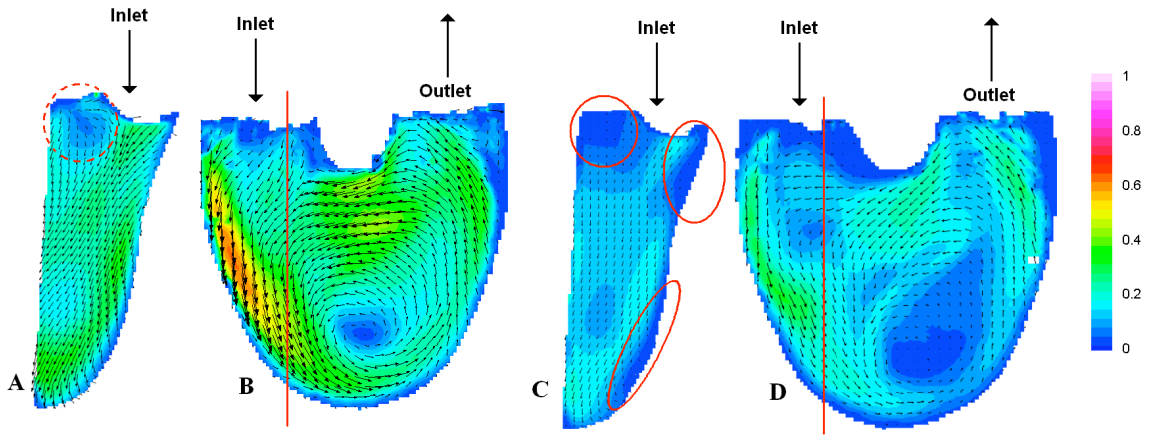

Figure 64: The (A, C) 11.25 mm normal inlet planes and (B, D) 8.2 mm parallel planes at 87% of diastole for (A, B) 75 and (C, D) 50 bpm. At 50 bpm the 11.25 mm inlet plane (C) contains overall low flow and areas of stagnation as highlighted by the red ovals. At 75 bpm there is greater fluid movement, however an area near the inlet port, highlighted with a red dashed circle, does show some early signs of possible stagnation.

Corresponding flow characteristics by 50 bpm were also observed in the normal planes of the outlet port. As shown in Figure 65, at a condition of 75 bpm and during the same time step 87% into diastole, the 11.25 mm normal outlet plane contains an area of rotational flow in the outlet port of the device. This could be advantageous to the flow because it keeps the blood moving instead of allowing areas of stagnation to develop throughout systole. In comparison, at the same point in diastole, the 50 bpm condition does not show similar movement and the fluid in the outlet port remained stagnant. This stagnation could lead to more platelet adhesion on the surfaces of the outlet port in comparison to the higher beat rate.

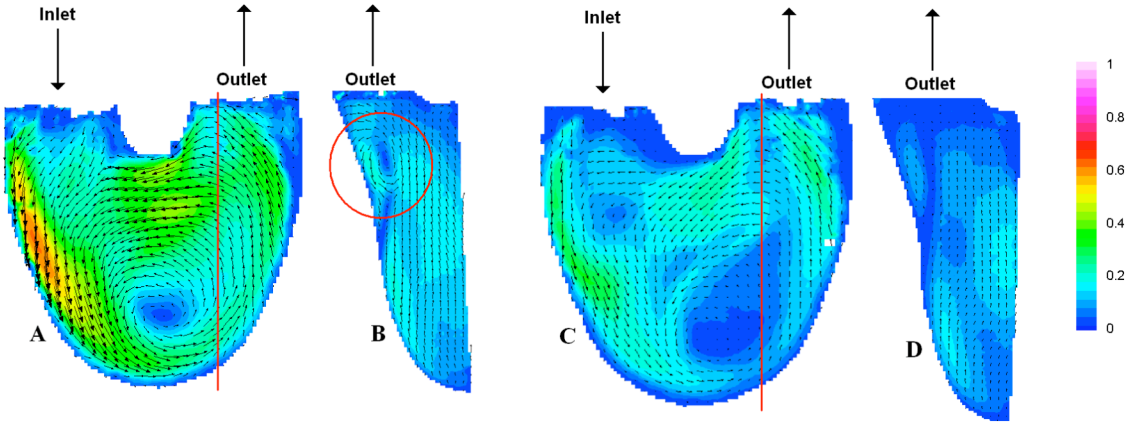

Figure 65: The (A, C) 8.2 mm parallel and (B, D) 11.25 mm normal outlet planes at 87% of diastole for (A, B) 75 and (C, D) 50 bpm. At 75 bpm the outlet plane shows an area of recirculation in the outlet port, highlighted by a red circle, that is not seen at 50 bpm. This could help keep fluid moving and reduce stagnation in the outlet port during diastole.

4.4.2 Transition From Diastole to Systole

As the cardiac cycle transitions from diastole to systole, the 75 bpm condition continues to maintain a tight center of rotation until just after the end of diastole. This good rotational pattern allows for a smooth transition into systole. This smooth transition is desirable because it maintains motion in the fluid and reduces the chances of stagnant

areas that could lead to clot deposition. In comparison at 50 bpm, the center of rotation starts to subside 63% into the diastolic cycle, and the rotational flow breaks down even more at the transition to systole. This leads to more areas of stagnation at 50 bpm. These differences can be observed in previous Figures 50 and 56.

4.4.3 Systole

The flow patterns during systole show more similarities between the two beat rates than what was observed during diastole. This is related to the similar cycle times, as 75 bpm has a systolic duration of 340 ms and 50 bpm has a systolic duration of 400 ms. Both beat rates show a dominant movement in the flow towards the outlet port about 40% into systole. Both also show slightly higher velocities along the outside of the outlet port soon after, which is highlighted in Figure 66.

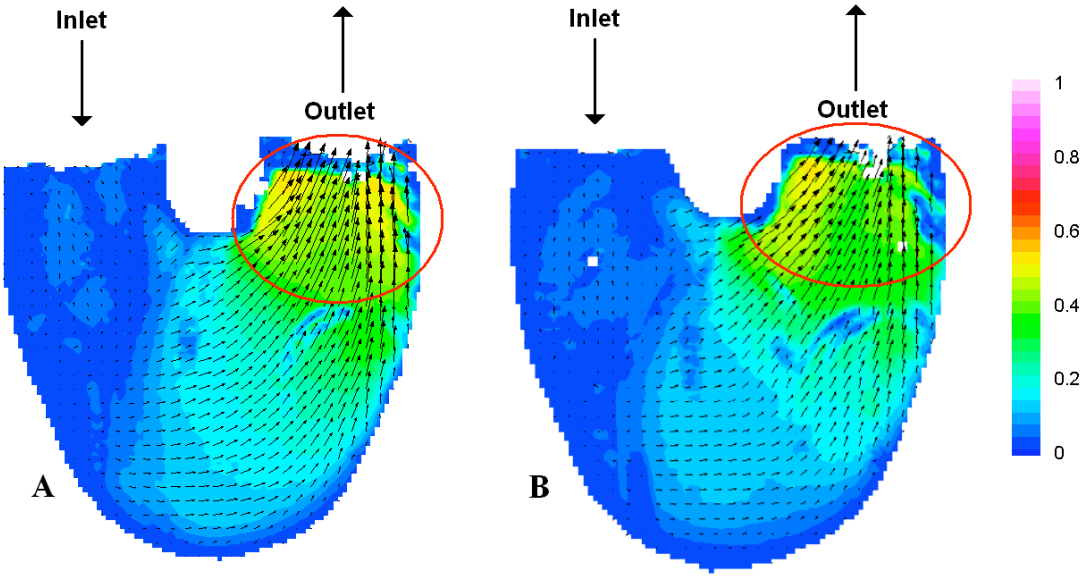

Figure 66: The 8.2 mm plane at 40% of the systolic cycle for (A) 75 and (B) 50 bpm. The beat rates show similar flow patterns as the fluid is ejected through the outlet port.

The two beat rates also show similar wall shear rates along the wall of the outlet port. As highlighted in Figure 67, the wall shear rates along Surface 4, which is located along the upper side of the outside wall of the outlet port, have similar patterns. However, at 75 bpm there is an increase in the magnitude of the wall shear, which is expected due to the increased flow rate.

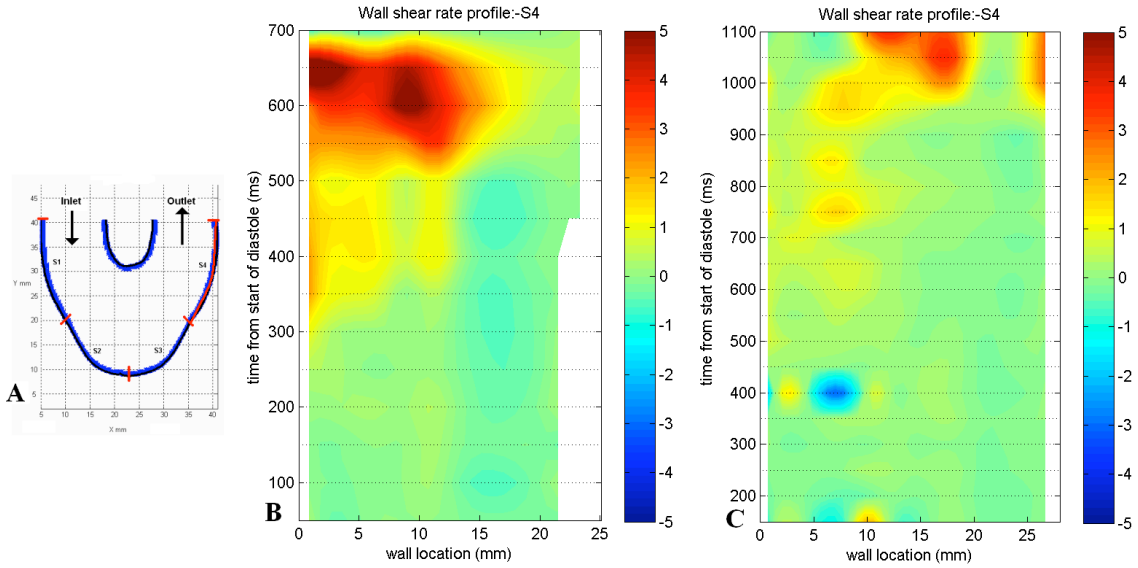

Figure 67: Surface 4 (S4), which is the upper outlet surface highlighted in (A) in red, of the 8.2 mm plane at (B) 75 and (C) 50 bpm. Both beat rates show an increase in wall shear along the outlet wall during mid to late systole. At 75 bpm the magnitude of the wall shear is higher, which is expected due to the increase in flow rate.

Both beat rates also contained an area of flow blockage upstream of the outlet valve in late systole. As shown previously in Figures 51 and 58, this blockage occurred in front of the strut of the BSM outlet valve. This characteristic could cause an increase in blood damage from the high near valve velocities. Previous studies concluded that the superior flow patterns observed by the BSM valve outweighed the concern of the blockage (Cooper 2008). Because there was no change in the blockage at the reduced beat rate, this conclusion remains.

One difference seen during systole between the two beat rates is the movement in the inlet port. At 40% systole, the time for which both beat rates show movement towards the outlet port, there is a drop in flow by both beat rates on the inlet side of the port seen in the parallel planes. However, as highlighted in Figure 68, normal planes through the inlet port at this time in systole show cross flow at 75 bpm that indicates movement not captured by the parallel planes. In contrast at 50 bpm the same normal plane showed the same stagnant flow as the parallel planes. This information helps confirm the concerns of overall low flow found at 50 bpm in comparison to the 75 bpm condition.

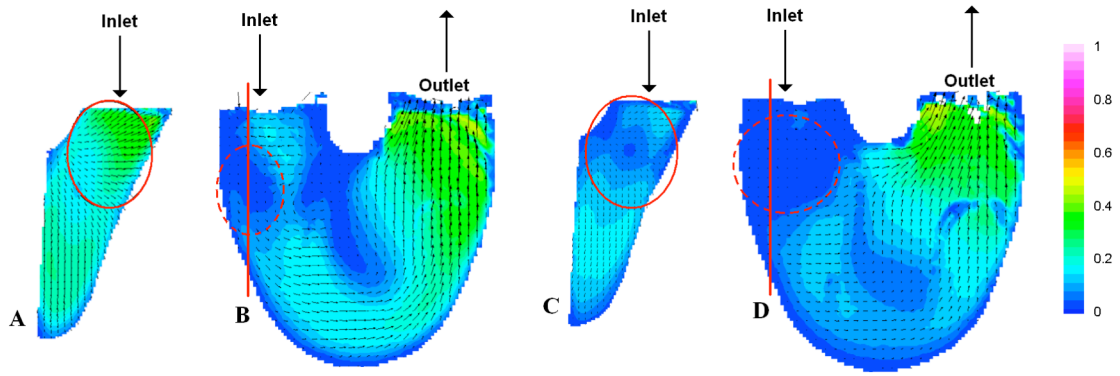

Figure 68: The (A, C) 3.75 mm normal inlet plane and (B, D) 8.2 mm parallel plane at 40% into systole for (A, B) 75 and (C, D) 50 bpm. As highlighted with red dashed ovals, the 8.2 mm planes of both beat rates contain areas of stagnation. However, normal planes crossing through the inlet port show that there is more cross flow at 75 bpm, which helps reduce stagnant areas in the inlet port during systole. Similar cross flow was not seen at 50 bpm.

4.5 Conclusion

The reduction in beat rate used in this study showed that the reduced flow rate corresponded to a reduction in the flow elements necessary to prevent platelet deposition and thrombus formation. At the beat rate of 50 bpm, the break down in the rotational flow field during mid to late diastole led to an increase in areas of low flow and stagnation throughout the device. There was also a decrease in the wall shear rates. These poorer flow characteristics must also be combined with a longer blood residence time because of the increase in the cardiac cycle. The result is an environment conducive to thrombus formation. Therefore, this reduced beat rate condition is not recommended for use with the PVAD in weaning.

These conclusions mean that other methods of flow rate reduction should be considered in order to wean patients from the PVAD during bridge-to-recovery. The major concerns of the beat rate reduction method were the reduction in wall washing and the break down of the rotational flow. These elements are both influenced by lower velocities seen during the filling of the device, and the increase in the diastolic cycle length. In order to aid these characteristics considerations should be taken in the filling of the device and the length of the diastolic cycle. In the next chapter, an effort was made to find a better filling solution and also use a stroke reduction method that does not require increasing the diastolic cycle time.

Chapter 5

STROKE VOLUME REDUCTION STUDY

5.1 Specific Aim

Because we found a reduction in beat rate to be an unacceptable method for flow rate reduction due to the increase in thrombogenic flow conditions, it was necessary to explore other options for weaning. For adult devices researchers had used reductions in stroke volume (SV) as part of a weaning protocol and found that this method had a less abrupt and more physiologically stable transition to the native ventricle when compared to rate reduction (Slaughter 2006). A SV reduction protocol was also appealing because it maintained the same cardiac cycle time as the flow rate was reduced, which avoided the increased residence times during beat rate reduction which might be thrombogenic.

For this study the SV of the PVAD was reduced in increments. Two different filling conditions were employed, which we term quick and slow, because studies by Cooper et al. showed that filling time had a lasting effect on the flow (Cooper 2010). High speed videography was used to map diaphragm motion while flow visualization was performed using particle image velocimetry (PIV) in 10 planes throughout the cardiac cycle.

5.2 Conditions

A previous study by the LVAD working group found that patients undergoing LVAD implantation with an ejection fraction (EF) of > 40% by their native ventricle were eligible for weaning towards explantation, whereas those at an EF of > 60% were eligible for device removal (Maybaum 2007). Our study made use of this observed range in SV. Using the assumption that the SV used for weaning corresponds to the EF of the patient's ventricle, we developed the range of PVAD conditions given in Table 1.

Table 1: The SV values of the PVAD being used at each weaning stage and the corresponding EF of the ventricle that would occur simultaneously.

Ejection Fraction of Ventricle	Stroke Volume of PVAD
0 % - 0 cc	100 % - 12 cc
20 % - 1.4 cc	80 % - 9.6 cc
40 % - 4.8 cc	60 % - 7.2 cc
60 % - 7.2 cc	40 % - 4.8 cc

We maintained full filling of the PVAD, for all conditions, while reducing the ejection fraction and therefore, the flow rate of the device. This differs from our previous studies in which complete ejection and filling of the PVAD were maintained, however this change allowed for the SV to be reduced and made PIV imaging possible.

In order to obtain the desired SV for the PVAD, we changed the conditions of the pneumatic driver. The beat rate of the pump remained at 75 bpm and the systolic duration at 340 ms. A mean aortic pressure was left constant at 75 mmHg, with maximum and minimum pressures around 90 and 60 mmHg. As the SVs were reduced, it became more difficult to maintain the range of maximum and minimum pressures with the existing compliance chamber used in the mock circulatory loop. Therefore, while the mean of 75

mmHg was maintained, the maximum and minimum pressures could not be kept exactly at 90 and 60 mmHg. The maximum pressure never fell below 82 mmHg, while the minimum never exceeded 67 mmHg. The systolic and diastolic pressures of the pneumatic driver were altered to obtain the desired flow rate.

When clinically implanted, the PVAD will experience a range of filling conditions. Because of this, we decided that mimicking the extremes of these conditions would be the most effective way to observe the potential change to flow. Therefore, two filling conditions were used at each SV: a 'quick' and a 'slow' condition. These two conditions were obtained by changing the end-diastolic delay (EDD), which was described in Chapter 4 and is shown in Figure 47. The 'quick' filling condition uses a large EDD between the end of inflow and the beginning of systole, so that the device fills rapidly and a high velocity, short duration inlet jet provides momentum for the rotational flow in the body of the device. The 'slow' filling condition, which allowed for the inflow to occur over the entire diastolic period and a very short EDD. Conceptually, we felt that a slow continuous inflow would allow for good rotation and movement to occur throughout the entire diastolic cycle. There are eight separate measurement conditions. The flow, pressure and EDD values for these are listed in Table 2 and the waveforms for each condition are given in Figures 69 - 72.

Table 2: Conditions of each stroke volume and filling method that was observed, including flow rates, pressures and the end-diastolic delay.

Stroke Volume	Filling Condition	Inflow Rate (average) (L/min)	Outflow Rate (average) (L/min)	Diastolic Pressure (maximum) (mmHg)	Systolic Pressure (minimum) (mmHg)	Outlet Pressure (max/min) (mmHg)	Inlet Pressure (max/min) (mmHg)	EDD (ms)
12 cc	Quick	0.91	0.89	170	-240	89/60	54/24	135
12 cc	Slow	0.89	0.91	145	-60	87/59	45/26	3
9.6 cc	Quick	0.73	0.78	150	-259	90/61	52/27	185
9.6 cc	Slow	0.72	0.78	128	-36	88/62	41/21	20
7.2 cc	Quick	0.54	0.58	127	-275	90/61	50/28	130
7.2 cc	Slow	0.53	0.53	111	-12	89/63	42/28	15
4.8 cc	Quick	0.36	0.36	94	-260	85/65	41/25	280
4.8 cc	Slow	0.36	0.36	90	-2	82/67	41/29	90

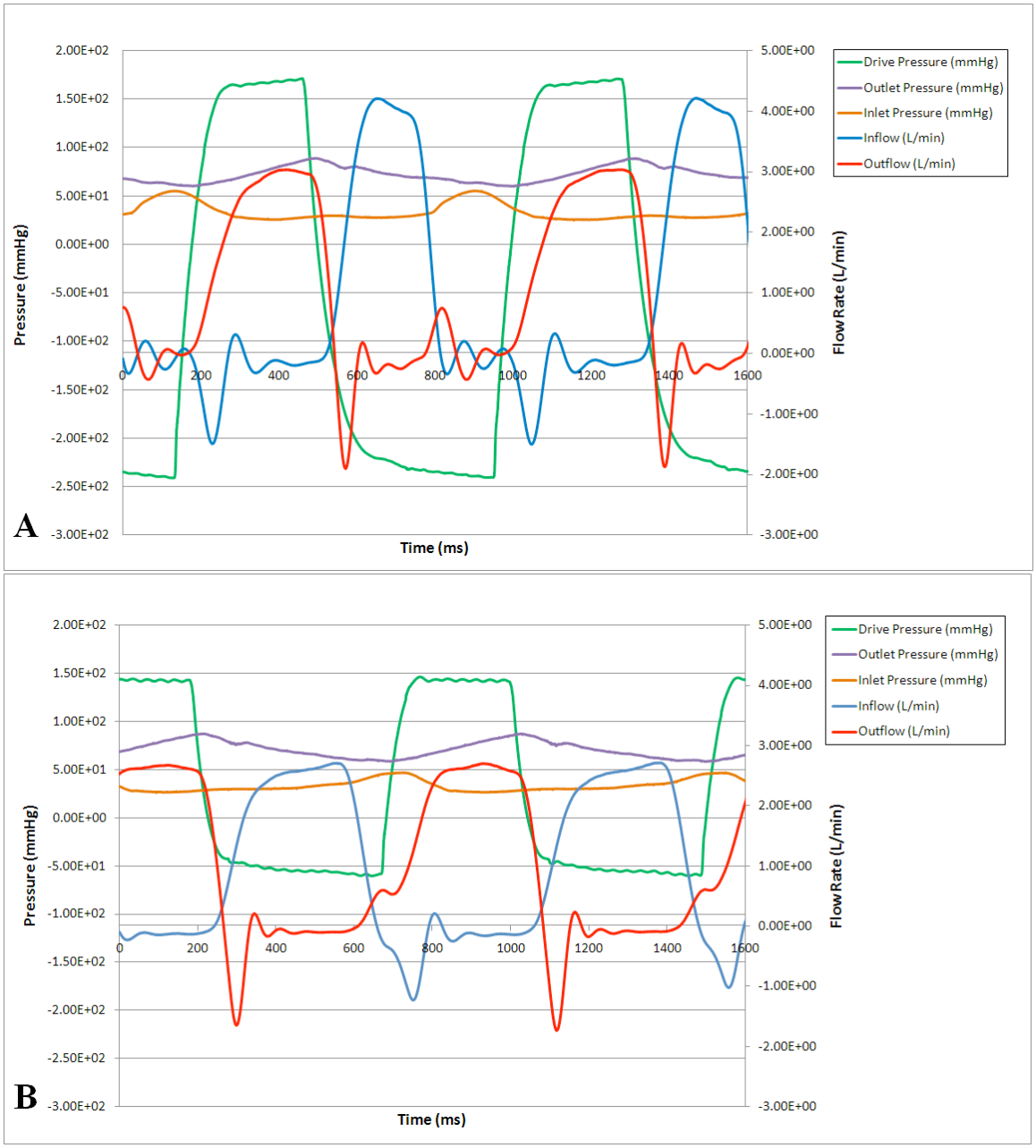

Figure 69: Waveforms representative of the (A) quick and (B) slow filling conditions at a 12 cc SV. The drive pressure (green) is the pressure waveform from the airline of the pneumatic driver used to run the pump. The inlet pressure (orange) is representative of the atrial pressure and is obtained from the compliance chamber upstream of the PVAD. The outlet pressure (purple) is representative of the aortic pressure and is obtained from the compliance chamber downstream of the PVAD. The inflow waveform is measured just upstream of the PVAD inlet valve and the outflow waveform just downstream of the outlet valve.

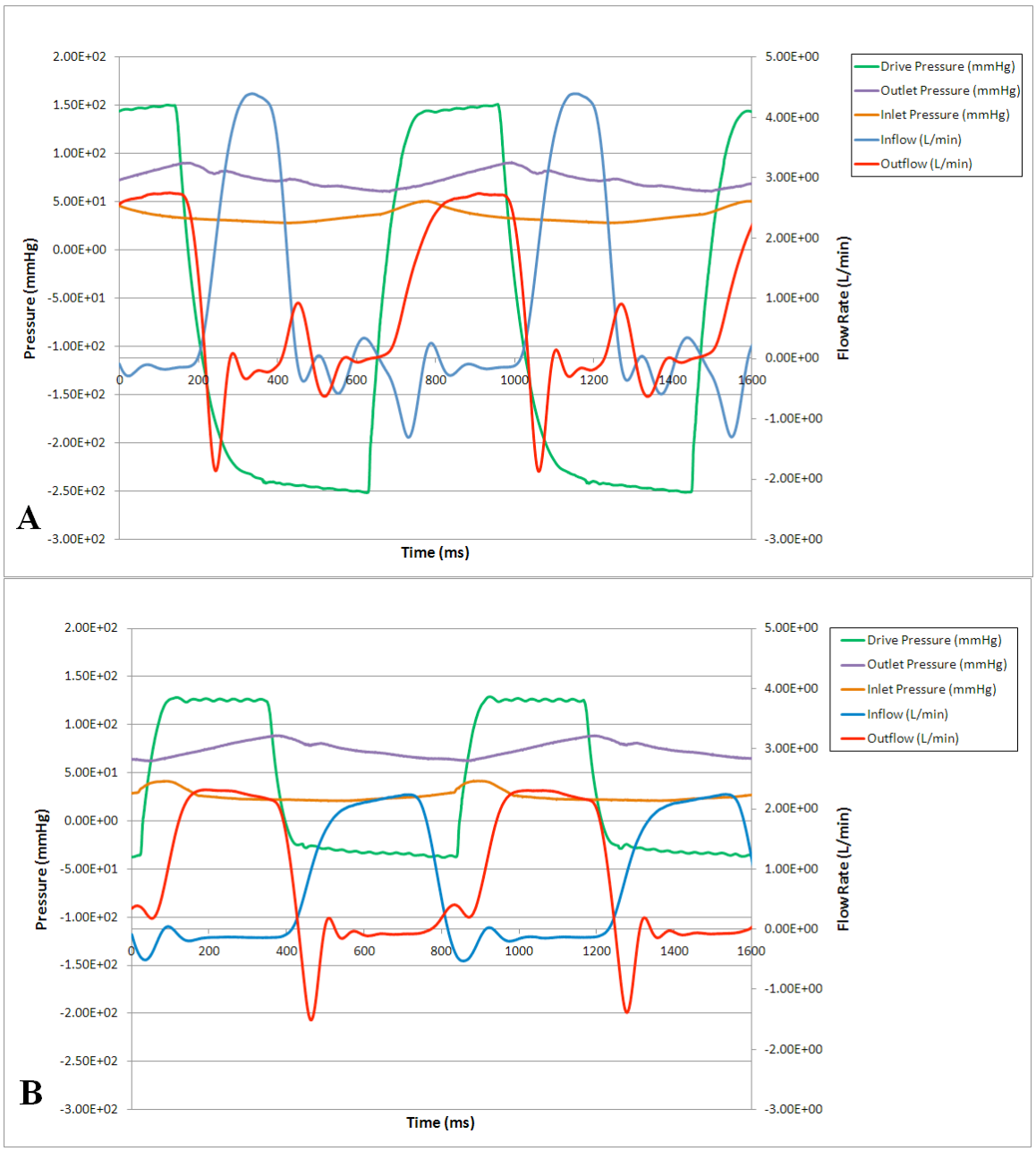

Figure 70: Waveforms representative of the (A) quick and (B) slow filling conditions at a 9.6 cc SV. The drive pressure (green) is the pressure waveform from the airline of the pneumatic driver used to run the pump. The inlet pressure (orange) is representative of the atrial pressure and is obtained from the compliance chamber upstream of the PVAD. The outlet pressure (purple) is representative of the aortic pressure and is obtained from the compliance chamber downstream of the PVAD. The inflow waveform is measured just upstream of the PVAD inlet valve and the outflow waveform just downstream of the outlet valve.

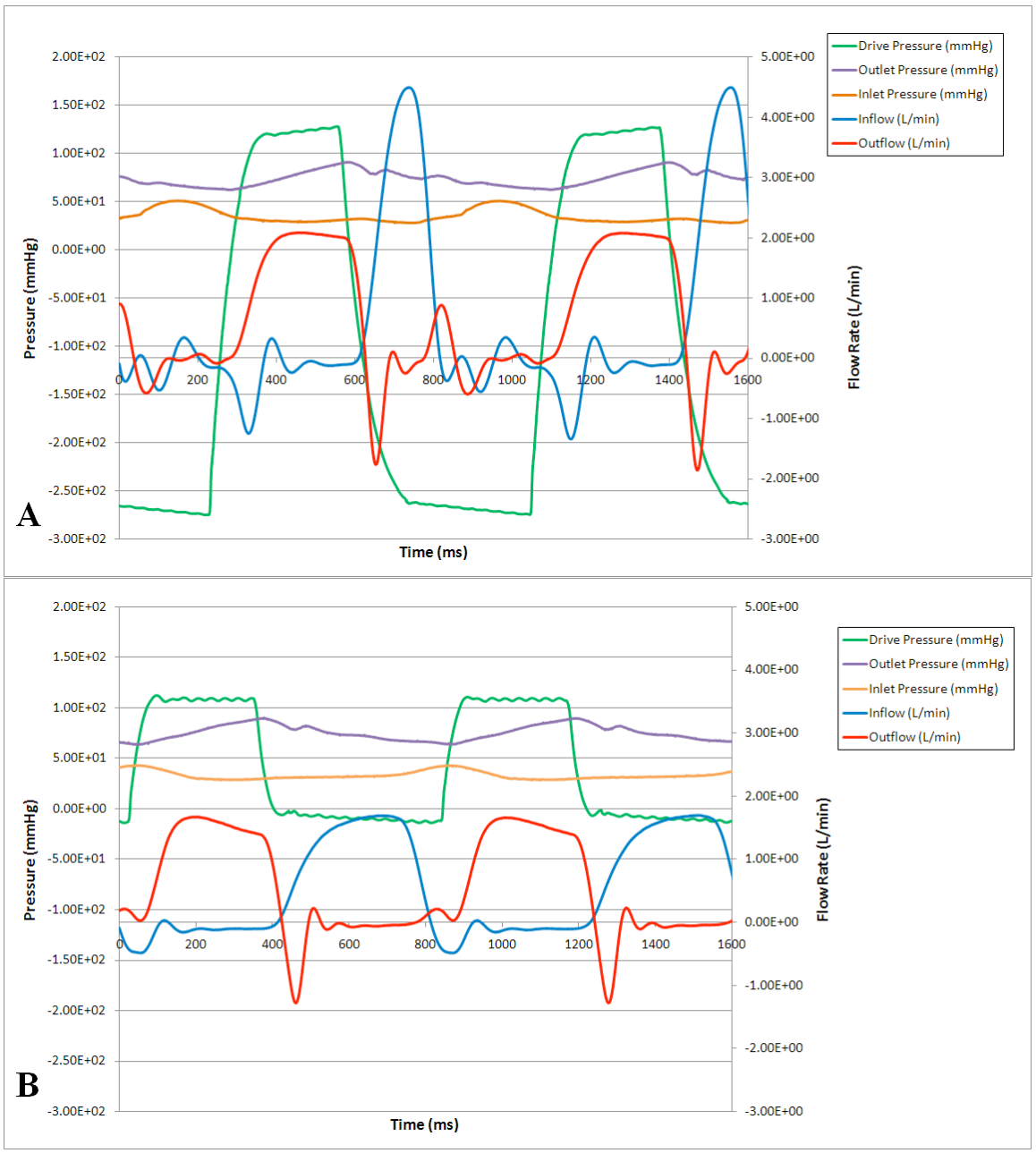

Figure 71: Waveforms representative of the (A) quick and (B) slow filling conditions at a 7.2 cc SV. The drive pressure (green) is the pressure waveform from the airline of the pneumatic driver used to run the pump. The inlet pressure (orange) is representative of the atrial pressure and is obtained from the compliance chamber upstream of the PVAD. The outlet pressure (purple) is representative of the aortic pressure and is obtained from the compliance chamber downstream of the PVAD. The inflow waveform is measured just upstream of the PVAD inlet valve and the outflow waveform just downstream of the outlet valve.

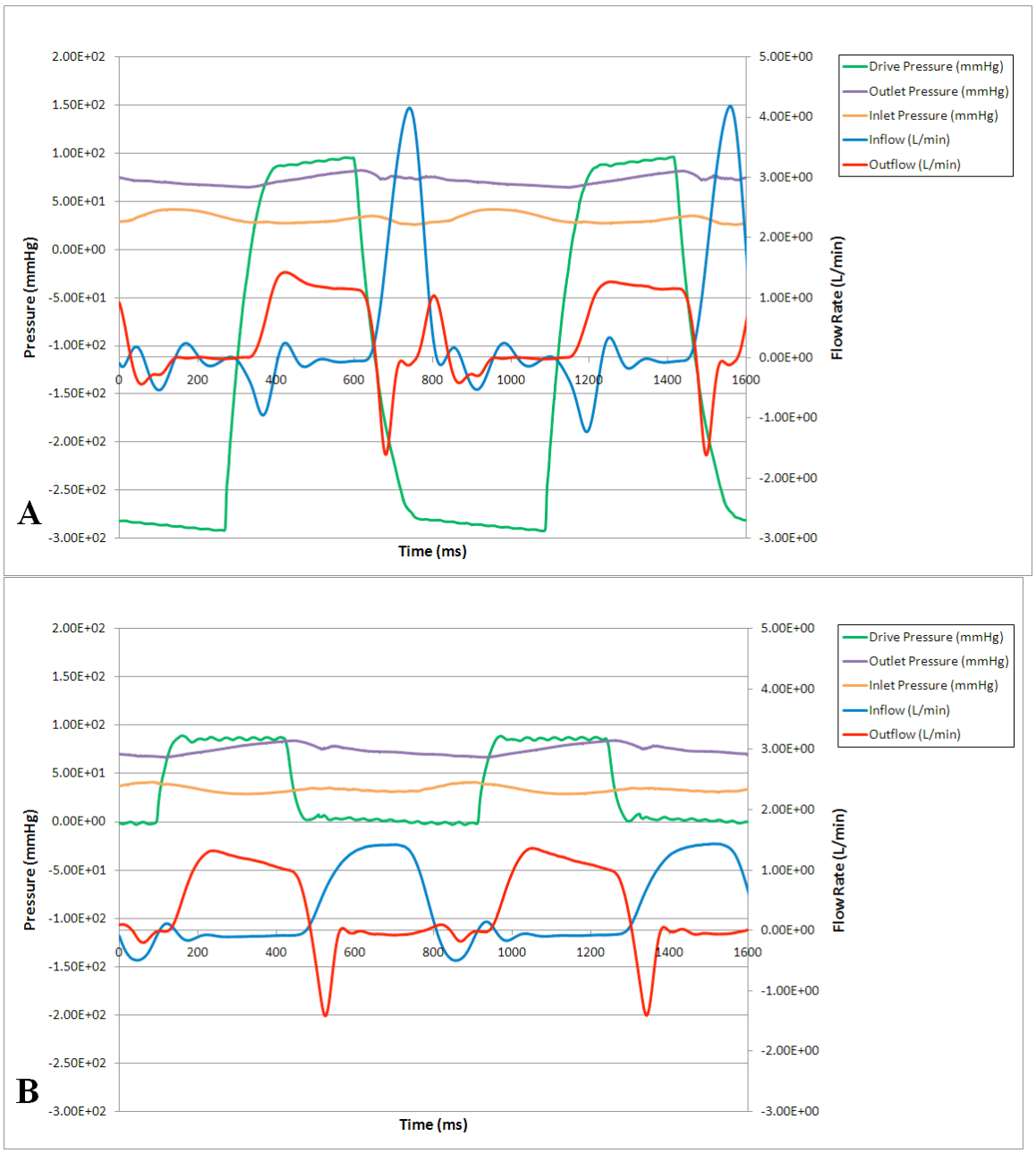

Figure 72: Waveforms representative of the (A) quick and (B) slow filling conditions at a 4.8 cc SV. The drive pressure (green) is the pressure waveform from the airline of the pneumatic driver used to run the pump. The inlet pressure (orange) is representative of the atrial pressure and is obtained from the compliance chamber upstream of the PVAD. The outlet pressure (purple) is representative of the aortic pressure and is obtained from the compliance chamber downstream of the PVAD. The inflow waveform is measured just upstream of the PVAD inlet valve and the outflow waveform just downstream of the outlet valve.

The change in stroke volume led to different diaphragm motions than those observed in our earlier studies. The changes in diaphragm shape and movement, as a function of stroke volume was recorded with high speed videography. Recordings were taken normal to the diaphragm at 500 frames per second.

In order to obtain fluid mechanic information of several conditions in a timely manner, PIV was chosen for flow visualization. Data was taken at three planes parallel to the diaphragm at a resolution of approximately 60 μm/pixel and seven normal planes at a resolution of about 37 μm/pixel. These planes were shown previously in Figure 40. The laser pulse delay, ΔT, varied from 150 to 400 μs depending on the flow rate and the time in the cardiac cycle.

5.3 Results

5.3.1 Diaphragm Motion

Because a full filling, partial ejection method was used to reduce the SV, the diaphragm motion is different for each condition. When the SV is reduced the diaphragm is only partially deployed. Images were captured of the maximum deployment for each SV using both quick and flow fills. Typical quick fill images are shown in Figure 73.

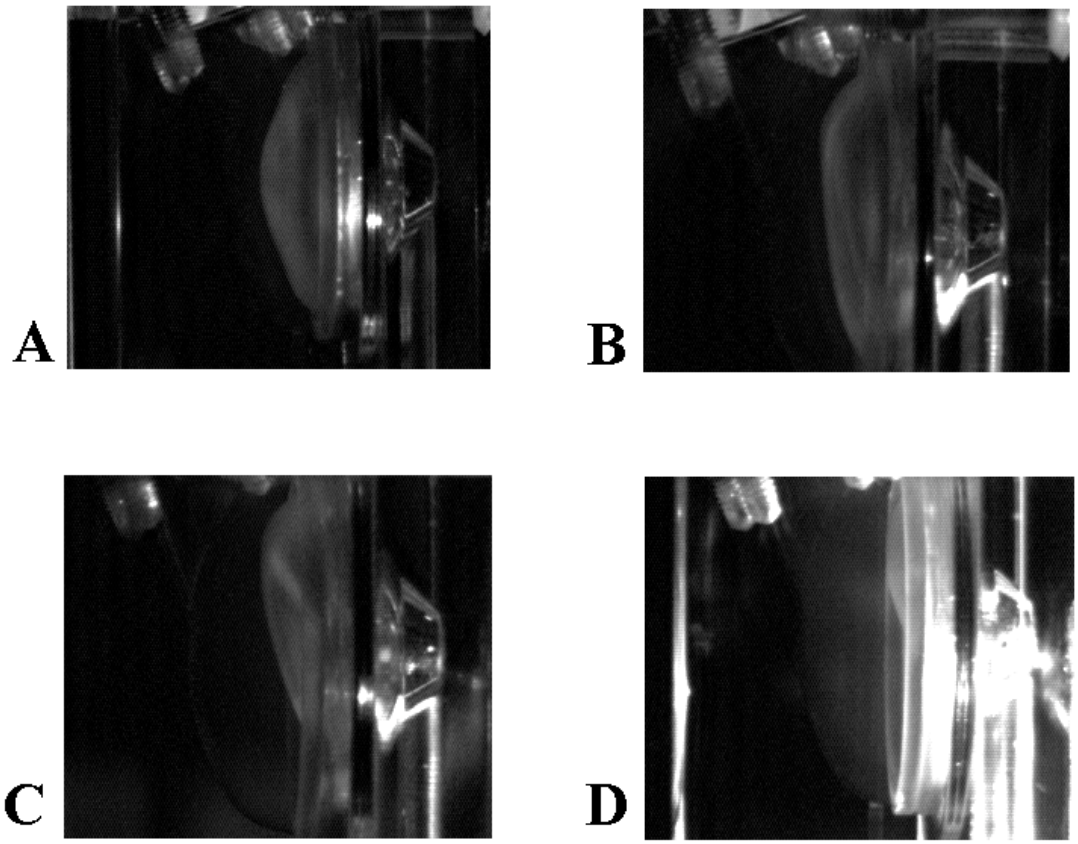

Figure 73: A snapshot of the diaphragm at its location of maximum deployment for SVs of (A) 12, (B) 9.6, (C) 7.2 and (D) 4.8 cc. Besides the 12 cc SV, which shows full deployment of the diaphragm, the diaphragm is biased toward deploying at the top initially.

The maximum deployment location and shape of the diaphragm is the same for both the quick and slow filling conditions at each SV. As would be expected, the time taken to

deploy and collapse the diaphragm is different for each condition, and particularly between the quick and slow fills. Table 3 presents the time between deployment and collapsing of the diaphragm at each condition. The start of deployment is defined as the time when the diaphragm could first be seen in the image. The end of deployment, which is also the start of the collapse, is defined as the time the diaphragm reached its maximum depth. The end of diaphragm collapse is defined as the time the diaphragm is no longer visible.

Table 3: The deployment and collapse times for each condition during one cycle as captured by the high speed videography.

Stroke Volume	Filling Method	Deployment Time (ms)	Collapse Time (ms)
12 cc	Quick	224	152
12 cc	Slow	264	260
9.6 cc	Quick	194	120
9.6 cc	Slow	216	204
7.2 cc	Quick	172	64
7.2 cc	Slow	208	172
4.8 cc	Quick	116	30
4.8 cc	Slow	214	86

As presented in Table 3, the quick fills have shorter diaphragm collapse times, which is consistent with the compressed inlet flow waveform. Quick fills also result in a shorter deployment time, which ranges from 20 to 40 ms for each SV. This means there is a difference in the systolic behavior between the two filling methods as well. This is of interest because the systolic durations of all eight conditions are set to be the same at 340 ms. As the SV is reduced the collapsing and deployment times show a corresponding reduction in time.

5.3.2 PIV Results

5.3.2.1 12 cc Quick Fill

With the 12 cc quick fill, a strong inlet jet is visible at 50 ms into the cycle. The peak jet velocity of 1.67 m/s is observed at 100 ms. The inlet jet forms along the outside of the inlet port, consistent with the location of the major orifice opening of the BSM valve. The portion of the jet that moves through the minor orifice of the jet shows a less defined pattern. As shown in Figure 74, this behavior appears in both the parallel and normal inlet planes.

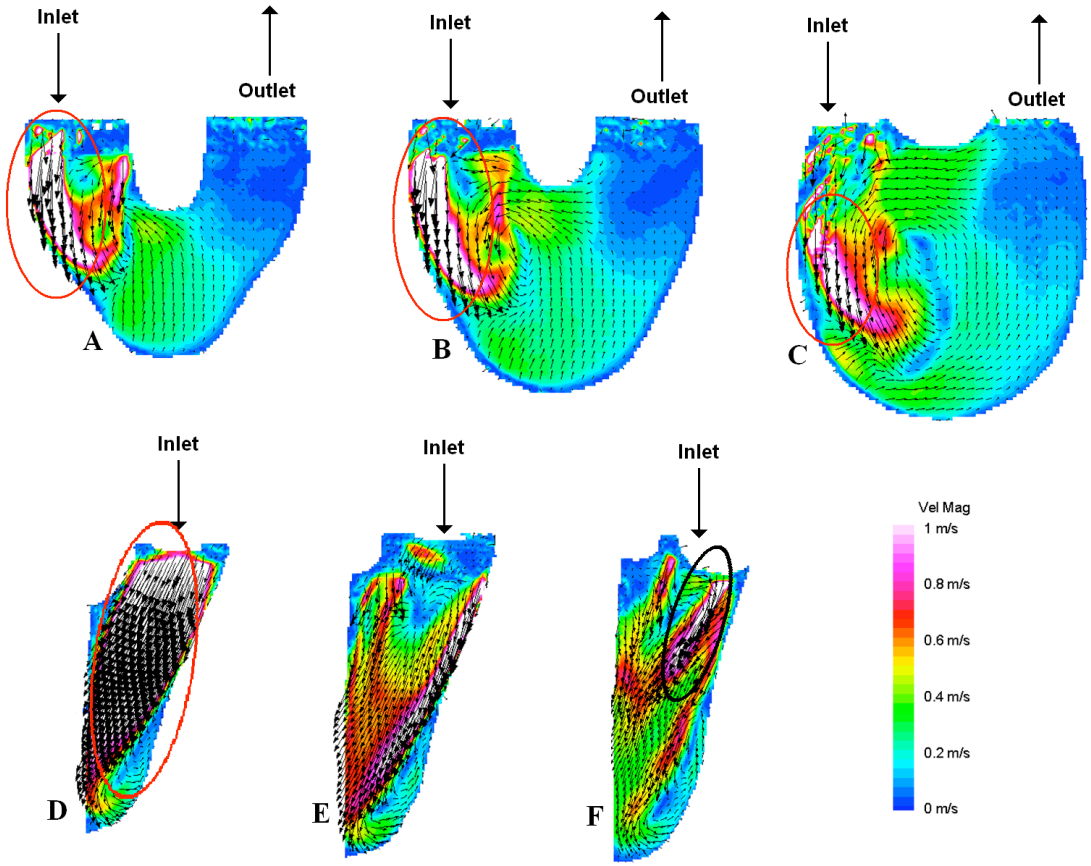

Figure 74: The (A) 7, (B) 8 and (C) 11 mm parallel planes and (D) 3.75, (E) 7.5 and (F) 11.25 mm inlet normal planes of the 12 cc quick fill condition at 100 ms. As observed in A, B, C and D a strong inlet jet has formed along the outside wall where the major orifice of the valve is located, highlighted in red. A smaller minor orifice jet is seen in F and is circled in black.

The inlet jet reaches the bottom of the device at 150 ms into diastole. This penetration also marks the start of the rotational flow field in the parallel planes. A rotational center is also seen in all of the parallel planes at this point in the cycle. The 11.25 mm inlet normal plane shows an area of recirculation at the bottom of the device. The penetration to the bottom of the device appears in all the parallel planes and normal inlet planes, as shown in Figure 75.

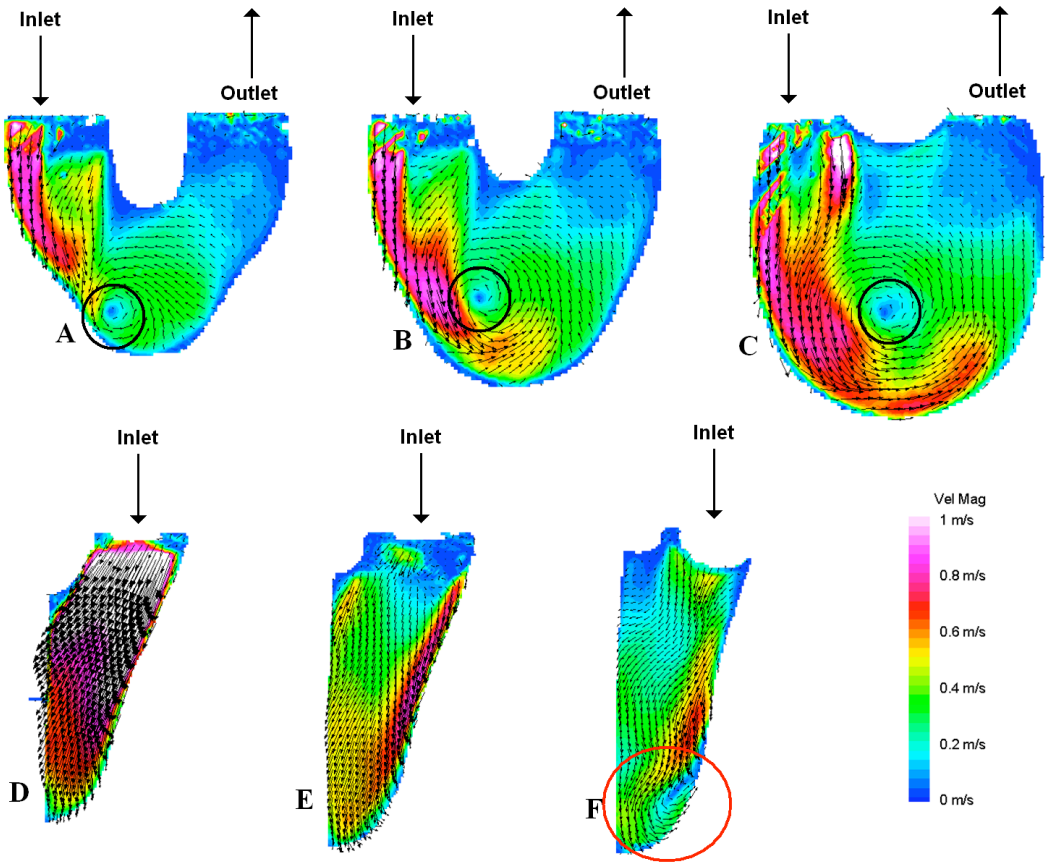

Figure 75: The (A) 7, (B) 8 and (C) 11 mm parallel planes and (D) 3.75, (E) 7.5 and (F) 11.25 mm inlet normal planes of the 12 cc quick fill condition at 150 ms. At this point in diastole the inlet jet has moved along the outside wall of the pump and penetrated the bottom of the device, which can be seen in all the above planes. A center of rotation has also formed in (A, B, C) all three parallel planes, as circled in black, which indicates formation of the desired rotational flow. There is also an area of recirculation visible in F at the bottom of the device, which is highlighted in red.

At 200 ms near the outlet, an increase in velocity magnitudes in the body of the device confirm that the rotational flow does not encompas the outlet side of the model. As shown in Figure 76, this velocity increase is observed in all three normal planes, however the 3.75 mm plane, which is closest to the outside wall, contains the highest magnitude at 0.72 m/s. This is consistent with the inlet jet formation along the outside wall of the device.

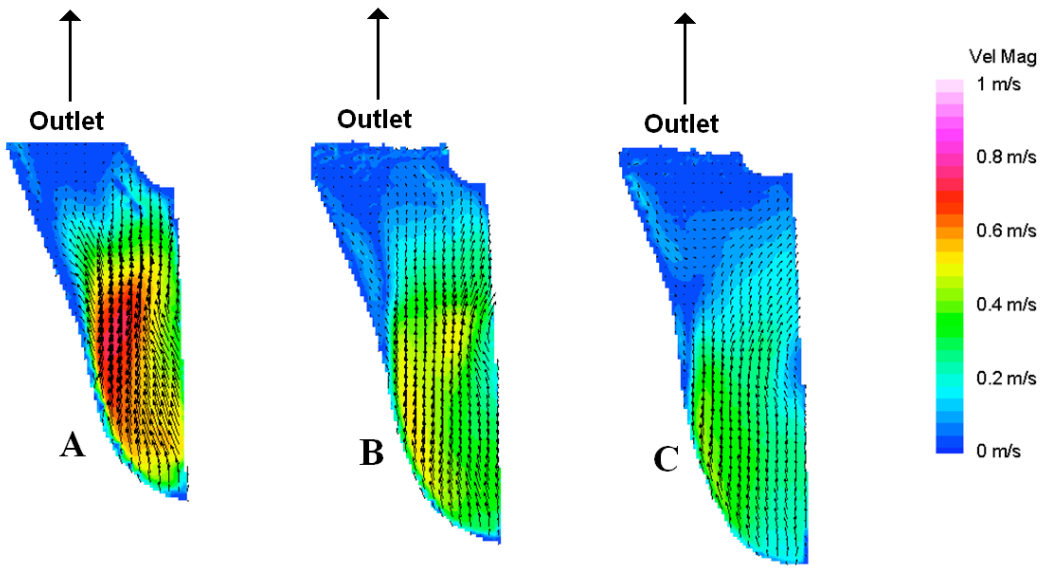

Figure 76: The (A) 3.75, (B) 7.5 and (C) 11.25 mm outlet normal planes of the 12 cc quick fill condition at 200 ms. The increased velocity magnitudes of the vectors in the body of the device towards the outlet port indicate that the flow from the outside wall of the device has rotated up to the outlet side, a sign of rotational flow.

As the magnitude of the inlet jet begins to decrease, there is a drop in the velocity magnitudes in all planes to below 0.4 m/s. However, even with the reduction in velocity a rotational flow in the parallel planes continues through diastole. A center of rotation can be seen in all three parallel planes until 500 ms, which is the beginning of systole. For example, Figure 77 shows this rotation in the 8.2 mm plane.

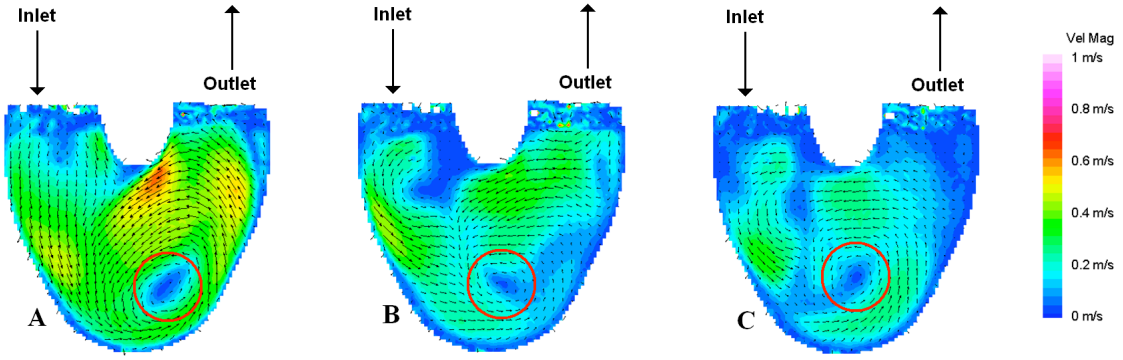

Figure 77: The 8.2 mm parallel plane of the 12 cc quick fill condition at (A) 250, (B) 350 and (C) 450 ms. While the velocity magnitudes decrease as the flow moves through diastole, the center of rotation remains tight throughout the cycle. This is circled in red.

As diastole progresses, the flow in the normal planes is consistent with a continuation of rotational flow in the body of the device and a drop in velocity magnitude. While the outlet normal planes also show a drop in velocity magnitude, there are also areas of regurgitation and recirculation observed in the outlet port during mid to late diastole. In Figure 78 the 3.75 mm plane for example shows regurgitation, while the 7.5 and 11.25 mm planes contain recirculation regions.

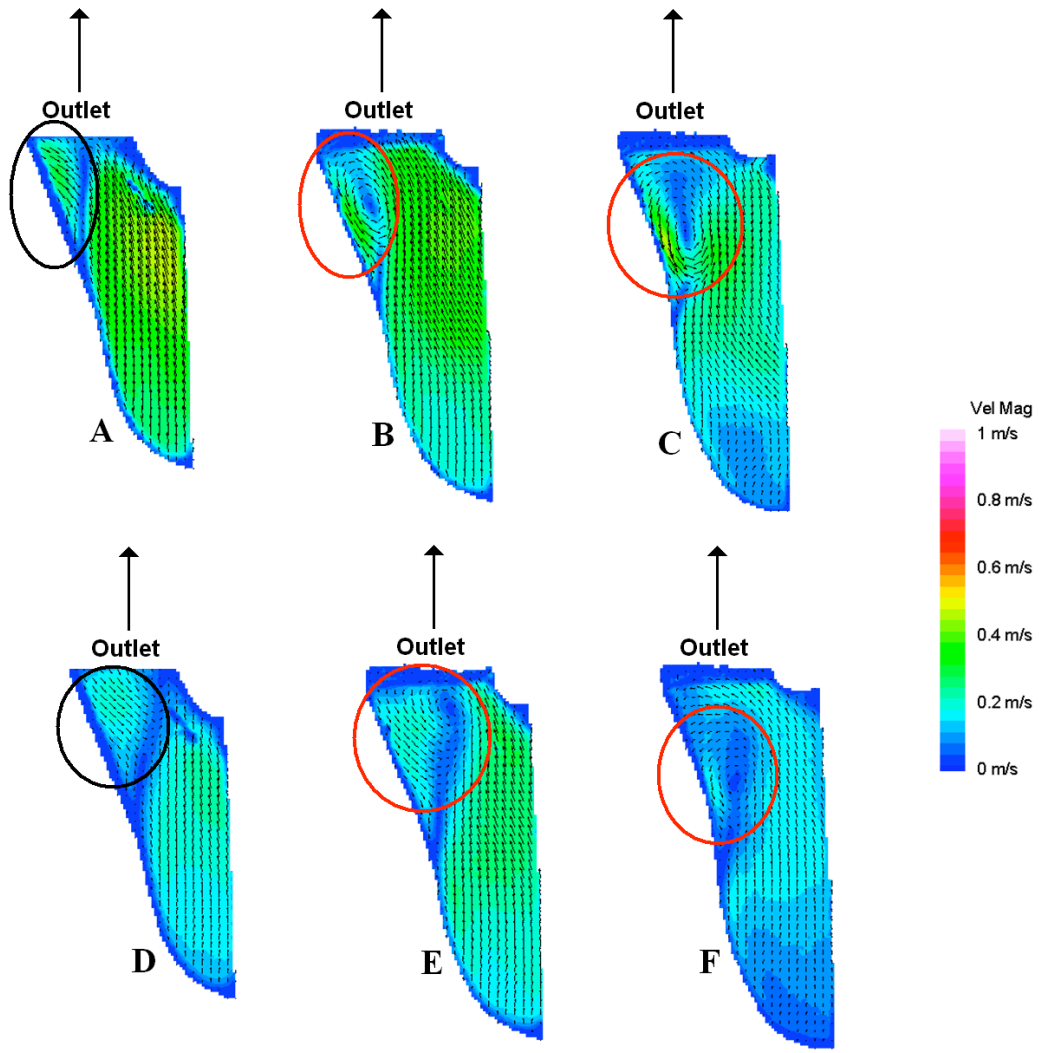

Figure 78: The (A, D) 3.75, (B, E) 7.5 and (C, F) 11.25 mm outlet normal planes of the 12 cc quick fill condition at (A, B, C) 300 and (D, E, F) 400 ms. As the flow moves through the body of the outlet side during the diastole rotational flow areas of regurgitation (highlighted in black) and recirculation (highlighted in red) have formed in the outlet port.

As systole begins, the parallel planes all show a smooth transition to the ejection phase of the cycle. That is, the dominant movement of the flow is towards the outlet port, as shown in Figure 79, without undesirable features such as areas of recirculation or blockages in the flow.

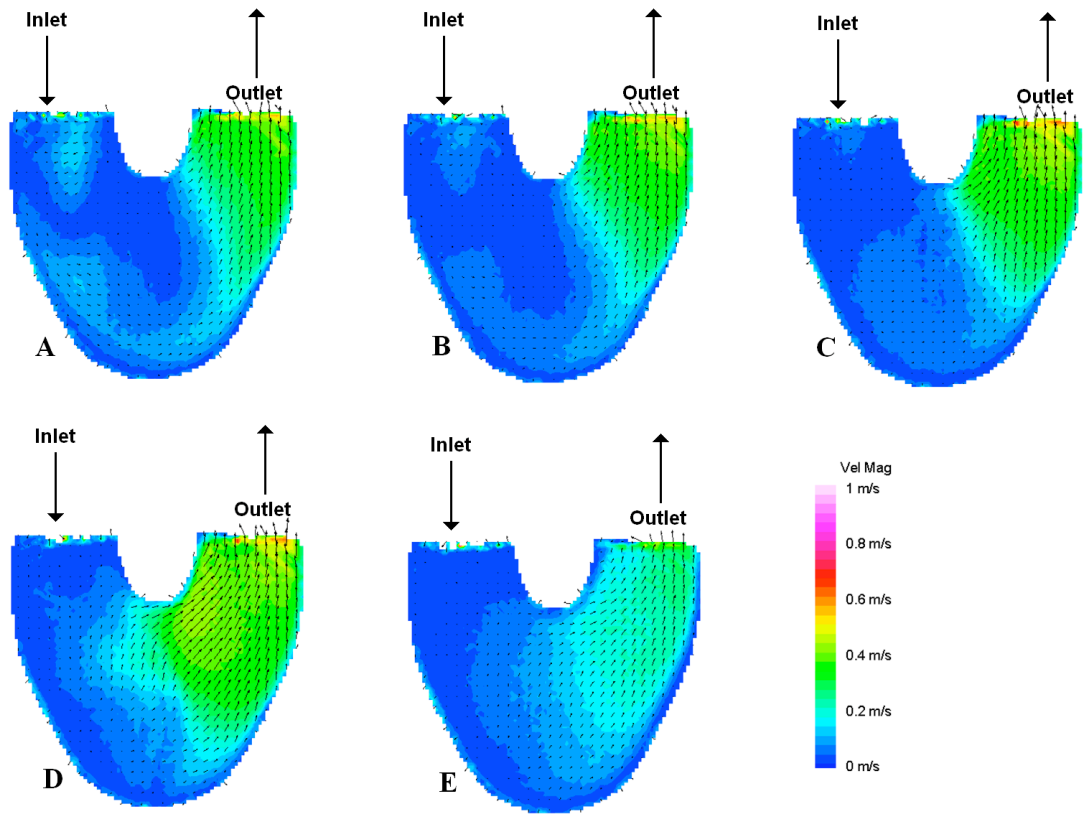

Figure 79: The 8.2 mm plane of the 12 cc quick fill condition during systole, (A-E) 600-800 ms. The flow in the outlet port does not show any signs of blockage as the flow moves smoothly through the outlet valve.

While the systolic flow is smooth, there are areas of low flow (< 0.1 m/s) and stagnation in the inlet port, in both the parallel and normal inlet planes. This is to be expected because of the fluid's movement to the outlet port, and was most noticeable in the 11.25 mm normal inlet plane as shown in Figure 80.

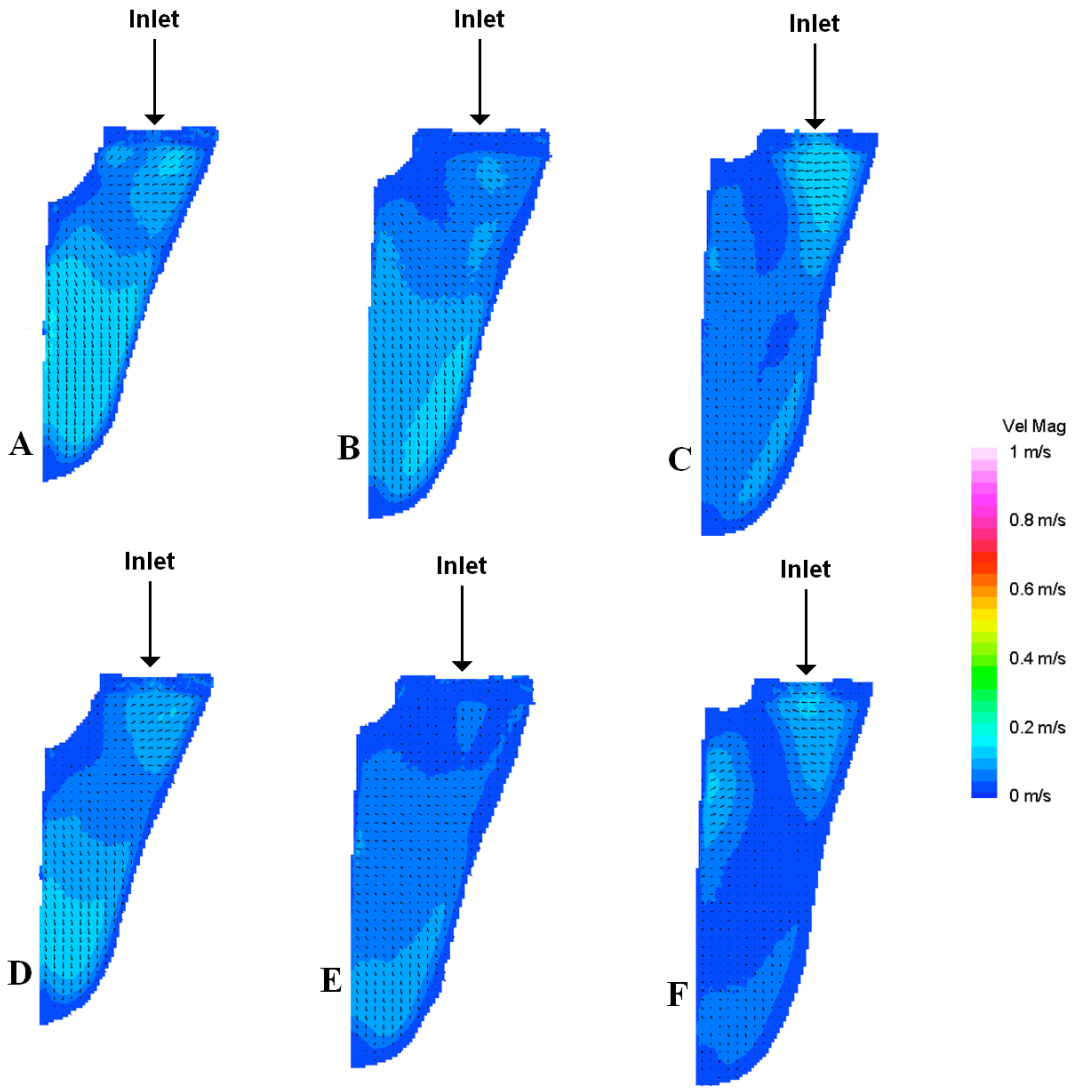

Figure 80: The (A, D) 3.75, (B, E) 7.5 and (C, F) 11.25 mm inlet normal planes of the 12 cc quick fill condition at (A, B, C) 600 and (D, E, F) 650 ms. In mid systole the inlet planes show very low flow (< 0.1 m/s), shown by the color legend as regions of dark blue.

A smooth transition to systole is also observed in the outlet normal planes. The areas of recirculation observed earlier during diastole are replaced by uniform movement through the outlet valve. One characteristic seen in previous studies that was not observed at this condition is an area of blockage upstream of the strut of the BSM outlet valve. As shown in Figure 81, the flow through the outlet valve during late systole does not show any such blockage in the parallel or normal planes.

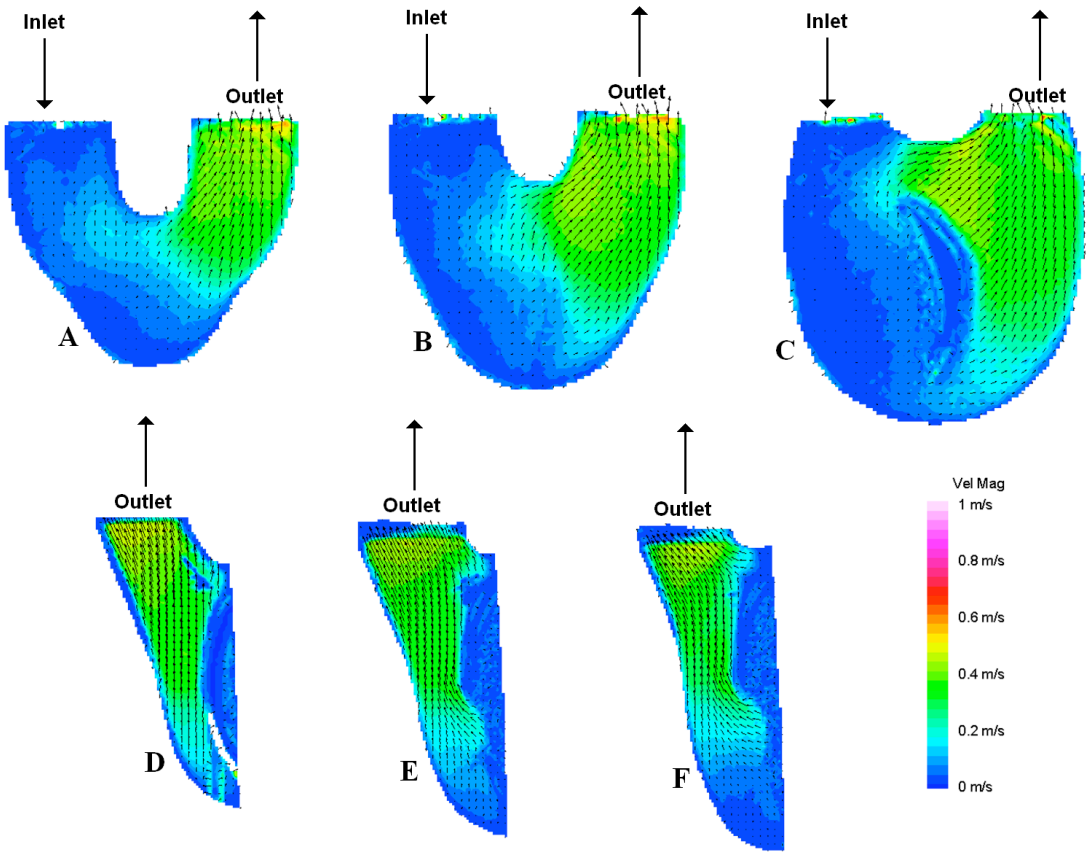

Figure 81: The (A) 7, (B) 8 and (C) 11 mm parallel planes and (D) 3.75, (E) 7.5 and (F) 11.25 mm outlet normal planes of the 12 cc quick fill condition at 750 ms. There is no area of blockage observed upstream of the outlet valve during late systole, something found in previous studies.

5.3.2.2 12 cc Slow Fill

When driven at the 12 cc slow fill conditions, the inlet jet becomes visible at 100 ms into the cycle. The jet continues to grow during early to mid diastole, reaching its maximum velocity of 0.94 m/s at 300 ms into diastole. The flow from the jet is concentrated along the outside wall of the inlet, where the major orifice of the BSM opens. There is a small jet from the minor orifice side of the jet that dissipates as the major jet increases in velocity. Figure 82 presents this jet growth during diastole in the 7 mm plane. Similar patterns were seen in the other parallel planes.

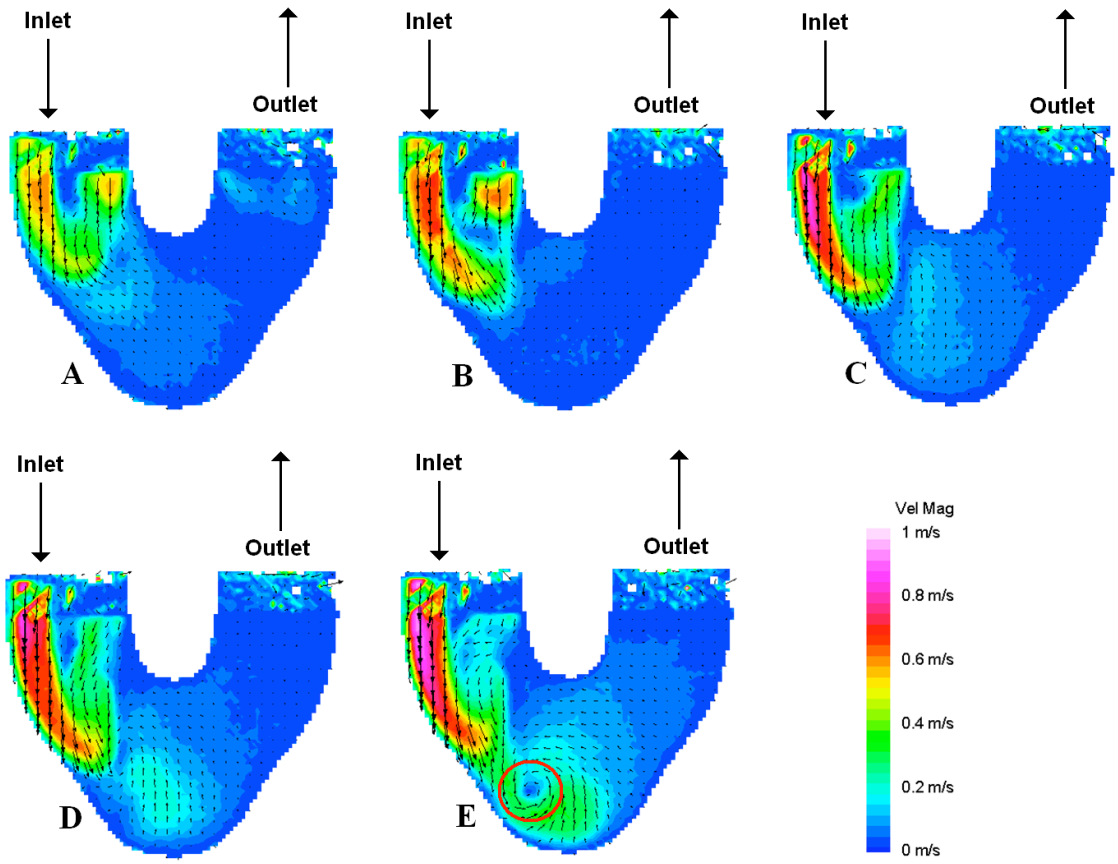

Figure 82: The 7 mm plane of the 12 cc slow fill condition during early to mid diastole, (A-E) 100-300 ms. The inlet jet is visible at (A) 100 ms and continues to grow through mid diastole. The start of rotational flow occurs at (E) 300 ms, where a center of rotation is observed as highlighted in red.

This inlet jet behavior is visible in the inlet normal planes as well. The inlet planes show similar growth of the inlet jet through early to mid diastole. These planes also confirm the concentration of flow towards the outside wall of the inlet port and little influence from the minor orifice jet. As the flow moves through diastole, an area of recirculation at the bottom of all three planes is observed. This area forms from the inlet jet and develops into a counterclockwise rotation at the bottom of the device. These inlet characteristics are highlighted in Figure 83.

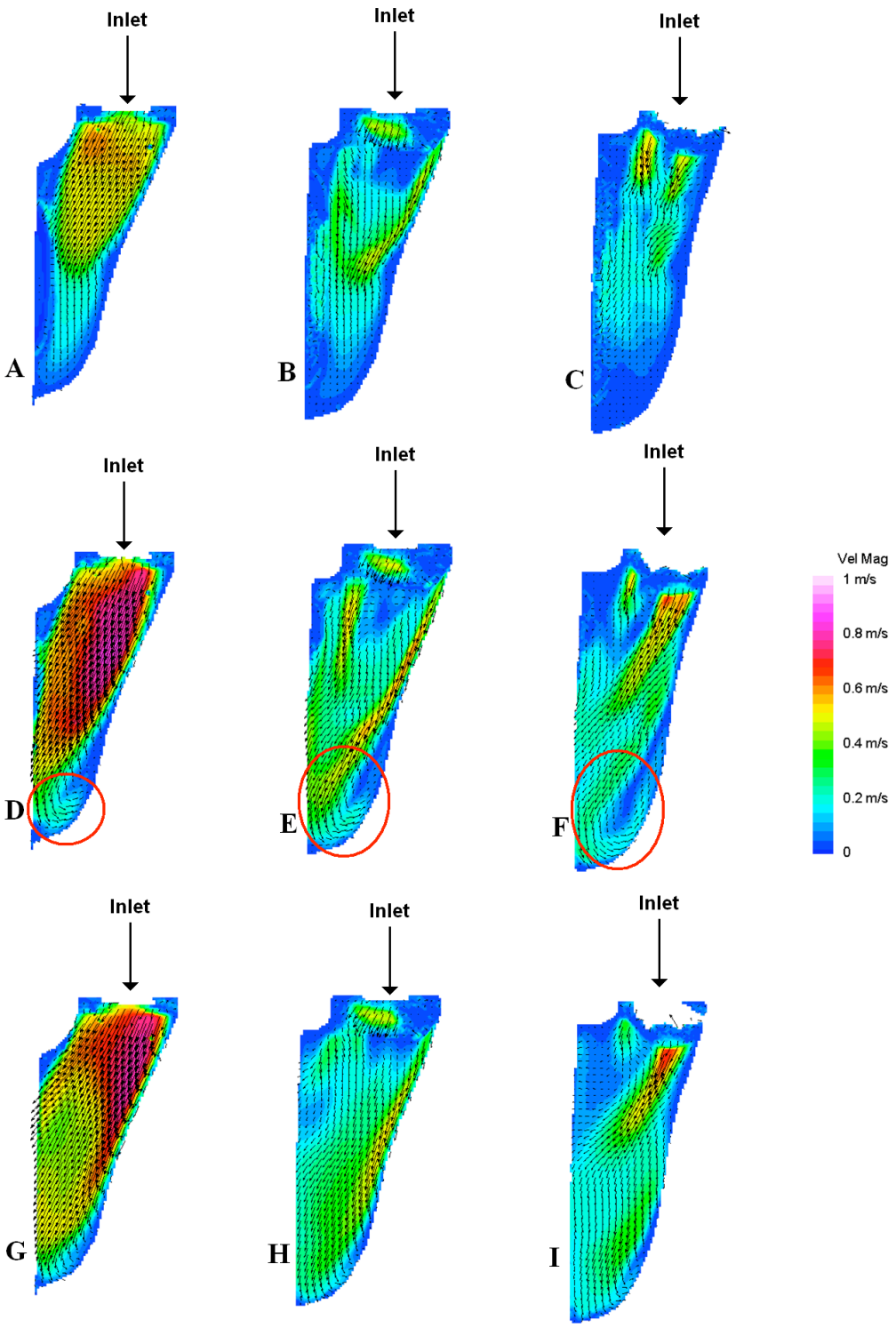

Figure 83: The (A, D, G) 3.75, (B, E, H) 7.5 and (C, F, I) 11.25 mm inlet normal planes of the 12 cc slow fill condition at (A, B, C) 100, (D, E, F) 200 and (G, H, I) 300 ms. As diastole progresses the inlet jet can be seen moving towards the bottom of the device. At (D, E, F) 200 ms an area of recirculation is visible in all three normal planes, as highlighted in red.

The normal outlet planes show little fluid movement during early diastole. An increase in fluid velocity at 300 ms implies that the rotational flow through the body of the device had begun. A center of rotation appears in all three parallel planes at 300 ms into the cycle. This center disappears from the 7 mm plane at 400 ms, and the rotational flow in this plane remains patchy through the end of diastole. This patchy rotation includes a large area of stagnant flow in the inlet port, which is also visible in the inlet normal planes as shown in Figure 84.

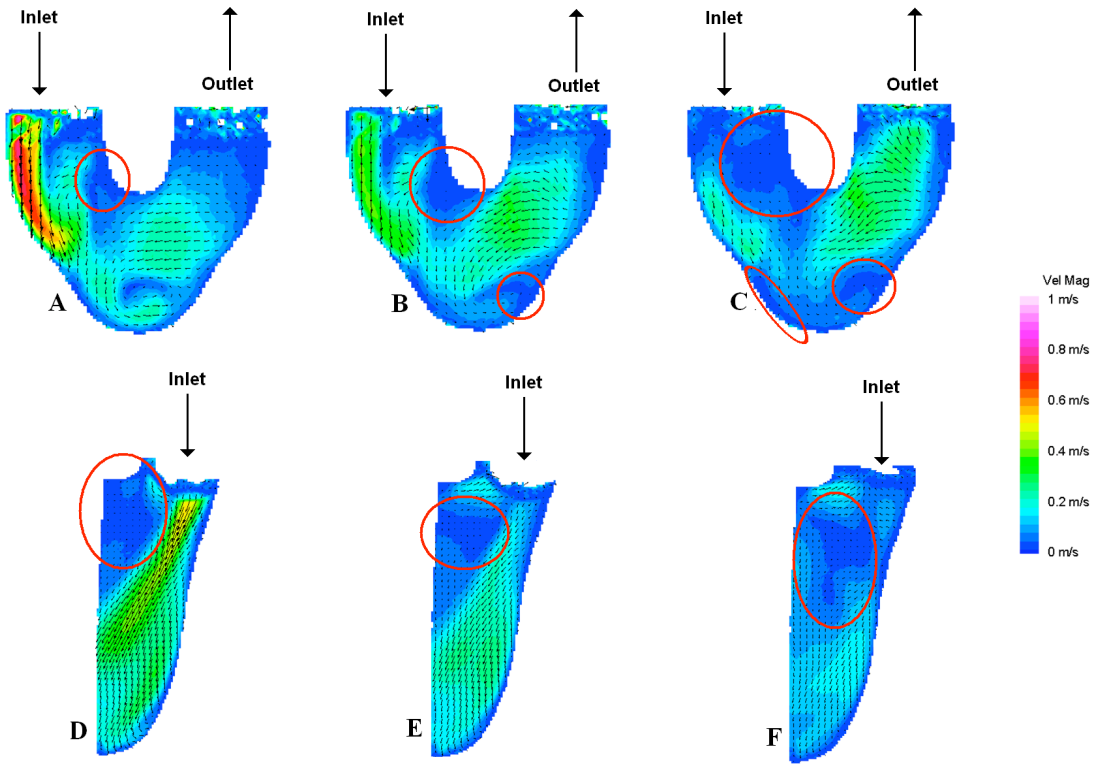

Figure 84: The (A, B, C) 7 mm parallel plane and (D, E, F) 11.25 mm normal inlet plane of the 12 cc slow fill condition during mid to late diastole, (A, D) 350, (B, E) 400, and (C, F) 450 ms. As the flow progresses through the end of diastole areas of stagnation are noticeable in the flow field, as highlighted in red.

In the 8.2 and 11 mm planes, the center of rotation is maintained throughout diastole, however the size of the low flow area of this center increases in size and the rotational flow is less defined. Figure 85 highlights this behavior in these parallel planes.

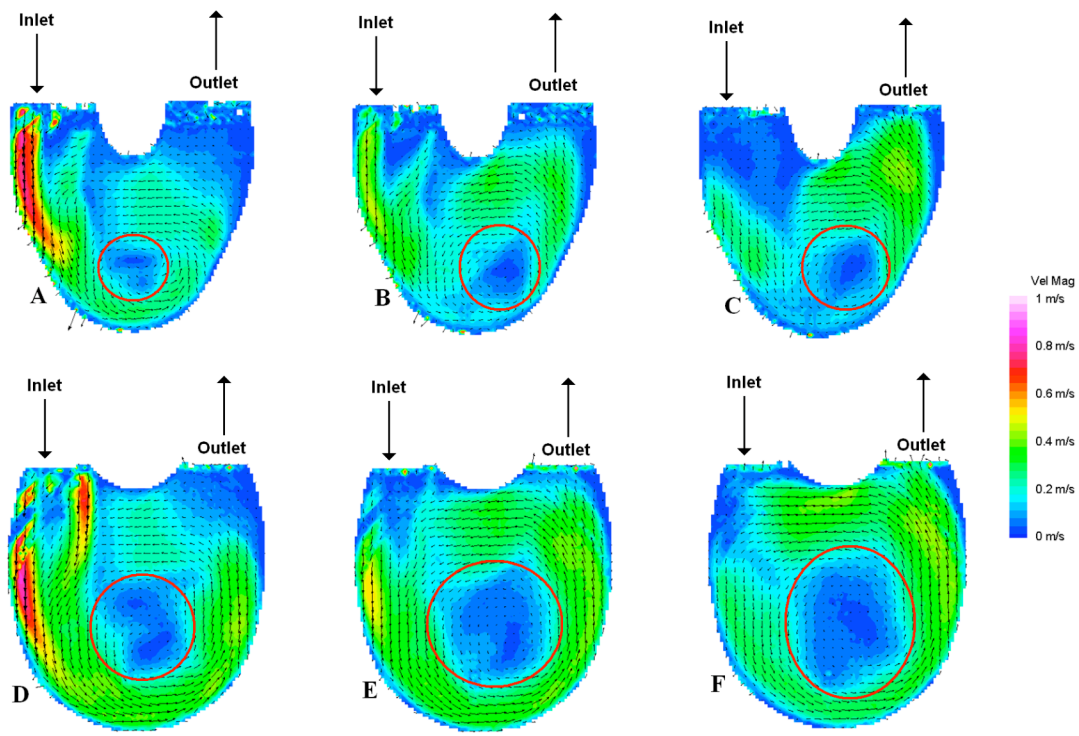

Figure 85: The (A, B, C) 8.2 and (D, E, F) 11 mm parallel planes of the 12 cc slow fill condition during mid to late diastole, (A, D) 350, (B, E) 400, and (C, F) 450 ms. As the parallel planes progress through diastole the center of rotation (circled in red) expands, indicating a looser rotational flow field.

As the flow transitions from diastole to systole, there is smooth movement of fluid towards the outlet port. The parallel and inlet planes show no areas of blockage or recirculation, however they do contain very low flow and some areas of stagnation in the inlet side of the device, as shown in Figure 86.

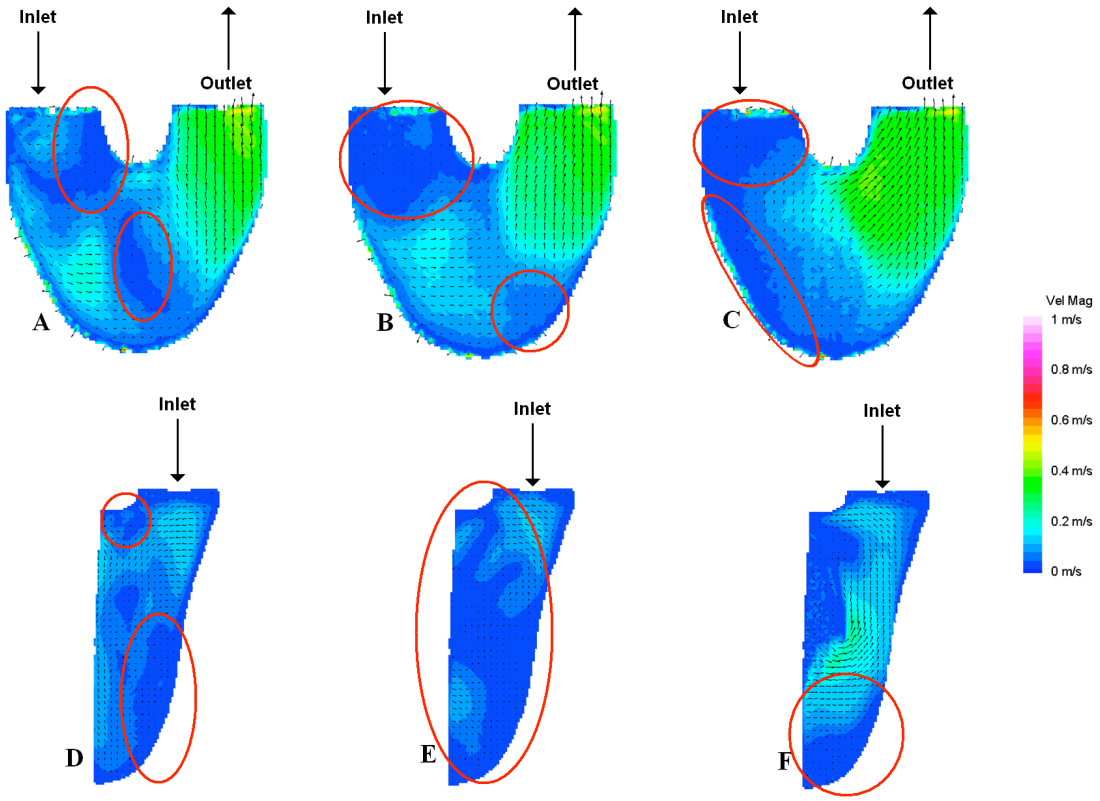

Figure 86: The (A, B, C) 8.2 mm parallel plane and (D, E, F) 11.25 mm normal inlet plane of the 12 cc slow fill condition during systole, (A, D) 550, (B, E) 650, and (C, F) 750 ms. While a smooth flow is seen through the outlet port, there are many areas of low flow and stagnation (highlighted in red), especially seen in the inlet side of the device.

The 11.25 normal outlet plane contains an area of recirculation in the outlet port during early systole. A slight area of recirculation is also seen in the 7.5 mm plane at the very end of diastole. These characteristics are both highlighted in Figure 87. None of the planes show signs of a blockage upstream of the outlet valve, which had been observed in previous experiments.

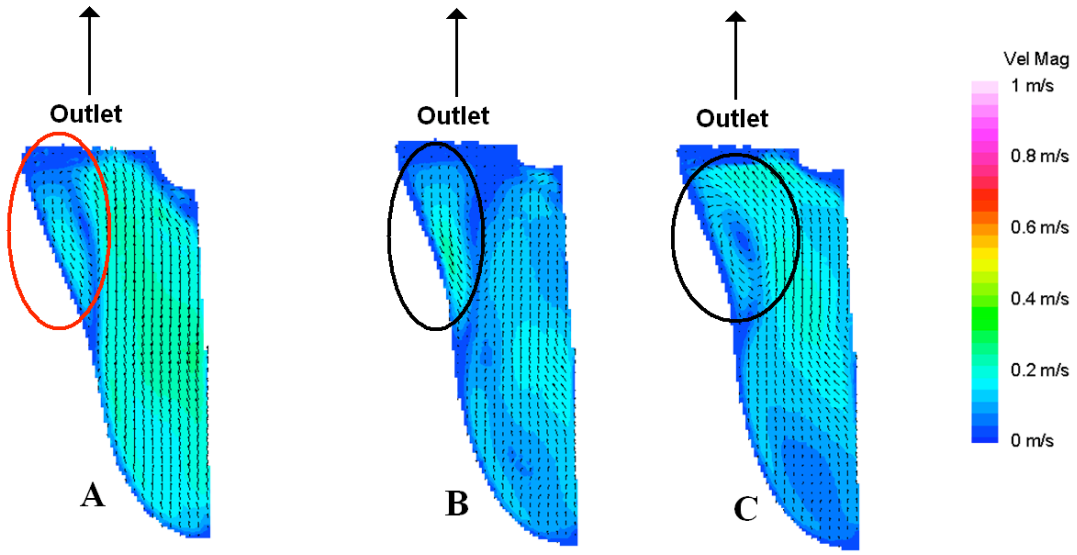

Figure 87: The (A) 7.5 mm outlet normal plane at 450 ms and the 11.25 mm outlet normal plane at (B) 450 and (C) 500 ms of the cycle at the 12 cc slow fill condition. The (A) 7.5 mm plane contains an area of recirculation at the end of diastole, circled in red. The 11.25 mm plane contains an area of regurgitation (B) that becomes an area of recirculation 50 ms later (C), both of which are highlighted in black.

5.3.2.3 9.6 cc Quick Fill

At a SV of 9.6 cc for the quick fill, a strong inlet jet is observed 50 ms into the cycle, with the highest velocities appearing at 100 ms. The maximum velocity in the jet at this time step is 1.69 m/s. While the major orifice jet is dominant along the outer inlet port wall, there is also flow through the minor orifice with maximum velocities close to 1.0 m/s. The inlet jet behavior is highlighted in Figure 88.

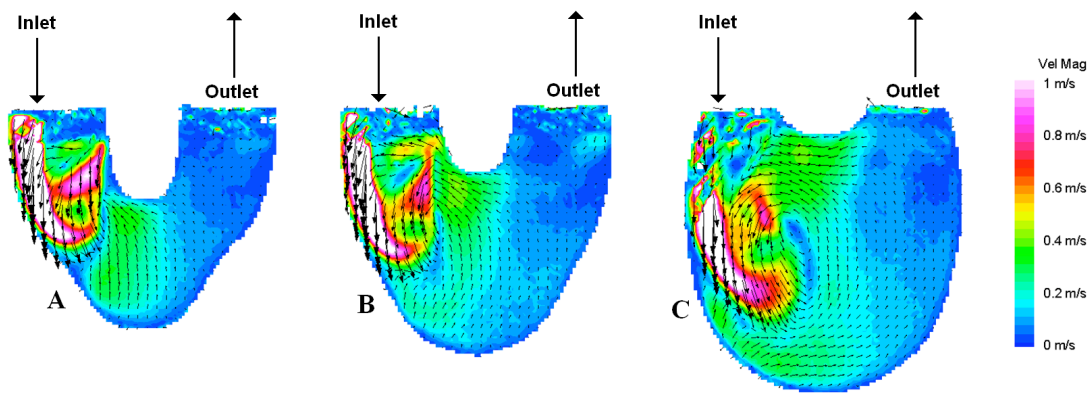

Figure 88: The (A) 7, (B) 8.2 and (C) 11 mm parallel planes of the 9.6 cc quick fill condition at 100 ms. A strong inlet jet has already formed along the outside wall of the inlet port.

The start of rotational flow is apparent at 150 ms into diastole, with movement from the bottom of the device forming a center of rotation in both the 8.2 and 11 mm parallel planes. The 7 mm plane shows a slightly different pattern as the center of rotation begins near the apex of the device and moves into the body of the plane as diastole continues. The comparison between the flow in the parallel planes is shown in Figure 89.

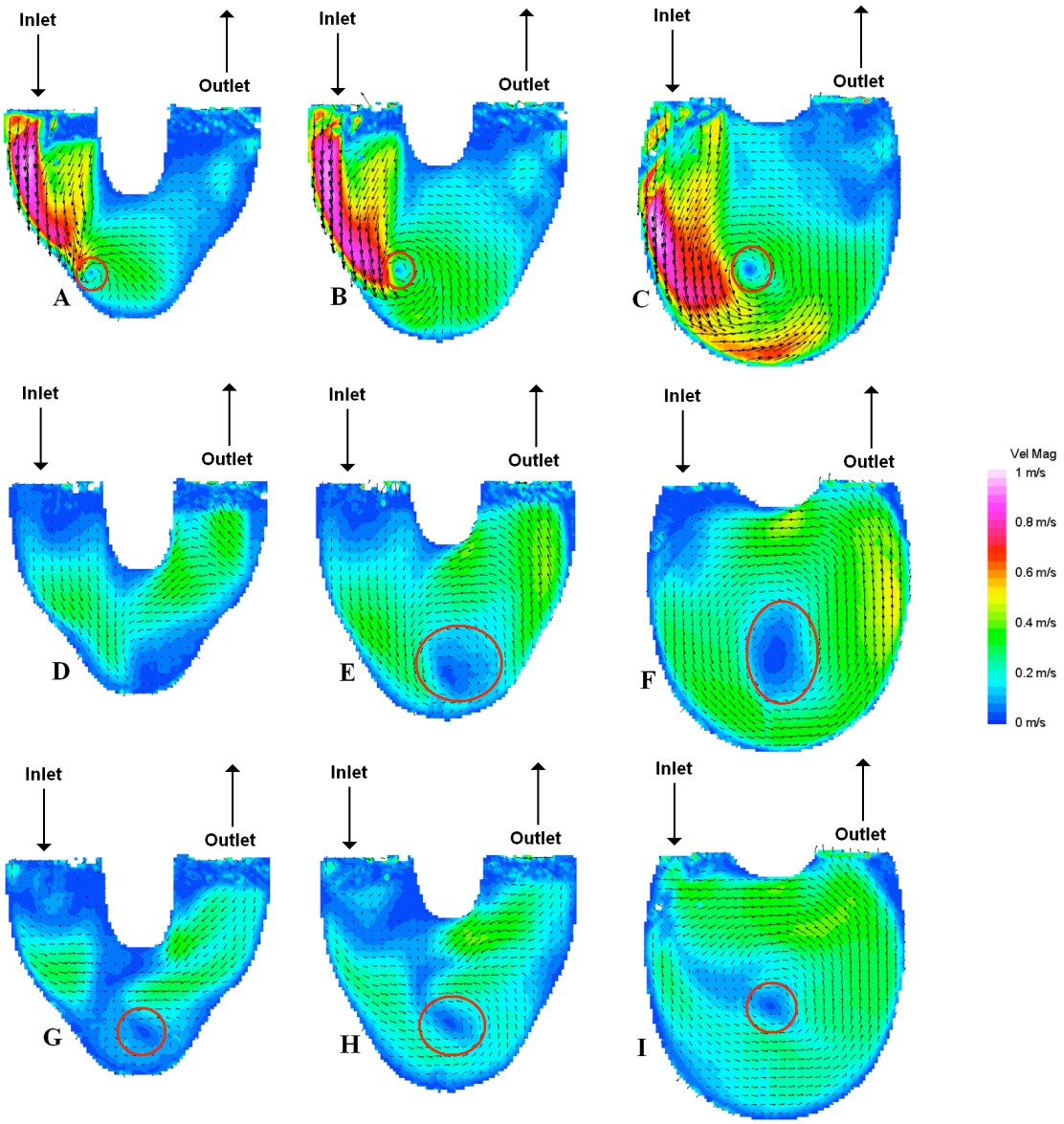

Figure 89: The (A, D, G) 7, (B, E, H) 8.2 and (C, F, I) 11 mm parallel planes of the 9.6 cc quick fill condition at (A, B, C) 150, (D, E, F) 250 and (G, H, I) 350 ms. The center of rotation, highlighted in red, can be seen at 150 ms for all three planes. At 250 ms the center shows some expansion in all three planes, but then returns to a tighter rotation 450 ms later.

As shown in Figure 89, the rotational flow pattern is maintained in the parallel planes throughout diastole. There is, however, a reduction in the velocity magnitudes to around 0.5 m/s.

The inlet port normal planes show a consistent behavior of the inlet jet and rotational flow field. Again, flow penetration into the bottom of the device is seen at 150 ms. There is also decrease in magnitude in the flow velocity around mid-diastole, which is most noticeable in the 11.25 mm inlet plane, located farthest from the inlet jet. This is shown in Figure 90.

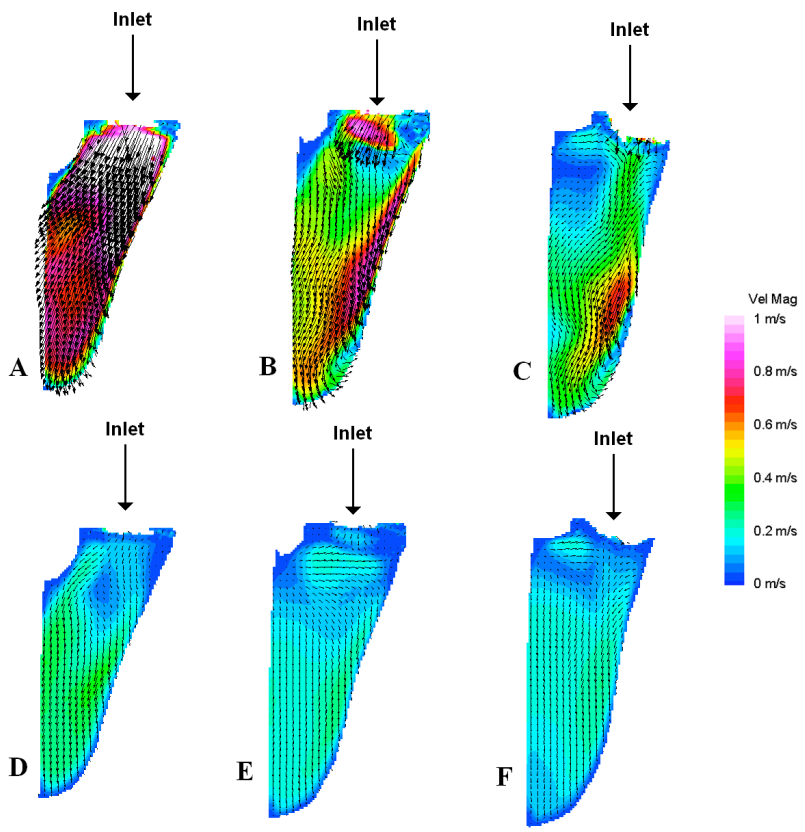

Figure 90: The (A, D) 3.75, (B, E) 7.5 and (C, F) 11.25 mm inlet normal planes of the 9.6 cc quick fill condition at (A, B, C) 150 and (D, E, F) 250 ms. The planes show penetration to the bottom of the device at 150 ms, but 100 ms a loss of velocity magnitude can be seen.

The outlet normal planes at 150 ms into the cycle show flow moving in the body of the device, indicating rotational flow has begun. The greatest magnitudes are in the 3.75 mm normal outlet plane, indicating that the rotation is setting up along the outside wall. This is shown in Figure 91.

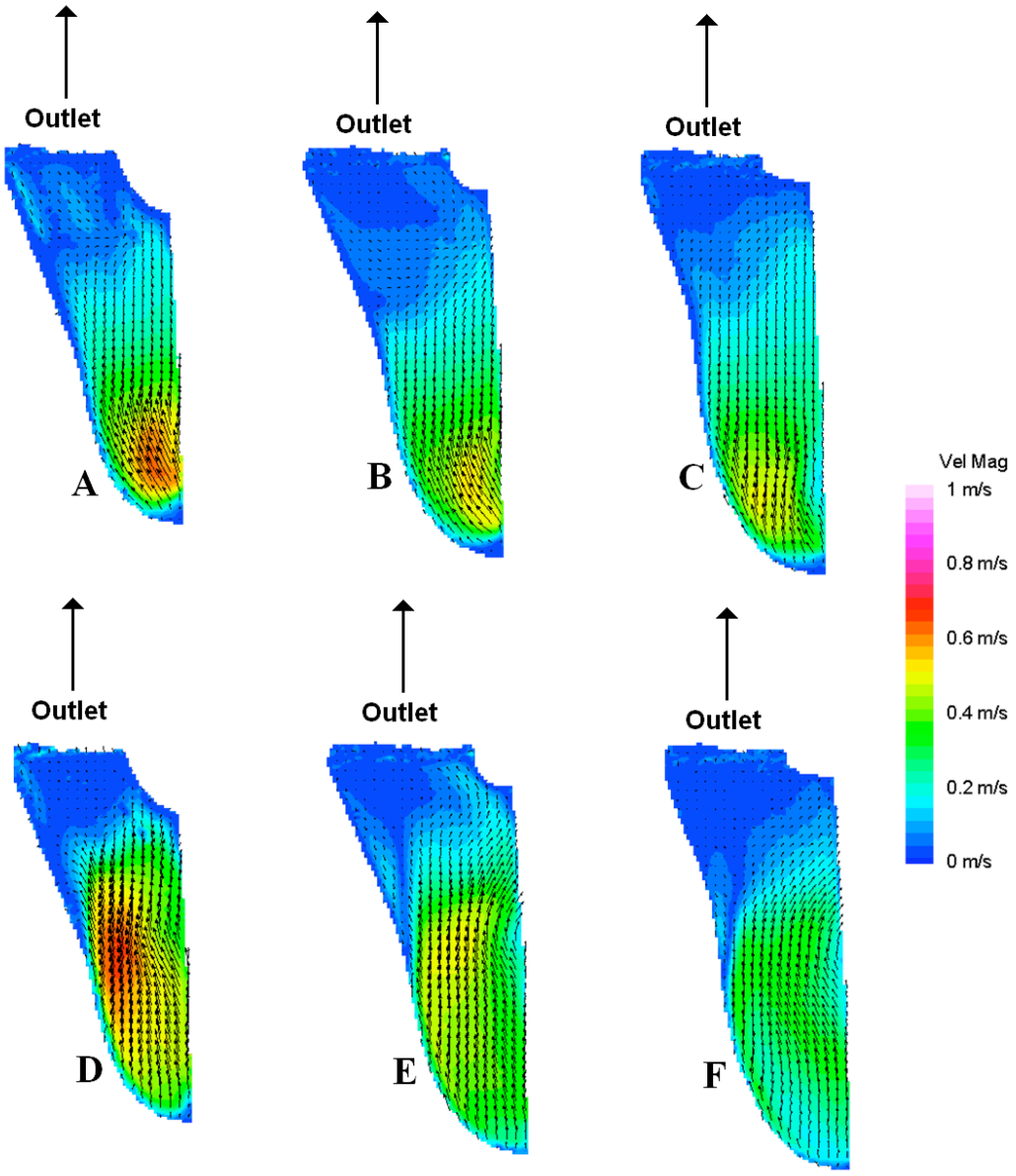

Figure 91: The (A, D) 3.75, (B, E) 7.5 and (C, F) 11.25 mm outlet normal planes of the 9.6 cc quick fill condition at (A, B, C) 150 and (D, E, F) 200 ms. The increased velocity magnitudes of the vectors in the body of the device towards the outlet port indicate that the flow from the outside wall of the device has rotated up to the outlet side, a sign of rotational flow. The largest velocities are observed in the (A, D) 3.75 mm inlet normal plane, meaning the strongest portion of the flow remains along the outer wall of the device.

As diastole progresses areas of recirculation in the outlet port are observed in the 7.5 and 11.25 mm normal outlet planes. As shown in Figure 92, these areas begin in mid-diastole and continue until the beginning of systole. The 3.75 mm plane does not contain an area of recirculation, but does contain regurgitation in the port area during the same time period.

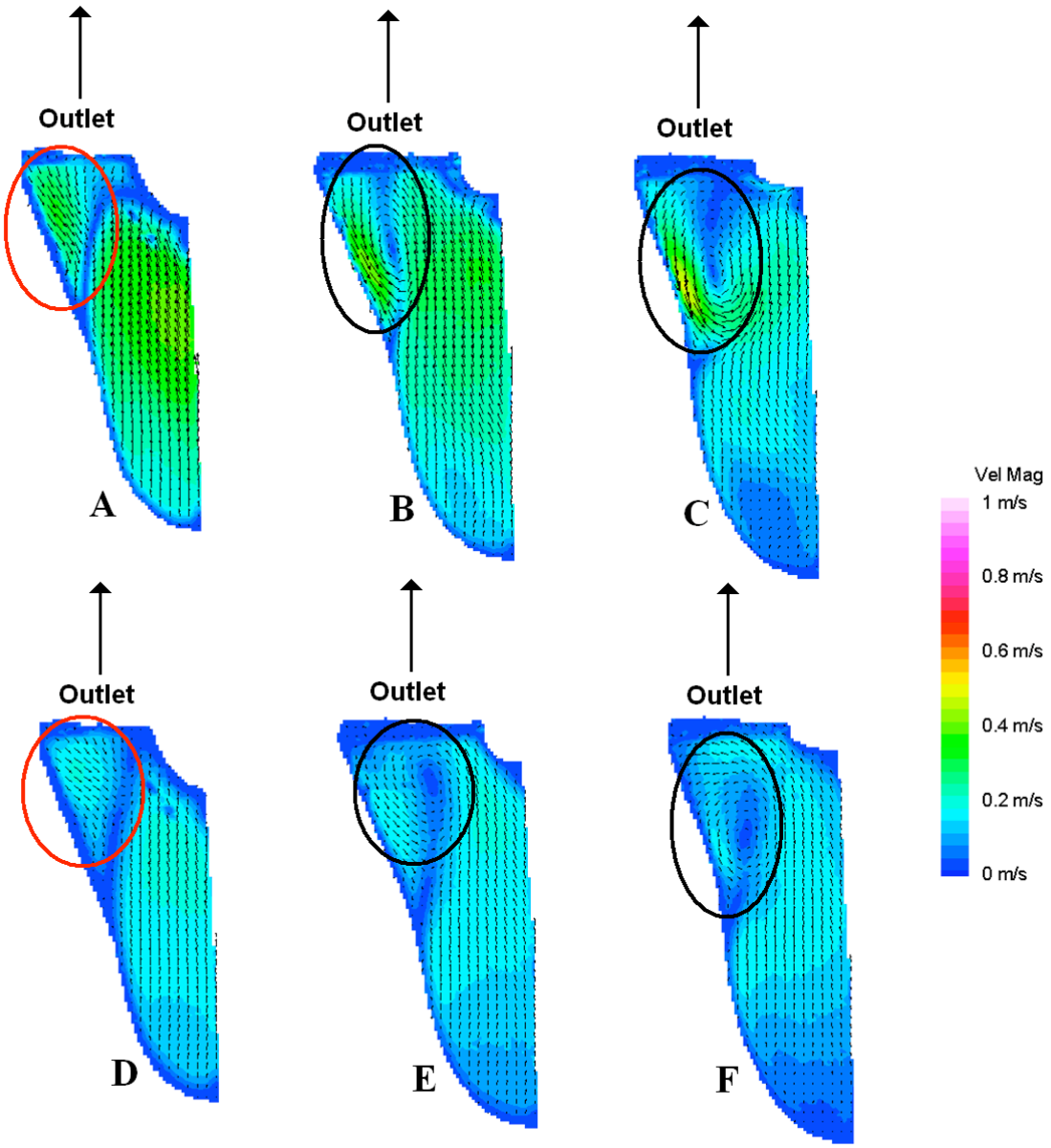

Figure 92: The (A, D) 3.75, (B, E) 7.5 and (C, F) 11.25 mm outlet normal planes of the 9.6 cc quick fill condition at (A, B, C) 300 and (D, E, F) 400 ms. An area of regurgitation can be seen in the 3.75 mm plane, highlighted in red, and areas of recirculation are observed in the 7.5 and 11.25 mm planes, highlighted in black.

As the flows transitions into systole there are areas of near stagnation with flow velocities < 0.1 m/s, most noticeably in the inlet port and along the bottom of the device. These areas are most prevalent in the 7 mm parallel plane and the 11.25 mm inlet normal plane as shown in Figure 93. Aside from these areas of stagnation, the flow transitions smoothly as it is ejected from the pump. The area of blockage previously seen upstream of the outlet valve does not appear.

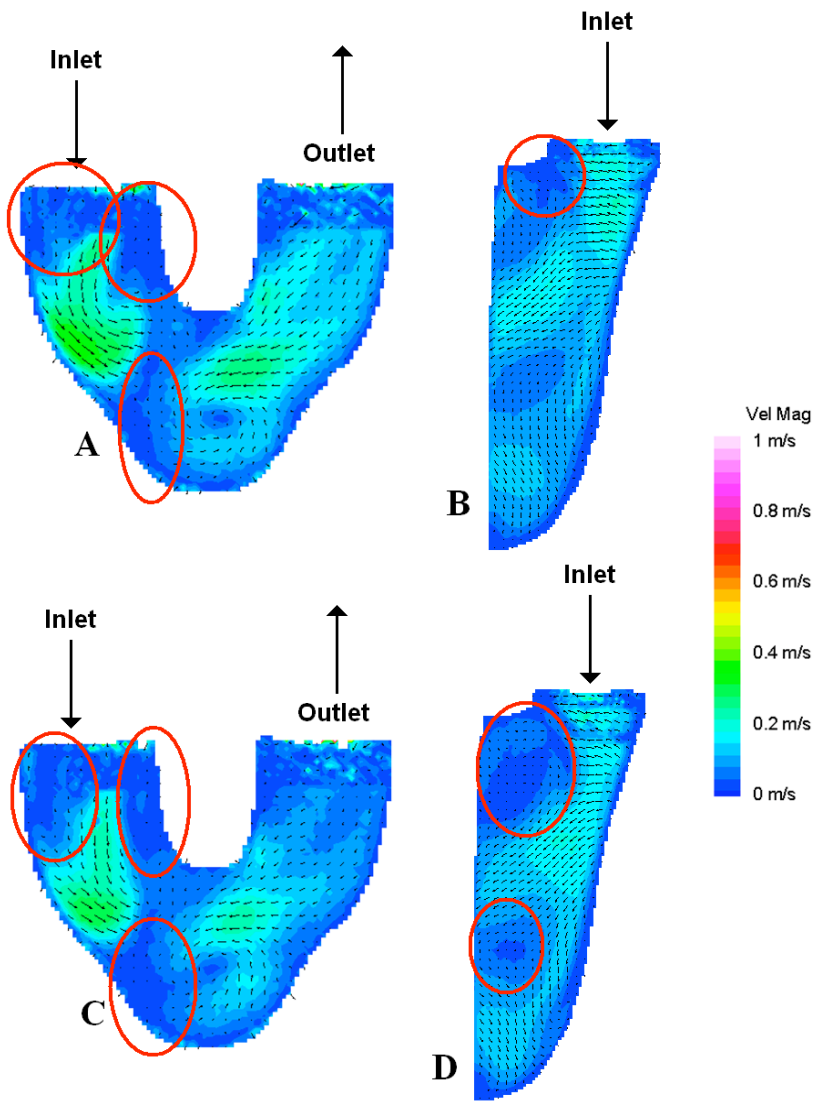

Figure 93: The (A, C) 7 mm parallel and (B, D) 11.25 mm normal inlet planes of the 9.6 quick fill condition at (A, B) 400 and (C, D) 450 ms. During late diastole the flow begins to contain many areas of stagnation, which are shown in dark blue and highlighted in red.

5.3.2.4 9.6 cc Slow Fill

During the slow filling of the 9.6 cc SV, the inlet jet formation can be seen starting at 100 ms into diastole. The jet continues to strengthen as diastole continues, reaching its maximum velocity of 0.73 m/s at 250 ms into the cycle. The minor orifice jet shows a similar development, with comparable velocities to that of the major orifice jet. This behavior is shown in Figure 94.

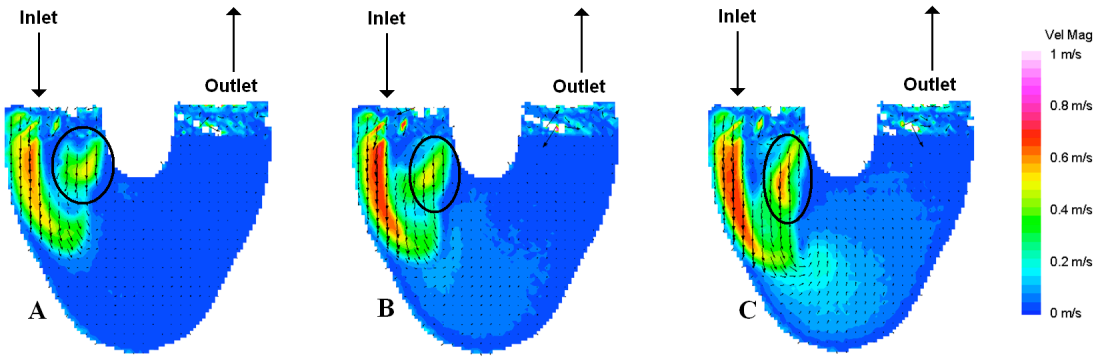

Figure 94: The 8.2 mm parallel plane of the 9.6 cc slow fill condition at (A) 150, (B) 200 and (C) 250 ms. The major orifice jet can be observed strengthening along the outer wall of the inlet port as it moves towards the device bottom. A minor orifice jet, highlighted in black, also appears and strengthens to similar velocities as the major orifice jet.

The penetration of flow to the bottom of the device and rotational flow set up does not begin until after mid diastole, where it is first observed in the 11 mm plane at 300 ms. While the penetration occurs in the 8.2 mm plane 50 ms later, the penetration and rotational flow field in the 7 mm plane never fully develops as shown in Figure 95.

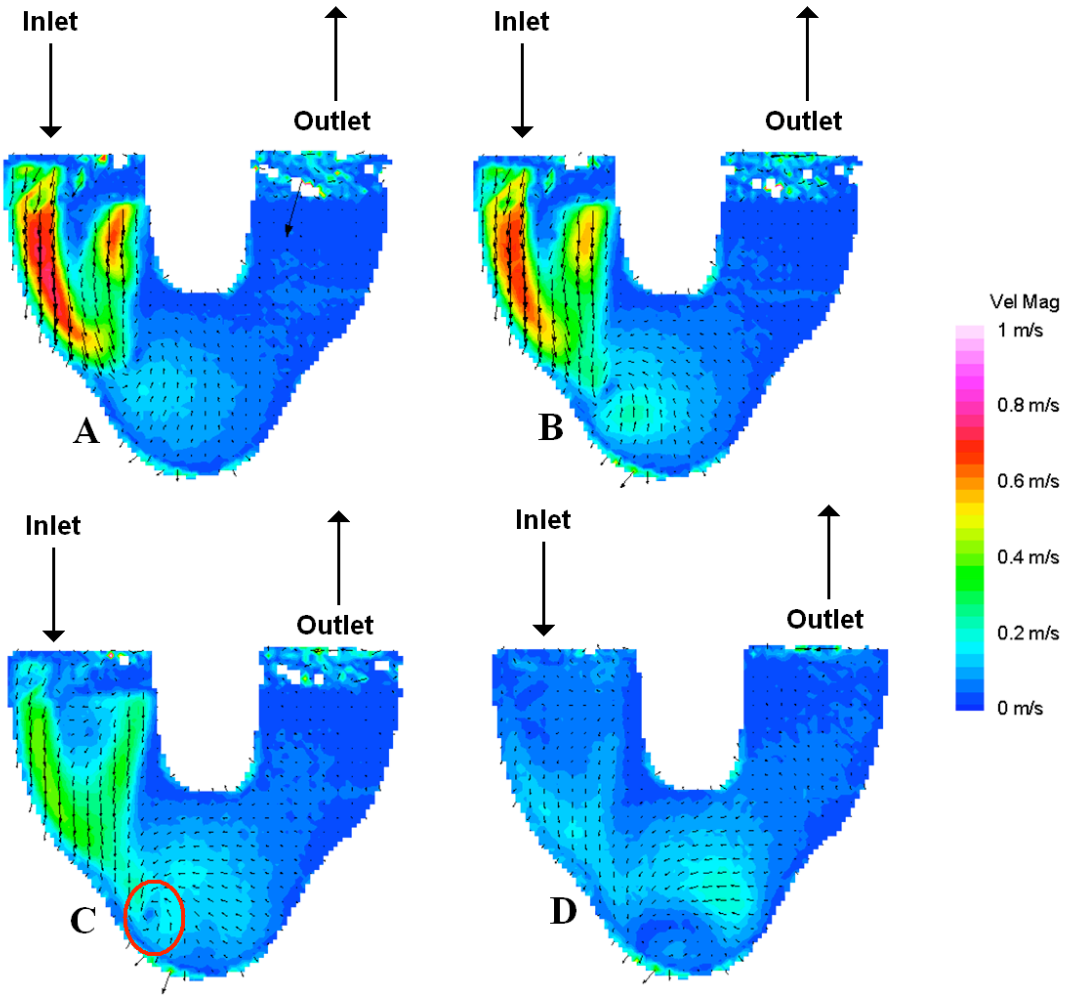

Figure 95: The 7 mm parallel plane of the 9.6 cc slow fill condition at (A) 250, (B) 300, (C) 350 and (D) 400 ms. While the flow field shows a small center of rotation at (C) 350 ms (circled in red) a rotational flow field never truly develops, and 50 ms later (D) the flow becomes very low.

The inlet normal planes also show penetration around 250 ms into diastole. The 7.5 and 11.25 mm inlet normal planes also contain areas of recirculation near the bottom of the device. These occur during mid diastole prior to the start of the uniform rotational flow. Figure 96 highlights this behavior in these planes.

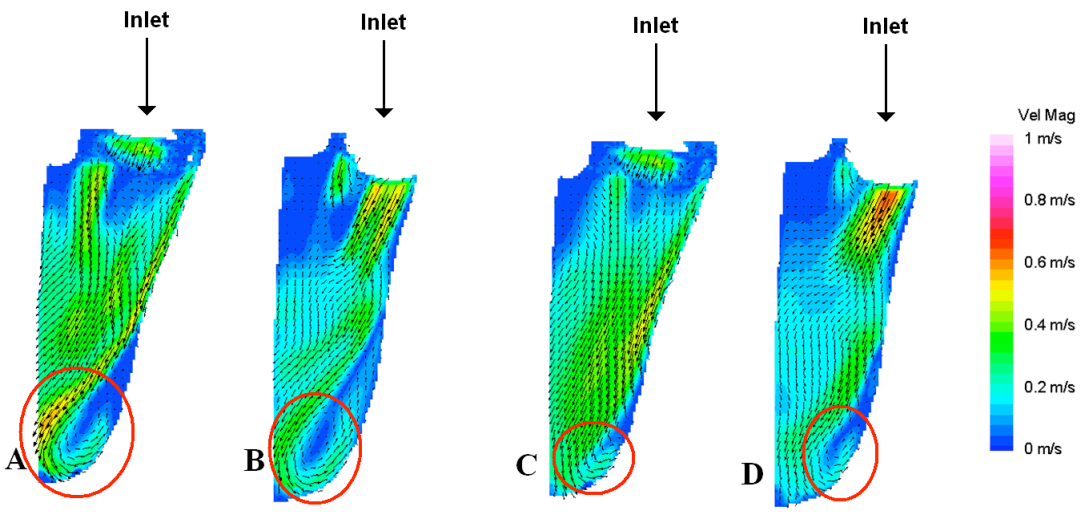

Figure 96: The (A, C) 7.5 and (B, D) 11.25 mm inlet normal planes of the 9.6 cc slow fill condition at (A, B) 250 and (C, D) 300 ms. Areas of recirculation are seen at the bottom of both planes, as highlighted in red.

The start of rotational flow at mid diastole is also seen in the normal outlet planes. In all three planes, there is flow in the body of the device observed at 300 ms, with magnitudes around 0.4 ms. There is no area of recirculation seen in the outlet port during diastole.

As just mentioned, a rotational flow field is never fully developed in the 7 mm parallel plane, and correspondingly, the rotational flow field seen in the 8.2 and 11 mm planes dissipates quickly. The center of rotation expands in size during late diastole and the flow magnitudes reduce to a maximum of 0.3 m/s before the transition to systole. This loss of rotational flow is shown in Figure 97.

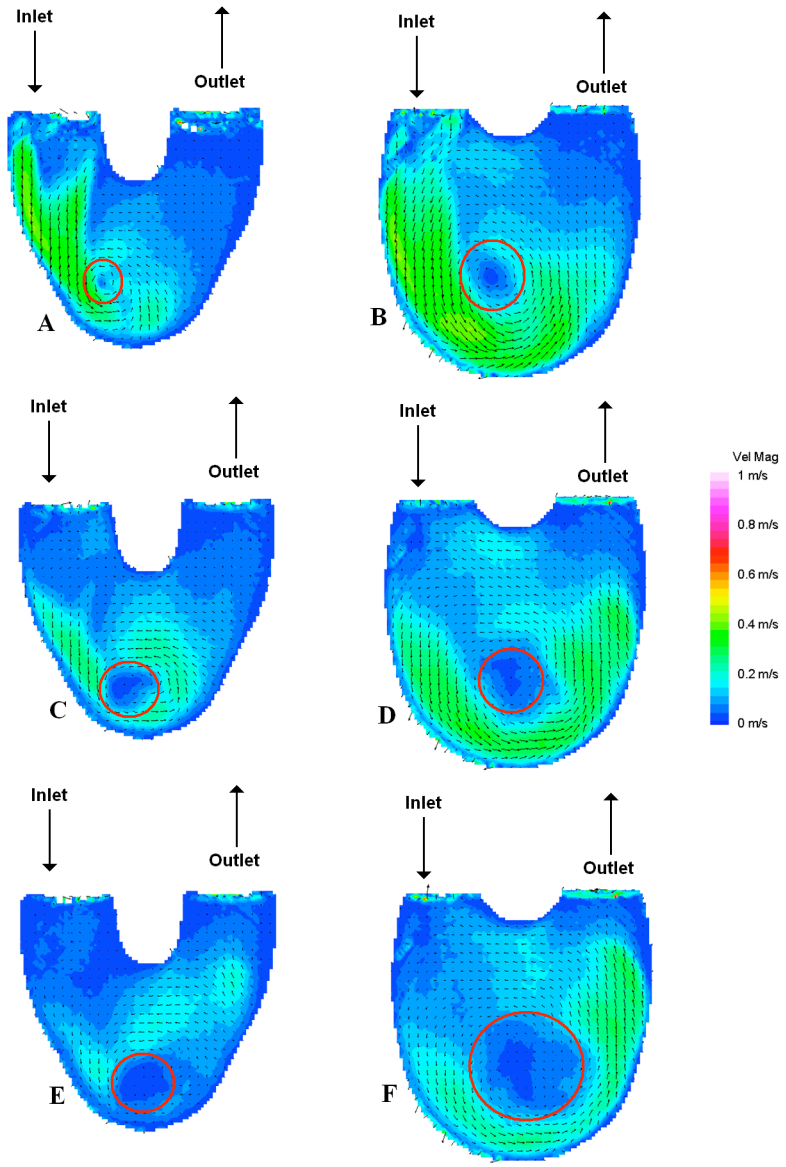

Figure 97: The (A, C, E) 8.2 and (B, D, F) 11 mm parallel planes of the 9.6 cc slow filling condition at (A, B) 350, (C, D) 400 and (E, F) 450 ms. A rotational flow field can be observed in the planes, however the center of rotation (circled in red) shows expansion as diastole progresses. This expansion, combined with the lower velocity magnitudes, indicates a loose rotational flow.

The loss of the rotational flow during diastole leads to more areas of stagnation observed in both the parallel and inlet planes during mid to late diastole and in the transition to systole. Some examples of this in both the parallel and inlet normal planes during late diastole are shown in Figure 98.

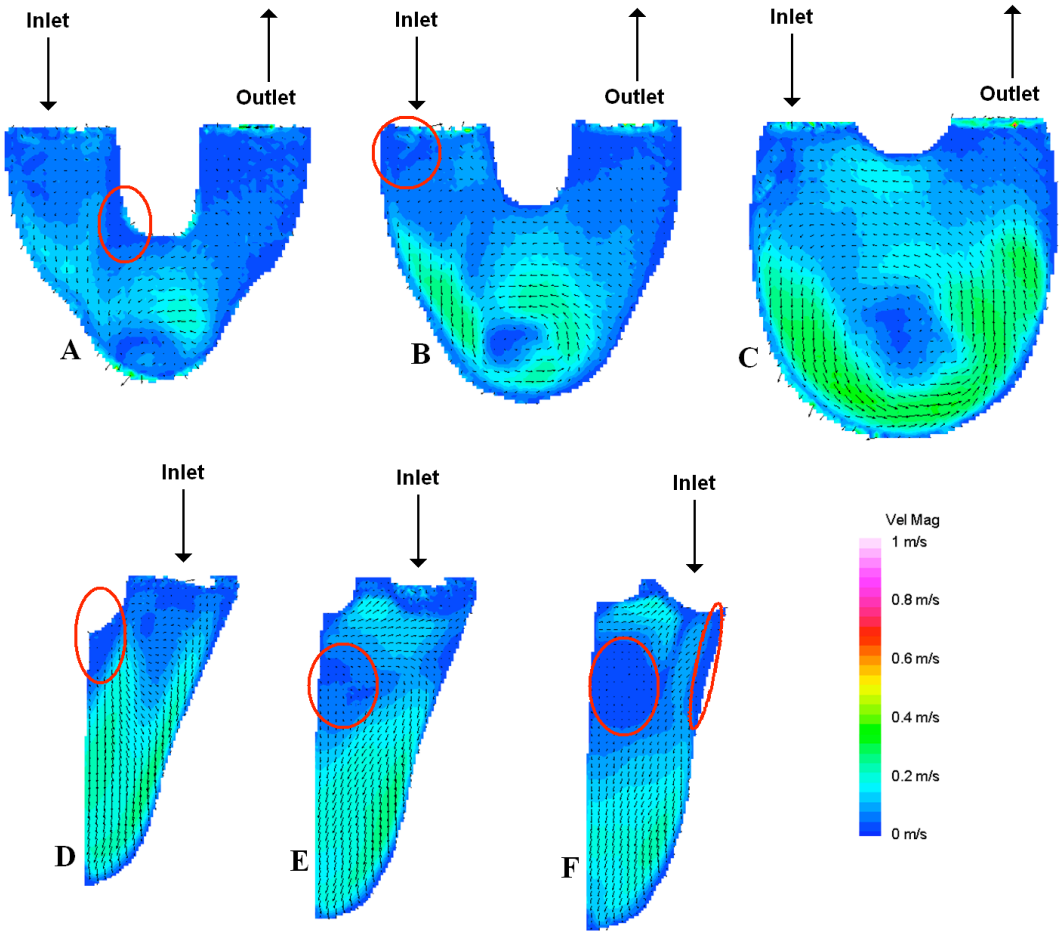

Figure 98: The (A) 7, (B) 8.2 and (C) 11 mm parallel planes and the (D) 3.75, (E) 7.5 and (F) 11.25 mm inlet normal planes of the 9.6 cc slow fill condition at 400 ms. At this point late in diastole there are many areas of low flow and stagnation (highlighted in red), most notably in the inlet side of the device.

As the flow transitions into systole, there are no areas of blockage, but the only fluid movement seen is associated with the outflow. The inlet side of the device remains stagnant in all parallel planes and in the inlet normal planes for half of the systolic time, as observed in Figure 99.

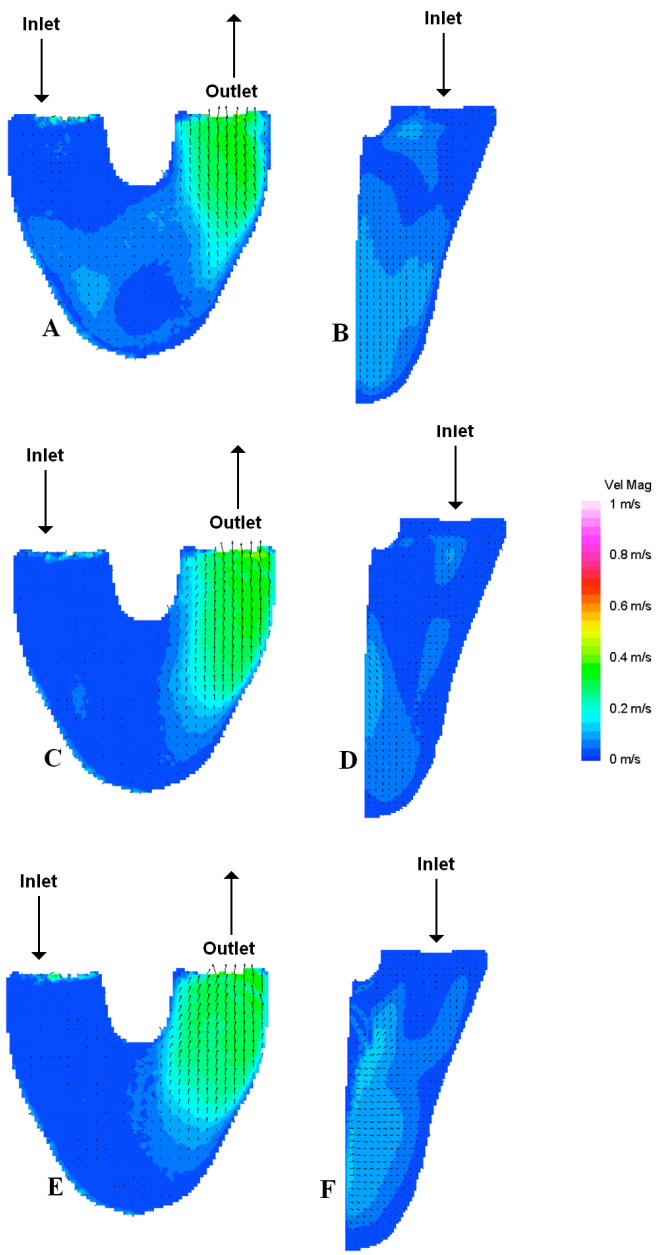

Figure 99: The (A, C, E) 8.2 mm parallel plane and (C, D, F) 7.5 mm inlet normal plane of the 9.6 cc slow fill condition at (A, B) 500, (C, D) 600 and (E, F) 700 ms. The systolic flow of the device is concentrated in the outlet port of the device. This leaves the inlet side and body of the device with many areas of stagnation, shown here in dark blue.

5.3.2.5 7.2 cc Quick Fill

The inlet jet of the 7.2 cc quick fill condition appears at 50 ms into diastole, reaching its highest velocity magnitude of 1.7 m/s at 100 ms. The start of the rotational flow field is also observed at 150 ms in all three parallel planes. A distinct center of rotation is apparent at 100 ms in the 11 mm planes, and 50 ms later in the 7 and 8.2 mm planes. The jet is concentrated along the outside of the inlet wall, consistent with the opening of the major orifice of the valve. A jet from the minor orifice can be observed in the 7 and 8.2 mm planes at 50 and 100 ms. The inlet jet behavior in the parallel planes is presented in Figure 100.

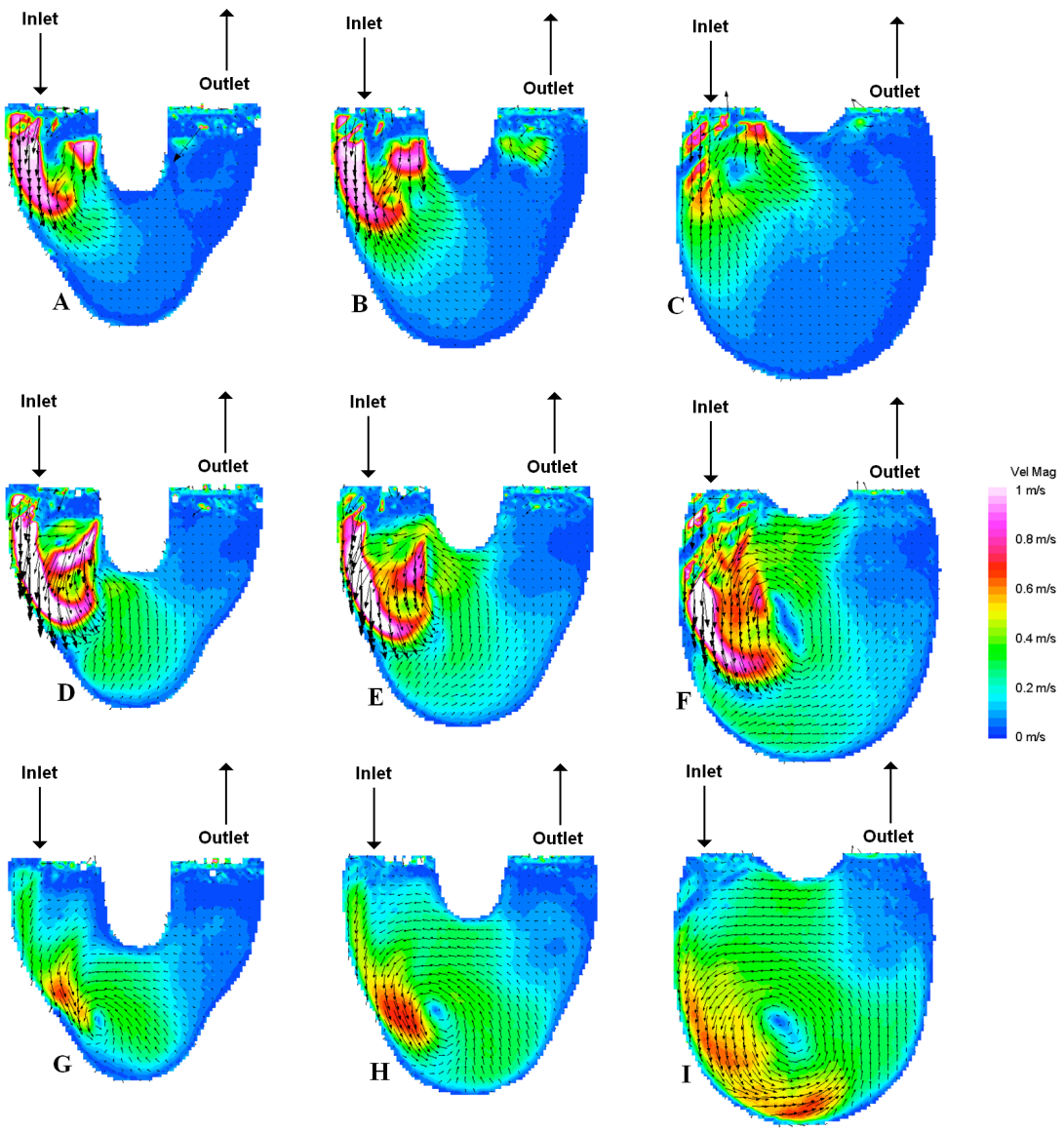

Figure 100: The (A, D, G) 7, (B, E, H) 8.2 and (C, F, I) 11 mm parallel planes of the 7.2 cc quick filling condition at (A, B, C) 50, (D, E, F) 100 and (G, H, I) 150 ms. A strong inlet jet is observed early in diastole and reaches its maximum at 100 ms. This develops into rotational flow 50 ms later where centers of rotation are observed in all three parallel planes.

The 3.75 and 7.5 mm normal inlet planes show the early development and penetration of the inlet jet to the device bottom at 150 ms into diastole. At this same time point the 11.25 mm plane contains an area of recirculation at the device bottom. Figure 101 shows the flow behavior in all three planes.

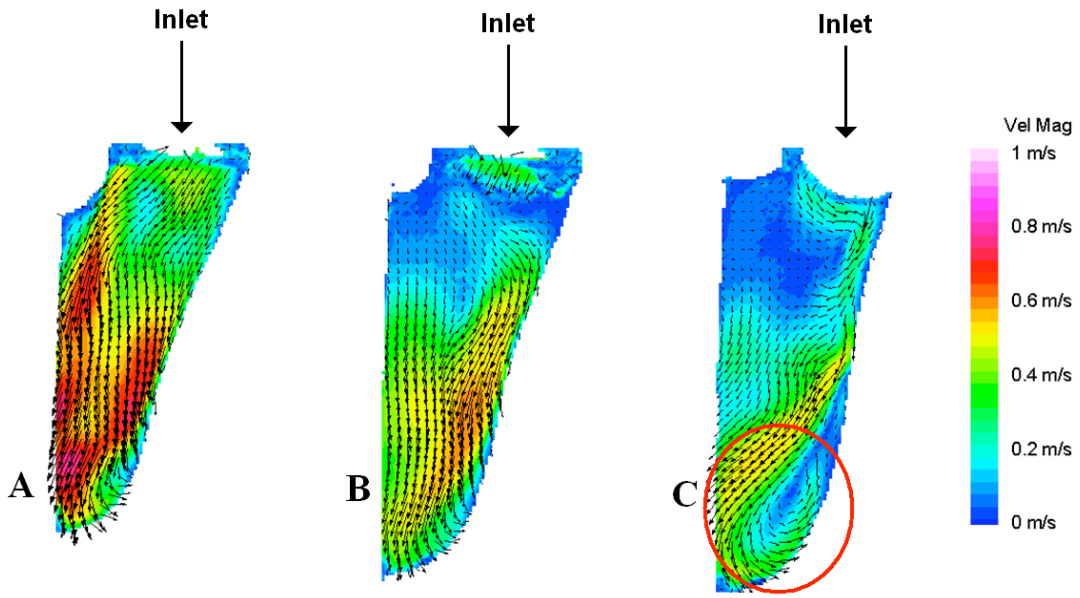

Figure 101: The (A) 3.75, (B) 7.5 and (C) 11.25 mm inlet normal planes of the 7.2 cc quick filling condition at 150 ms. At this point diastole the flow has reached the bottom of the device, as observed in A and B. An area of recirculation, highlighted in red, appears at the bottom C.

The increased velocity in the body of the device near the outlet further confirms the start of the rotational flow at 150 ms into diastole. Similar to flow at previous quick fill conditions, the outlet normal planes at 7.2 cc also contain areas of recirculation during diastole. The 7.5 and 11.25 mm planes contain areas of recirculation in the outlet port during mid to late diastole, while the 3.75 mm plane contains an area of regurgitation during the same time period. These are highlighted in Figure 102.

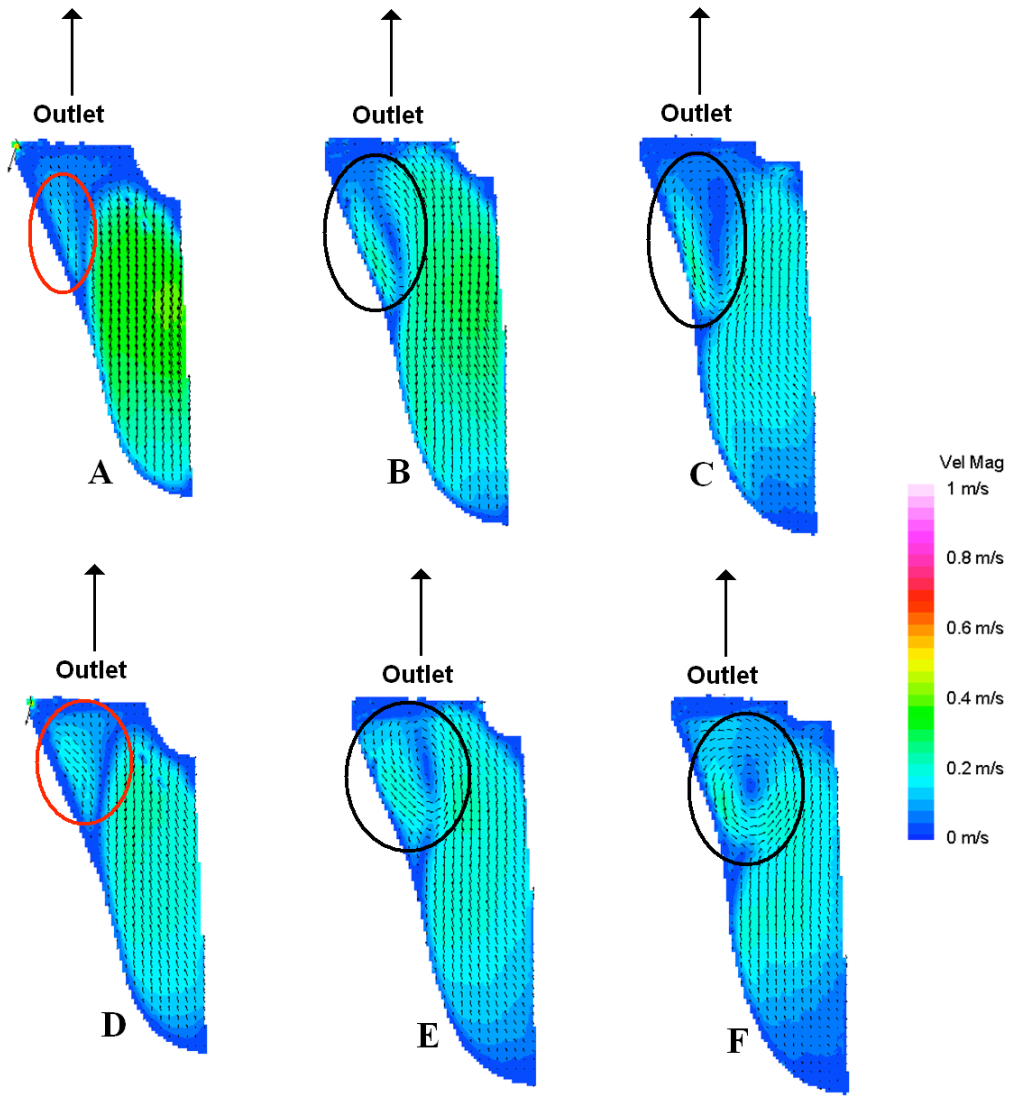

Figure 102: The (A, D) 3.75, (B, E) 7.5 and (C, F) 11.25 mm outlet normal planes of the 7.2 cc quick filling condition at (A, B, C) 300 and (D, E, F) 400 ms. An area of regurgitation is seen in the 3.75 mm plane (A, D), and is highlighted in red. The 11.25 and 7.5 mm planes (B, C, E, F) contain areas of recirculation, which are highlighted in black.

As the flow moves through diastole, the center of rotation and the general rotational flow pattern is maintained in all three parallel planes. However, the flow is less cohesive than what was observed at the high cardiac output conditions. This is most noticeable in the 7 and 8.2 mm planes, where areas of stagnation are present during late diastole, as shown in Figure 103.

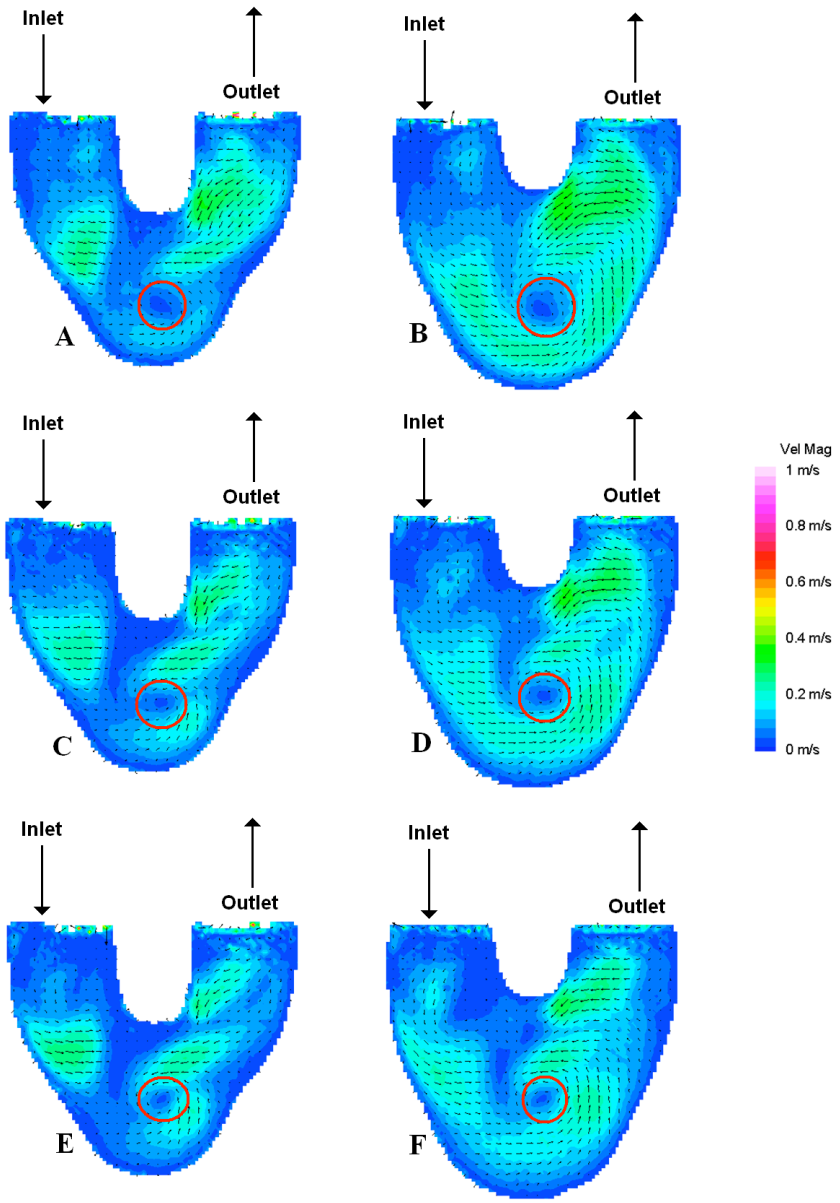

Figure 103: The (A, C, E) 7 and (B, D, F) 8.2 mm parallel planes of the 7.2 cc quick filling condition at (A, B) 350, (C, D) 400 and (E, F) 450 ms. While the planes maintain centers of rotation, circled in red, there is a "patchy" appearance to the flow with non-uniform areas of higher (> 0.3 m/s) flow, indicated by the green color on the legend.

The inlet normal planes also show a less cohesive flow and increase in areas of stagnation during mid diastole as the flow is reduced in the inlet port, which is shown in Figure 104.

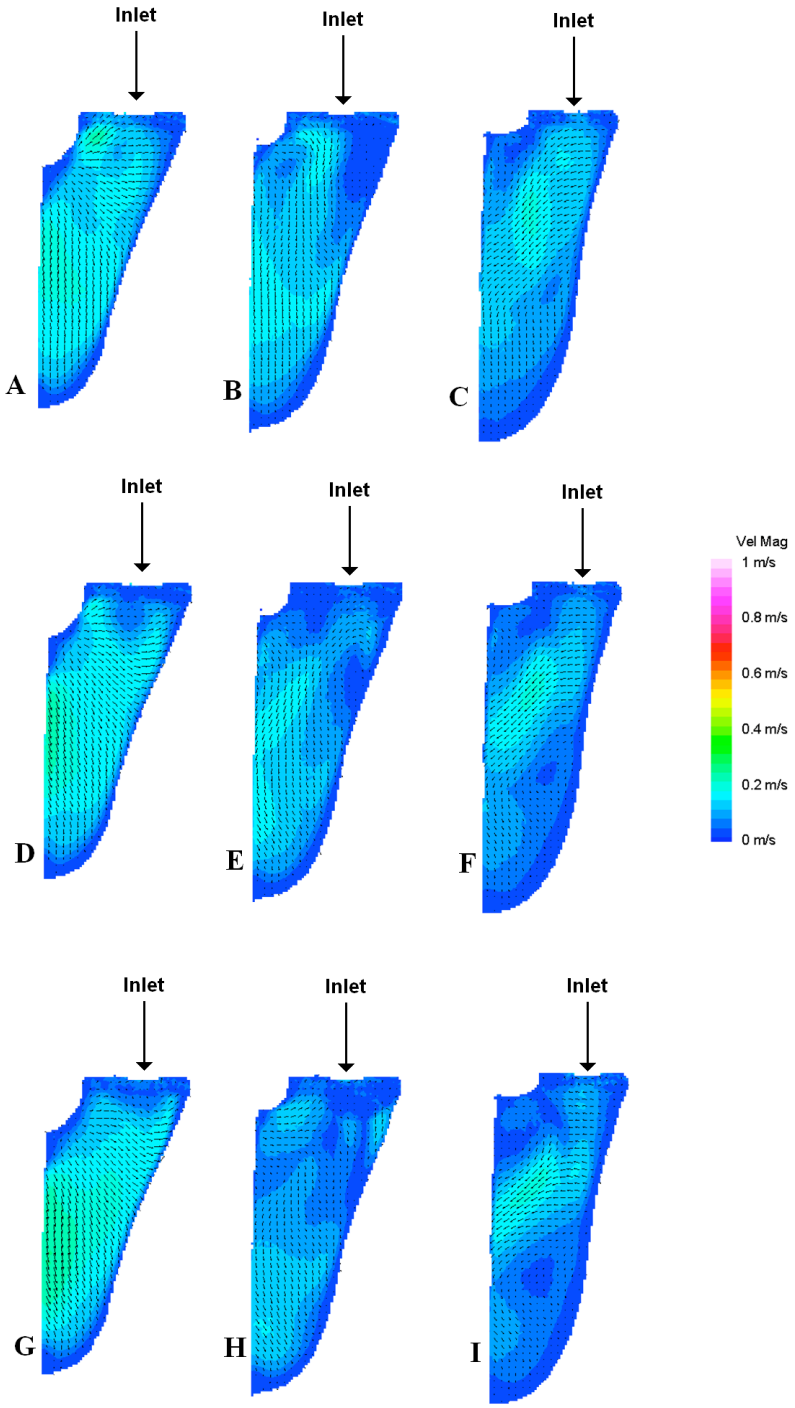

Figure 104: The (A, D, G) 3.75, (B, E, H) 7.5 and (C, F, I) 11.25 mm normal inlet planes of the 7.2 quick filling condition at (A, B, C) 350, (D, E, F) 400 and (G, H, I) 450 ms. During mid to late diastole, the inlet port contains reduced flows, all below 0.25 m/s.

This reduction in velocity magnitude continues as the flow transitions to systole. The flow moves towards the outlet port without areas of blockage, however there are many areas of stagnation and low flow throughout the parallel planes and normal inlet planes, as presented in Figure 105.

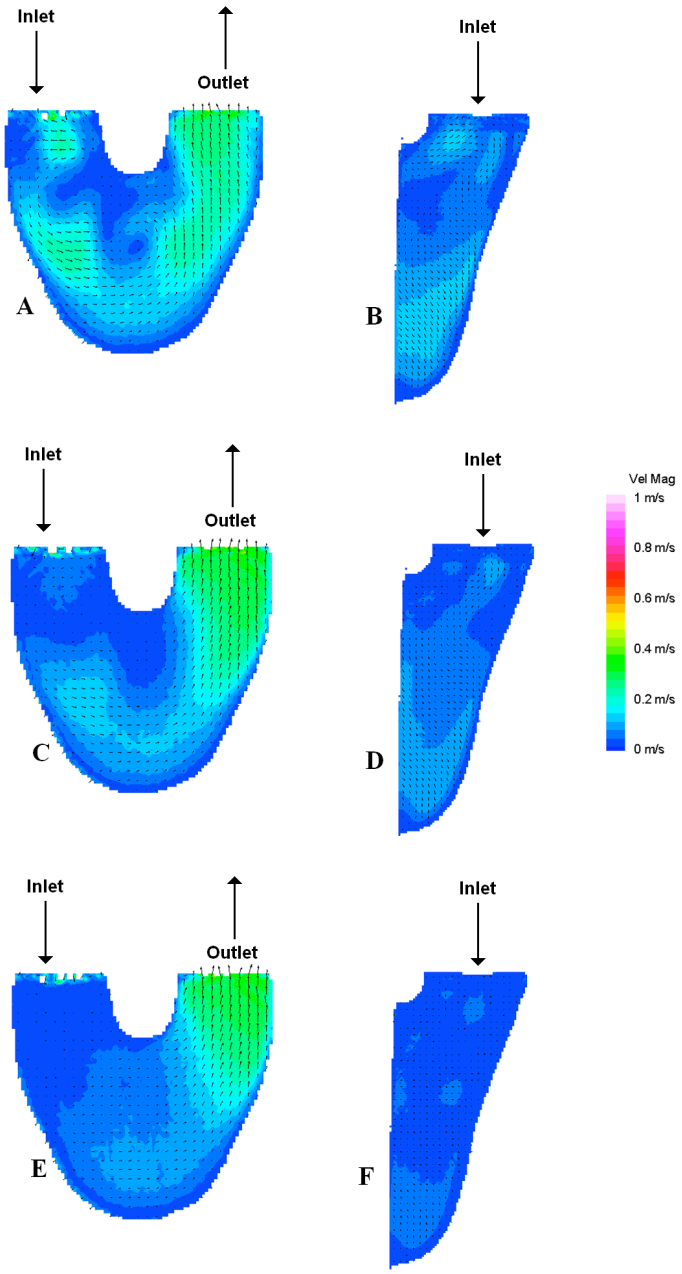

Figure 105: The (A, C, E) 8.2 mm parallel and plane and (B, D, F) 7.5 mm inlet normal plane of the 7.2 quick filling condition at (A, B) 550, (C, D) 650 and (E, F) 750 ms. As the systolic flow moves though the outlet valve the flow in the inlet side of the pump remains quite stagnant, as observed by the dark blue areas of the above planes.

5.3.2.6 7.2 cc Slow Fill

In general, at a SV of 7.2 cc with a slow fill, the flow field is nearly stagnant. A maximum velocity of 0.59 m/s is observed within the inlet jet at 250 ms into diastole. While a similar pattern is observed in the development of the inlet jet at higher SVs, a true rotational flow pattern is not observed in the parallel planes. This is most evident in the 7 mm plane, where the flow in the body of the device remains below 0.1 m/s throughout the cycle with the exception of the inlet jet flow and of the outflow during systole, as highlighted in Figure 106.

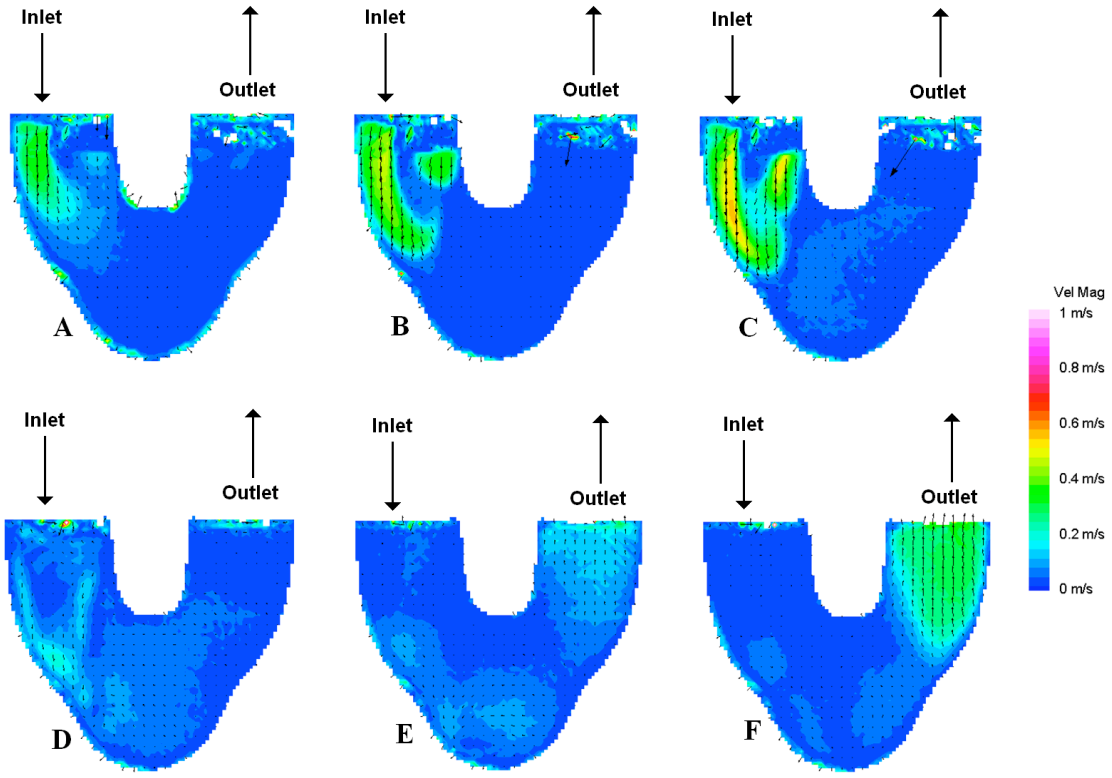

Figure 106: The 7 mm parallel plane of the 7.2 cc slow filling condition at (A) 100, (B) 200, (C) 300, (D) 400, (E) 500 and (F) 600 ms. The inlet jet forms through early and mid diastole (A, B, C), however this does not result in a rotational flow field being established during mid to late diastole (D and E). The flow remains stagnant (indicated by dark blue) in the body of the device. Besides the inlet jet, the only velocity vectors about 0.1 m/s are seen as the fluid leaves the device during systole (F).

During early and mid diastole, the 8.2 and 11 mm parallel planes show similar behavior to that of the 7 mm plane, with the only fluid movement coming from the inlet jet development. However, in contrast to the 7 mm plane, these planes do show some fluid movement in the bottom of the device during late diastole, as shown in Figure 107.

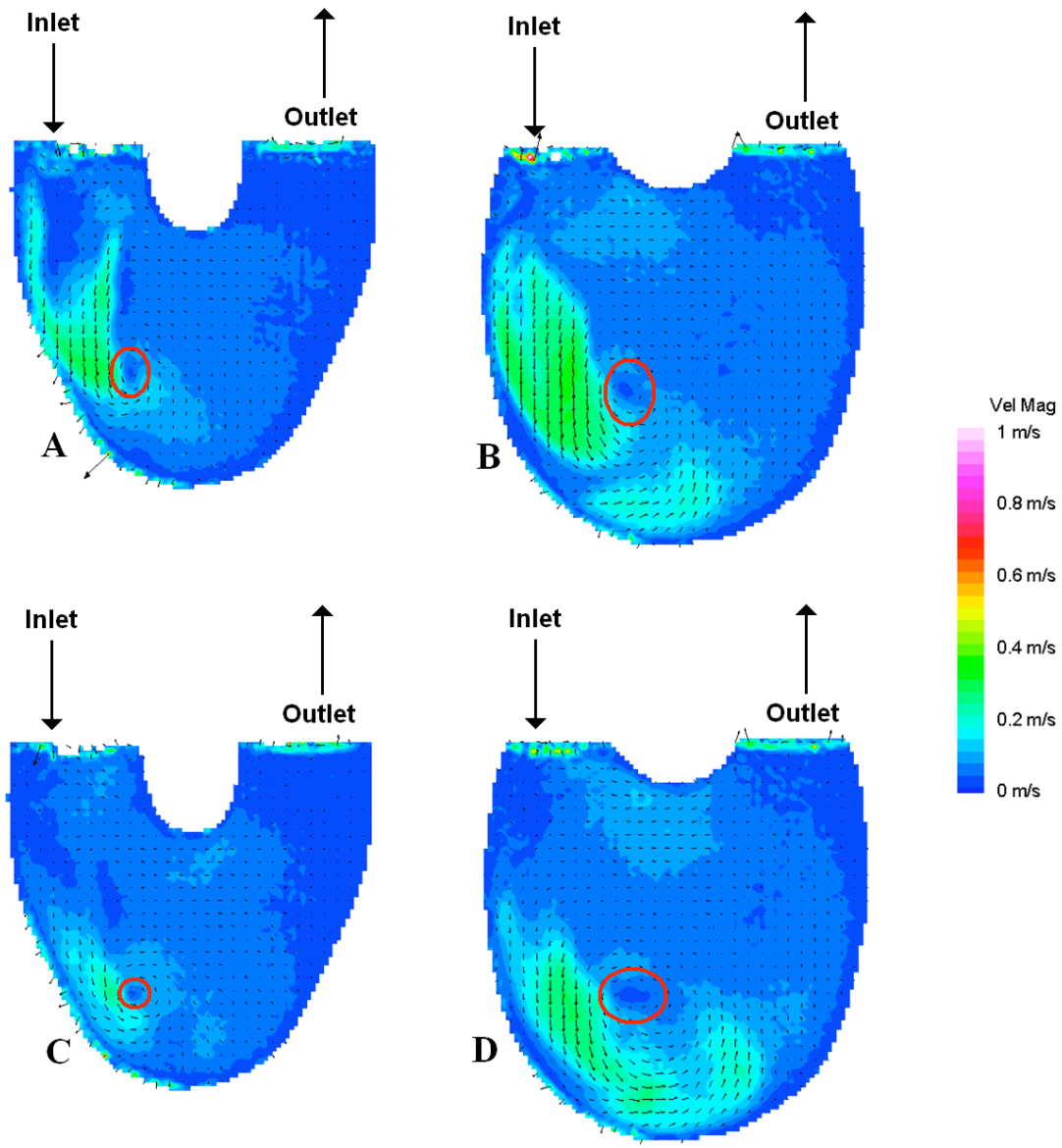

Figure 107: The (A, C) 8.2 and (B, D) 11 mm parallel planes of the 7.2 cc slow filling condition at (A, B) 400 and (C, D) 450 ms. These planes contain faint centers of rotation, which are highlighted in red, and appear to have some penetration to the bottom of the device. In general the flow remains low and a rotational flow field is never fully developed.

The normal inlet planes confirm the inlet jet behavior seen in the parallel planes. The 3.75 mm plane, closest to the outside wall, shows a slow development of the inlet jet through diastole. An area of stagnation remains at the bottom of the plane until 400 ms into the cycle. This development is shown in Figure 108.

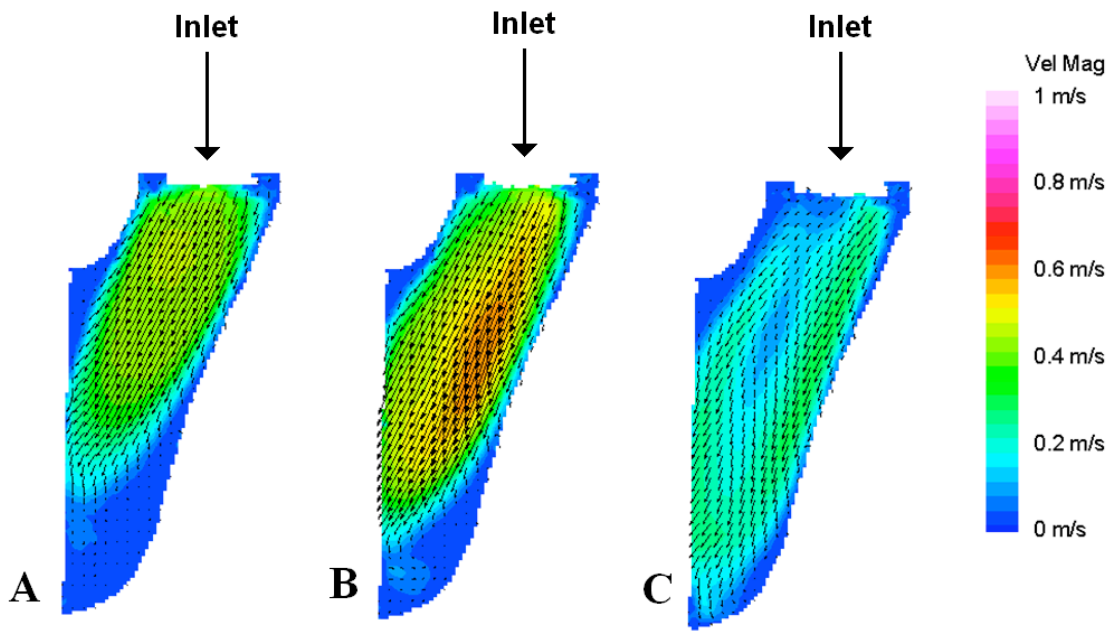

Figure 108: The 3.75 mm inlet normal plane of the 7.2 cc slow filling condition at (A) 200, (B) 300 and (C) 400 ms. The planes show a slow development of the inlet jet, which results in a penetration to the bottom of the device at late diastole.

In comparison the 7.5 and 11.25 mm inlet normal planes show flow penetration to the device bottom at 300 ms into diastole when areas of recirculation develop. Besides the inlet jet development and these recirculation areas, the 7.5 and 11.25 mm inlet normal planes show little flow throughout diastole, particularly around the inlet port of the device. These characteristics are shown in Figure 109.

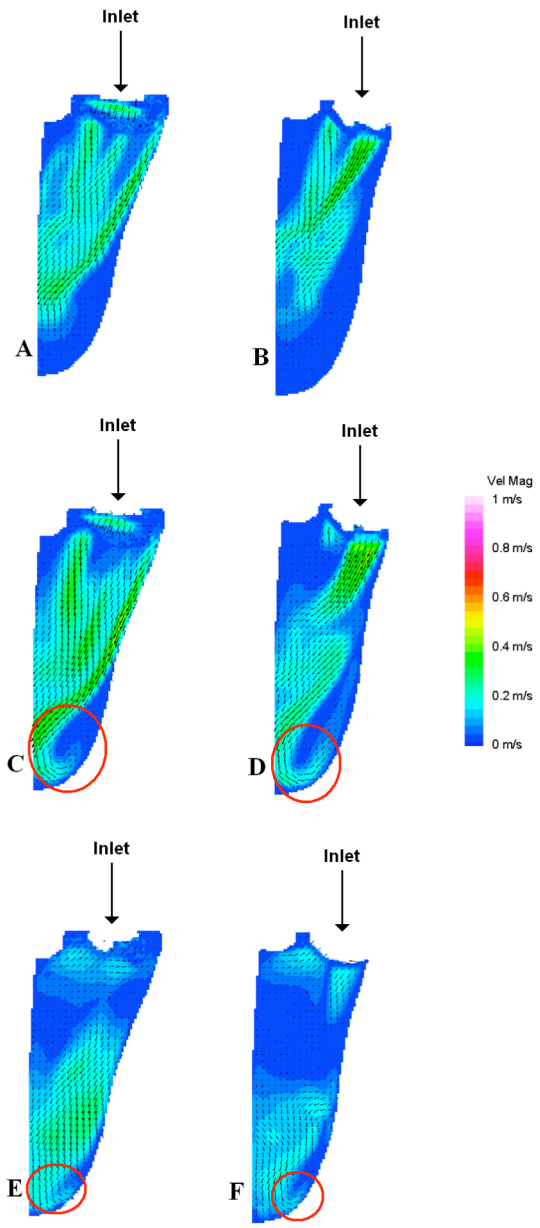

Figure 109: The (A, C, E) 7.5 and (B, D, F) 11.25 mm normal inlet planes of the 7.2 cc slow filling condition at (A, B) 200, (C, D) 300 and (E, F) 400 ms. Both of these inlet planes contain areas of recirculation, highlighted in red, that dissipate as the flow penetrates the bottom.

Flow containing velocities around 0.2 m/s is found in the outlet normal planes at 400 ms into diastole. This observation shows that there is a rotational flow field set up in the device, even if the flow is lower and develops late in the cycle. The flow in the outlet port remains stagnant until the onset of systole, and there are no areas of recirculation seen in the port area of any of the three normal planes. An example of this behavior in the 7.5 mm is shown in Figure 110.

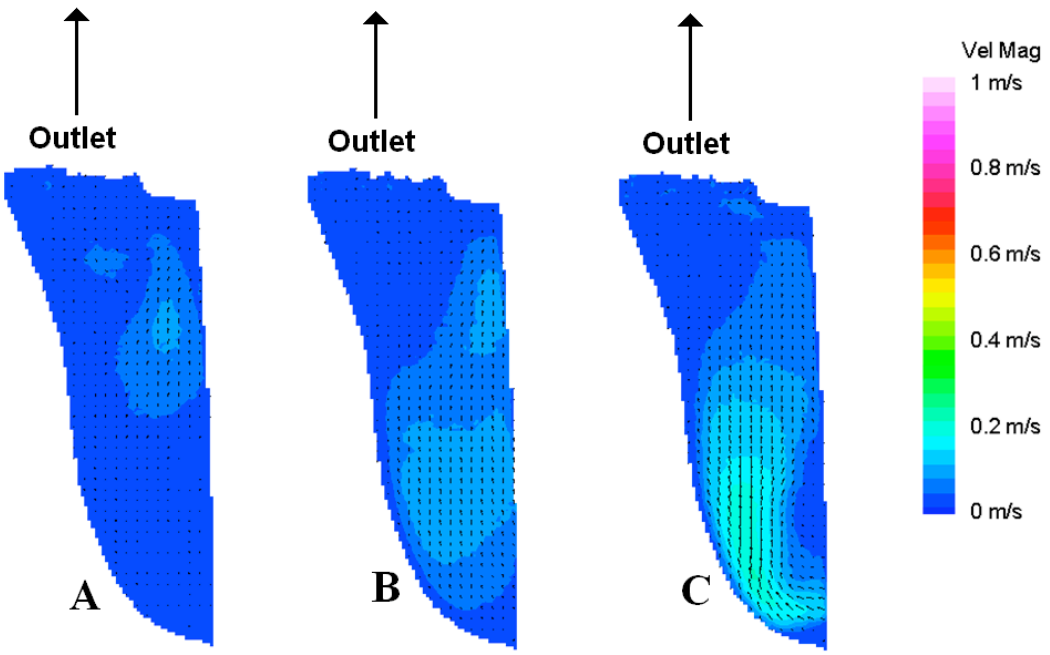

Figure 110: The 7.5 mm outlet normal plane of the 7.2 cc slow filling condition at (A) 200, (B) 300 and (C) 400 ms. The flow in the outlet side remains largely stagnant, as shown in dark blue, and there are not areas of recirculation in the outlet port as had been seen in other conditions. There is an increase in velocity during late diastole, indicating that there is some rotation of flow from the inlet side.

As established, much of the device flow during diastole is low (< 0.3 m/s) and contains many areas of stagnation, a pattern that continues during systole. The flow transitions to systole and moves smoothly through the outlet port, leaving the remaining areas of the device largely stagnant. This is observed in both the parallel and inlet normal planes, as presented in Figure 111.

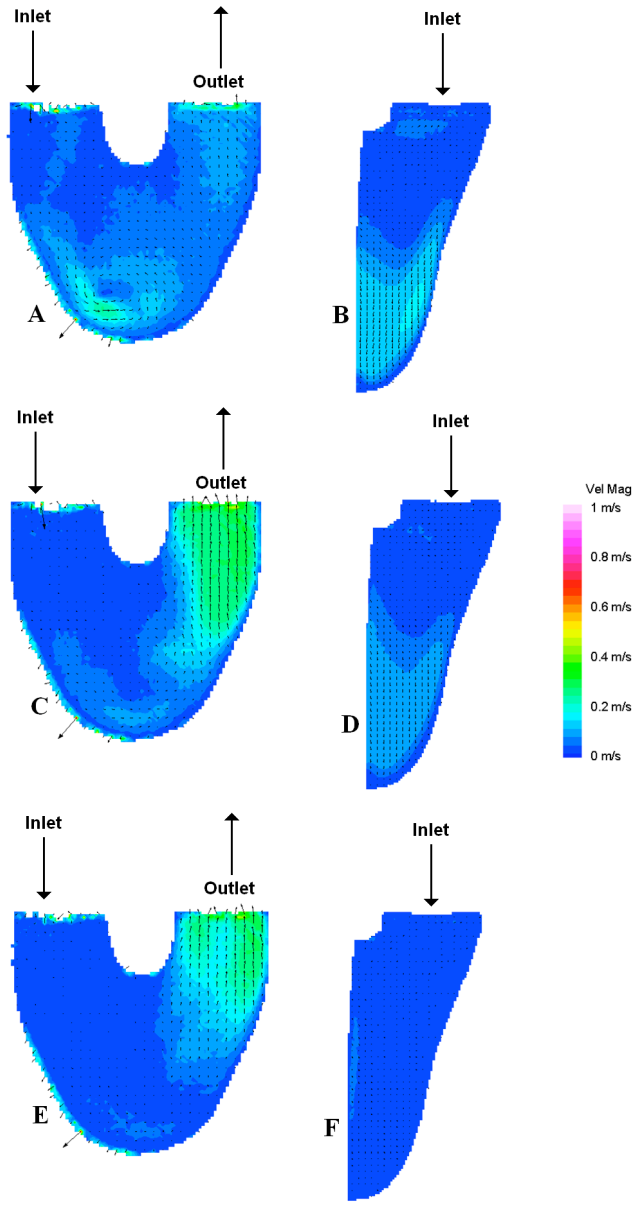

Figure 111: The (A, C, E) 8.2 mm parallel plane and (B, D, F) 7.5 mm inlet normal plane of the 7.2 cc slow filling condition at (A, B) 500, (C, D) 600 and (E, F) 700 ms. As the device moves through systole the flow in the inlet side and body of the device remains stagnant, as seen by the areas of dark blue.

Along with the larger stagnation regions during systole, the outflow jet also dissipates before the end of systole. This is evident in both the parallel and normal outlet planes as shown in Figure 112.

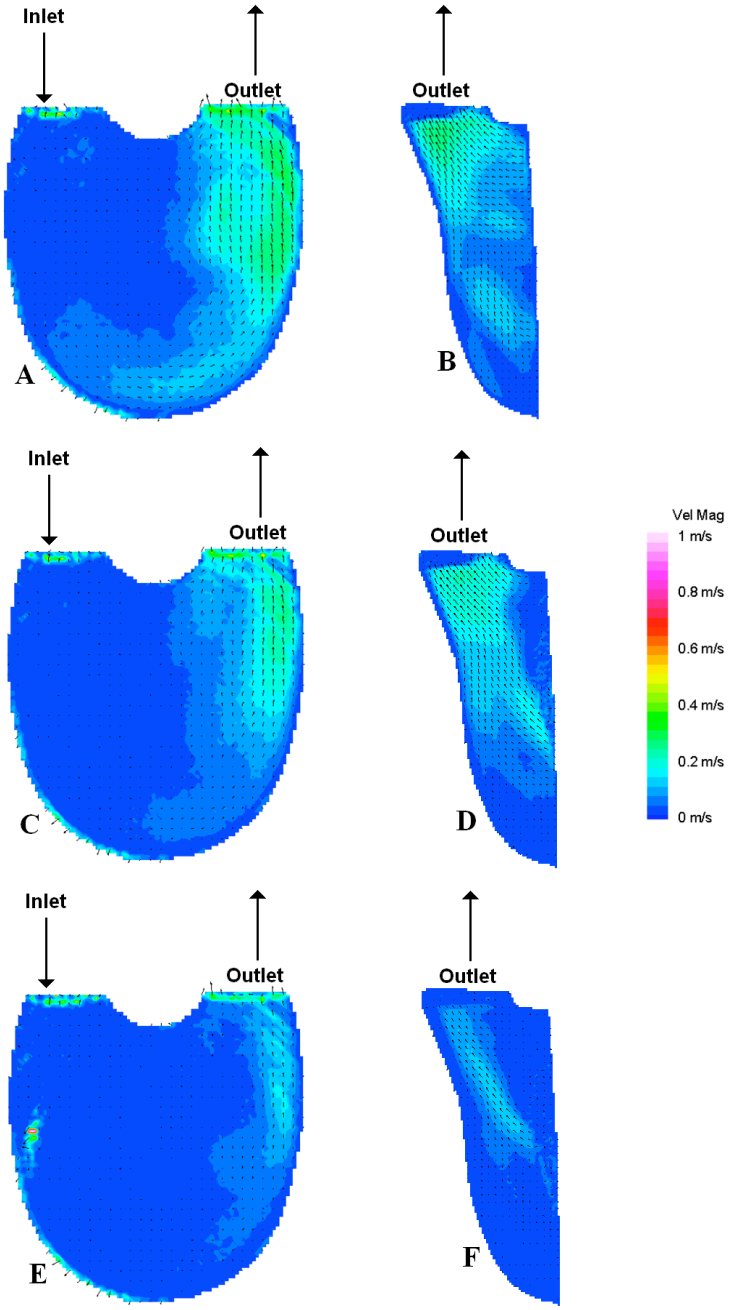

Figure 112: The (A, C, E) 11 mm parallel plane and (B, D, F) 11.25 mm outlet normal plane of the 7.2 cc slow filling condition at (A, B) 600, (C, D) 700 and (E, F) 800 ms. The outflow jet shows a dissipation from mid to late systole, as the velocities decrease below 0.2 m/s with the flow in the device at almost complete stagnation at the end of systole, indicated by the dark blue areas.

5.3.2.7 4.8 cc Quick Fill

The quick filling condition at a SV of 4.8 cc contains a strong inlet jet at the beginning of diastole, with the maximum fluid velocity reaching 1.22 m/s 50 ms into diastole. This strong jet is observed in all of the parallel planes and the inlet normal planes, however there is a quick reduction in magnitude only 100 ms later to less than half the maximum velocity (~0.5 m/s). This change is shown in Figure 113.

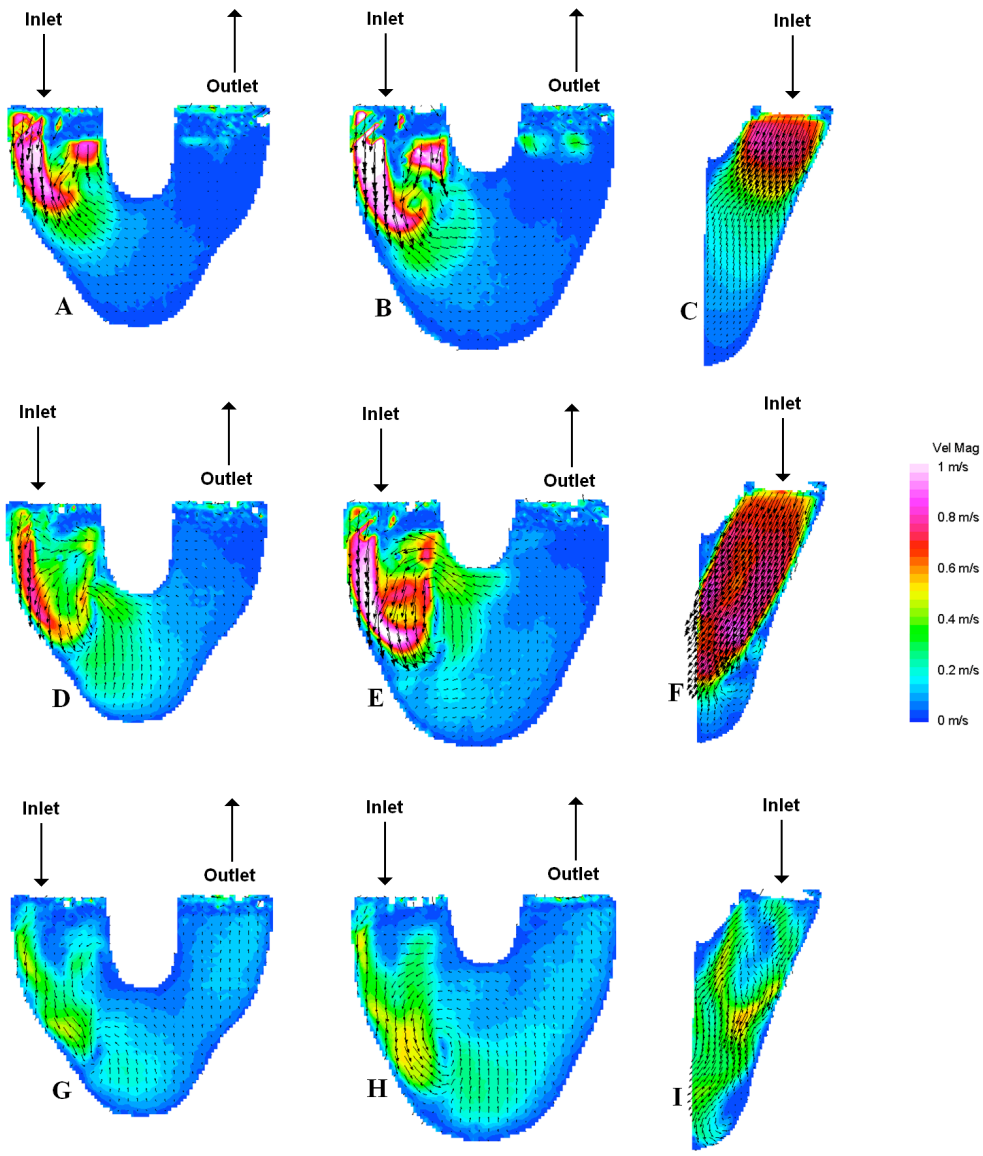

Figure 113: The (A, D, G) 7 and (B, E, H) 8.2 mm parallel planes and (C, F, I) 3.75 mm inlet normal plane of the 4.8 cc quick filling condition at (A, B, C) 50, (D, E, F) 100, and (G, H, I) 150 ms. A strong inlet jet is seen in early diastole (A-F), but a drop in magnitude is seen as the flow penetrates the bottom of the device (G-I).

This rapid change in velocity magnitude corresponds to a loss of momentum for the rotational flow field, which is never fully developed in the 7 mm plane. The 8.2 and 11 mm planes show the formation of a center of rotation, however this center quickly expands and the rotational flow field loses coherence, in a manner similar to the flow observed in the parallel planes of the 7.2 cc SV quick fill condition (Figure 103). This "patchy" appearance includes many areas of stagnation in the parallel planes, especially in the inlet port and at the bottom of the device. Figure 114 highlights this behavior in the parallel planes.

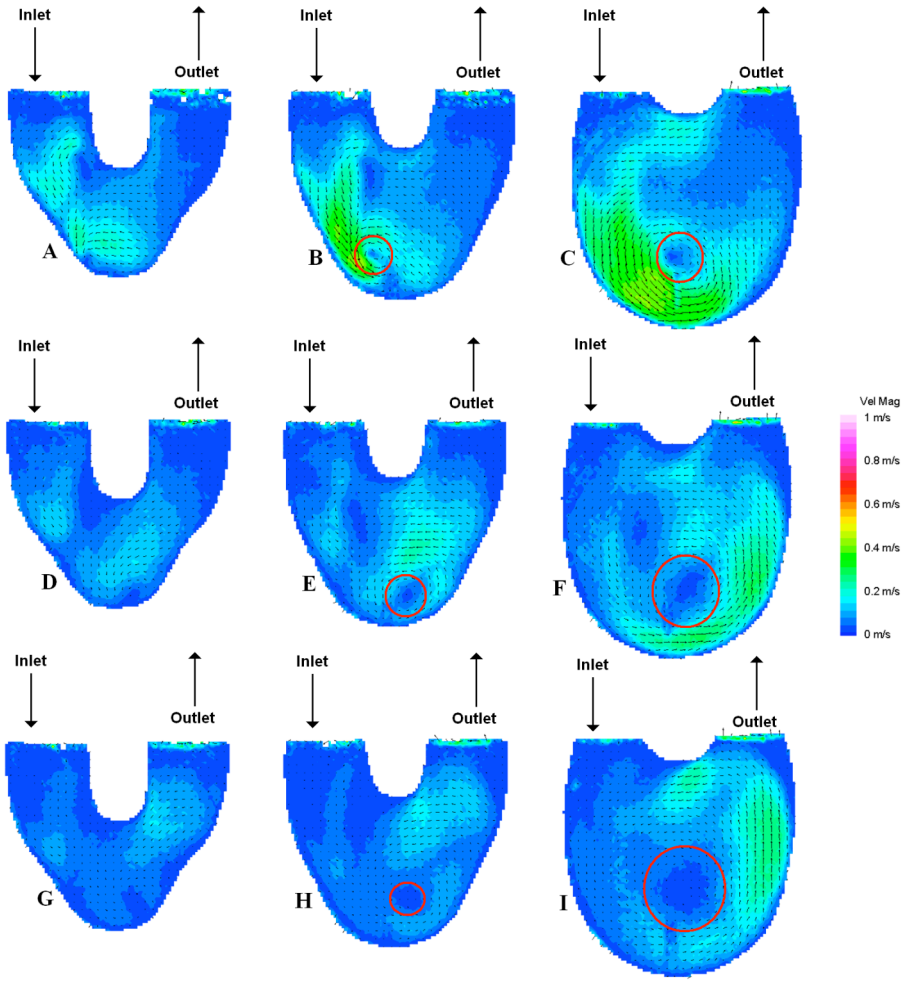

Figure 114: The (A, D, G) 7, (B, E, H) 8.2 and (C, F, I) 11 mm parallel planes of the 4.8 cc quick filling condition at (A, B, C) 200, (D, E, F) 300 and (G, H, I) 400 ms. The parallel planes show a poor rotational flow field. While there is a center of rotation, circled in red, observed in some of the planes this quickly expands as the flow dissipates.

The normal outlet planes show fluid movement in the body of the device at 250 ms into the cycle. This indicates that there is some rotational flow at this point in diastole. In general the flow in the outlet port of the planes remains stagnant during diastole, however, the 11.25 mm plane contains a small area of regurgitant flow during late diastole, the location of which is similar to areas of recirculation observed at other conditions. This flow behavior in the 11.25 mm plane is shown in Figure 115.

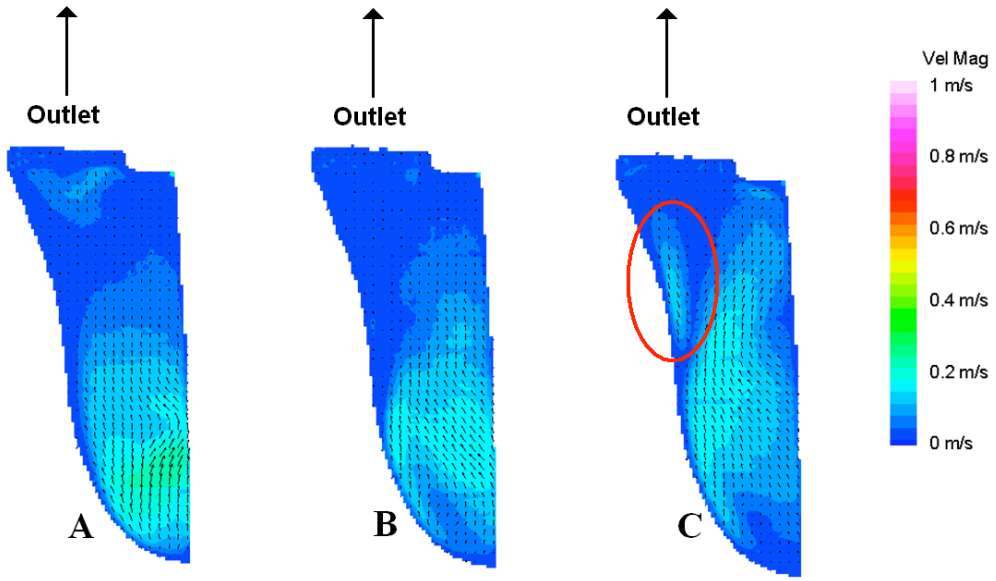

Figure 115: The 11.25 mm outlet normal plane of the 4.8 cc quick filling condition at (A) 250, (B) 350 and (C) 450 ms. Movement in the body of the device a mid diastole indicates that there is some rotation to the outlet side of the device. Unlike previous SVs there is no area of recirculation seen in the outlet port, only a small region of regurgitation, highlighted in red, in the 11.25 mm outlet plane at late diastole.

The weak rotational flow leads to similar patterns as the cycle transitions to systole. The flow shifts to the outlet port leaving large areas of stagnation throughout the device, especially along the inlet side and bottom walls. The outlet flow contains maximum velocities around 0.4 m/s and there are no areas of blockage around the valve. The systolic behavior is shown in Figure 116.

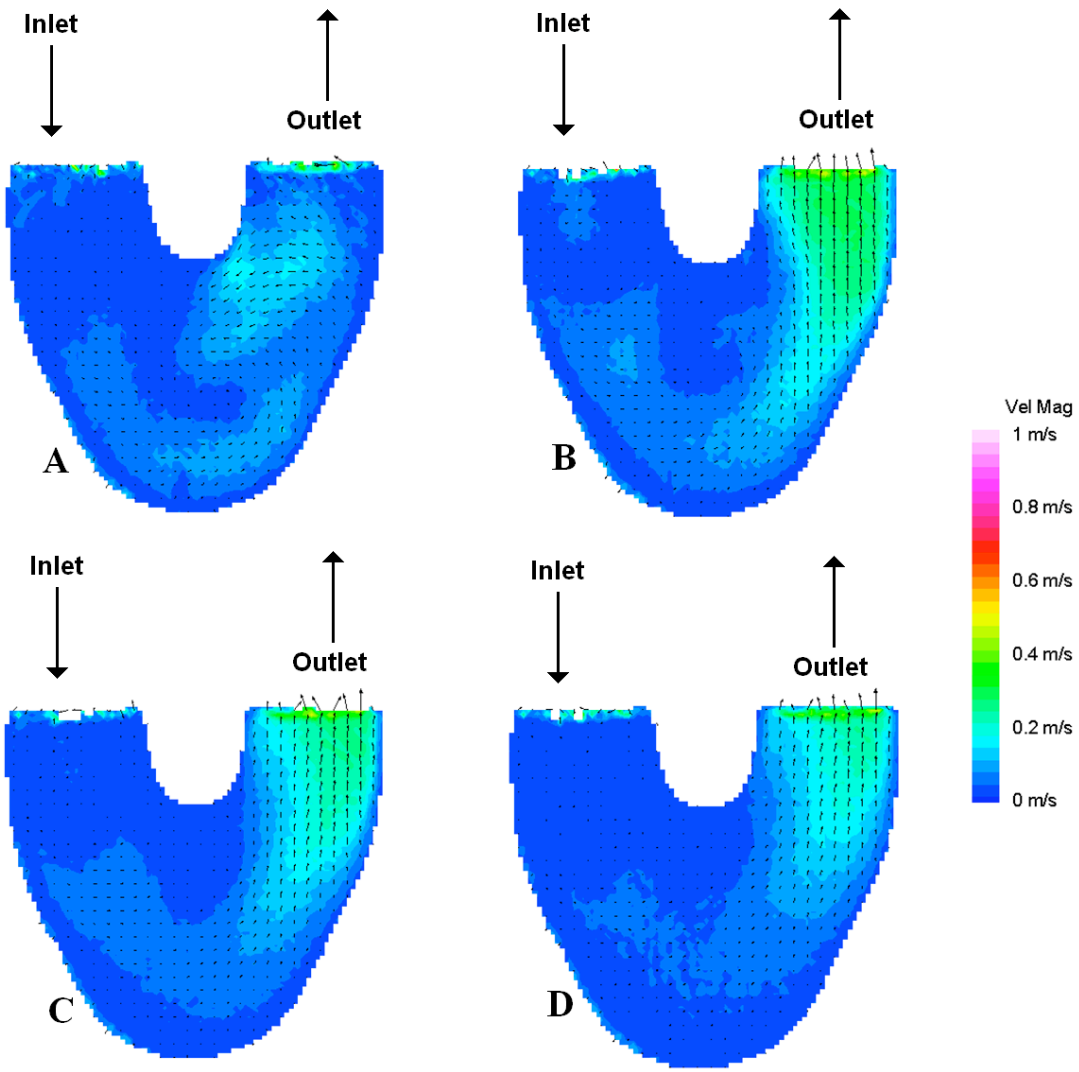

Figure 116: The 8.2 mm parallel plane of the 4.8 cc quick filling condition at (A) 500, (B) 600, (C) 700 and (D) 800 ms. No areas of blockage are seen as the flow progresses through systole. In general the flow not associated with the outflow remains stagnant, as noted by the dark blue.

5.3.2.8 4.8 cc Slow Fill

While running the device at a SV of 4.8 cc and using a slow fill condition the flow field remains largely stagnant. The flow reaches a maximum velocity of 0.47 m/s at 250 ms into the cycle, in the inlet jet, which drops to velocities below 0.2 m/s only 100 ms later. Examples of this jet behavior are shown in Figure 117.

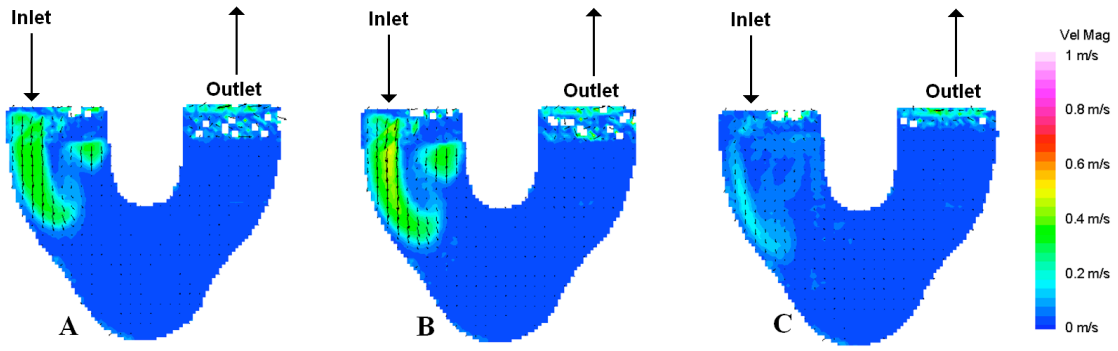

Figure 117: The 7 mm parallel plane of the 4.8 slow filling condition at (A) 150, (B) 250 and (C) 350 ms. The only non-stagnant flow observed in the planes during diastole is from the inlet jet development, which dissipates just after mid diastole as seen in C.

After the break down of the inlet jet in mid diastole a large portion of the device flow is stagnant until the onset of systole. This is observed in all of the parallel and normal inlet and outlet planes as shown in Figure 118.

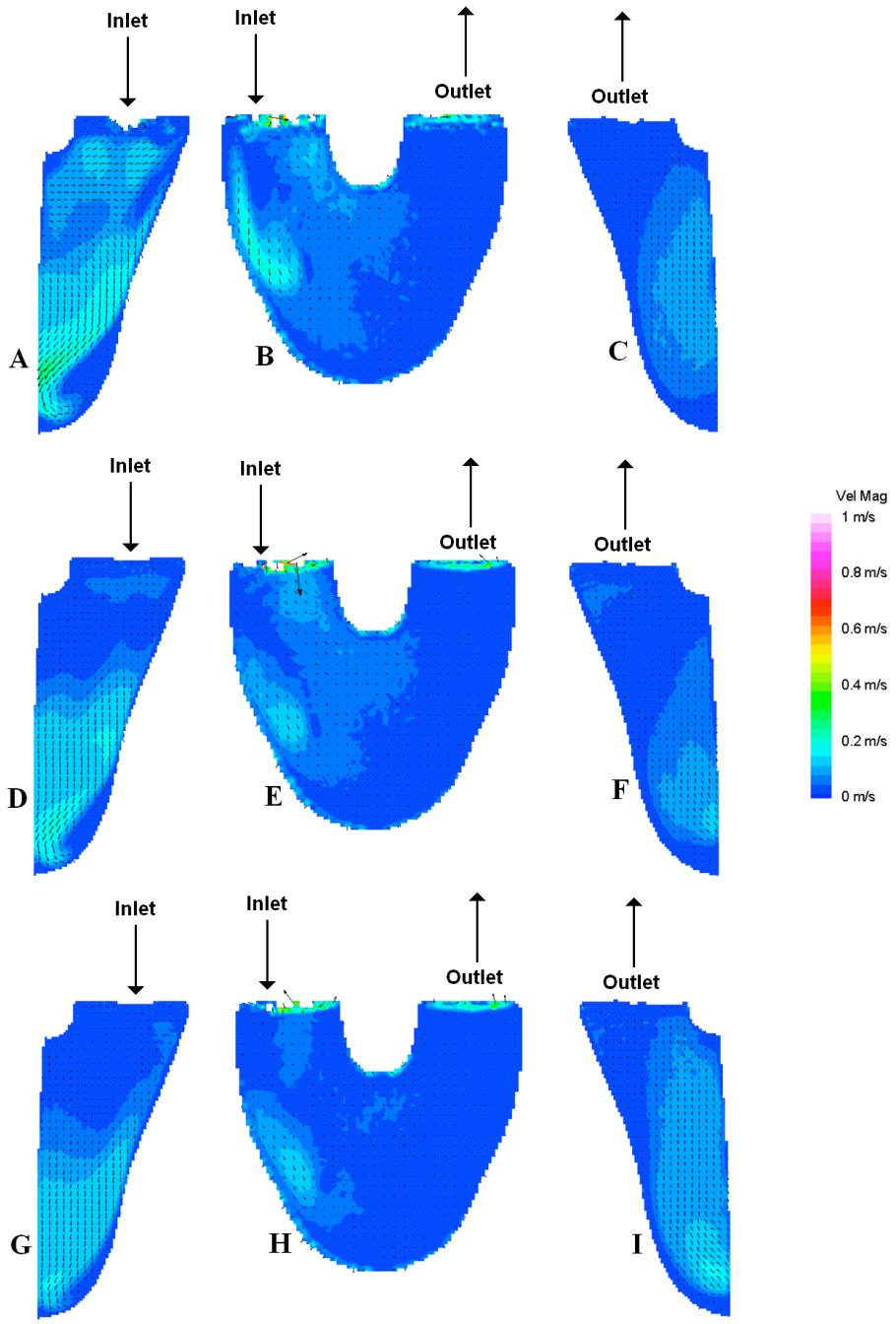

Figure 118: The (B, E, H) 8.2 mm parallel plane and 7.5 mm (A, D, G) inlet and (C, F, I) outlet normal planes of the 4.8 cc slow filling condition at (A, B, C) 350, (D, E, F) 400 and (G, H, I) 450 ms. An example of the stagnation seen in all planes during mid to late diastole.

As systole begins the only fluid movement observed is in the outlet port of the device. While the 7 and 8.2 mm planes show slow but uniform movement of flow through the outlet port, the 11 mm plane does not contain a uniform outflow and velocities in the outlet port remain below 0.1 m/s. This is shown in Figure 119.

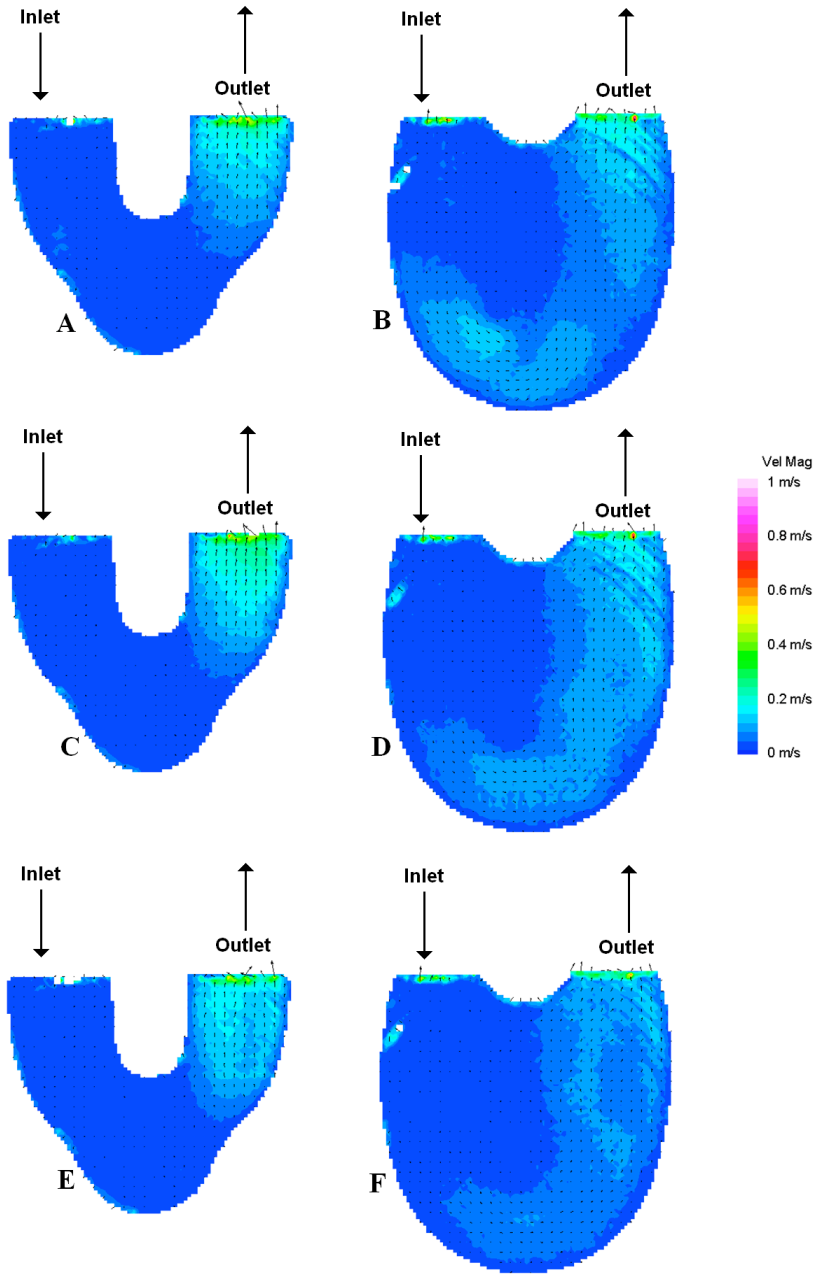

Figure 119: The (A, C, E) 7 and (B, D, F) 11 mm parallel planes of the 4.8 cc slow filling condition at (A, B) 550, (C, D) 650 and (E, F) 750 ms. Through systole there is a very low outflow through the outlet port of the device, while the remainder of the pump remains stagnant.

5.4 Discussion

In order to compare the flow fields and wall shear rates of each condition, we first compare the effect of SV reduction on each filling condition and then compare the difference between the two filling conditions. Because of the large amount of data obtained during the study, each section focuses on the characteristics of the flow field considered important regarding thrombogenicity, as this is the focus of the fluid mechanic studies of the PVAD. These characteristics include the inlet jet formation, rotational flow field development, transition to systole, and areas of blockage, stagnation, regurgitation or recirculation.

5.4.1 Stroke Volume Comparison – Quick Fill

As shown previously in Figure 73, the maximum deployment location and shape of the diaphragm observed at each SV is different. Despite this noticeable difference, the flow fields of the 12, 9.6 and 7.2 cc SVs using a quick fill method maintained highly similar patterns. The 4.8 cc SV resulted in a much more stagnant flow. The important characteristics of each SV are compared below.

5.4.1.1 Inlet Jet Formation

A strong inlet jet with velocities above 1 m/s is observed in all four SVs at the first time step of diastole, 50 ms. The inlet jet of the 12, 9.6 and 7.2 cc SVs continues to strengthen into the next time step, 100 ms, where the maximum velocities for all three were observed at around 1.7 m/s. In comparison the velocity of the 4.8 cc inlet jet decreases at this point in diastole. Figure 120 shows this behavior in the 7 mm plane for all four SVs.

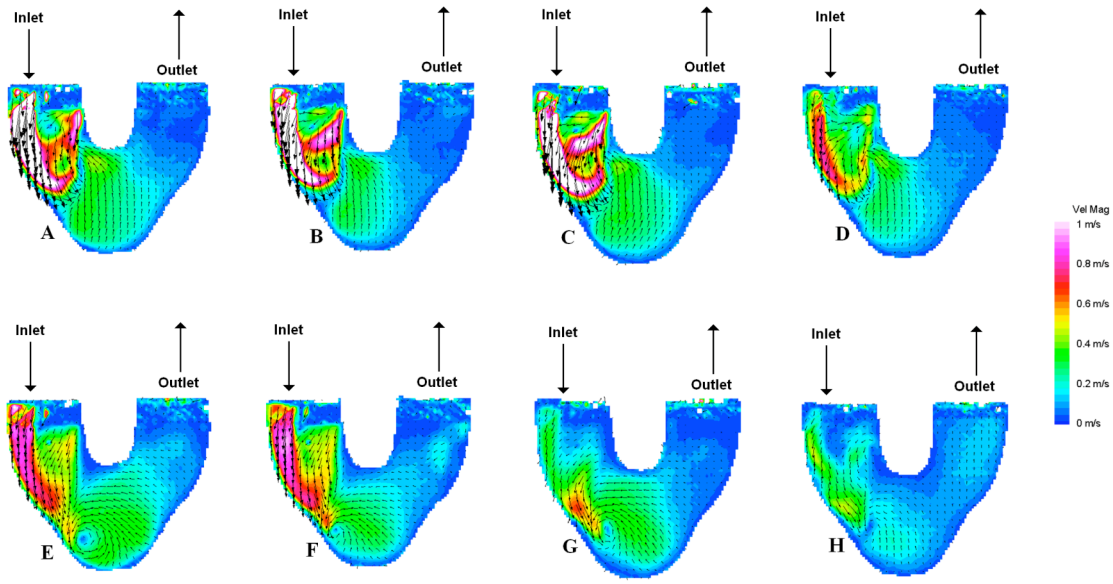

Figure 120: The 7 mm parallel plane of the (A, E) 12, (B, F) 9.6, (C, G) 7.2 and (D, H) 4.8 cc quick filling conditions at (A-D) 100 and (E-H) 150 ms. As strong inlet jet is observed during early diastole (100 ms) for all four SVs. The start of the rotational flow field is observed 50 ms later. The 4.8 cc SV (D, H) contains reduced inlet jet velocities compared to the larger SVs.

The wall shear rates along surface 1, located on the upper outside wall of the inlet port, for all four SVs contain high wall shear rates (>1000 s^{-1}) during early diastole. As shown in Figure 121, the 12, 9.6 and 7.2 cc SVs contain these high rates across a large portion of the surface, while the 4.8 cc SV shows a less consistent pattern.

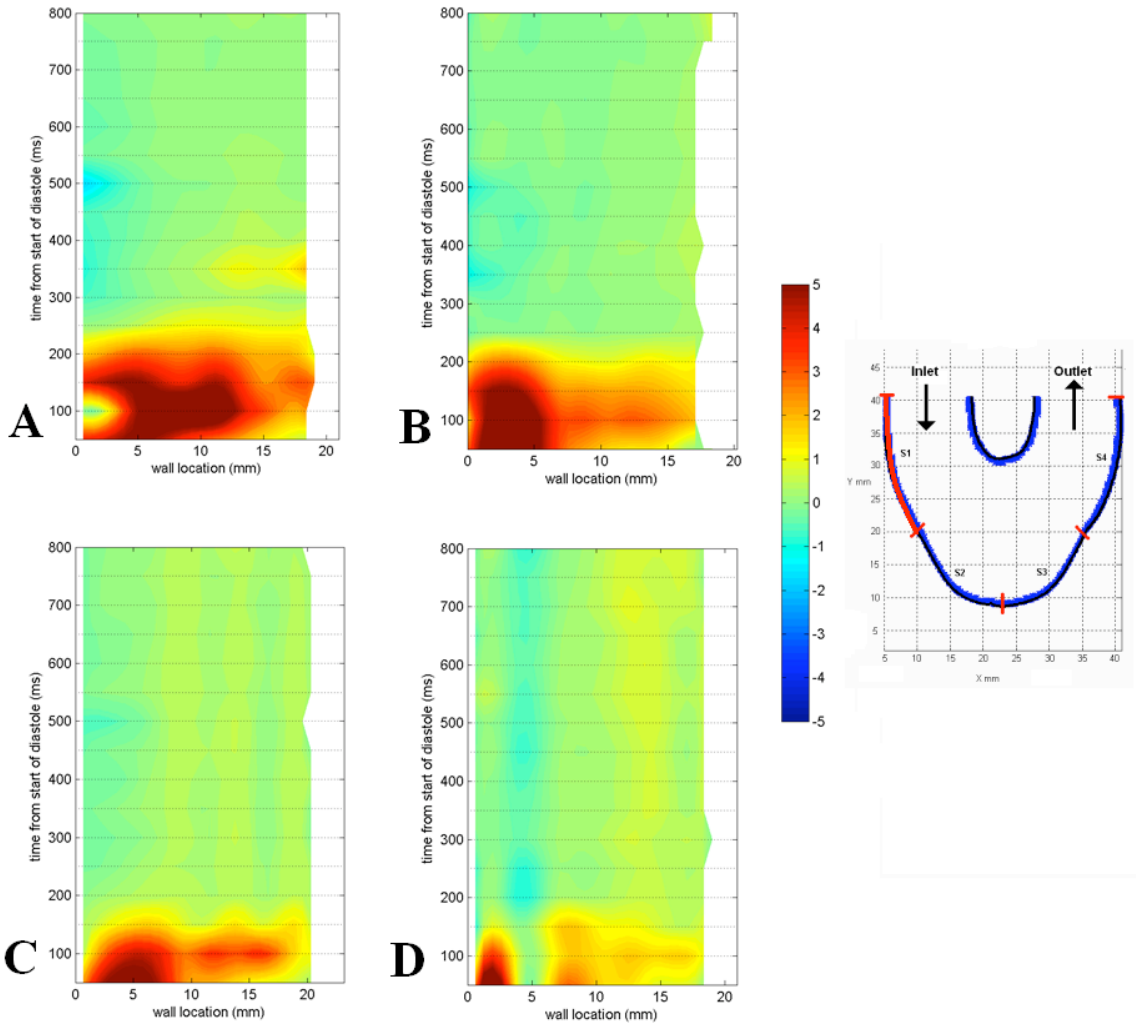

Figure 121: Surface 1 of the 7 mm parallel plane, located along the outside inlet wall and highlighted in red to the right, of the (A) 12, (B) 9.6, (C) 7.2 and (D) 4.8 cc quick filling conditions. All four SVs contain high wall shear rates, however the three larger SVs maintain these along the entire surface. The 12 cc SV contains these higher rates for the longest duration.

Figure 121 also shows how the 12 cc SV maintains these higher wall shear rates for the longest portion of the cycle. This corresponds well with the inlet jet behavior seen in the flow maps. As diastole continues the inlet jets of all the SVs decrease in velocity as the rotational flow field begins to develop. The 12 cc SV maintains the highest velocities for the longest duration, which is consistent with the larger flow rate associated with this SV. The development and breakdown of the inlet jets of each SV in the 8.2 mm planes are shown in Figure 122.

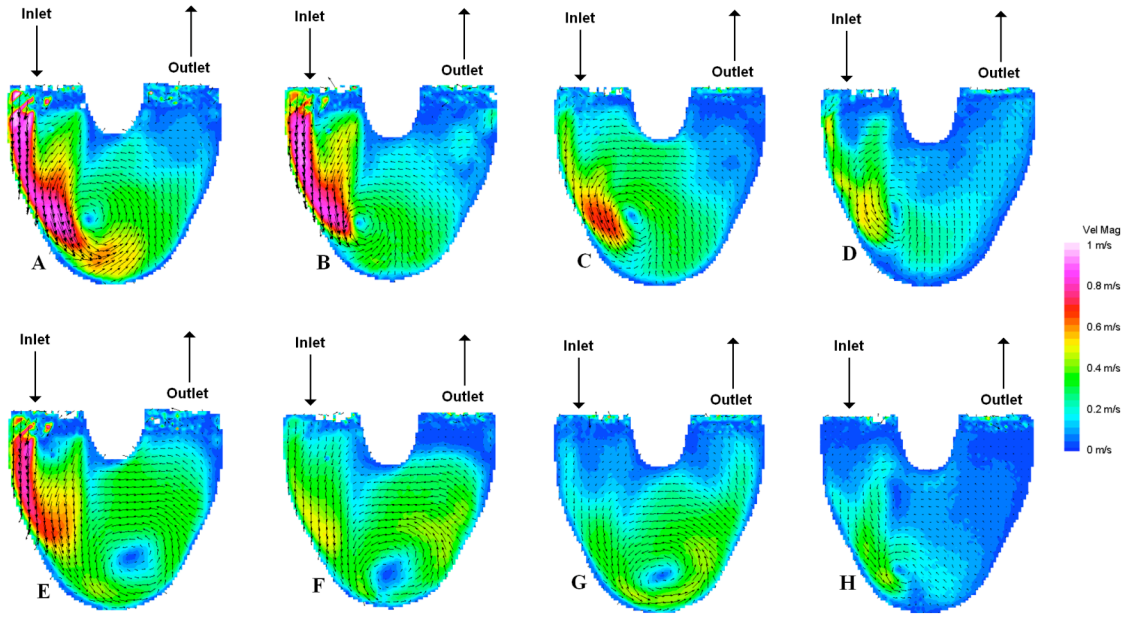

Figure 122: The 8.2 mm parallel plane of the (A, E) 12, (B, F) 9.6, (C, G) 7.2 and (D, H) 4.8 cc quick filling conditions at (A-D) 150 and (E-H) 200 ms. As the flow progresses to mid diastole the inlet jets begin to dissipate, the lower SVs showing the largest drops in velocity magnitude.

Similar results are clearly seen in the inlet normal planes. The 3.75 mm inlet plane shows a similar development and breakdown of the inlet jet for all four SVs. Also the wall shear rate maps along this plane contain high wall shear rates during early diastole, where again the 12 cc SV maintains the high shear rates for the longest period. Figure 123 shows the progression of the inlet jet in the 3.7 mm inlet plane and Figure 124 presents the wall shear rate maps along surface 4, located just below the inlet port.

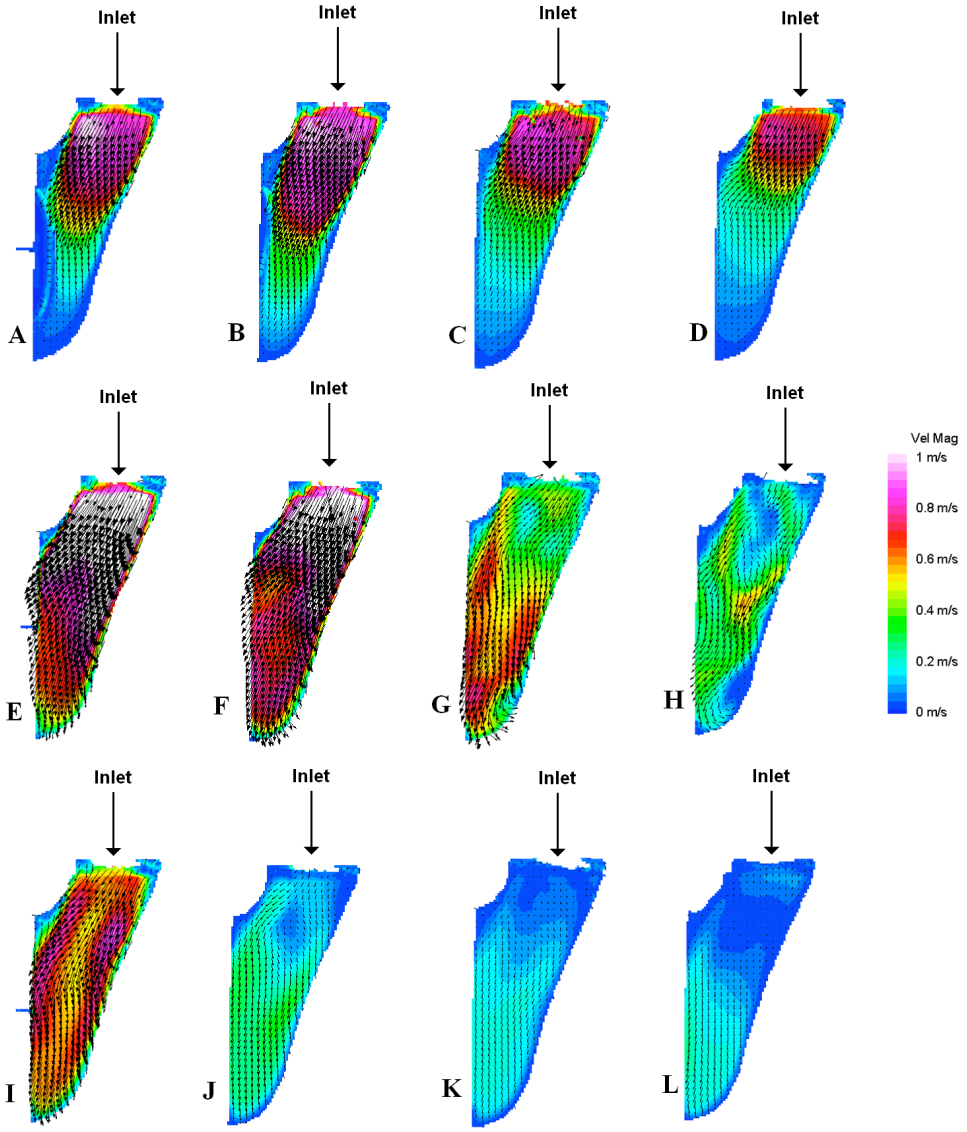

Figure 123: The 3.75 mm normal inlet plane of the (A, E, I) 12, (B, F, J) 9.6, (C, G, K) 7.2 and (D, H, L) 4.8 cc quick filling conditions at (A-D) 50, (E-H) 150, and (I-L) 250 ms. The inlet jet formation in the outermost normal inlet plane shows the early onset of the jet, and the early dissipation as the SV is reduced.

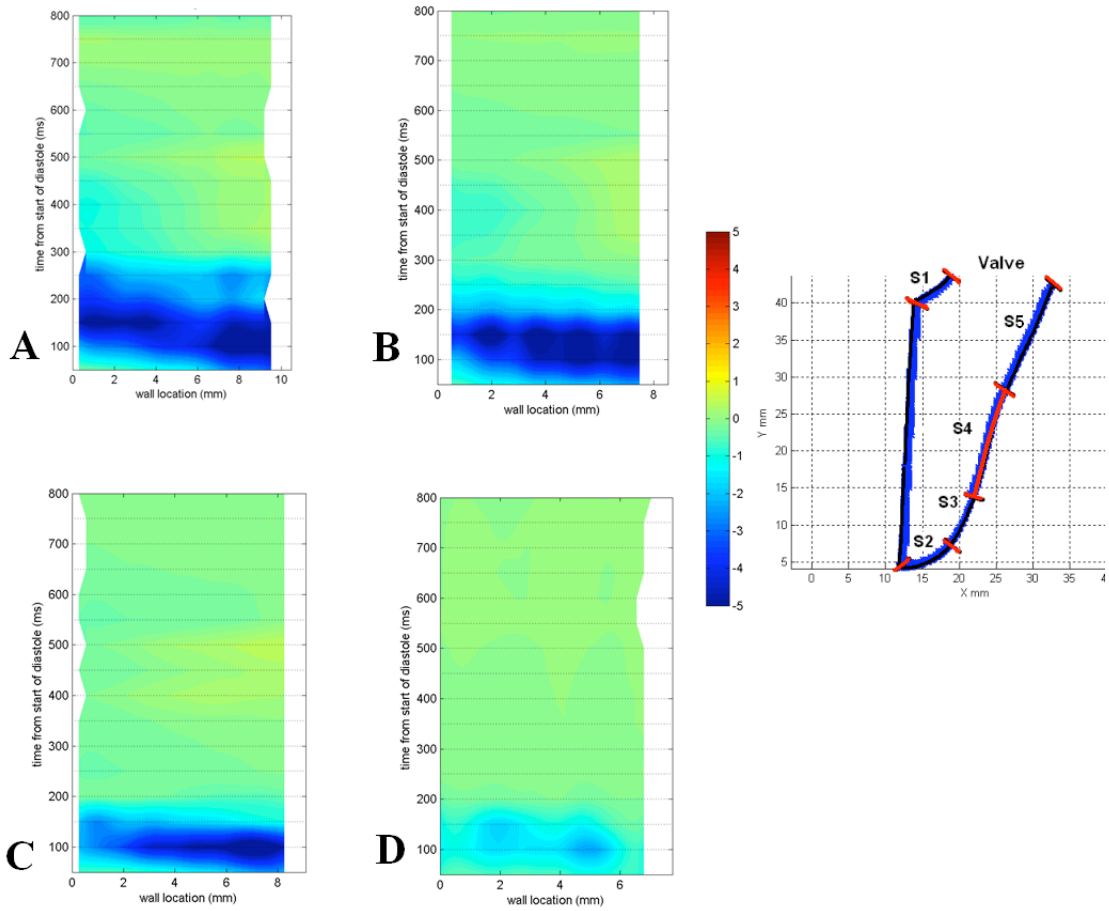

Figure 124: Surface 4 of the 3.75 mm normal inlet plane, located in the middle of the fluid side of the inlet as highlighted in red to the right, of the (A) 12, (B) 9.6, (C), 7.2 and (D) 4.8 cc quick filling conditions. Similarly to the wall shear rate maps of the 7 mm parallel plane seen in Figure 121, high wall shear rates (> 1000 s^{-1}) are observed early in diastole for all SVs except 4.8 cc. The 12 cc SV also still contains the highest wall shear rates for the longest duration.

The quick development of the inlet jet using this filling method provides wall washing along the inlet port. SVs from 12 to 7.2 cc all contain similar peak velocities and high wall shear rates, however, as the SV is reduced so is the magnitude of the velocity and wall shear rates and the duration washing period. This is most noticeable at the 4.8 cc SV, a reduction to which may largely increase the chance of thrombus deposition.

5.4.1.2 Rotational Flow Development

With the exception of the 4.8 cc SV, a rotational flow field is visible in the parallel planes of all the conditions. The strong inlet jet seen during early diastole penetrates to the bottom of the device by 150 ms into the cycle and a coherent center of rotation can be found. Nevertheless, the decreased velocity magnitude and duration of the reduced SVs does affect this rotation. To illustrate the change in inlet jet velocity, the maximum velocities of the 8.2 mm parallel plane for each SV are plotted against time in Figure 125. This plot shows the three largest SVs reach similar maximum velocities, and then begin to lessen one at a time. First, this is the 7.2 cc SV at 150 ms, than the 9.6 cc SV at 200 ms, and finally, the 12 cc SV drops at 300 ms and all three are again at the same maximum velocity. The maximum velocities of the 4.8 cc SV remain low throughout diastole.

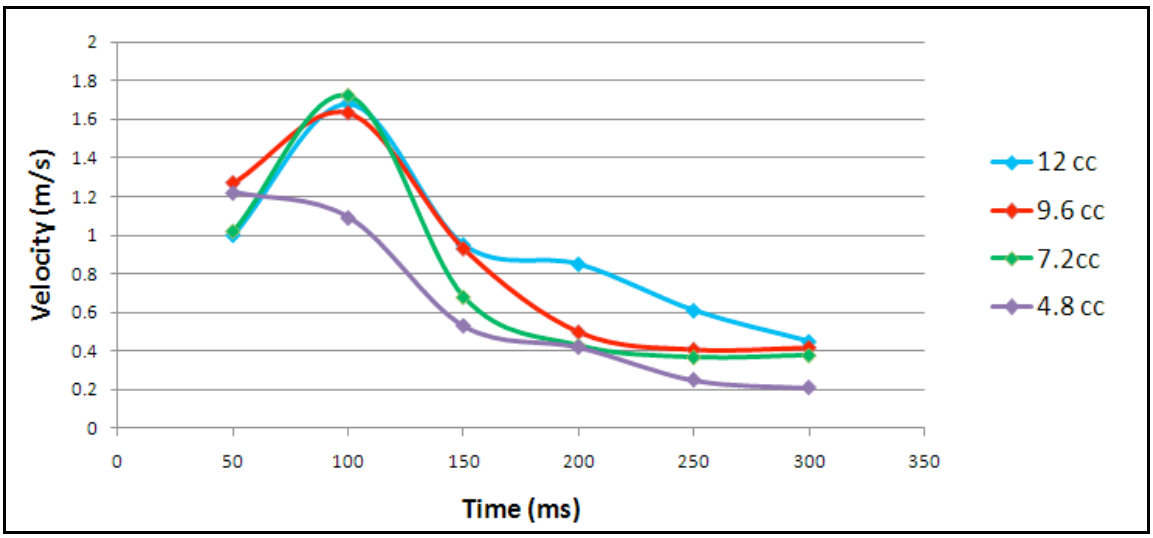

Figure 125: A plot of the maximum velocities versus time of all four quick fill SVs in the 8.2 mm parallel plane. A loss of velocity strength can be seen with each SV.

The effect of this velocity change is observed as the rotational flow field of the 9.6 and 7.2 cc SVs begin to lose strength during late diastole. This breakdown is due to the reduced momentum resulting from the weaker inlet jet. As shown previously in Figure 114, the 4.8 cc SV never fully develops a rotational flow field, and the device contains many areas of stagnation through the entire cycle. Figure 126 shows the rotational behavior of the three larger SVs in the 11 mm parallel plane.

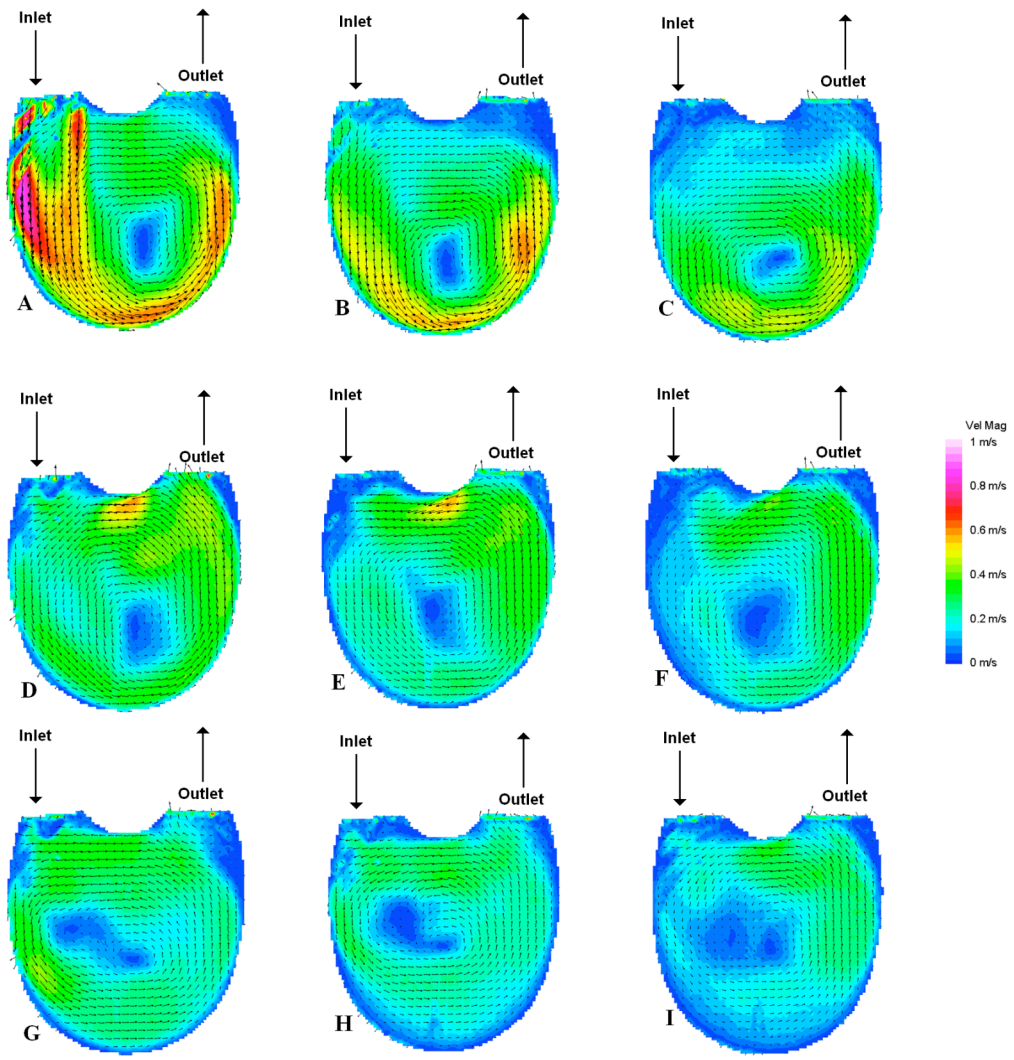

Figure 126: The 11 mm parallel plane of the (A, D, G) 12, (B, E, H) 9.6, and (C, F, I) 7.2 cc quick filling conditions at (A-C) 200, (D-E) 300 and (G-I) 400 ms. All three SVs show a strong rotational flow field at mid diastole (200 ms), however the 9.6 and 7.2 cc SVs show more dissipation of this rotation before the end of diastole (H, I) than the 12 cc SV (G).

The wall shear rate maps confirmed the difference in the strength of the rotational flow fields. High wall shear rates are observed during early to mid diastole along surface 3, located at the bottom of the outlet side, of the 11 mm plane shown in Figure 127. The 12 cc SV again contains the highest wall shear rates for the longest duration. These are correspondingly reduced with the reduction in SV as shown in Figure 127.

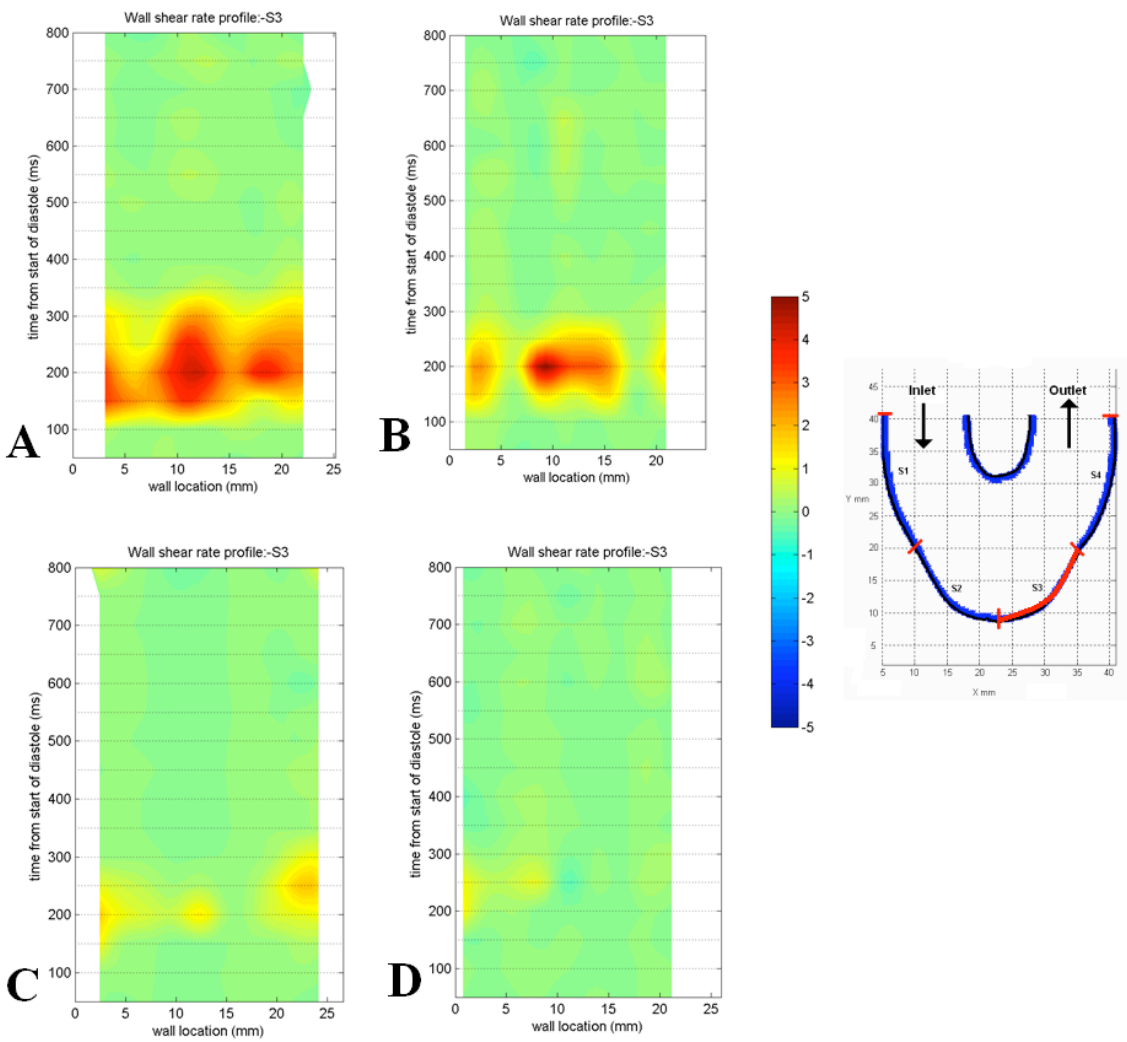

Figure 127: Surface 3 of the 11 mm parallel plane, located at the bottom wall of the outlet side as highlighted in red to the right, of the (A) 12, (B) 9.6, (C) 7.2 and (D) 4.8 cc quick filling conditions. As shown previously on the inlet walls the 12 cc SV maintains higher wall shear rates for the longest duration. The lower SVs then show a drop in both wall shear rate magnitude and duration, with very low wall shear seen at the 7.2 and 4.8 cc SVs (C, D).

As is observed in Figure 124, the reduction in SV results in a loss of wall washing as the strength of the rotational flow field lessens. This could, in turn, increase the chance of thrombus formation along the sac surfaces. This is especially true of the 4.8 cc SV, as shown previously in Figures 114-116. In comparison to the 4.8 cc SV reductions the 9.6 and 7.2 cc SVs do maintain rotational flow field throughout diastole and wall shear rates above the 500 s^{-1} threshold for portions of the sac surfaces. This is especially true when the SV reduction results are compared to the beat rate reduction ones, an evaluation which is discussed in section 5.4.4.

5.4.1.3 Diastole Recirculation

During diastole an area of recirculation appears in the 11.25 mm inlet normal plane at the bottom of the device, examples of which were shown previously in Figures 75 and 101. These areas, shown in Figure 128, contain areas of positive wall shear rates along the bottom of the device before the flow is uniformly directed towards the outlet side of the device as the rotational flow field begins, indicated by a shift to negative wall shear rates. This shows that the recirculation areas are providing some wall washing at the bottom of the device. This could be beneficial since this is an area prone to thrombus deposition. This recirculation does not appear to interfere with the penetration of the flow through the device bottom, or the development of rotational flow. Similar to previous wall shear rate maps, the 12 cc SV maintains the highest magnitudes during this washing.

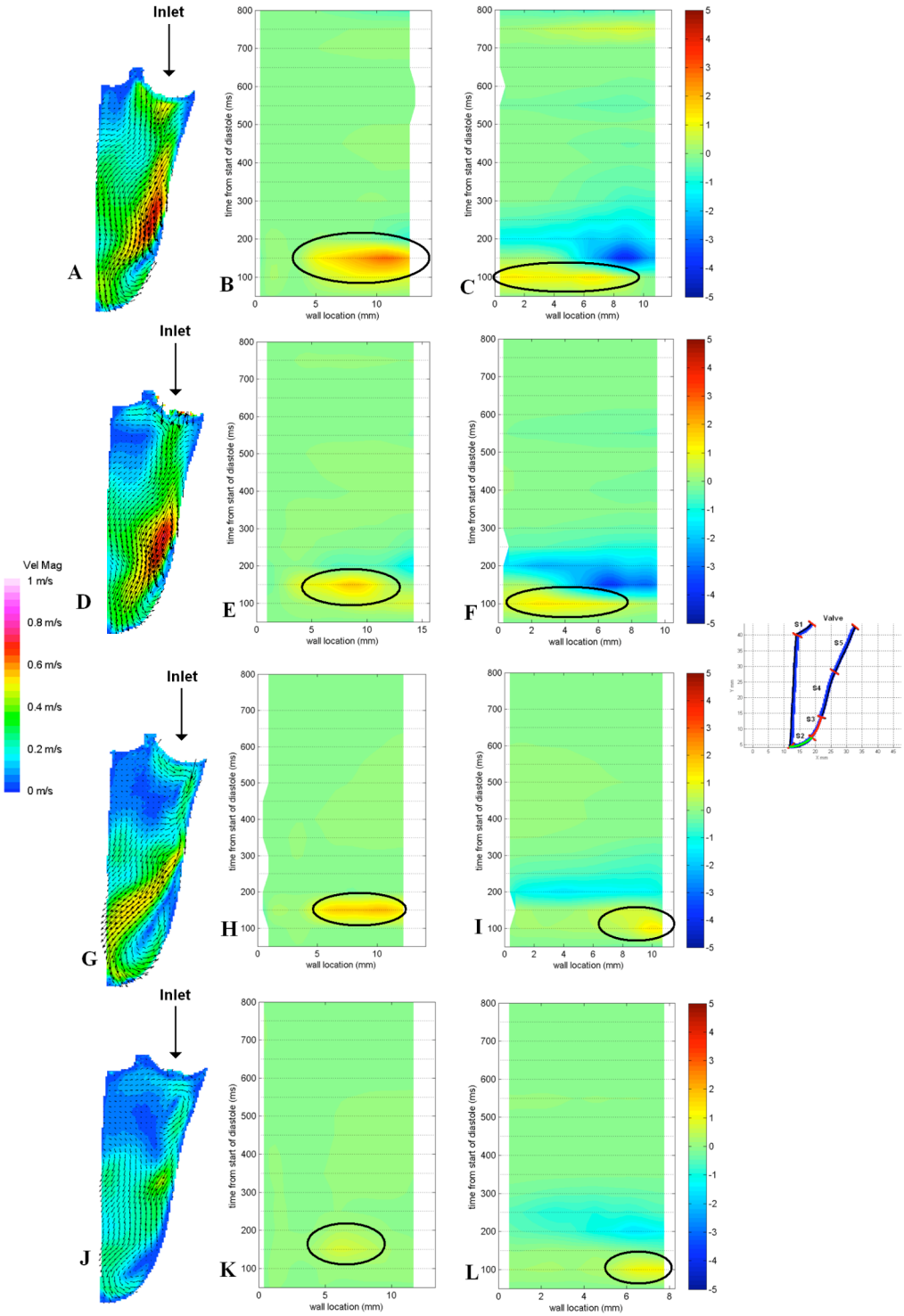

Figure 128: The 11.25 mm inlet normal plane of the (A) 12, (D) 9.6, (G) 7.2 and (J) 4.8 cc quick filling methods at 150 ms. Also, surfaces 2 (highlighted in green) and 3 (highlighted in red), which are located along the bottom of the 11.25 mm normal inlet plane, of the (B, C) 12, (E, F) 9.6, (H, I) 7.2 and (K, L) 4.8 cc quick filling conditions. The areas of recirculation seen at the bottom of the flow field maps provide some increase in positive wall shear rates (highlighted in black) along the bottom of the device during early diastole (around 150 ms) before the flow is directed through the bottom and this is replaced by negative wall shear rates (around 200 ms).

5.4.1.4 Outlet Port Recirculation

As shown in Figures 78, 92 and 102, the 12, 9.6 and 7.2 cc SVs contain areas of recirculation in the outlet port during mid to late diastole. These were observed in previous flow studies, and can be considered beneficial because they reduce stagnation in the port during diastole, as long as they do not disturb the rotational flow field (Roszelle, 2010a). The areas seen in this study contain velocity magnitudes < 0.5 m/s, and do not interfere with the rotational flow field observed in the parallel planes. A similar area is not observed at the 4.8 cc condition, resulting in stagnant flow in the outlet port during diastole. Figure 129 presents the wall shear rate maps along surface 2 of the 11.25 mm outlet normal plane, located along the middle of the fluid side outlet wall. The maps show some wall shear rates above the 500 s^{-1} threshold at the 12, 9.6, and 7.2 cc SVs.

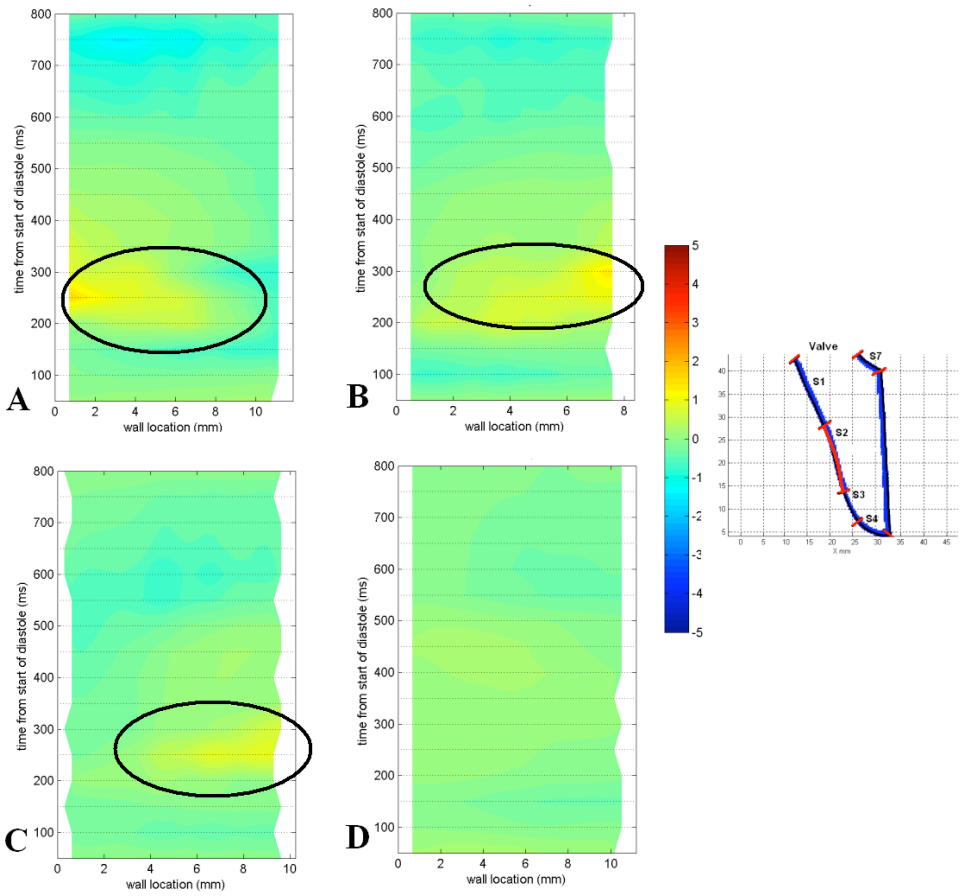

Figure 129: Surface 2, located along the middle of the fluid side of the device, of the 11.25 mm outlet normal plane at the (A) 12, (B) 9.6, (C) 7.2 and (D) 4.8 cc SV quick filling conditions. The three larger SVs show a slight increase in the wall shear rates, highlighted in black, during mid diastole when the recirculation area occurs in the outlet port.

Overall, the quick filling of the SVs at 12, 9.6 and 7.2 cc maintained strong inlet jets and rotational flow fields. While the strength of the jet and rotational flow, as well as the amount and strength of the wall washing observed, decreased as the SV was reduced, these basic patterns remained. This observation indicates that a SV reduction method could maintain desirable flow patterns as the flow rate was reduced during myocardial recovery situations. At a reduction to SV of 4.8 cc, however, a rotational flow field could not be observed, and the overall wall washing was very poor. Therefore, a reduction to 40% of the SV would not be recommended.

5.4.2 Stroke Volume Comparison – Slow Fill

As would be expected, the slow filling method resulted in an inlet jet that developed over a longer portion of diastole, with the maximum velocities appearing in the flow fields around mid diastole. This also resulted in a rotational flow field that began midway through diastole, and for the lower SVs, was never fully developed.

5.4.2.1 Inlet Jet Formation

In all four SVs the formation of the inlet jet can be seen at 100 ms into the cycle. The jet then continues to strengthen until just after mid diastole where maximum velocities of 0.94, 0.73, 0.59 and 0.47 m/s are observed in the 12, 9.6, 7.2 and 4.8 cc SVs, respectively. As evident from the maximum velocities, the strength of the inlet jet decreases with the reduction in SV. This slow jet development still provides wall shear rates above the 500 s^{-1} threshold along the inlet surface from early to late diastole. However, as the SV is reduced, the wall shear rates lose magnitude and do not reach across the entire surface. This behavior is highlighted in the both the flow fields and the wall shear maps in Figures 130 and 131.

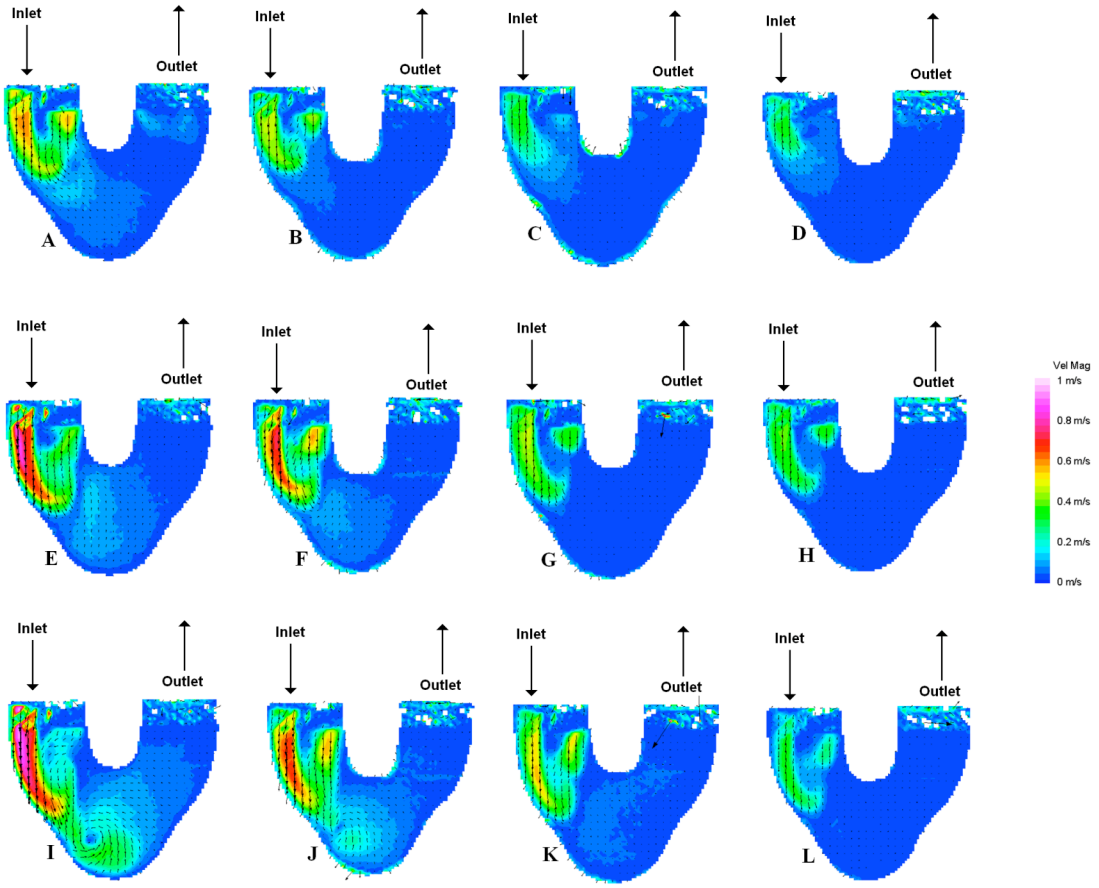

Figure 130: The 7 mm parallel plane of the (A, E, I) 12, (B, F, J) 9.6, (C, G, K) 7.2 and (D, H, L) 4.8 cc slow filling conditions at (A-D) 100, (E-H) 200 and (I-L) 300 ms. The inlet jet can be seen developing throughout diastole. The 12 and 9.6 cc SVs show a rotational flow beginning after mid diastole (I, J).

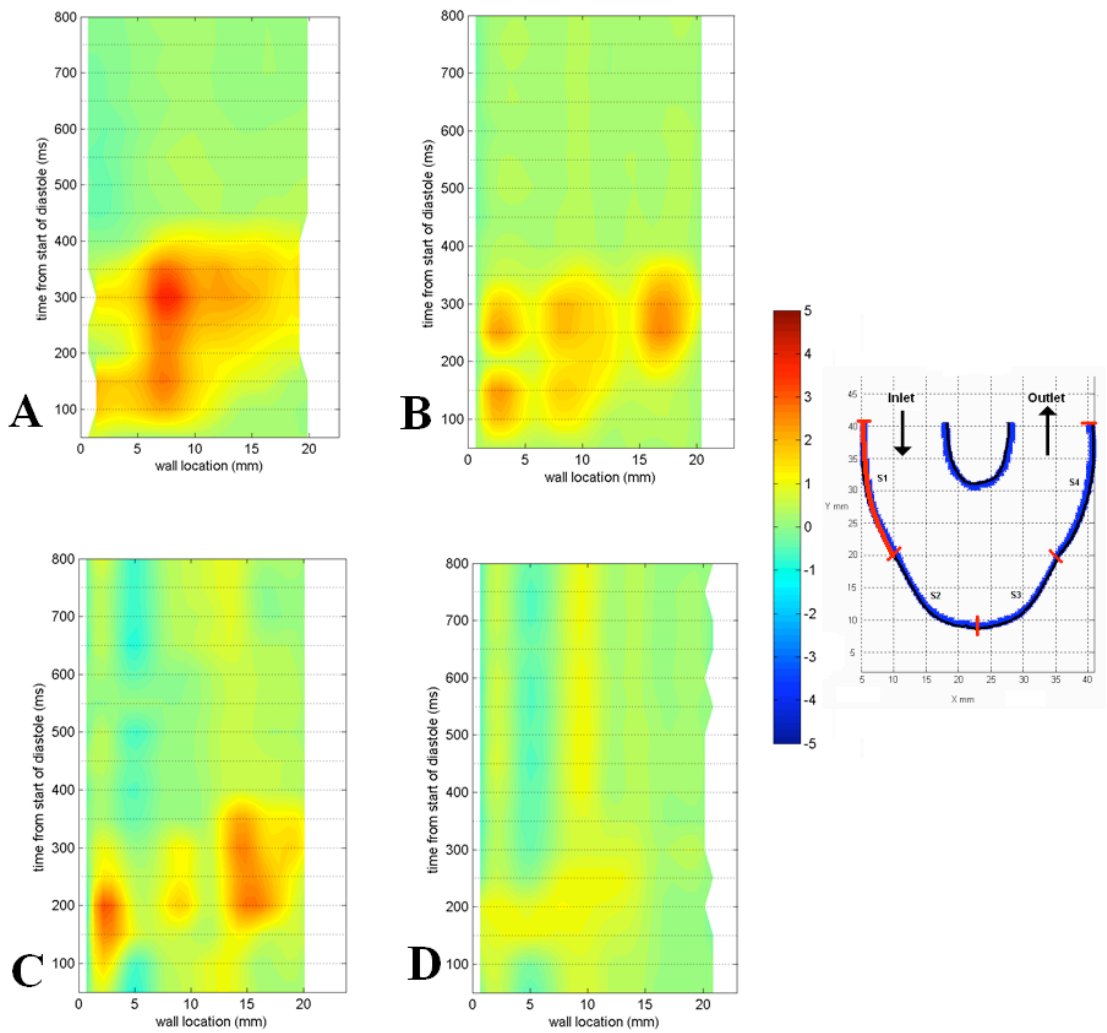

Figure 131: Surface 1 of the 7 mm parallel plane, located along the outside inlet wall and highlighted in red to the right, of the (A) 12, (B) 9.6, (C) 7.2 and (D) 4.8 cc slow filling conditions. The 12 cc SV conditions contains wall shear rates above the 500 s^{-1} threshold for a large portion of diastole, however the smaller SVs show less uniform washing of the inlet surface.

The patchy appearance of the wall shear rates means the entire surface is not being properly washed, increasing the chance of thrombus deposition. The 3.75 mm inlet normal plane, located closest to the outside inlet wall, shows the same inlet jet formation as the parallel planes, presented in Figure 132. These planes contain wall shear rates above the threshold along the walls of the inlet port during this development for the 12

and 9.6 cc SVs. However, the two smallest SVs, 7.2 and 4.8 cc, contain very low wall shear rates along these plane walls as shown in Figure 133.

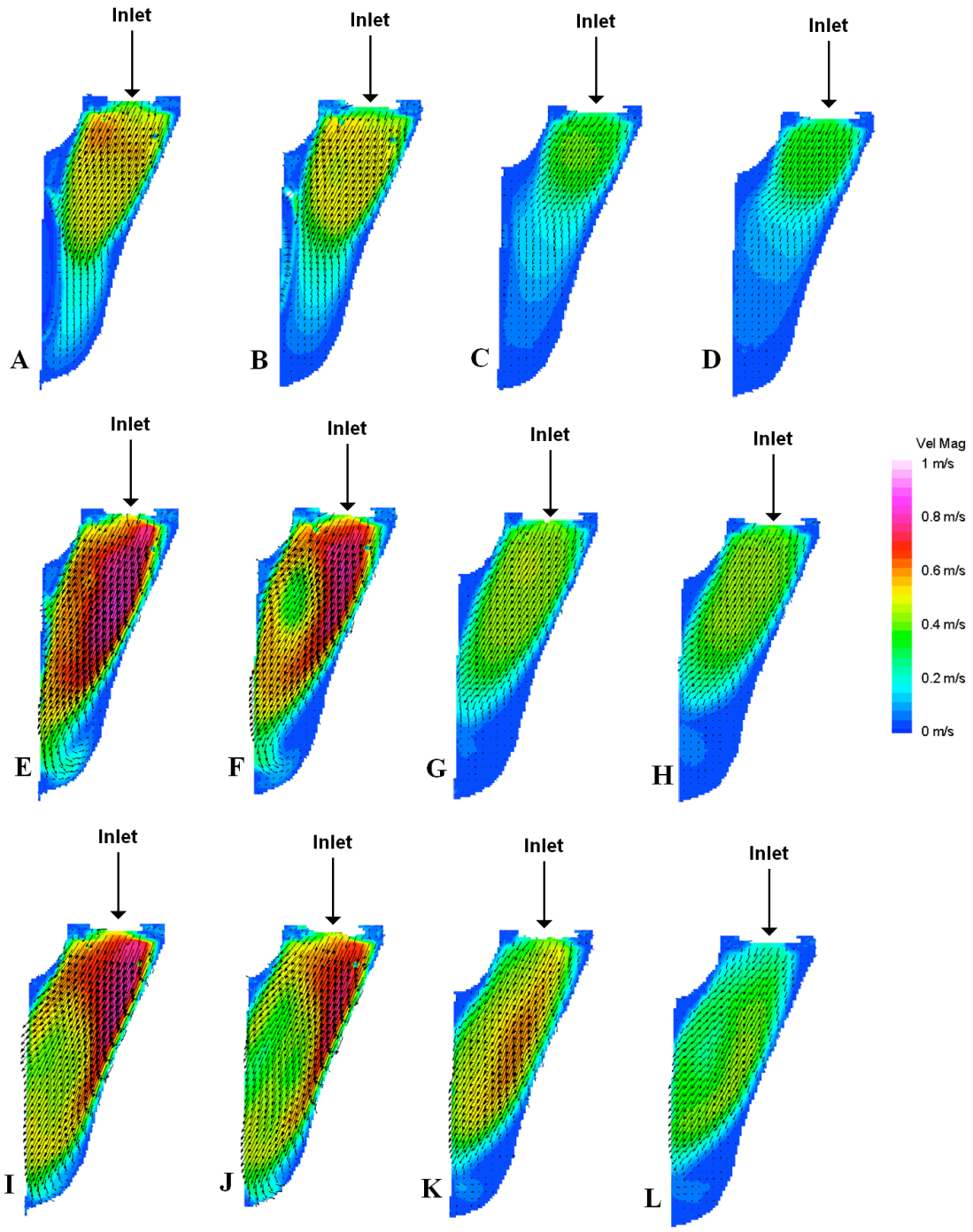

Figure 132: The 3.75 mm inlet normal plane of the (A, E, I) 12, (B, F, J) 9.6, (C, G, K) 7.2 and (D, H, L) 4.8 cc slow filling conditions at (A-D) 100, (E-H) 200 and (I-L) 300 ms. The 12 and 9.6 cc SVs show penetration after mid diastole (I, J), but the inlet jets of the 7.2 and 4.8 cc SVs have not reached the bottom of the device at this point (K, L).

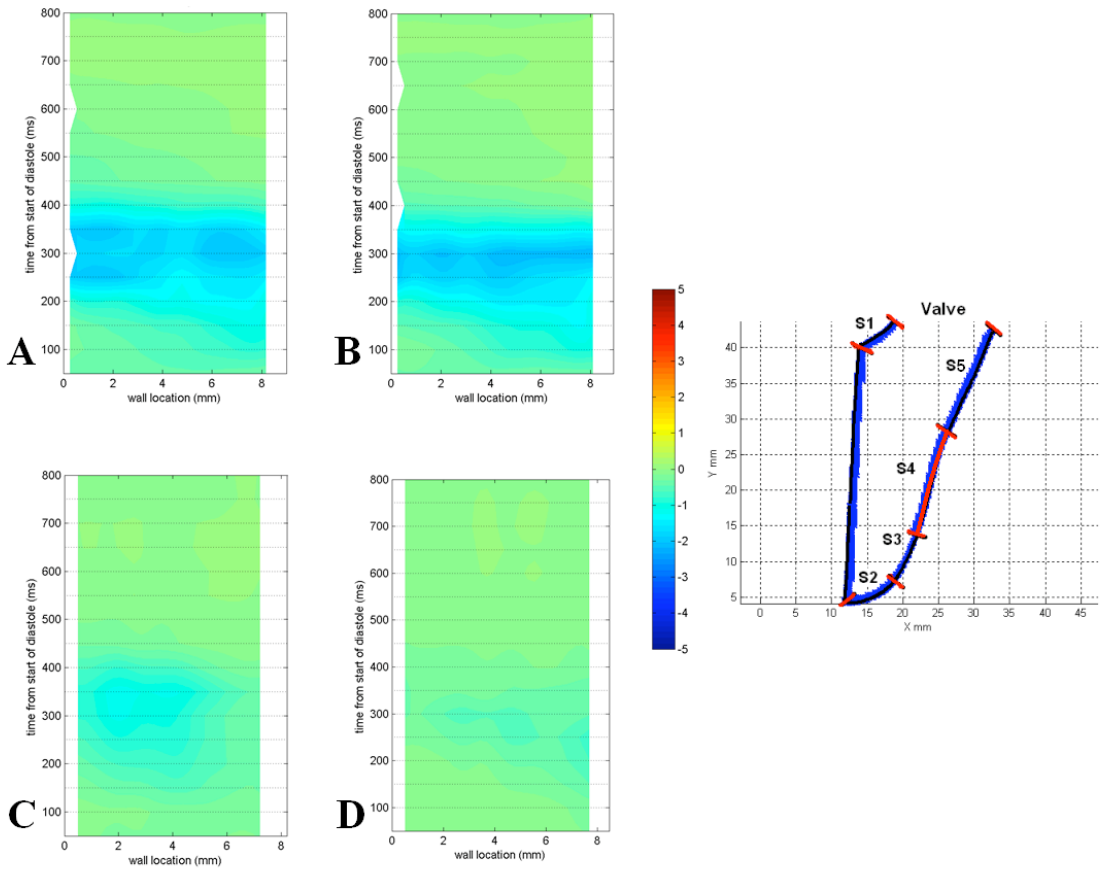

Figure 133: Surface 4 of the 3.75 mm normal inlet plane, located in the middle of the fluid side of the inlet as highlighted in red to the right, of the (A) 12, (B) 9.6, (C), 7.2 and (D) 4.8 cc slow filling conditions. The (A) 12 and (B) 9.6 cc SVs show some wall shear rates above the 500 s^{-1} threshold during mid diastole (300 ms). The wall shear rates of the (C) 7.2 cc and (D) 4.8 cc SVs along this surface remain low throughout the cycle.

The wall shear rates along the inlet surfaces during the jet formation indicate that using a slow filling method with SVs of 7.2 and 4.8 cc results in unacceptable conditions. The 12 cc and 9.6 cc SVs result in better wall shear rates results, however the slow development of the inlet jet results in a slower rotational flow set up.

5.4.2.2 Rotational Flow Development

Because the inlet jet development does not reach maximum velocity until mid diastole, the penetration into the bottom of the device and start of rotational flow is also delayed

until later in diastole. The flow reaches the bottom of the device at 300 ms at SVs of 12 and 9.6 cc as shown in Figures 82 and 95, respectively. The 7.2 cc SV shows penetration in the 8.2 and 11 mm parallel planes at the end of diastole, 450 ms, but a rotational flow field never develops (Figure 106 and 107). The 4.8 cc SV shows little movement in the body of the device throughout diastole and into systole (Figure 118), and this lack of a strong rotational flow field results in low wall shear rates along the bottom surfaces of the device. Figure 134 shows surfaces of the 11 mm plane for all the SVs.

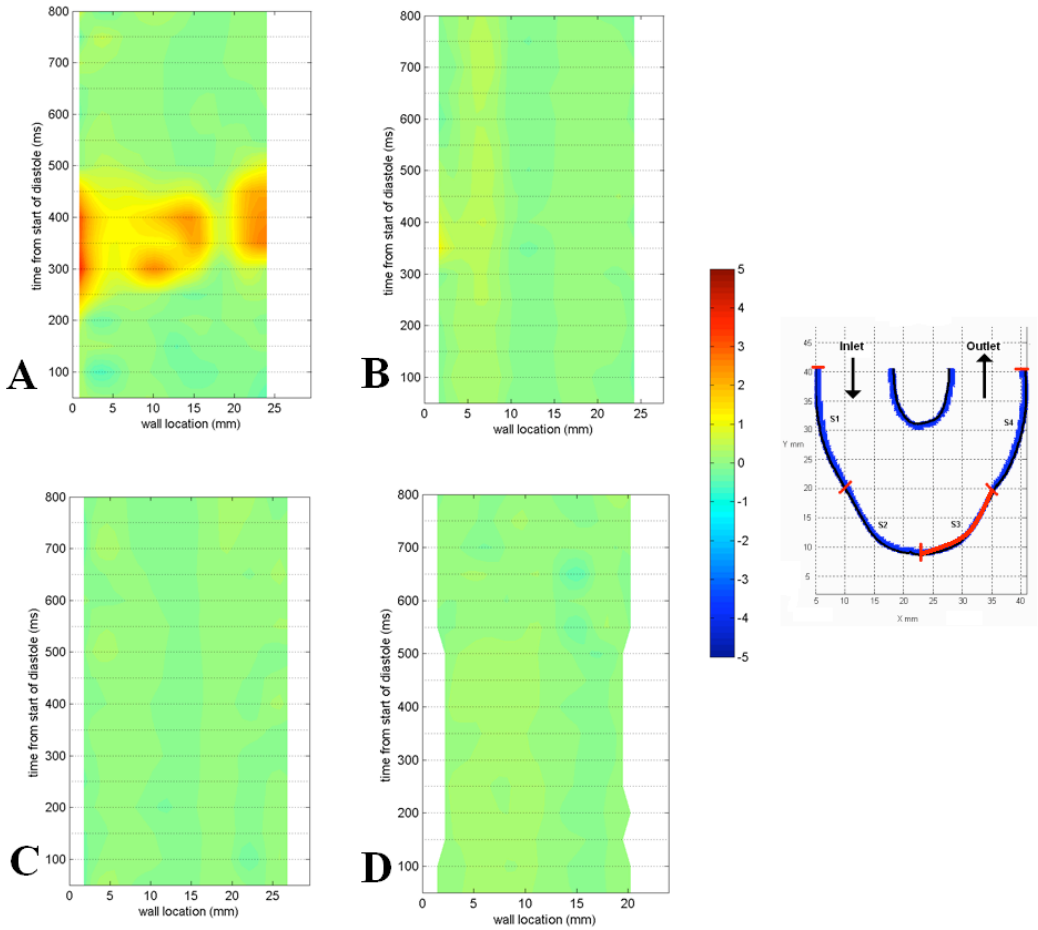

Figure 134: Surface 3 of the 11 mm parallel plane, located at the bottom wall of the outlet side as highlighted in red to the right, of the (A) 12, (B) 9.6, (C) 7.2 and (D) 4.8 cc slow filling conditions. The (A) 12 cc SV is the only condition with wall shear rates above the desired 500 s^{-1} threshold. The other three SVs show almost no change in the wall shear rates across the entire cycle for this surface.

The weak rotational flow fields and poor wall washing indicates that a SV reduction using a slow filling method does not result in desirable flow field conditions. The 12 cc SV is the only condition where an adequate rotational flow pattern and wall shear rates above the established threshold were observed.

5.4.2.3 Diastole Recirculation

The slow filling method contains an area of recirculation in the bottom of the device in the normal planes. This area was seen in the 7.5 and 11.25 mm inlet normal planes as well as the normal body plane of all four SVs, with the exception of the 7.5 mm plane of the 4.8 cc SV. As shown previously in Figures 83, 96 and 109, these areas develop from the inlet jet and rotate towards the fluid side of the device during mid to late diastole. These areas could be beneficial because they keep the fluid in the bottom of the device moving, reducing the stagnation in an area where thrombus formation is known to be a problem. As shown in Figure 135, the wall shear rate maps along surface 3, located near the bottom of the inlet planes, do show an increase in shear rates due to this recirculation. However, the wall shear rate values are not above the 500 s^{-1} threshold and therefore, would not adequately prevent thrombus deposition.

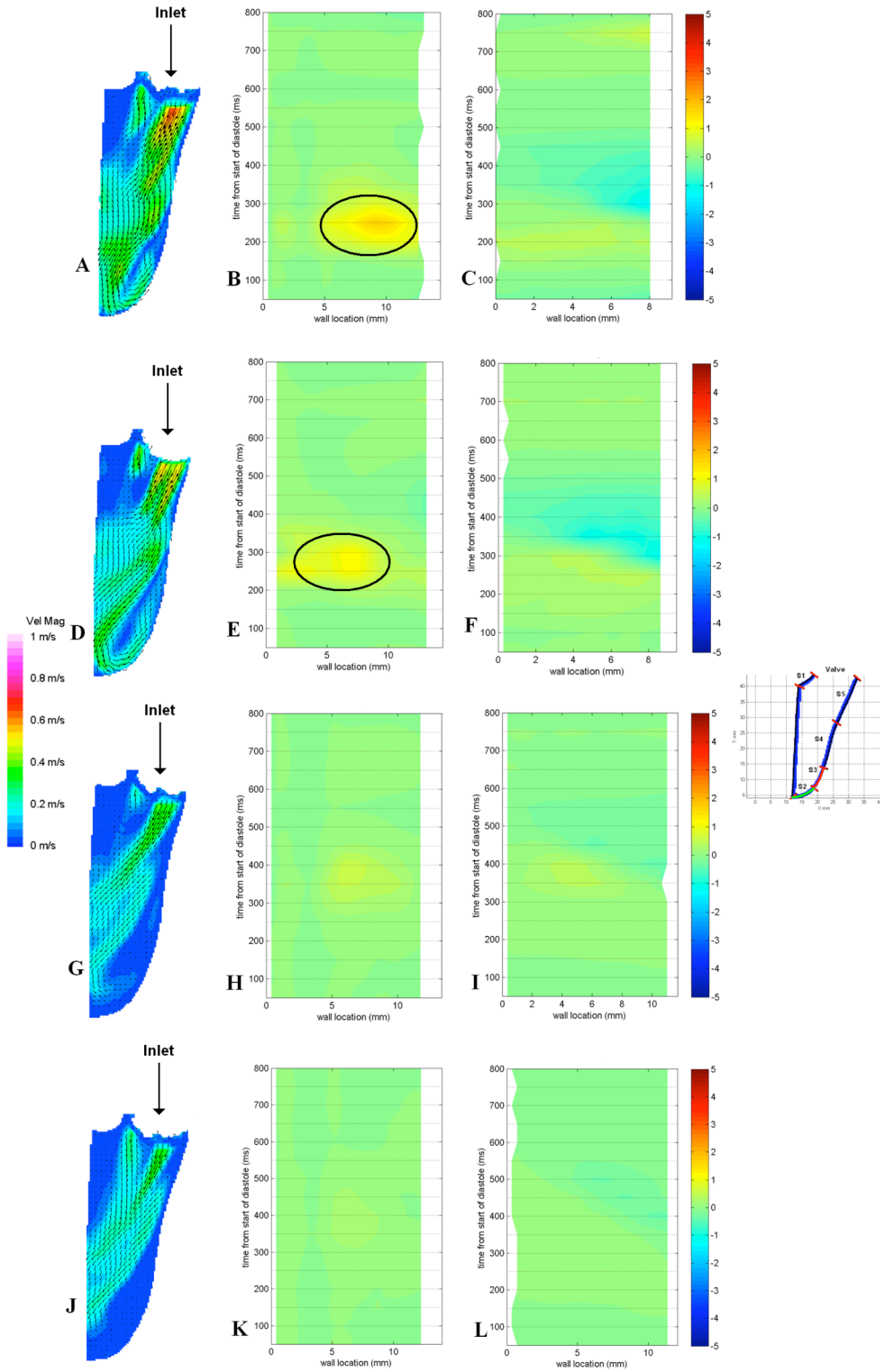

Figure 135: The 11.25 mm inlet normal plane of the (A) 12, (D) 9.6, (G) 7.2 and (J) 4.8 cc slow filling methods at 250 ms. Also, surfaces 2 (highlighted in green) and 3 (highlighted in red), which are located along the bottom of the 11.25 mm normal inlet plane, of the (B, C) 12, (E, F) 9.6, (H, I) 7.2 and (K, L) 4.8 cc flow filling conditions. The 12 and 9.6 cc SVs show some wall shear rates at the 500 s^{-1} threshold, highlighted in black, however most of the flow for all four conditions remains fairly stagnant.

In general, using the slow filling method resulted in poor rotational flow patterns and low wall shear rates as the SV is reduced. It would not be recommended to use this method for weaning.

5.4.3 Filling Method Comparison

The two filling methods observed in this study focused on the extreme ends of the conditions by compressing and expanding the inflow as much as possible. These result in a shorter, stronger inlet jet with the quick method and a longer, steady development of the inlet jet with the slow method. The differences between the methods can be seen in the development and strength of the rotational flow field and the wall shear rates observed.

The wall shear rates along the inlet surfaces mimic the behavior of the inlet jets developed by each filling method. As shown in Figure 121, the quick filling method results in a burst of high magnitude wall shear rates (>1000 s^{-1}) early in diastole. Figure 131 showed wall shear rates of lower magnitudes for a longer duration when the slow filling method was used. Overall, the quick filling method maintains more desirable wall shear rates along the inlet because the magnitudes are above the 500 s^{-1} threshold across the entire surface for at least a portion of the cycle at the 12, 9.6 and 7.2 cc SVs. Even the 4.8 cc SV contains wall shear rates above the thresholds for some portion of the surface. The slow fill method does not show sufficient wall shear along the entire surface at each SV.

When employing the quick filling method, the penetration into the bottom of the device and the set up of the rotational flow field occurs earlier in diastole. As shown previously in Figure 126, a coherent center of rotation is maintained throughout diastole for the 12, 9.6 and 7.2 cc SVs. In comparison the rotational flow using the slow filling method does not develop until mid diastole and breaks down around the same time as the quick method. This means there are more areas of stagnation in the body and outlet side of the device during diastole using the slow method. A comparison of this using the 9.6 cc SV parallel planes is given in Figure 136.

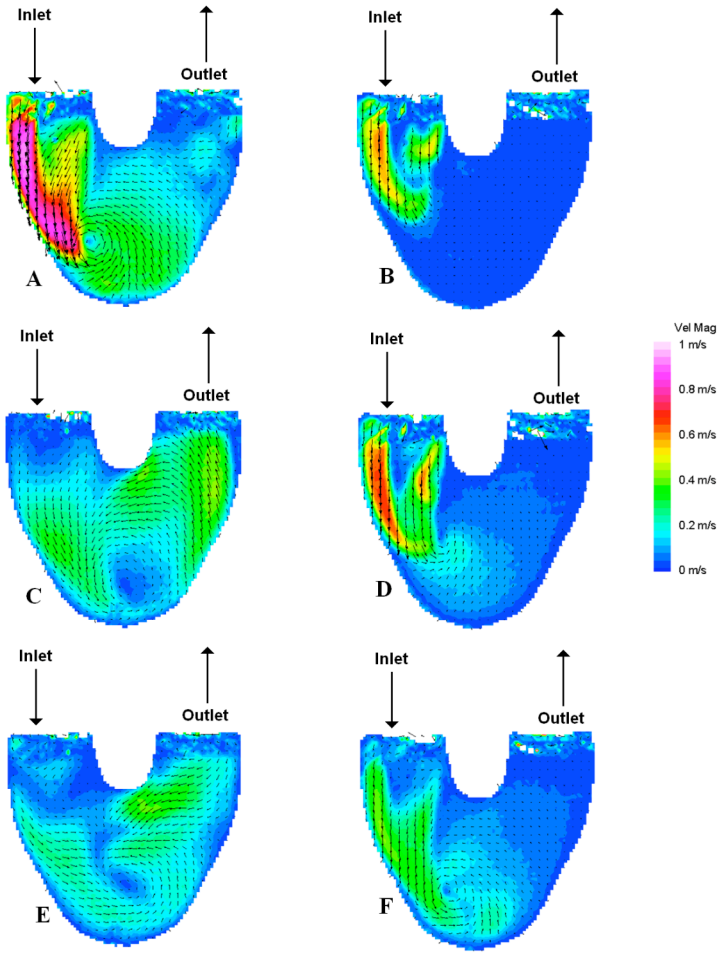

Figure 136: The 8.2 mm parallel plane of the 9.6 cc (A, C, E) quick and (B, D, F) slow filling methods at (A, B) 150, (C, D) 250 and (E, F) 350 ms. Comparisons between the two filling methods show an earlier onset of rotational flow by the quick filling method (A), as well as a stronger inlet jet. The slow filling method results in slower rotational set up and large areas of stagnation in the outlet side of the device, which remain until after mid diastole.

The quicker and tighter rotational flow field observed with the quick filling method also results in higher wall shear rates along the bottom surfaces of the device. This was shown earlier in Figures 127 and 134, along the bottom outlet surface of the 11 mm parallel plane.

As described in the Introduction, a previous study of end-diastolic delay (EDD) times using a beat rate of 50 bpm found an EDD of 50 ms to be best (Cooper 2010). This EDD was selected over a shorter EDD of 10 ms, similar to that of the slow fill method, and a longer EDD of 100 ms, similar to that of the quick fill method. At 50 bpm the longer EDD led to a strong inlet jet and quick onset of rotation, similar to what was seen in the current study. However, because the diastolic duration of 50 bpm was almost twice as long as that of the 75 bpm used here, the rotational flow field breaks down before the onset of systole. In this case the dissipation does not occur, with the exception of the 4.8 cc SV, before systole. Therefore, the stronger inlet jet and quicker rotational flow set up combined with better wall washing makes the quick fill method, which employs the longer EDD, more desirable when using a SV reduction.

5.4.4 Reduction Method Comparison

When a beat rate reduction method was employed, as described in Chapter 4, the device flow rate was reduced from 1.35 L/min at a beat rate of 75 bpm to 0.88 L/min at a beat rate of 50 bpm. The current SV reduction study ran the device at 75 bpm and 4 different SVs, 100 – 40%, resulting in flow rates of 0.91, 0.73, 0.54 and 0.35 L/min. The higher flow rate observed at 75 bpm during the beat rate reduction study was due to the

operation of the pump using a complete filling and ejection method that resulted in a SV larger than its nominal 12 cc size. Because of this, the 50 bpm flow rate in the beat rate reduction study is similar to the 12 cc SV condition in the current study. Therefore, these two conditions will be compared in order to evaluate the two flow rate reduction methods. Also because of its selection as the superior filling method, the quick fill condition will be used for comparisons.

The inlet jet of the 12 cc quick condition set up quickly and a center of rotation was located at 32% of diastole. In contrast, the inlet jet of the 50 bpm condition set up over the first half of the diastolic cycle and a center of rotation was observed at 50% of diastole. The early set up by the 12 cc quick fill condition led to less stagnation in the outlet side during diastole and a tighter rotational flow field. This comparison is shown in Figure 137.

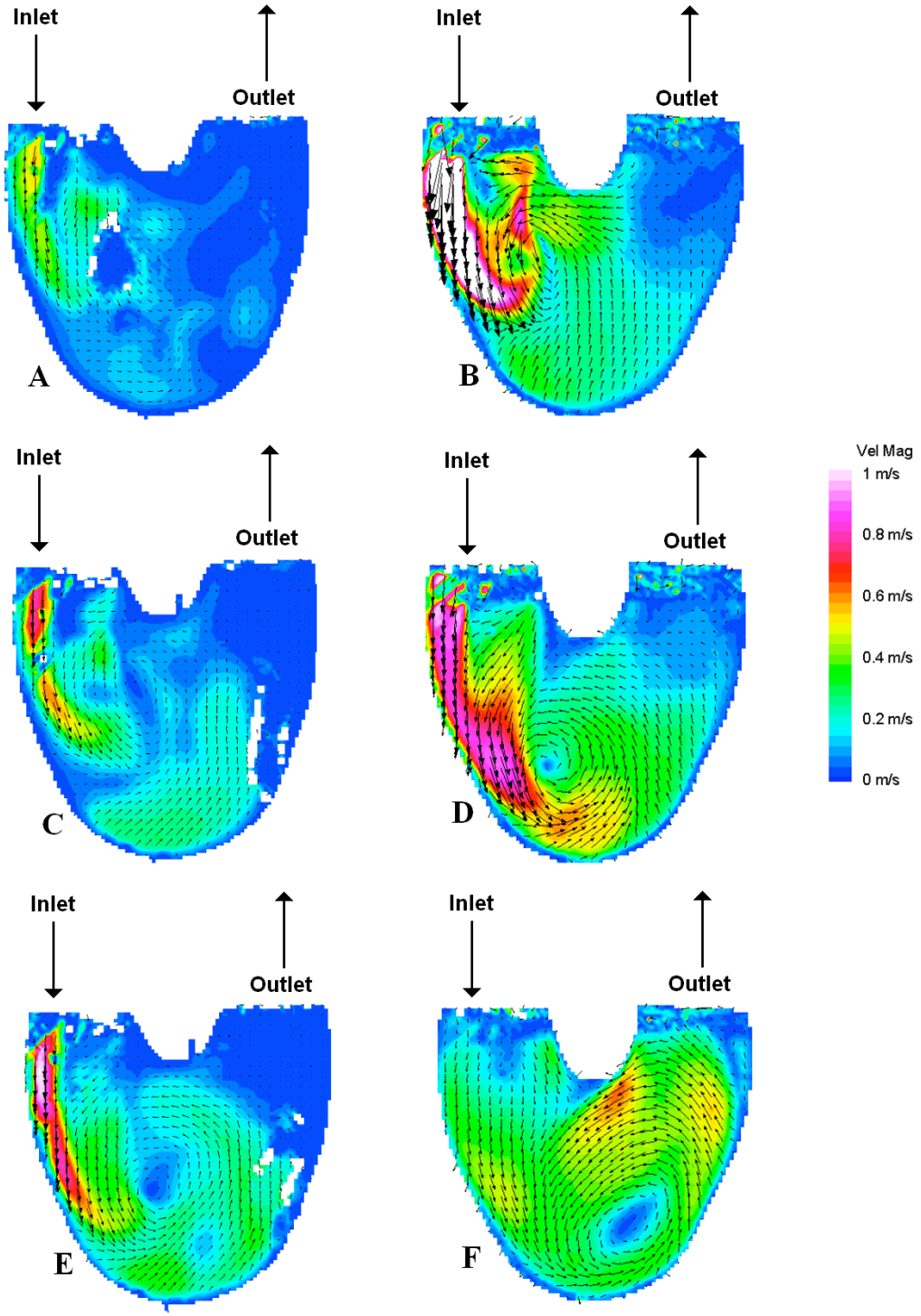

Figure 137: The 8.2 mm plane of the (A, C, E) 50 bpm and (B, D, F) 12 cc quick fill conditions at (A, B) 25%, (C, D) 35% and (E, F) 50% of the diastolic cycle. At 50 bpm the center of rotation is observed later in the cycle (E) and the outlet side of the device contains large areas of stagnation, shown in dark blue, through diastole.

These differences in the inlet jet formation and rotational set up led to differences in the wall washing of the device surfaces. For surface 1 in the parallel planes, located along the outer inlet port wall, the 12 cc condition maintained high wall shear rates (>1000 s^{-1}) across the entire surface for around 30% of the diastolic cycle. In comparison, the 50 bpm condition had some high wall shear rates (> 1000 s^{-1}) along about 20% of the surface for approximately 60% of diastole, with a few other spotty areas of high wall shear rates throughout diastole. This comparison, shown in Figure 138, shows better and more uniform wall washing of the inlet surfaces by the 12 cc quick condition.

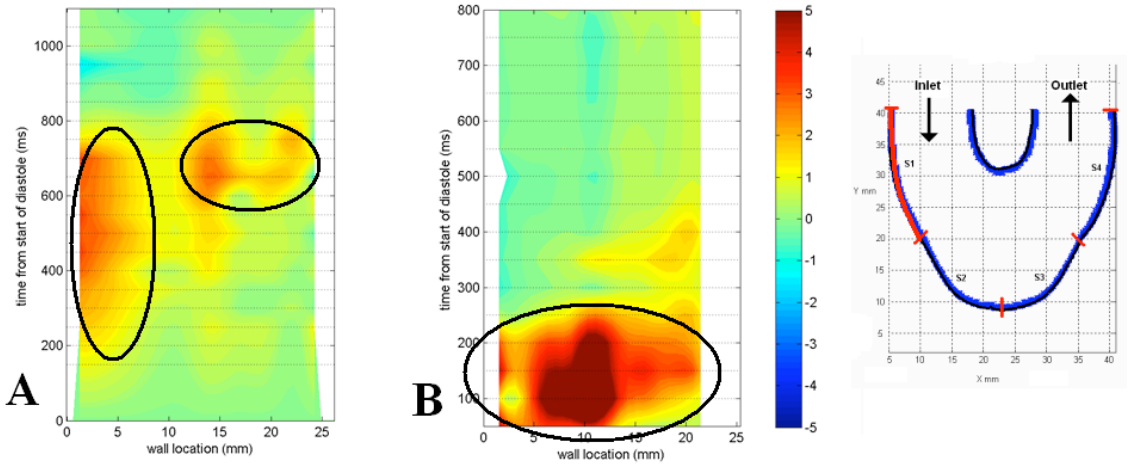

Figure 138: Surface 1 of the 8.2 mm parallel plane, located along the outside inlet wall and highlighted in red to the right, of the (A) 50 bpm and (B) 12 cc quick fill conditions. The (A) 50 bpm conditions contains areas of wall washing, highlighted in black, for a smaller area of the inlet surface and these areas are of lower wall shear rate magnitude. The (B) 12 cc quick fill condition maintains an area of wall washing across the entire surface, highlighted in black, that is concentrated at the beginning of diastole.

The 12 cc quick fill condition also maintains better wall washing at the bottom of the device as diastole progresses. Figure 139 presents surface 3 of the 11 mm parallel plane, located along the bottom half of the outlet side of the device, at both conditions. The 12 cc quick filling condition contains high wall shear rates (> 1000 s^{-1}) across the entire surface during early to mid diastole. The same surface of the 50 bpm condition remains stagnant through the entire cardiac cycle, indicating no wall washing is taking place.

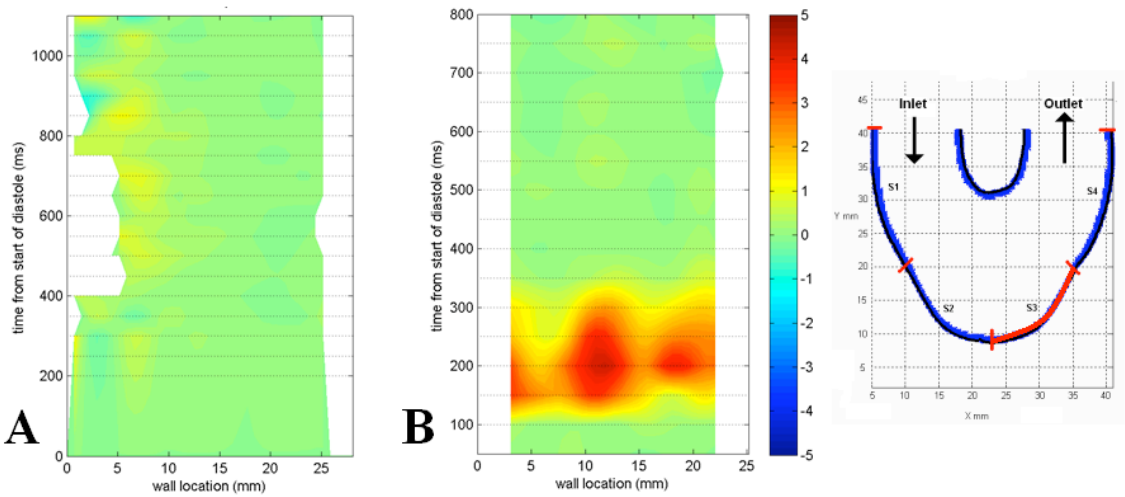

Figure 139: Surface 3 of the 11 mm parallel plane, located at the bottom wall of the outlet side as highlighted in red to the right, of the (A) 50 bpm and (B) 12 cc quick fill conditions. While the (B) 12 cc quick condition contains wall shear rates above the desired 500 s^{-1} threshold, the (A) 50 bpm condition does not show any signs of wall washing.

Overall, the SV method of flow reduction contains more desirable flow characteristics than the beat rate reduction method. Comparisons between the two methods employing the same flow rate indicated that the quick fill SV reduction method led to a stronger, tighter rotational flow field that lasted through diastole and better, more uniform wall washing of the device surfaces.

5.5 Conclusion

This study found that a SV reduction protocol has good potential for flow rate reduction of the PVAD for weaning applications. A stroke volume reduction from 100 to 60% using a quick filling method resulted in flow fields with strong inlet jet formation, penetration to the device bottom, a continuous rotational flow field through diastole and areas of adequate wall washing of device surfaces. This method of flow rate reduction was selected over a beat rate reduction method, as well as a slow filling stroke volume reduction method. The latter two methods resulted in poor rotational flow fields and large areas of stagnation in the device, which led to poor wall washing of the device surfaces and increased thrombgenicity potential. Therefore, a stroke volume reduction with a quick fill method would be the best choice.

This method of flow reduction is not without its own problems. Some device surfaces, especially when using the 7.2 cc SV, remain without adequate wall washing, which could increase the chance of thrombus deposition. Further investigation of possible operational protocol changes with this method is necessary. This may include changes to the systolic duration, which would decrease blood residence times. Also further studies of the quick fill parameter may provide better insight into maximizing the effect of a strong inlet jet while still maintaining a continuous rotational flow field.

The study also concluded that a reduction in SV to 4.8 cc, which is 40% of the total stroke volume, led to poor flow conditions regardless of the method used. This indicates that this level of flow reduction would not be possible in clinical applications. Studies of

adult VAD patients show that an EF of 60% is often a benchmark for consideration of device explantation. This is a good indication that a reduction of device stroke volume to 40% may not be necessary. However, reductions close to this level may be used and therefore, a better method to reduce thrombogenicity of these low flow conditions should be established. This should include investigations of operational protocol changes that focus on these very low flows.

This study has further confirmed that the use of *in vitro* physiological flow visualization tools are beneficial for testing the PVAD over multiple conditions. The ability to change conditions and collect timely data means that the effect of using the PVAD in different clinical applications can be observed. While this study has provided a good amount of information about flow rate reduction in pulsatile devices, there is much more to be learned about optimizing the flow field for the use in weaning applications. The methods used in this study can continue to aid in the development of the PVAD as a versatile and successful device for pediatric patients.

Chapter 6

DEVELOPMENT OF A THROMBUS SUSCEPTIBILITY POTENTIAL METRIC FOR PIV DATA

6.1 Specific Aim

It is desirable to objectively measure or infer device thrombogenicity from *in vitro* measurements. Flow visualization tools, such as PIV, provide information about the magnitude and direction of velocity vectors throughout the device. This information can then be used to calculate flow related parameters.

One example of this is the wall shear rate maps used in our flow studies. These were developed from the wall location and the corresponding near wall velocity information calculated from PIV images (Hochareon, 2003b). While helpful for identifying areas of low or high wall shear rates, comparing maps of similar characteristics, to determine thrombus potential is largely a subjective exercise. Therefore, the goal of this study is to develop a more objective metric for the likelihood of thrombus deposition along the surface, based on the information from the wall shear rate map.

6.2 Thrombus Susceptibility Potential Metric Development

In formulating a thrombus susceptibility potential (TSP), we find that there are a large number of factors that should be taken into consideration. Virchow's triad separates them into three categories: the properties of the blood, the properties of the blood contacting surface, and the fluid mechanics of the blood (Didisheim 1994). For this study, which focuses on the device fluid mechanics, the blood contacting surfaces and properties of the blood are considered constant. This is a reasonable assumption because the devices all

contain the same blood sacs, and the patients are usually on similar anti-coagulation protocols. This then allows the variables of the TSP to be related to the fluid mechanics.

6.2.1 Equation

To develop a TSP metric from our PIV data, we use a CFD study of an adult sized VAD, by Medvitz, in which wall shear rates were used to develop a device TSP (Medvitz 2008). Experimental data has shown there is a peak wall shear rate ($\dot{\gamma}_{peak}$) below which there is significant platelet deposition on a surface. At or below $\dot{\gamma}_{peak}$, the deposition of platelets is constant. Once the wall shear rate becomes greater than $\dot{\gamma}_{peak}$, the amount of platelet deposition begins to decrease. The amount of platelet deposition continues to drop until a second critical value, known as the cutoff wall shear rate ($\dot{\gamma}_{cutoff}$) is reached, beyond which no platelet deposition occurs. These values are treated as constants in the model, and the measured wall shear rate at the surface ($\dot{\gamma}_{\omega}$) is used as the variable.

Another important element in the TSP is the exposure time of the wall shear rates. The exposure time is important when dealing with pulsatile VADs because the flow is unsteady. Therefore, the wall shear rate across a surface will change throughout the device cycle. Following a study by Balasurbramanian et al. we assume that the longer a surface is exposed to shear rates above $\dot{\gamma}_{peak}$ the less platelet deposition occurs (Balasubramanian 2002). Therefore, the exposure time (t) of the wall shear rates is important. We also assume that there is some minimum time (t_{crit}) that the surface needs to be exposed to $\dot{\gamma}_{cutoff}$ in order to prevent platelet deposition.

Following Medvitz, the TSP equation is given in 13.

$$TSP = 1 - \sum_{0}^{N} \frac{\Delta t \dot{\gamma}_{\omega}}{\dot{\gamma}_{cutoff} t_{crit}} \bullet \frac{e^{((\dot{\gamma}_{\omega} - \dot{\gamma}_{peak})/(\dot{\gamma}_{cutoff} - \dot{\gamma}_{peak}))} - 1}{e^{1} - 1} \qquad (13)$$

Here, 1 designates a high potential of thrombus deposition, and 0 represents a very low potential (Medvitz 2008). For PIV applications, N is the number of time steps taken over the entire cycle and Δt is the length of the time step between each acquisition time. The exponential function is a weighing parameter, which results in wall shears close to the $\dot{\gamma}_{peak}$ having little influence on reducing the TSP.

6.2.2 Use with PIV Data

Once the equation was selected, it was necessary to consider how to apply it to the PIV data. The wall shear rate maps are produced from locating the wall of the PIV image and the near wall velocity from the average PIV vector fields, as described earlier in section 3.5.2. This process results in a matrix of wall shear rates based on location along the wall and time in the cycle. Because it is assumed that peak platelet deposition occurs at $\dot{\gamma}_{peak}$ or below, any value of $\dot{\gamma}_{\omega}$ less than $\dot{\gamma}_{peak}$ is set to $\dot{\gamma}_{peak}$, which corresponds to a TSP of one. Similarly, we assume that any wall shear rate at or above $\dot{\gamma}_{cutoff}$ results in no platelet deposition, and therefore, any value of $\dot{\gamma}_{\omega}$ larger than $\dot{\gamma}_{cutoff}$ is set to $\dot{\gamma}_{cutoff}$, which corresponds to a TSP of zero. After these maximums and minimums are set, the TSP equation is applied to each wall shear rate value along the surface. The locations of the shear rate values are based on the placement of the interrogation regions along the

surface. The values at each location are summed over the entire cycle to calculate the TSP at each wall location across the device surface. These TSPs can then be plotted to show what locations along a surface have a high potential for thrombus deposition, or they may be averaged to establish a single TSP for each wall shear map that can be used for comparisons. An example wall shear rate map, TSP surface plot and total TSP is given in Figure 140.

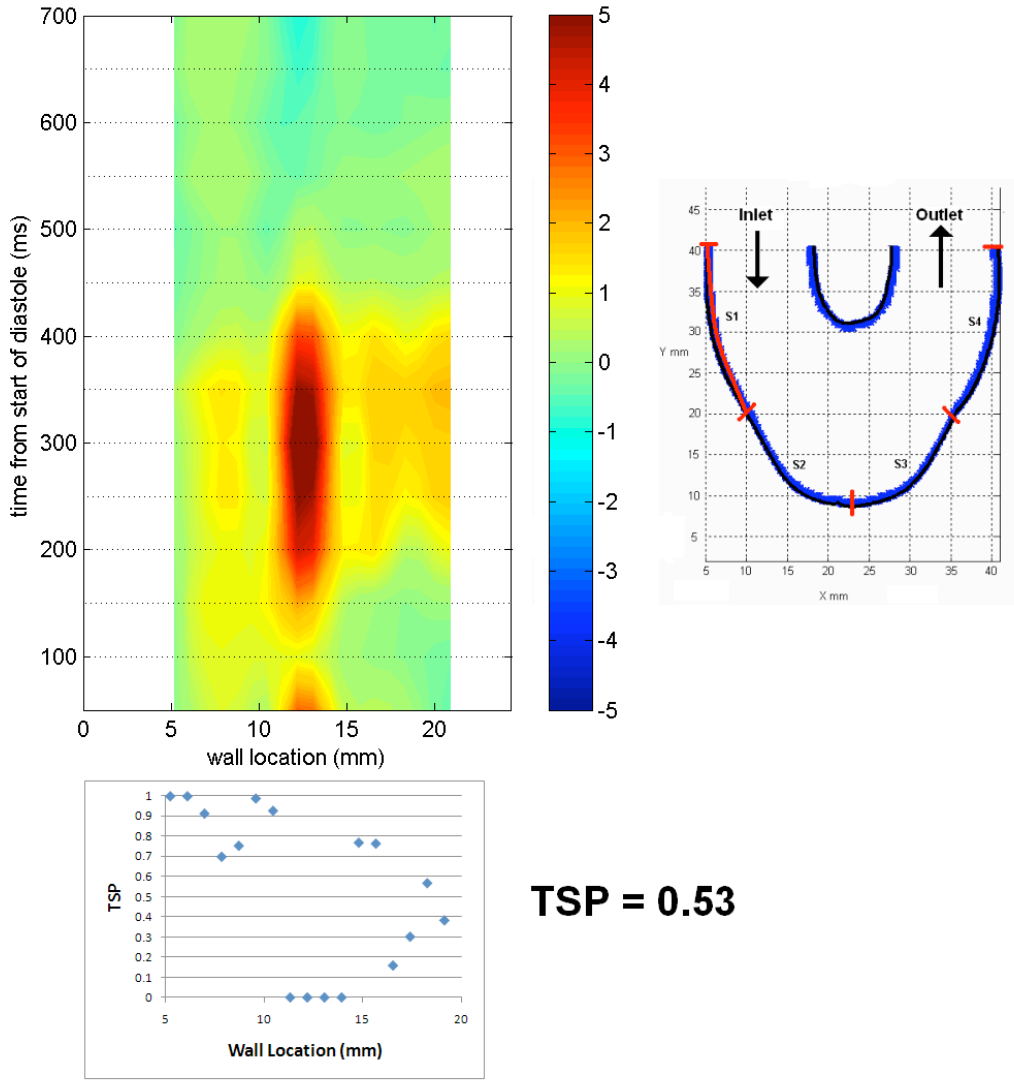

Figure 140: An example of a wall shear rate map and TSP plot along surface 1 of the 8.2 mm parallel plane, as highlighted red to the right. The TSPs at each wall location are plotted on the graph below the wall shear rate map. A total TSP of 0.53 was calculated for this data.

6.2.3 Limitations

6.2.3.1 Temporal Study

One limitation of the PIV data used in the PVAD studies is that it is acquired over a finite number of time steps throughout the cycle. In a previous study, we acquired data every 10 ms instead of our standard 50 ms intervals. The wall shear maps contained similar results, and it was concluded that 50 ms intervals was adequate for our studies. We revisit this question here for the TSP. The TSP was found at both 10 and 50 ms intervals. Examples of a surface with low wall shear rates, and a surface with some high wall shear rates are shown in Figure 141.

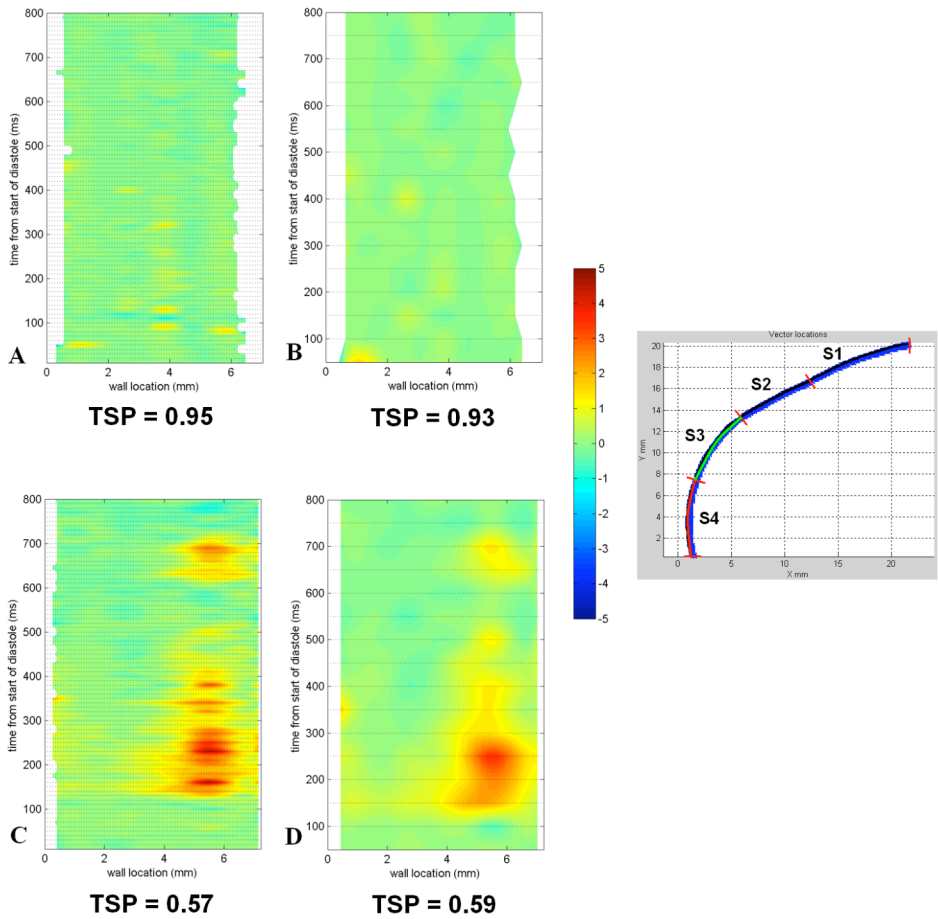

Figure 141: The wall shear rate maps along surfaces (A, B) 3 and (C, D) 4, found along the bottom of the device and highlighted in green and red, respectively, to the right, of a normal operating condition data taken every (A, C) 10 ms and every (B, D) 50 ms. The wall shear rate maps show very similar patterns, and the TSP values are also very close in value.

Surface 3, which at low wall shear rates, had a very high TSP at both 10 and 50 ms intervals, with only a 0.02 difference between the two. Surface 4 had a "high" wall shear rate pattern, but the TSP remained similar between the two time steps, with a difference of 0.03. This study suggests that 50 ms time intervals are probably adequate for our TSP PVAD studies.

6.2.3.2 Metric Sensitivity

Here, we observed the effect of changing $\dot{\gamma}_{peak}$, $\dot{\gamma}_{cutoff}$, and t_{crit} on the value of the TSP. We used existing wall shear rate data of the PVAD. The $\dot{\gamma}_{peak}$, $\dot{\gamma}_{cutoff}$, and t_{crit} were each given an initial value. The $\dot{\gamma}_{peak}$ was set at 500 s^{-1}, which has been established as the threshold value for peak thrombus deposition on materials similar to that used in the PVAD (Hubbell and McIntire 1986). The $\dot{\gamma}_{cutoff}$ was set at 1000 s^{-1}, which is an established experimental value for the inhibition of platelet deposition (Balasubramanian 2002). The t_{crit} was set at 100 ms, which was twice the length of a PIV time step. We selected this time because it helped reduce the effect of a short burst of high wall shear rates at a single time step. The data used were the wall shear rates maps at surface 1 and 2 of the 8.2 mm parallel plane of the PVAD under normal operating conditions (75 bpm with a systolic duration of 340 ms, the valves were set at 0° angles, and a 40% hematocrit non-Newtonian blood analog). The original shear maps of the data are shown in Figure 142.

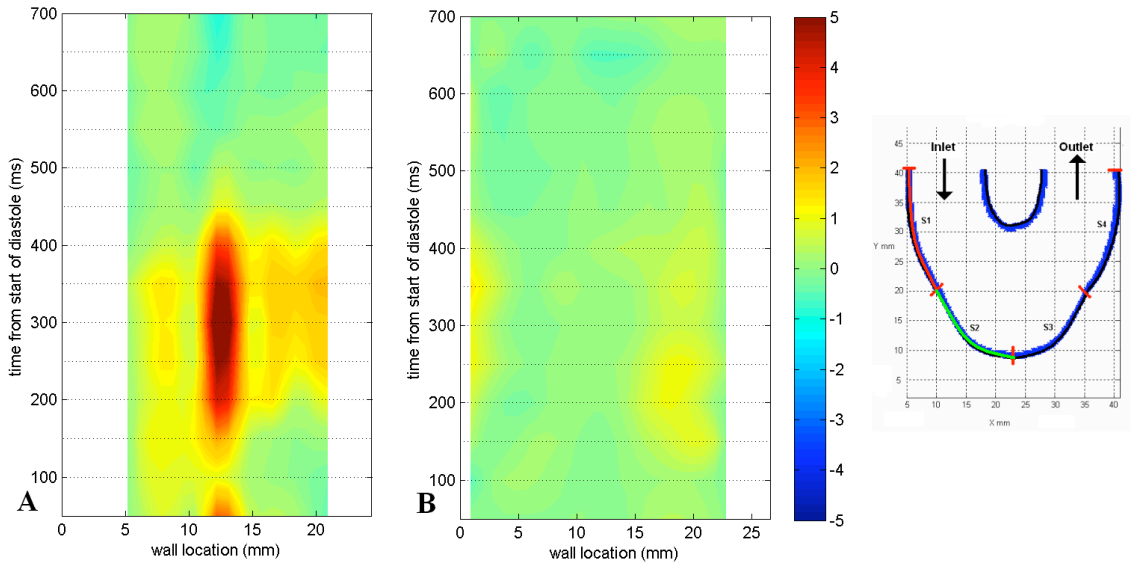

Figure 142: The wall shear rate maps of surfaces (A) 1 and (B) 2 of the 8.2 mm parallel plane, which are along the inlet side of the pump and highlighted in red and green, respectively, to the right, of the pump at normal operating conditions. These surfaces were used in the TSP sensitivity study.

The TSP was found for each data set using these values. The TSP was then calculated again as two of the values were held constant, and the third was varied incrementally. The TSP was then plotted, so that the slope of the curve was a measure of sensitivity. The sensitivity plots of both surfaces for each variable are shown in Figures 143-145.

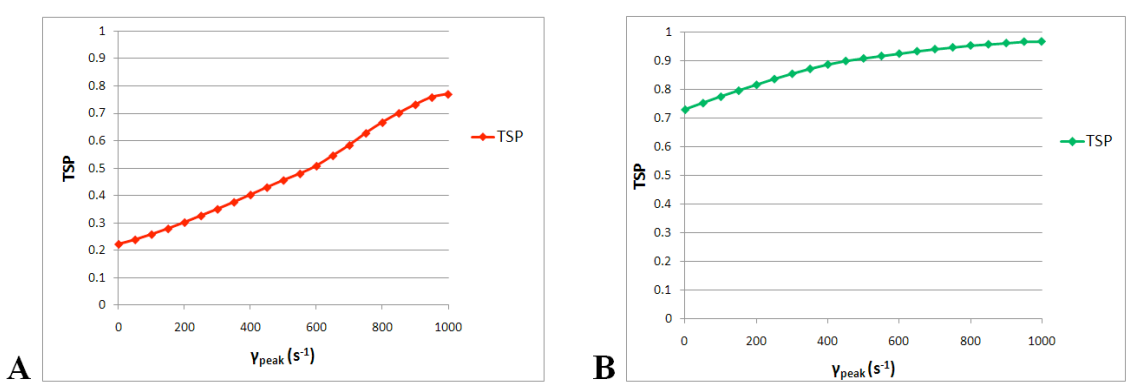

Figure 143: The sensitivity curve of the TSP along surfaces (A) 1 and (B) 2 with a variable $\dot{\gamma}_{peak}$. The $\dot{\gamma}_{peak}$ was varied from 0 to 999 s^{-1} at increments of 50 s^{-1}. Both surfaces showed an increase in TSP as the $\dot{\gamma}_{peak}$ was increased.

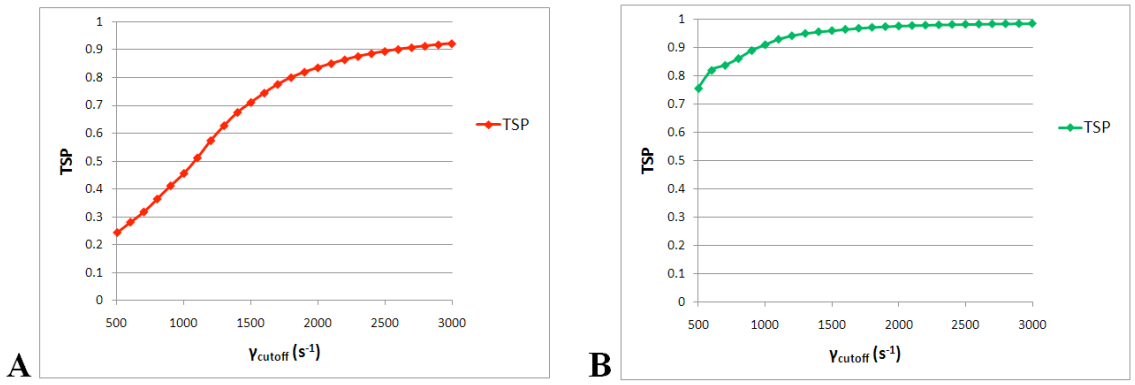

Figure 144: The sensitivity curve of the TSP along surfaces (A) 1 and (B) 2 with a variable $\dot{\gamma}_{cutoff}$. $\dot{\gamma}_{cutoff}$ was varied from 501 to 3000 s^{-1} in increments of 100 s^{-1}. At both surfaces the TSP increased with an increase in $\dot{\gamma}_{cutoff}$.

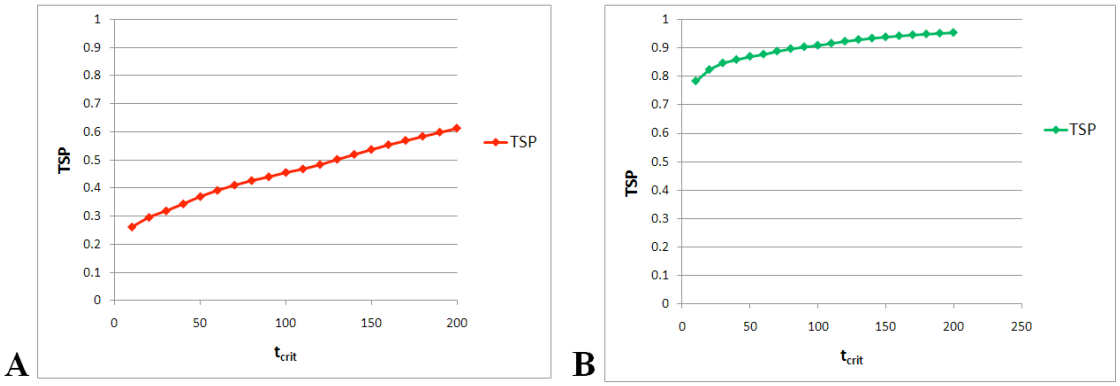

Figure 145: The sensitivity curve of the TSP along surfaces (A) 1 and (B) 2 with a variable t_{crit}, which was varied from 10 to 200 ms in increments of 10 ms. The TSP of both surfaces increased with an increase in t_{crit}.

We found that the TSP is increased with increasing $\dot{\gamma}_{peak}$, $\dot{\gamma}_{cutoff}$, and t_{crit} for each of the surfaces. This means that information obtained from the TSP is not appropriate for inference of thrombus deposition *in vivo,* as $\dot{\gamma}_{peak}$, $\dot{\gamma}_{cutoff}$, and t_{crit} are not well defined. For each of $\dot{\gamma}_{peak}$, $\dot{\gamma}_{cutoff}$, and t_{crit} surface 1 had larger a slope; therefore, showing greater sensitivity. Surface 2 also had a higher TSP, which showed less sensitivity. This would indicate that surfaces with a larger TSP are less affected by change, i.e. a poorly washed

surface will have a high TSP regardless of the changes to constants. In the current study we maintain constant $\dot{\gamma}_{peak}$, $\dot{\gamma}_{cutoff}$, and t_{crit} throughout and use this TSP study for comparisons only.

As mentioned previously, the lack of information about the behavior of thrombus deposition on surfaces such as those found in the PVAD limits the ability to directly correlate our measured TSP with *in vivo* thrombus deposition. This led to the question of how more information about the deposition behavior could help the accuracy of this tool. For example, if it had been proven that a material surface experiencing a wall shear rate of 500 s^{-1} or more for at least 20 ms would contain no platelet deposition it would be easy to find such locations along the wall using the TSP. However, if it was observed that 50 ms of exposure time was required, the problematic locations could be vastly different. To illustrate this point the TSP was found along surface 4 of the high magnitude data shown in Figure 141. This data was selected because it had the greatest temporal resolution with data points every10 ms throughout the cycle. The t_{crit} was varied from 10 to 100 and the resulting TSPs along the surface are shown in Figure 146.

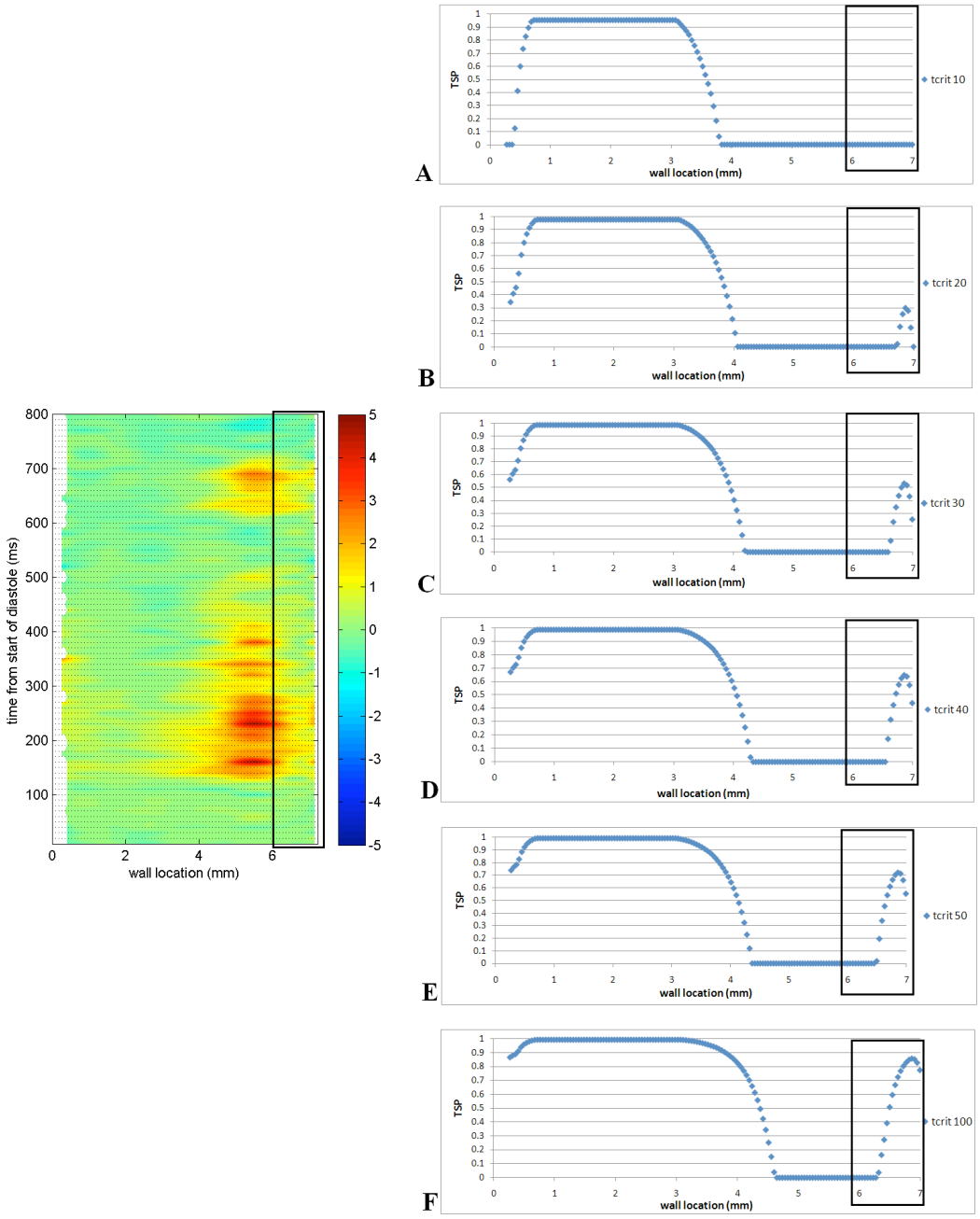

Figure 146: The TSP surface plots along surface 4 of the high magnitude data, the wall shear rate map for which is shown to the left. The plots were found using varying t_{crit} of (A) 10, (B) 20, (C) 30, (D) 40, (E) 50 and (F) 100 ms. An area of interest, highlighted in black, is from 6 to 7 mm across the surface, where the TSP pattern changes greatly as the t_{crit} is varied.

The TSP value across the entire surface ranges from 0.42 to 0.65 for the t_{crit} values used. While this mimics what was observed in the previous sensitivity study, it is more interesting to observe the effect of changing the t_{crit} on the surface TSP plot. As shown in Figure 146, the TSP pattern between each t_{crit} value remains similar between 0 and 6 mm across the surface. While the size of the high and low thrombus potential areas changes slightly, the general trend is that the low wall shear rate region from 0 to 3 mm along the surface has a high thrombus potential, while the high wall shear rate region from 4 to 6 mm has a low thrombus potential. The area of most interest is from 6 to 7 mm, highlighted with a black box in Figure 146, where the shear rate is neither very high nor low. This area shows the most variation between the t_{crit} values, going from no thrombus potential at 10 ms to a high potential at 100 ms. These observations indicate, that better information about *in vivo* deposition would be most beneficial for areas of shear in between $\dot{\gamma}_{peak}$ and $\dot{\gamma}_{cutoff}$.

This study questions the previous temporal study, which showed that time intervals of 10 and 50 ms both resulted in similar TSPs. To check our original conclusion, the surface TSPs were plotted for both time step intervals, with t_{crit} of both 10 and 50 ms. As shown in Figure 147, the surfaces maintain similar patterns. This means that the sensitivity of t_{crit} is related to its value, and not the temporal resolution of the data points. However, having better resolution does result in more options when using the TSP and is desirable for when better t_{crit} information is available.

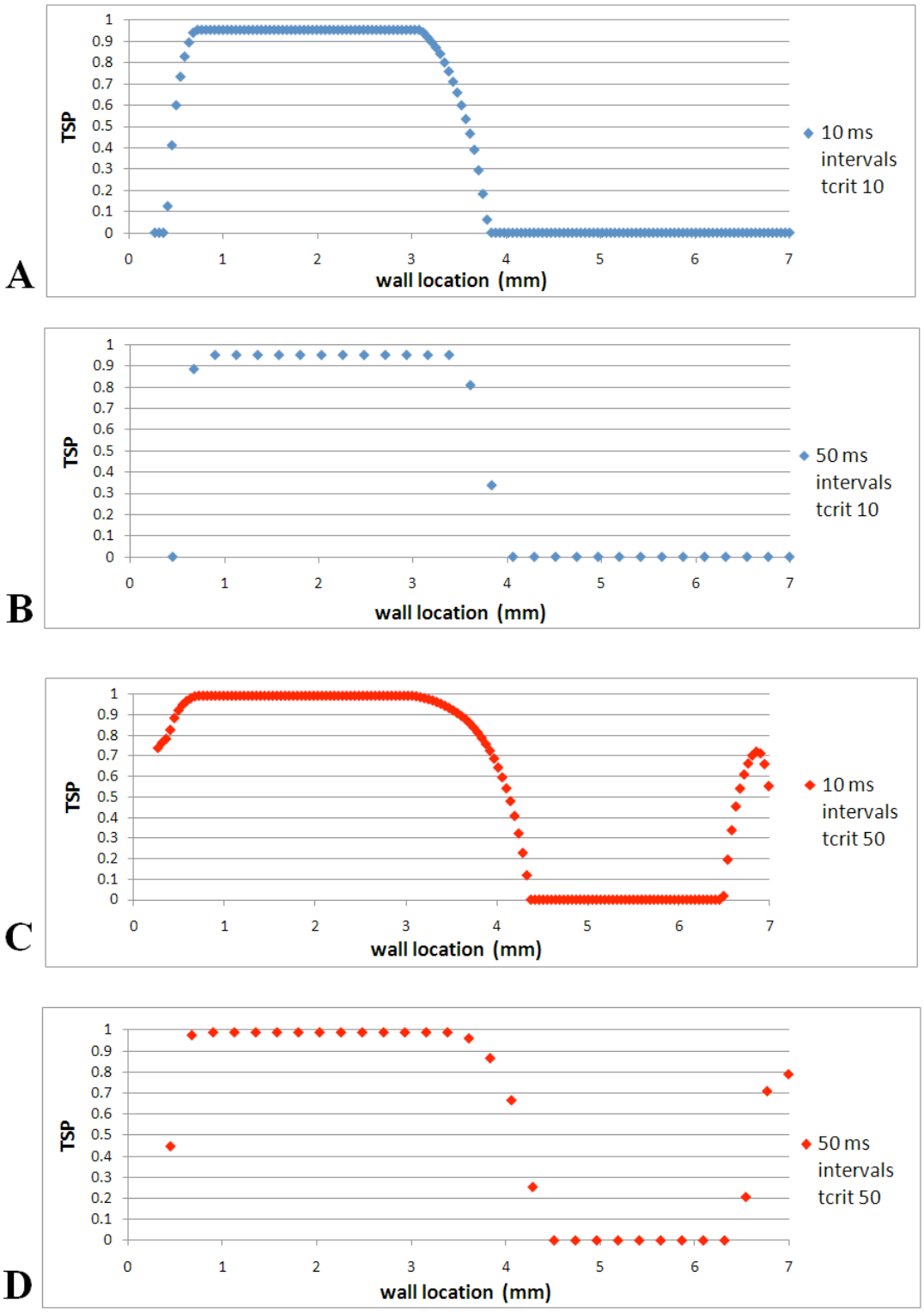

Figure 147: The surface TSP plots for (A) 10 ms intervals at 10 ms t_{crit}, (B) 50 ms intervals at 10 ms t_{crit}, (C) 10 ms intervals at 50 ms t_{crit}, and (D) 50 ms intervals at 50 ms t_{crit}. As observed in the plots, the TSP surface patterns remain similar between the two sets of intervals with the changing t_{crit}.

6.3 TSP Application

The TSP metric was applied to past PVAD studies, as well as the current flow reduction studies.

6.3.1 Valve Orientation Study

As described previously in section 1.3.3, we ran a parametric study of valve orientation on the PVAD (Roszelle 2010b). Several orientation combinations of the inlet and outlet BSM valves were tested and resulted in a +15° angle being selected for both valves. Because the TSP metric had not been developed at the time of this study, it was desirable to examine these results using this additional metric.

6.3.1.1 Results

The TSP constants were set at a $\dot{\gamma}_{peak}$ of 500 s^{-1}, a $\dot{\gamma}_{cutoff}$ of 1000 s^{-1}, and a t_{crit} of 100 ms. The metric was found for the 8.2 mm parallel surface of each of the orientations. These are reported in Table 4.

Table 4: The TSP values across all 4 surfaces of the 8.2 mm parallel plane for the full range of valve orientations.

Orientation	TSP Surface 1	TSP Surface 2	TSP Surface 3	TSP Surface 4
0° Inlet 0° Outlet	0.48	0.99	0.56	0.33
0° Inlet +15° Outlet	0.05	0.67	0.29	0.10
0° Inlet +30° Outlet	0.04	0.92	0.60	0.09
+15° Inlet 0° Outlet	0.23	0.79	0.56	0.53
+15° Inlet +15° Outlet	0.00	0.65	0.30	0.17
+15° Inlet +30° Outlet	0.00	0.85	0.41	0.07
+30° Inlet 0° Outlet	0.07	0.80	0.66	0.30
+30° Inlet +15° Outlet	0.08	0.71	0.73	0.21
+30° Inlet +30° Outlet	0.15	0.80	0.80	0.57

6.3.1.2 Discussion

The TSP values corresponded well to the behavior observed on the wall shear rate maps. An example of this is surfaces 2 and 3 of the 0°-0° orientation. As highlighted in Figure 148, surface 2 contains very low wall shear rates across the entire region, with very few areas above the $\dot{\gamma}_{peak}$. This resulted in a TSP of 0.99, which indicates a high probability of thrombus deposition. Surface 3 of the same plane contains wall shear rates at or above $\dot{\gamma}_{peak}$ along more than half the surface for a portion of the cycle. The resulting TSP of 0.56 would indicate that the surface was less likely to have thrombus deposition than surface 2, but there is still a chance of deposition. The plots of the individual location TSPs also show that lower TSP of surface 3 is biased to one side. This information is helpful in locating specific areas along the surface that may prove problematic. Similar conclusions to those found by the TSP data would have been made by observing the wall shear rate maps alone.

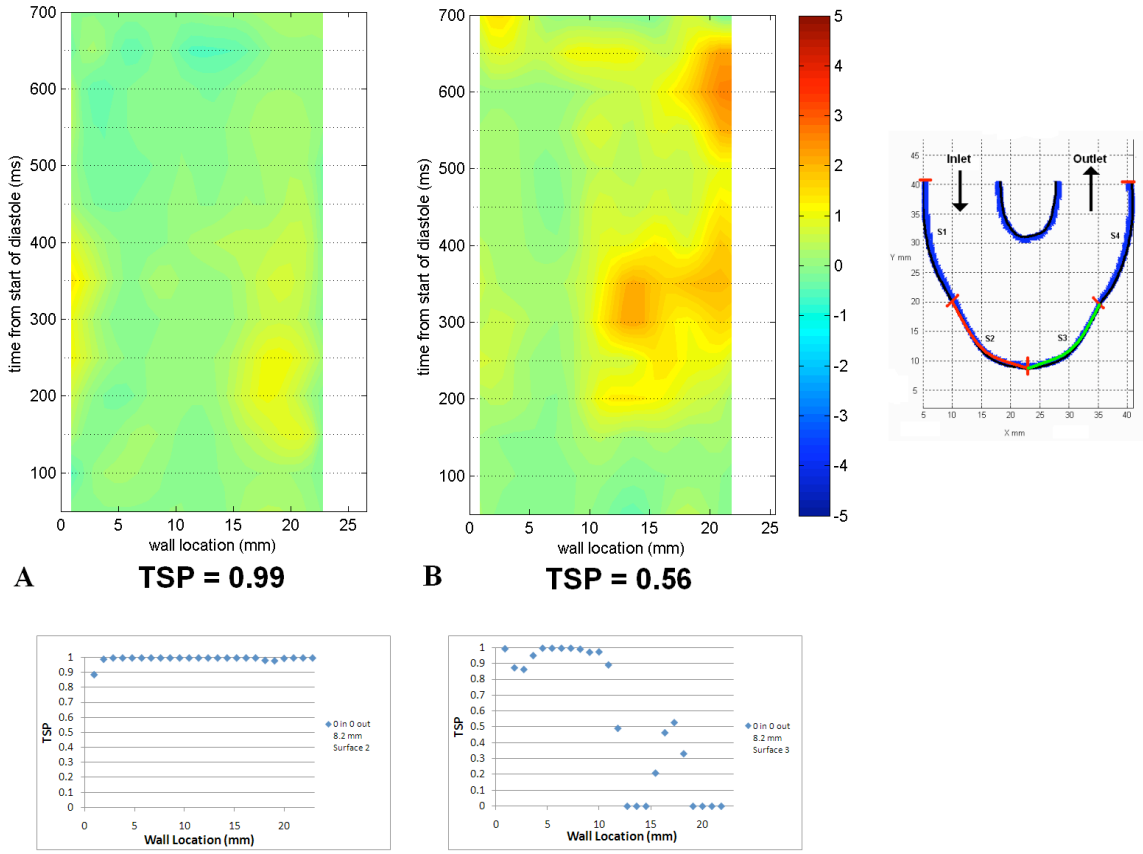

Figure 148: The wall shear rate maps along surfaces (A) 2 and (B) 3, which are located along the bottom of the plane and are highlighted in red and green, respectively, to the right, of the 0° inlet 0° outlet 8.2 mm parallel plane. The TSP results correspond well to the conclusions that would have been drawn from the wall shear rate maps alone.

The TSP also corresponded well to previous conclusions made from the data. For example a rotation of the inlet valve towards the fluid side led to better inlet jet formation and higher wall shear rates along the inlet wall. The TSPs of the wall shear maps along surface 1, shown in Figure 149, decreased from 0.48 to 0.23 to 0.07 as the inlet valve was shifted from 0° to +15° to +30°, respectively.

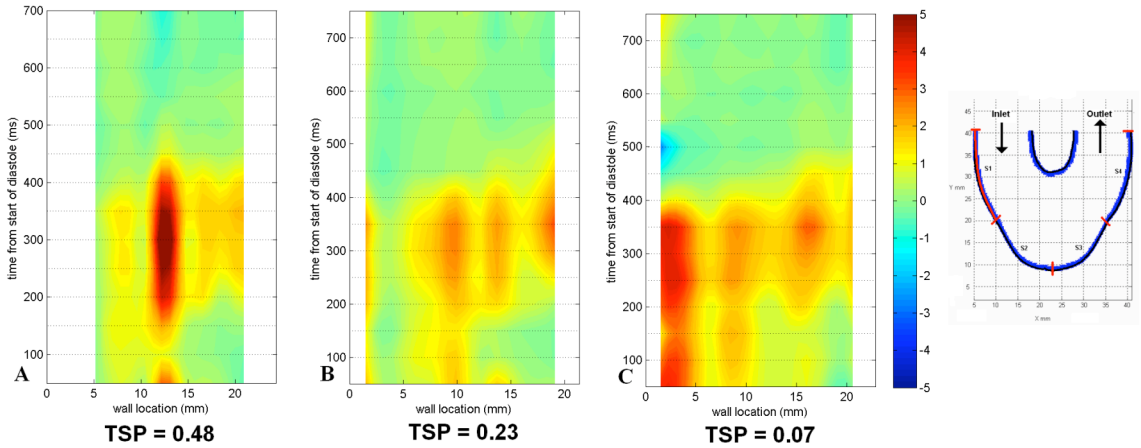

Figure 149: The wall shear rate maps along surface 1, located on the inlet side and highlighted in red to the right, of the 8.2 mm plane of the (A) 0° inlet 0° outlet, (B) +15° inlet 0° outlet, (C) and +30° inlet 0° outlet valve orientations. The reduction in TSPs corresponded with the previous conclusion that an increased valve orientation towards the fluid side provided better wall washing.

A smoother outflow, including higher wall shear rates across the entire surface, was also observed with a rotation of the outlet valve towards the fluid side of the device. The TSPs along surface 4 when the outlet valve was rotated from 0 to +15 to +30 were 0.33, 0.10 and 0.09, respectively. In comparison to the decrease in TSP seen with the inlet valve change, the TSP along the outlet surface remained nearly the same at both +15 and +30. When observing the wall shear rate maps, shown in Figure 150, both these orientations contain wall shear rates above the $\dot{\gamma}_{cutoff}$ across nearly the entire surface. The visible differences in the maps come from the duration and magnitude of the wall shear rate; however, the TSP at each location reaches a value of zero once the $\dot{\gamma}_{cutoff}$ has been reached

for the t_{crit} because this is considered enough to prevent thrombus deposition. Therefore, a value of zero can look different in the shear maps, but the single surface TSP reaches the same result. This illustrates the need to use the TSP in addition to the wall shear rate map, and not alone.

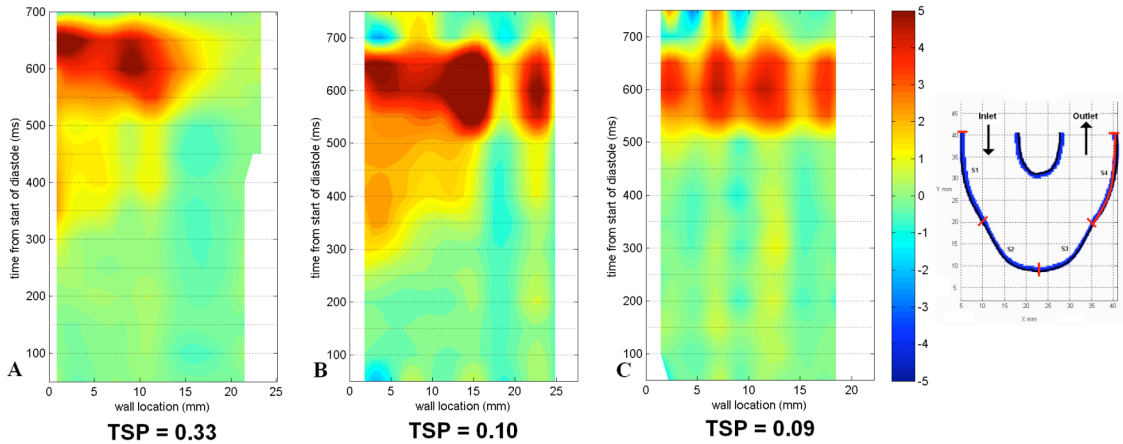

Figure 150: The wall shear rate maps along surface 4, located on the outlet side and highlighted in red to the right, of the 8.2 mm plane of the (A) 0° inlet 0° outlet, (B) 0° inlet +15° outlet, (C) and 0° inlet +30° outlet valve orientations. The TSPs did not show a large change between orientations.

The plots of the TSPs at each location along surface 4 provide a better picture of problematic locations and are shown in Figure 151. For the 0° outlet valve orientation, the surface plots show an increase in potential thrombus formation along the latter part of the wall. In comparison the +15° and +30° outlet valve orientations have similar patterns.

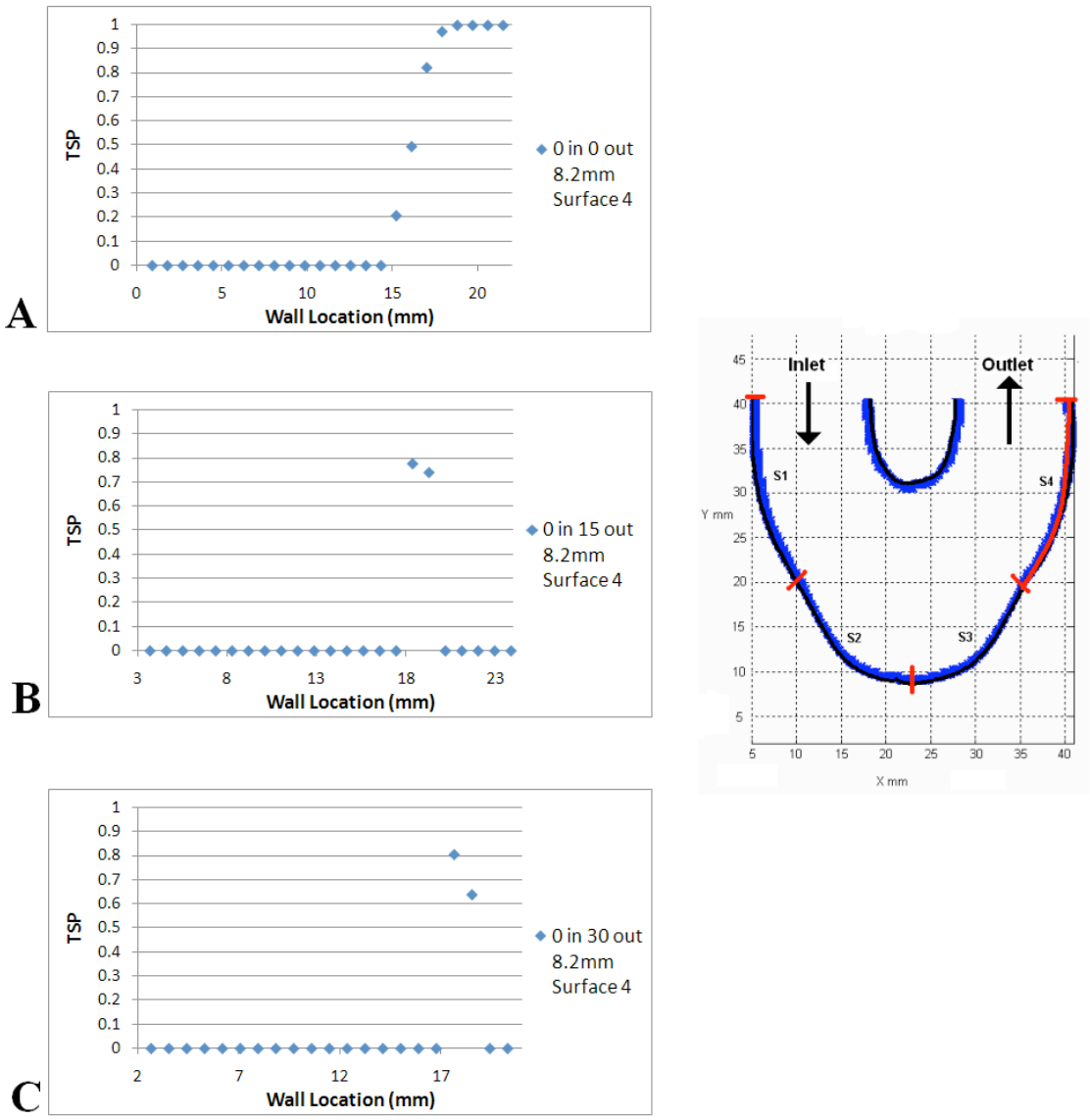

Figure 151: The TSP plots along surface 4 of the 8.2 mm parallel planes for the (A) 0° inlet 0° outlet, (B) 0° inlet +15° outlet, (C) and 0° inlet +30° outlet valve orientations. These plots helps located areas that could be prone to thrombus formation.

The valve orientation study concluded that a +15° inlet and +15° outlet orientation provided the best flow fields and wall washing. The TSPs confirmed that this combination had the least thrombus potential when looking at all four surfaces. However, it should also be noted that the 0° inlet and +15° outlet also had very similar TSPs at each surface. When comparing the wall shear rate plots of all four surfaces for the two conditions, shown in Figure 152, we notice that many of the characteristics are similar. The inlet surface, surface 1, contains wall shear rates above the $\dot{\gamma}_{cutoff}$ across the entire surface. Surfaces 2 and 3 contain shear rates above $\dot{\gamma}_{peak}$ around the same magnitudes and locations. A similar pattern is also seen at surface 4, including a low shear zone near the end of the outlet port.

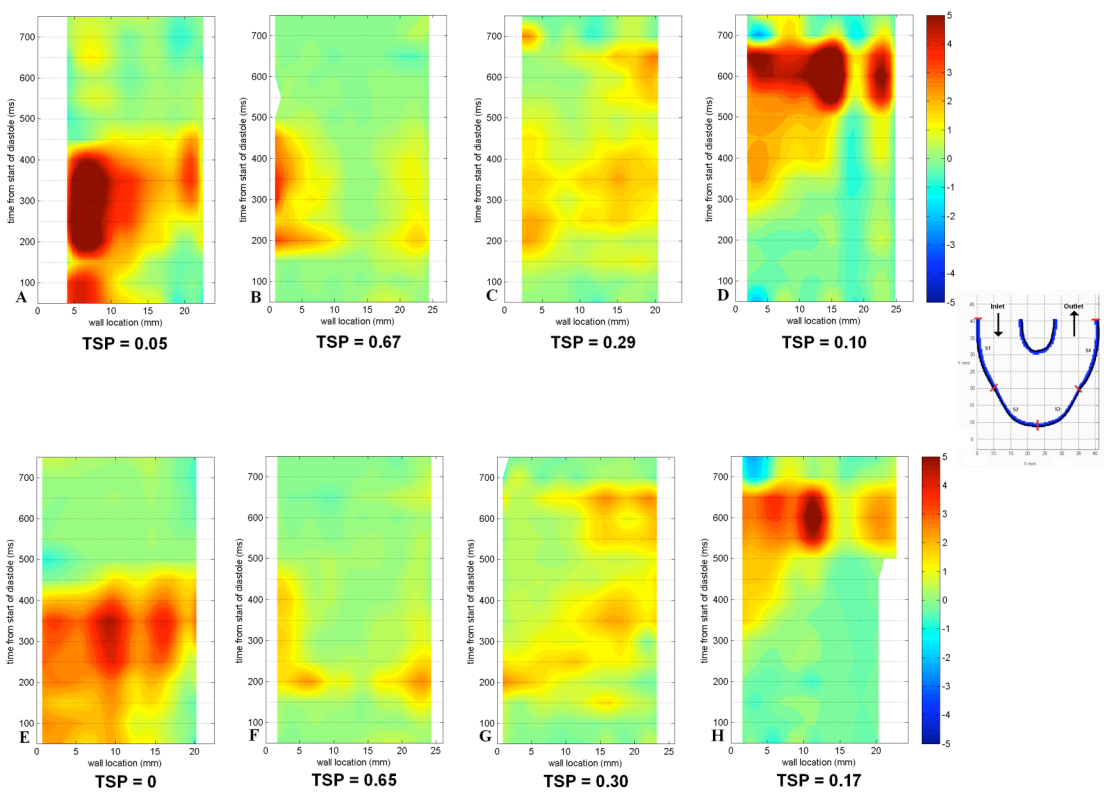

Figure 152: The wall shear rate maps for all four surfaces, shown to the right, of the (A-D) 0° inlet +15° outlet and (E-H) +15° inlet +15° outlet orientations. The two orientations maintained similar flow maps and similar TSPs along all four surfaces, except for surface 1 (A, E) which had a noticeable change due to the difference in the inlet valve orientation.

The surface plots of the TSP values at each location also contain very similar patterns and values, as shown in Figure 153. Both valve orientations show very low TSP values along the inlet and outlet surface. They also both contain high TSP values along the bottom of the device. This indicates that the potential for thrombus deposition between these two orientation conditions is very similar. These plots also show how the TSP can be helpful in locating specific problematic areas across the device surface.

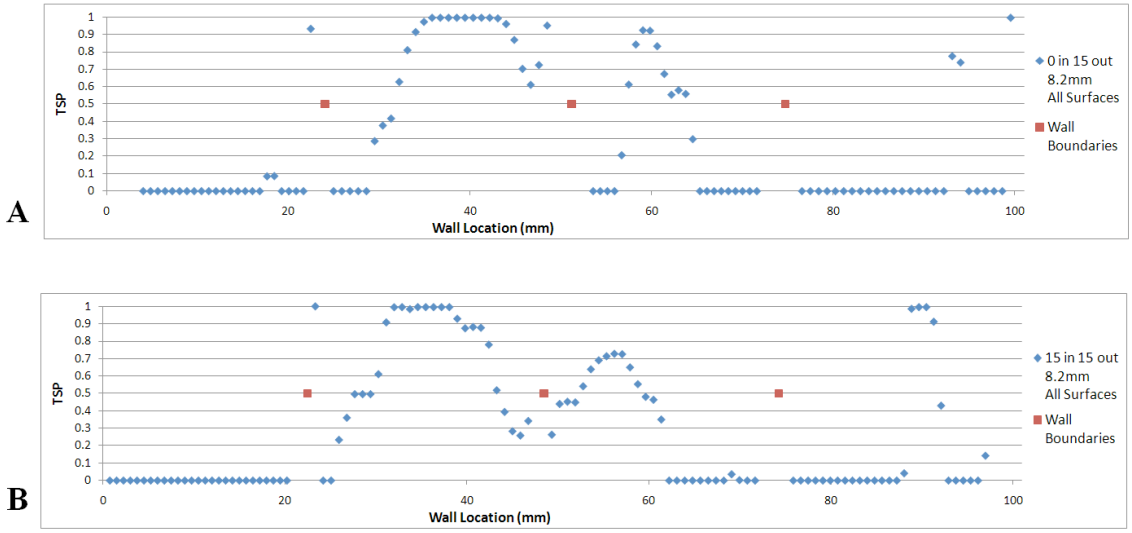

Figure 153: The TSP plots along the entire outer wall of the 8.2 mm plane for the (A) 0° inlet +15° outlet and (B) +15° inlet +15° outlet. This includes surfaces 1-4 from left to right, and the boundaries between each surface are indicated by the red square. The TSP values along the outer wall show similar values and patterns for the two sets of orientations, indicating similar potentials for thrombus deposition.

When considering the overall flow patterns, the original valve orientation selection of +15° inlet and +15° outlet remains. However, the TSP has proven to be an additional tool that helps narrow the focus of the analysis. This is especially helpful when dealing with a large amount of data.

6.3.2 Stroke Volume Reduction Study

6.3.2.1 Results

After confirming that the TSPs were a helpful tool for comparison, it was desirable to use them to look at some of the conclusions from the flow reduction study. Because of the large amount of data, examples were selected from the discussion of the stroke volume (SV) reduction study. These included surface 1 of the 7 mm parallel plane, which highlighted the behavior of the inlet jet and diastolic wall washing. It also included surface 3 of the 11 mm parallel plane, which helped indicate the strength of the rotational flow field. The TSPs for both of these surfaces are listed in Table 5 for each SV condition.

Table 5: TSP values for the surfaces used for comparison for the SV reduction study

Condition	TSP 7 mm Plane Surface 1	TSP 11 mm Plane Surface 3
12 cc Quick	0.02	0.06
9.6 cc Quick	0.09	0.57
7.2 cc Quick	0.23	0.93
4.8 cc Quick	0.50	0.99
12 cc Slow	0.21	0.38
9.6 cc Slow	0.45	0.99
7.2 cc Slow	0.55	1
4.8 cc Slow	0.99	1

6.3.2.2 Discussion

The effect of SV reduction while using the quick fill method showed that the wall washing along the inlet decreased in duration and magnitude as the SV was reduced. The TSP values mimicked this decrease. The TSP increased for each reduction in SV from 0.02 for the 12 cc SV to 0.5 for the 4.8 cc SV. These values correspond well with what was observed in the wall shear rate maps, which are shown in Figure 154.

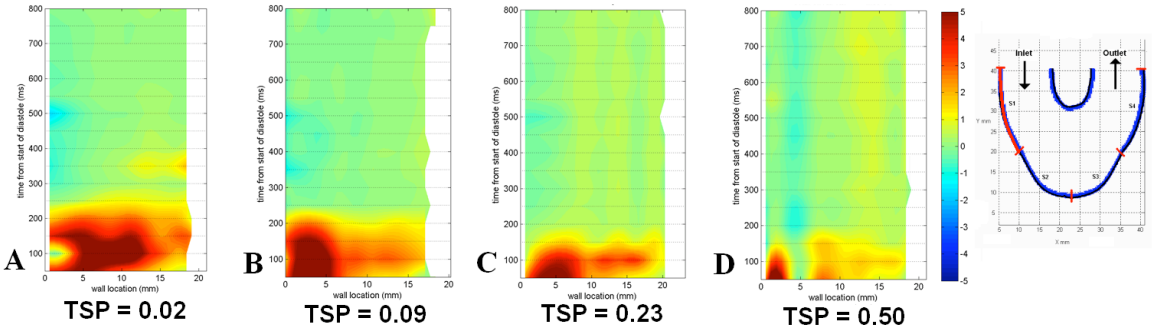

Figure 154: The wall shear rate maps along surface 1, located along the inlet and highlighted in red to the right, of the 7 mm parallel plane for the (A) 12 cc, (B) 9.6 cc, (C) 7.2 cc and (D) 4.8 cc SV quick filling conditions. The TSP showed an increase as the SV was reduced, mimicking the conclusions made by the wall shear rate map analysis.

Previous results also indicated that the quick filling method resulted in a reduction in rotational strength as the stroke volume was reduced. This was confirmed by the patterns seen along surface 3, which is along the bottom of the outlet side of the device. The TSP results along this surface of the 11 mm parallel plane found that the 12 cc SV had a low potential of only 0.06. The TSP then jumped up considerably to 0.57 at 9.6 cc and nearly to 1 for the lowest two SVs. These results agree with the original conclusions that rotational flow is lost with SV reduction. However, they also indicate that the 7.2 cc SV has a large increase in thrombus potential. This means this condition may need to be investigated further to see if the wall washing is adequate for use.

The slow filling method contained lower magnitude wall shear rates than the quick, but for longer durations. The TSP values along the inlet surface agreed that the 12 cc SV contained the best washing with a value of 0.21. Interestingly, the 9.7 cc and 7.2 cc SVs had similar TSP values, and when the wall shear rate maps are compared, this is confirmed. The characteristics of the two maps are similar, as shown in Figure 155, which indicates that the TSP is mimicking these results accurately.

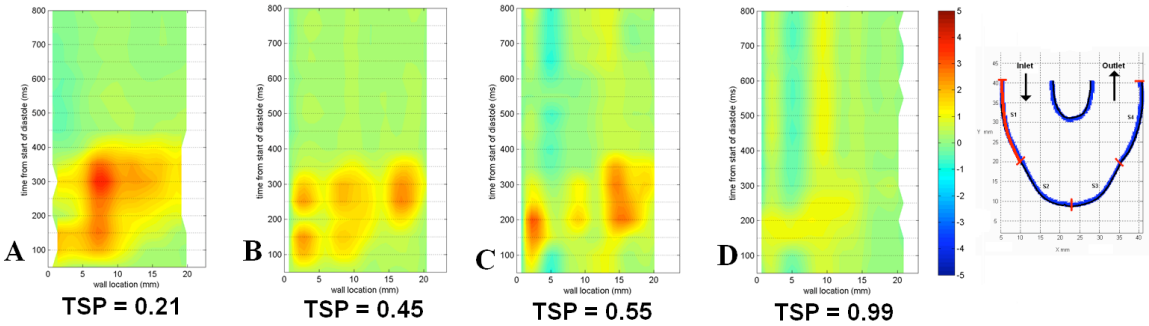

Figure 155: The wall shear rate maps along surface 1, located along the inlet and highlighted in red to the right, of the 7 mm parallel plane for the (A) 12 cc, (B) 9.6 cc, (C) 7.2 cc and (D) 4.8 cc SV slow filling conditions. The TSP showed an increase as the SV was reduced but not in expected increments.

With the exception of the 12 cc SV, the slow filling method results in a poorer rotational flow field. This was confirmed by the TSP values along surface 3. While the 12 cc SV had a TSP of 0.38 along this surface of the 11 mm parallel plane, the other SVs had values at or near 1.

The TSP values also show the previous conclusion that the quick filling method provides better wall washing than the slow filling method. This is especially apparent at the inlet surface. With the quick filling method, the highest TSP occurs with the 4.8 cc, which is 0.54, while the slow filling method results in TSPs above 0.6 for all SVs except 12 cc. An interesting comparison is a plot of the TSP values of both filling conditions along the

inlet surface. As presented in Figure 156, the slow filling method results in a more varied TSP, meaning the surface is not being washed as uniformly as with the quick filling condition.

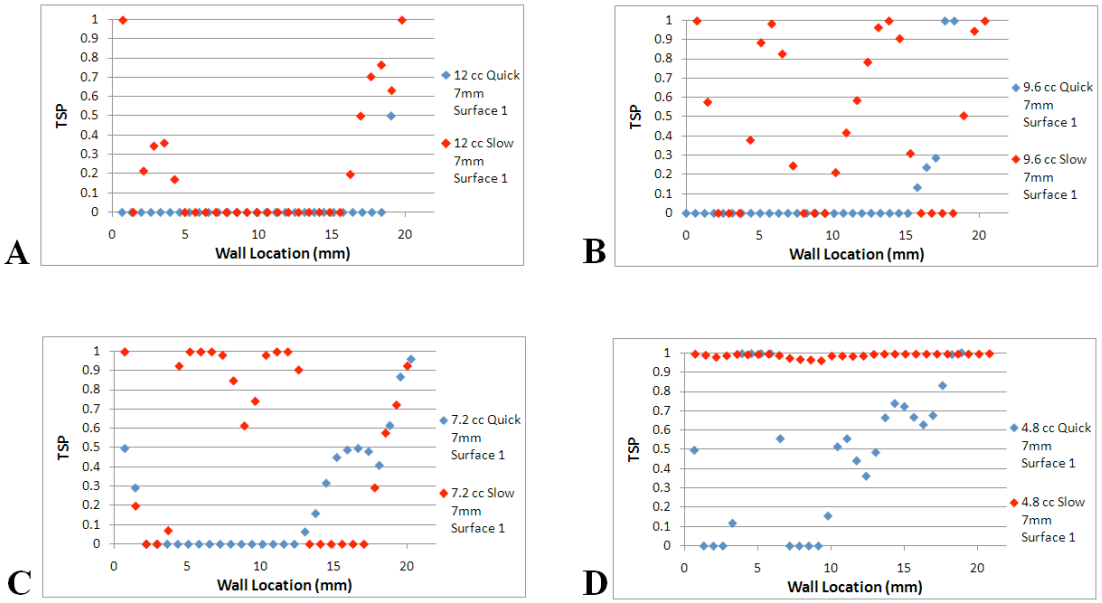

Figure 156: The TSP plots along surface 1 of the 7 mm plane for the (A) 12 cc, (B) 9.6 cc, (C) 7.2 cc and (D) 4.8 cc stroke volumes. Each plot contains the TSP values of both filling conditions along this inlet surface. The slow filling method TSPs, plotted in red, for the larger three SVs show a more sporadic pattern, indicating the wall washing along the surface is not as uniform. The 4.8 cc SV does not have this pattern because of the poor overall washing which results in high TSP values.

6.4 Conclusions

We have successfully developed a TSP metric that uses information from wall shear rate maps obtained from PIV data. This metric has shown logical correspondence with wall shear rate maps, and similar conclusions can be drawn from the two sets of results. The TSP serves as a way to use the often subjective wall shear rate maps and provide an objective metric. Comparisons using the TSP have the ability to narrow the focus of analysis when considering large amounts of data. This is especially helpful when considering parametric studies of device variations.

The metric is not, however, without its limitations. The use of constants in the equation leads to a limitation in the maximum amount of information obtained by the single metric. Two vastly different sets of data could result in the same TSP. While the TSP helps focus analysis, it cannot be used alone. The behavior of the flow maps is still of primary importance.

As shown by this study, the TSP equation also shows continuous sensitivity to the values of $\dot{\gamma}_{peak}$, $\dot{\gamma}_{cutoff}$, and t_{crit}. It may be used for comparisons, but cannot be correlated with *in vivo* thrombus deposition. A major reason for this is the lack of information about platelet and thrombus depositions in these types of flow fields. Better deposition information for pulsatile flows along these types of materials is critically needed. A better understanding of the behavior of platelet and thrombus formation throughout the cycle will produce better metrics for us in a TSP, making it a highly useful tool for VAD design.

Overall, this TSP is a new tool for helping analyze wall shear rate data for applications such as the PVAD. While the model is currently a simplification of the complex thrombus deposition process, it does allow for more objective comparisons between device variations. It also lays the foundation for a more accurate metric to be developed when better *in vivo* information becomes available.

Chapter 7

SUMMARY AND CONCLUSIONS

7.1 Summary

The desire to use ventricular assist devices for bridge-to-recovery remains a high priority for pediatric patients, the population with the lowest number of transplantable organs. Use of these devices for this purpose requires a change to the device operation during weaning. Because this often involves a reduction in device flow rate, these operational changes will affect the device fluid mechanics. Because of the relationship between device fluid mechanics and thrombus deposition, it was necessary to investigate the effect of these operational conditions on the pneumatically driven pulsatile Penn State pediatric ventricular assist device (PVAD).

The fluid mechanics of two flow rate reduction methods were studied using *in vitro* experiments. Particle image velocimetry was used to measure the flow through an acrylic model of the PVAD placed in a mock circulatory loop. The first of these methods looked at a beat rate reduction from 75 to 50 bpm. We found that reducing the beat rate led to a reduction in the flow elements necessary to prevent thrombus formation. This included a weaker rotational flow field, an increase in areas of stagnant flow throughout the device, and a reduced amount of wall washing. These combined elements resulted in an environment conducive to thrombus deposition and formation, demonstrating that a beat rate reduction was not a desirable form of flow rate reduction for weaning.

A second flow rate reduction study used a stroke volume (SV) reduction method for two filling conditions. When using a quick filling method, we found that for reductions in SV of up to 60% the desirable flow characteristics for preventing thrombus deposition, including strong, early rotational flow fields and adequate wall washing were maintained. In comparison, a slow filling method resulted in poor rotational flow fields, including poor wall washing and an increase in stagnant flow for all SV reductions. Even with the quick fill method, the reduction of SV to 40% gave large areas of stagnation and poor overall flow. A reduction in SV to this level is not recommended. Overall the SV reduction method proved to have better fluid mechanic characteristics than the beat rate reduction method.

The last part of this investigation looked at the formulation of a thrombus susceptibility potential (TSP) that could be applied to the wall shear rate data obtained from PIV. This was desirable in order to help focus the analysis of the large amounts of PIV data obtained during our *in vitro* studies. Therefore, a TSP metric that could be calculated from the wall shear rate maps was developed. This metric compared well to the wall shear rate maps and proved to be helpful for the comparisons between device or conditional variations. This metric is, however, limited in its ability to accurately predict *in vivo* thrombus deposition because of the lack of information regarding the behavior of platelets on polymer materials in pulsatile conditions.

7.2 Conclusions

We examined the effects of operational changes necessary for weaning on the fluid mechanics of the PVAD. We discovered that flow rate reduction led to changes in the flow field which could increase the chance of thrombus deposition within the device, while a stroke volume reduction method, employing a quick filling condition, contained the best flow patterns for the reduction of thrombus deposition.

7.3 Future Work

While this investigation indicates that a stroke volume reduction method produces more desirable flow fields for weaning the flow field is not ideal. Further investigations to improve these flow fields, including studies of more operational protocol changes including systolic duration lengths and more filling options, should be completed. The ultimate goal is to create a weaning protocol complete with operational limits that clinicians can use. The TSP metric developed here is a very simplistic tool. One way to improve this metric is to investigate better shear rate boundaries for the materials and flow fields being studied.

BIBLIOGRAPHY

American Heart Association: *Statistical Reference Book*, Texas, 2010.

American Heart Association: *Statistical Reference Book*, Texas, 2005.

Akagawa E, Lee H, Tatsumi E, Homma A, Tsukiya T, Katagiri N, Kakuta Y, Nishinaka T, Mizuno T, Ota K, Kansaku R, Taenaka Y: Effects of mechanical valve orifice direction on the flow pattern in a ventricular assist device. *Japanese Society of Artificial Organs* 10: 85-91, 2007.

Bachmann C, Hugo G, Rosenberg G, Deutsch S, Fontaine A, Tarbell JM: Fluid dynamics of a pediatric ventricular assist device. *Artificial Organs* 25: 362-372, 2000.

Balasubramanian V and Slack SM: The effect of fluid shear and co-absorbed proteins on the stability of immobilized fibrinogen and subsequent platelet interactions. *J Biomater Sci Polymer Edn* 13: 543-561, 2002.

Baldwin JT, Deutsch S, Geselowitz DB, Tarbell JM: LDA measurements of mean velocity and reynolds stress fields within an artificial heart ventricle. *J Biomech Eng* 116: 190-200, 1994.

Baldwin JT, Borovetz HS, Duncan BW, Gartner MJ, Jarvik RK, Weiss WJ, Hoke TR: The national heart, lung, and blood institute pediatric circulatory support program. *Circulation* 113: 147-155, 2006.

Black MD, Coles JG, Williams WG, Rebeyka IM, Trusler GA, Bohn D, Gruenweld C, Freedom RM: Determinants of successes in pediatric cardiac patients undergoing extracorporeal membrane oxygenation. *Ann Thorac Surg* 60: 133-138, 1995.

Colman RW: Mechanisms of thrombus formation and dissolution. *Cardiovasc Pathol* 2: 23S-31S, 1993.

Cooper BT, Roszelle BN, Long TC, Deutsch S, Manning KB: The 12 cc Penn State pulsatile pediatric ventricular assist device: fluid dynamics associated with valve selection. *ASME J Biomech Eng* 130: 041019, 2008.

Cooper BT, Roszelle BN, Long TC, Deutsch S, Manning KB: The influence of operational protocol on the fluid dynamics in the 12 cc Penn State pulsatile pediatric ventricular assist device: the effect of end-diastolic delay. *Artificial Organs,* 34: E122-E133, 2010.

Daily BB, Pettitt TW, Salvatore PS, Pierce WS: Pierce-Donachy pediatric VAD: progress in development. *Ann Thorac Surg* 61: 437-43, 1996.

del Nido PJ, Armitage JM, Fricker FJ, Shaver M, Cipriani L, Dayal G, Park SC, Siewers RD: Extracorpreal membrane oxygenation support as a bridge to pediatric heart transplantation. *Circulation* 90(5): 1166-1169, 1994.

Deutsch S, Tarbell JM, Manning KB, Rosenberg G, and Fontaine A: Experimental fluid mechanics of pulsatile artificial blood pumps *Ann Rev of Fluid Mechanics* 38:65-86, 2006.

Didsheim P: Current concepts of thrombosis and infection in artificial organs. *ASAIO J* 40(2): 230-237, 1994.

Duncan BW, Hraska V, Jonas RA, Wessel DL, Del Nido PJ, Laussen PC, Mayer JE, Lapierre RA, and Wilson JM: Mechanical circulatory support in children with cardiac disease. *J Thorac Cardiovasc Surg* 117: 529-42, 1999.

Duncan BW, Bohn DJ, Atz AM, French JW, Laussen PC, Wessel DL: Mechanical circulatory support for the treatment of children with acute fulminant myocarditis. *J Thoracic Cardiovasc Surg* 122: 440-448, 2001.

Farrar DJ, Holman WR, McBride LR, Kormos RL, Icenogle TB, Hendry PJ, Moore CH, Loisance DY, El-Banayosy A, and Frazier H: Long-term follow-up of Thoratec ventricular assist device bridge-to-recovery patients successfully removed from support after recovery of ventricular function. *J Heart Lung Transplant* 21: 516-521, 2002.

Frazier OH, Benedict CR, Radovancevic B, Bick RJ, Capek P, Springer WE, Macris MP, Delgado R, Buja LM: Improved left ventricular function after chronic left ventricular unloading *Ann Thorac Surg* 62: 675-682, 1996.

Goldstein JG, Oz MC, Rose EA: Implantable left ventricular assist devices. *The New England Journal of Medicine* 339: 1522-1533, 1998.

Grant I: Particle image velocimetry: a review. *Proc Instn Mech Engers* 211: C, 1997.

Hanson SR: Device thrombosis and thromboembolism. *Cardiovascular Pathology* 2: 157S-165S, 1993.

Hart DP: Super-resolution PIV processing by recursive local-correlation *J Visualization* 10: 187-194, 1999.

Health Resources and Services Administration, Healthcare Systems Bureau, Division of Transplantation: Annual Report of the U.S. Organ Procurement and Transplantation Network and the Scientific Registry of Transplant Recipients: Transplant Data 1996-2005, Maryland, 2006.

Hetzer R, Loebe M, Potapov EV, Weng Y, Stiller B, Henning E, Alexi-Meskishvili V, Lange PE: Circulatory support with pneumatic paracorporeal ventricular assist device in infants and children *Ann Thorac Surg* 66: 1498-1506, 1998.

Hochareon P, Manning KB, Fontaine AA, Deutsch S, Tarbell JM: Diaphragm motion affects flow patterns in artificial Artificial Organs 27(12): 1102-1109, 2003. (a)

Hochareon P: Development of particle image velocimetry (PIV) for wall shear stress estimation within a 50cc Penn State artificial heart ventricular chamber. PhD Thesis, The Pennsylvania State University, Dec 2003. (b)

Hochareon P, Manning KB, Fontaine AA, Tarbell JM, Deutsch S: Wall shear-rate estimation within the 50cc Penn State artificial heart using particle image velocimetry *J Biomech Eng* 126: 430-437, 2004. (a)

Hochareon P, Manning KB, Fontaine AA, Tarbell JM, Deutsch S: Correlation of in vivo clot deposition with the flow characteristics in the 50 cc Penn State artificial heart: a preliminary study *ASAIO J* 50: 537-542, 2004. (b)

Hubbell JA and McIntire LV: Visualization and analysis of mural thrombogenesis on collage, polyurethane and nylon *Biomaterials* 7: 354-363, 1986.

Ishino K, Loebe M, Ulemann F, Weng Y, Henning E, Hetzer R: Circulatory support with paracorpreal pneumatic ventricular assist device (VAD) in infants and children. *Eur J Cardiothorac Surg* 11: 965-972, 1997.

Kreider JW, Manning KB, Oley LA, Fontaine AA, Deutsch S: The 50 cc Penn State left ventricular assist device: a parametric study of valve orientation flow dynamics. *ASAIO J* 52: 123-131, 2006.

Lamson TC, Rosenberg G, Geselowitz DB, Deutsch S, Stinebring DR, Frangos JA, Tarbell JM: Relative blood damage in the three phases of a prosthetic heart valve flow cycle *ASAIO J* 39: M626-M633, 1993.

Long JA, Undar A, Manning KB, Deutsch S: Viscoelasticity of pediatric blood and its implications for the testing of a pulsatile pediatric blood pump *ASAIO J* 51: 563-566, 2005.

Medvitz RB: Development and validation of a computational fluid dynamic methodology for pulsatile blood pump design and prediction of thrombus potential. PhD Thesis, The Pennsylvania State University, May 2008.

Malaisrie SC, Pelletier MP, Yun JJ, Sharma K, Timek TA, Rosenthal DN, Wright GE, Robbins RC, Reitz BA: Pneumatic paracorpreal ventricular assist device in infants and children: initial Stanford experience. *J Heart Lung Transplant* 27: 173-177, 2008.

Mancini DM, Beniaminovitz A, Levin H, Catanese K, Flannery M, DiTullio M, Savin S, Cordisco ME, Rose E, Oz M: Low incidence of myocardial recovery after left ventricular assist device implantation in patients with chronic heart failure. *Circulation* 98: 2383-2389, 1998.

Manning KB, Wivholm BD, Yang N, Fontaine AA, Deutsch S: The flow behavior within the Penn State 12 cc pulsatile pediatric ventricular assist device. *Artificial Organs* 32: 442-452, 2008.

Maybaum S, Mancini D, Xydas S, Starling RC, Aaronson K, Pagani FD, Miller LW, Margulies K, McRee S, Frazier OH, Torre-Amione G: Cardiac improvement during mechanical circulatory support: a prospective multicenter study of the LVAD working group. *Circulation* 115: 2497-2505, 2007.

Morrow WR, Naftel D, Chinnock R, Canter C, Boucek M, Zales V, McGiffin DC, Kirklin JK: Outcome of listing for heart transplantation in infants younger than six months: predictors of death and interval to transplantation. *J Heart and Lung Transplant* 16: 1255-1266, 1997.

Ohye RG, Bove EL: Advances in congenital heart surgery. *Current Opinion in Pediatrics* 13(5): 473-481, 2001.

Olsen DB: The history of continuous-flow blood pumps. *Artificial Organs* 24(6): 401-404, 2000.

Phillips WM, Brighton JA, Pierce WS. Artificial heart evaluation using flow visualization techniques. *SAIO Trans* 18:194–99, 1972.

Potapov EV, Stiller B, Hetzer R: Ventricular assist devices in children: current achievements and future perspectives. *Pediatr Transplantation* 11: 241-255, 2007.

Prasad AK: Particle image velocitmetry. *Current Science* 79(1): 51-60, 2000.

Raffel M, Willert C and Kompenhans J: *Particle Image Velocimetry* Berlin, Springer, 1998.

Reinhartz O, Stiller B, Eilers R, Farrar DJ: Current clinical status of pulsatile pediatric circulatory support. *ASAIO J* 48: 455-459, 2002.

Rose EA, Gelijns AC, Moskowitz AJ, Heitjan DF, Stevenson LW, Dembitsky W, Long JW, Ascheim DD, Tierney AR, Levitan RG, Watson JT, Meier P, Ronan NS, Shapiro PA, Lazar RM, Miller LW, Gupta L, Frazier OH, Desvigne-Nickens P, Oz MC, and Poirier VL: Randomized evaluation of mechanical assistance for the treatment of congestive heart failure (REMATCH) study group. Long-term use of a left ventricular assist device for end-stage heart failure *N Engl J Med* 345: 1435-1443, 2001.

Rosenberg G, Phillips WM, Landis D, and Pierce WS: Design and evaluation of the Pennsylvania State University mock circulatory system *ASAIO J* 4: 41-49, 1981.

Roszelle BN, Cooper BT, Long TC, Deutsch S, Manning KB: Penn state 12 cc pulsatile pediatric ventricular assist device: flow field observations at a reduced beat rate with application to weaning. *ASAIO J* 54: 325-331, 2008.

Roszelle BN, Deutsch S, Manning KB. Flow visualization of three-dimensionality inside the Penn State pulsatile pediatric ventricular assist device. *Ann Biomed Eng* 38(2): 439-455, 2010.

Roszelle BN, Deutsch S, Manning KB. A parametric study of valve orientation on the flow patterns of the Penn State pulsatile pediatric ventricular assist device. *ASAIO J* 56: 356-363, 2010.

Slaughter MS, Silver MA, Farrar DJ, Tatooles AJ, Pappas PS: A new method of monitoring recovery and weaning the Thoratec left ventricular assist device *Ann Thorac Surg* 71: 215-218, 2001.

Slaughter MS, Sobieski MA, Koenig SC, Pappas PS, Tatooles AJ, Silver MA: Left ventricular assist device weaning: hemodynamic response and relationship to stroke volume and rate reduction protocols *ASAIO J* 52: 228, 2006.

Westerweel J: Theoretical analysis of the measurement precision in particle image velocimetry. *Experiments in Fluids* 29(S1): S003-S012, 2000.

Yano T, Sekine K, Mitoh A, Mitamura Y, Okamoto E, Kim D, Nishimura I, Murabayashi S, and Yozu R: An estimation method of hemolysis within an axial flow blood pump by computational fluid dynamics analysis. *Artificial Organs* 27(1):920-925, 2003.

Breigh Nonte Roszelle

Breigh Nonte Roszelle was born on June 5th, 1984 in Denver, Colorado. She was raised in Littleton, CO and graduated with high honors from Arapahoe High School in 2002. She went on to attend Colorado State University where she graduated in 2006 as a University Honors Scholar with a Bachelors of Science degree in Mechanical Engineering. While at CSU she became a member of Pi Tau Sigma and Tau Beta Pi, two engineering honor societies. After graduation she went to work in the Artificial Heart Lab at The Pennsylvania State University under Dr. Keefe Manning. Breigh received her Masters of Science in Bioengineering in 2008 while investigating the three-dimensional flow patterns of the Penn State pediatric ventricular assist device. Continuing to work in the field of biofluid mechanics, Breigh completed her PhD in Bioengineering in 2010. She has published work in the fields of ventricular assist devices and biofluid mechanics, as well as presented her work at multiple conferences around the World. She is currently a member of the American Society of Artificial Internal Organs and the Biomedical Engineering Society.